Analysis of chemotherapeutic-induced tumor dormancy in *Glioblastoma multiforme* and alternative therapy approaches

Dissertation

zur Erlangung des Doktorgrades der

Mathematisch-Naturwissenschaftlichen Fakultät der

Christian-Albrechts-Universität zu Kiel

vorgelegt von

Vivian Adamski

Kiel, August 2019

Erster Gutachter: Professor Dr. Axel Scheidig

Zweite Gutachterin: Professor Dr. Dr. Janka Held-Feindt

Tag der mündlichen Prüfung: 11. Oktober 2019

Zum Druck genehmigt: 11. Oktober 2019

Preface

This dissertation was partly written cumulative. Parts of this dissertation have already been published in the following two publications:

Adamski V*, Schmitt C*, Ceynowa F, Adelung R, Lucius R, Synowitz M, Hattermann K, Held-Feindt J. Effects of sequentially applied single and combined temozolomide, hydroxychloroquine and AT101 treatment in a long-term stimulation glioblastoma in vitro model. *J Cancer Res Clin Oncol*, 144:1475 – 1485, 2018. doi: 10.1007/s00432-018-2680-y

Adamski V, Hempelmann A, Flüh C, Lucius R, Synowitz M, Hattermann K#, Held-Feindt J#. Dormant glioblastoma cells acquire stem cell characteristics and are differentially affected by Temozolomide and AT101 treatment. *Oncotarget*, 8:108064 – 108078, 2017. doi: 10.18632/oncotarget.22514

*/# these authors contributed equally

In this dissertation, data, that are parts of the mentioned publications, are briefly described, albeit, additional, unpublished data are explained in more detail.

Abstract

Glioblastoma Multiforme (GBM) is an incurable, malignant, primary brain tumor. The poor prognosis of patients relies on the ability of the tumor to evade therapy regimen and rapidly develop tumor recurrences. The impeded entry of therapeutics into the brain tissue by the blood-brain barrier (BBB) yields subletal doses of agents in the tumor, resulting in chemotherapeutically triggered escape mechanisms like tumor dormancy, a resting state of a cell or tumor mass. This study aimed at both a more detailed understanding of molecular pathways as well as environmental influences on the therapeutically induced entry into and exit from dormancy of GBM cells and, based on this knowledge, the improvement of therapy by introducing alternative compounds and strategies.

Upon subletal treatment with temozolomide (TMZ), the standard therapeutic, GBM cells remained unproliferative. This state was not only described by dormant but also stem-cell features, indicated by an upregulation of typical dormancy and stem-cell markers and a high ability of dormant cells to form spheroids. Moreover, dormancy entry was characterized by an increased expression of *CCL2* and *SAA2*, while in dormancy exit, attained by further cultivation without TMZ treatment, *THSD4*, *FSTL3* and *VEGFC* were upregulated. Interestingly, co-stimulation with chemokines, mimicking an inflammatory environment, delayed the entry into and exit from dormancy, also mirrored in the reduction of the upregulation of identified genes.

The use of alternative drugs and stimulation schemes adapted to classic treatment appeared to be promising in overcoming therapy escape including dormancy. Especially, sequential application of TMZ+AT101, the R-(-)-enantiomer of the cottonseed-derived polyphenol gossypol, followed by AT101 alone increased glioma cell death in mono-cultures, but was less harmful for astrocytes. However, co-culturing of primary GBM cells, astrocytes and microglia in an incomplete tumor-resection model revealed a protective effect of normal brain cells to tumor cell death, while glioma cells enhanced astrocytic cell death.

Considering sequential application of TMZ and AT101, encapsulation of AT101 into cubosomes, to improve passaging across the BBB, resulted in an increased cytotoxicity in glioma cells but not normal brain cells. In order to neglect BBB restrictions, a PDMS implant with tetrapodal channels was developed showing a high drug loading capacity and a sustained, long-term release of AT101 in artificial liquor.

In conclusion, TMZ drives GBM-cell escape into dormancy, thereby surviving treatment and inducing tumor re-growth. Next to oral TMZ administration, sequential application of alternative drugs such as AT101 via local release from implants or in terms of nanoparticle co-treatment might improve therapy success for patients.

Zusammenfassung

Glioblastoma Multiforme (GBM) bezeichnet einen unheilbaren, malignen, primären Hirntumor. Die schlechte Prognose für Patienten beruht auf der Eigenschaft des Tumors, sich der Therapie zu entziehen und schnell Tumorredizive zu bilden. Durch das behinderte Eintreten von Therapeutika in das Hirngewebe durch die Blut-Hirn-Schranke erreichen lediglich subletale Wirkstoffkonzentrationen den Tumor. Dies führt zu einem chemotherapeutisch induzierten Resistenzmechanismus wie Tumordormanz, ein Ruhestadium von Zellen oder dem gesamten Tumor. Ziel dieser Arbeit war es, einerseits ein genaueres Verständnis der molekularen Eigenschaften und der Einflüsse der Umgebung auf das Therapie-induzierte Eintreten in und Austreten aus der Dormanz von Glioblastomzellen zu schaffen und andererseits aufgrund dieser neuen Erkenntnisse alternative Wirkstoffe zu erproben und verbesserte therapeutische Strategien zu verfolgen.

Durch die Verabreichung einer subletalen Dosis Temozolomids (TMZ), des Standardtherapeutikums, verblieben GBM-Zellen unproliferativ. Dieses Stadium war nicht nur durch dormante, sondern auch Stammzelleigenschaften charakterisiert, was sich über die Hochregulation von typischen Dormanz- und Stammzellmarkern und die erhöhte Fähigkeit von dormanten Zellen, Spheroide zu bilden, zeigte. Darüber hinaus wurde beim Eintreten in Dormanz die Expression von *CCL2* und *SAA2* hochreguliert, während das Austreten aus der Dormanz, welches über die Fortführung der Kultivierung ohne TMZ-Behandlung erlangt wurde, über die erhöhte Expression von *THSD4*, *FSTL3* und *VEGFC* gekennzeichnet wurde. Interessanterweise hat die Ko-Stimulation mit Chemokinen, um eine inflammatorische Umgebung zu suggerieren, sowohl den Eintritt in als auch den Austritt aus der Dormanz verzögert, welches sich ebenfalls in der Reduktion der Hochregulation der identifizierten Gene widerspiegelte. Die Verwendung alternativer Wirkstoffe und Stimulationschemata, die an die klassische Behandlung adaptiert sind, stellte sich als vielversprechend heraus, um Therapieresistenz einschließlich Dormanz zu umgehen. Insbesondere die sequenzielle Verabreichung von TMZ+AT101, dem R-(-)-Enantiomer des Polyphenols Gossypol aus der Baumwolle, gefolgt von AT101 allein erhöhte den Zelltod von Gliomzellen in Monokulturen und war weniger schädlich für Astrozyten. Allerdings zeigte sich in der Kokultur von primären GBM Zellen, Astrozyten und Mikroglia in einem inkompletten Tumorresektionsmodel, dass normale Gehirnzellen protektiv auf den Tumorzelltod wirken, während Gliomzellen den Zelltod in Astrozyten induzierten.

Unter Betrachtung der sequenziellen Gabe von TMZ und AT101 erhöhte die Einkapselung von AT101 in Kubosomen, um den Transfer über die Blut-Hirn-Schranke zu verbessern, die Zytotoxizität in Gliomzellen, jedoch nicht in normalen Hirnzellen. Um die Beschränkungen der Blut-Hirn-Schranke zu umgehen, wurde ein Implantat

aus PDMS mit tetrapodalen Kanälen entwickelt, welches eine hohe Ladekapazität von Wirkstoff und eine kontinuierliche, langfristige Freisetzung von AT101 in artifiziellem Liquor aufwies.
Abschließend lässt sich sagen, dass TMZ GBM-Zellen in die Dormanz treibt, in der sie die Behandlung überleben und dann das Tumorwachstum wieder induzieren. Neben der oralen Verabreichung von TMZ könnte die sequenzielle Applizierung von alternativen Wirkstoffen wie AT101 über lokale Freisetzung aus Implantaten oder in Form von Nanopartikeln den Erfolg der Therapie für Patienten verbessern.

Abbreviations

β-Actin	ACTB
aCSF	Artificial cerebrospinal fluid
ADAM	A disintegrin and metalloproteinase
ADAMTSL	(A disintegrin and metalloproteinase with thrombospondin motifs)-like
AIC	5-Amino-imidazole-4-carboxamide
ANOVA	Analysis of variances
APS	Ammonium persulfate
BBB	Blood-brain barrier
Bcl-2	B-cell lymphoma 2
BCNU	Bischloroethyl-cyclohexyl-nitrosourea
BH3	Bcl-2 homolog domain 3
bis-AAF-R110	Bis-alanyl-alanyl-phenylalanyl-rhodamine 110
BSA	Bovine serum albumin
Cas	Caspase
CAU	Christian-Albrechts university
CCNU	Chloroethyl-cyclohexyl-nitrosourea
CD133	Cluster of differentiation 133
CDKN	Cyclin-dependent kinase inhibitor
cDNA	Complementary DNA
CED	Convection-enhanced delivery
CIMP	Clomipramine
CNS	Central nervous system
CQ	Chloroquine
CRISPR	Clustered regularly interspaced short palindromic repeats
Cryo-TEM	Cryogenic transmission electron microscopy
CSF	Cerebrospinal fluid
CT	Cycle of threshold
CTC	Circulating tumor cell
DAPI	4',6-Diamidino-2-phenylindole
DLC [%]	Drug loading capacity
DLS	Dynamic light scattering
DMEM	Dulbecco's Modified Eagle's Medium
DMSO	Dimethyl sulfoxide
DNA	Deoxyribonucleid acid
DNase	Deoxyribonuclease
DPSE	1,2-Distearoyl-sn-glycero-3-phosphoethanolamine

DSC ..... Differential scanning calorimetry
DTT ..... Dithiothreitol
ECM ..... Extracellular matrix
EDTA ..... Ethylenediaminetetraacetic acid
EE [%] ..... Entrapment efficiency
EGFR ..... Epidermal growth factor receptor
ELDA ..... Extreme limiting dilution analysis
ELS ..... Electrophoretic light scattering
EphA5 ..... Ephrin type A receptor 5
EPR ..... Enhanced permeability and retention
FBS ..... Fetal bovine serum
FDA ..... Food and Drug Administration
FRET ..... Fluorescence resonance energy transfer
FSTL3 ..... Follistatin-like 3
GADD45α ..... Growth arrest and DNA damage-inducible protein 45 α
GAPDH ..... Glycerinaldehyde 3−phosphate dehydrogenase
GBM ..... *Glioblastoma multiforme*
GFAP ..... Glial fibrilliar acidic protein
GIMP ..... GNU Image Manipulation Program
GMO ..... Glyceryl monooleate
H2BK ..... Histone cluster 1 H2B family member K
HCQ ..... Hydroxychloroquine
HEPES ..... N-2-Hydroxyethylpiperazine-N'-2-ethane sulfonic acid
HIF-1 ..... Hypoxia-inducible factor-1
HLA ..... Human Leukocyte Antigen
HSPA5 ..... Heat shock protein family A member 5
IDH1 ..... Isocitrate dehydrogenase 1
IF ..... Immunofluorescence
IF ..... Immunofluorescence
IGFBP5 ..... Insulin-like growth factor-binding protein 5
IL18 ..... Interleukin-18
ISO ..... International Organization for Standardization
Ki67 ..... Kiel-67
KLF4 ..... Krüppel-like factor 4
M-CSF ..... Macrophage colony-stimulating factor
MAP2 ..... Microtubule-associated protein 2
MAPK ..... Mitogen-activated protein kinase
MGMT ..... 6-O-Methylguanine-DNA methyltransferase
min ..... Minutes

MRI ..... Magnetic resonance imaging
mRNA ..... Messenger ribonucleic acid
MRP ..... Multidrug resistance protein
MSI1 ..... Musashi-1
MTIC ..... 3-Methyl-(triazen-1-yl)imidazole-4-carboxamide
MWCO ..... Molecular weight cut-off
NF1 ..... Neurofibromin 1
NK ..... Natural Killer
NKG2D ..... Natural killer-group 2D
NMR ..... Nuclear magnetic resonance
No. ..... Number
OCT4 ..... Octamer-binding transcription factor 4
OS ..... Overall survival
PBS ..... Phosphate-buffered saline
PCL ..... Poly(ϵ-caprolactone)
PDGFRA ..... Platelet-derived growth factor receptor A
PDI ..... Polydispersity index
PDMS ..... Poly(dimethylsiloxane)
PEG ..... Poly(ethylene glycol)
PFS ..... Progression-free survival
PLCL ..... Poly(L-lactide-co-caprolactone)
PLGA ..... Poly(D,L-lactide-co-glycolide)
PTEN ..... Phosphatase and tensin homolog
qRT-PCR ..... Quantitative real-time polymerase chain reaction
QXN ..... Quinacrine
ROS ..... Reactive oxygen species
RT ..... Room temperature
SAA2 ..... Serum amyloid A2
SAXS ..... Small angle X-ray scattering
SD ..... Standard deviation
SDF1α ..... Stromal-cell derived factor 1α
SDS ..... Sodium dodecyl sulfate
SDS-PAGE ..... Sodium dodecyl sulfate polyacrylamide gel electrophoresis
sec ..... Seconds
SEM ..... Scanning electron microscopy
SOX2 ..... Sex-determining region Y-box 2
TBS ..... Tris-buffered saline
TCGA ..... The Cancer Genome Atlas
TEMED ..... Tetramethylethylenediamine

TGFβ1	Transforming growth factor β 1
THSD4	Thrombospondin type-1 domain containing 4
TMZ	Temozolomide
TP53	Tumor protein 53
U	Units
UV/Vis	Ultraviolet/visible
v/v	Volume per volume
VEGF	Vascular endothelial growth factor
w/v	Weight per volume
WB	Western Blot
WST-1	4-[3-(4-Iodophenyl)-2-(4-nitrophenyl)-2H-5-tetrazolio]-1,3-benzene disulfonate

Contents

1 Introduction

1.1 Characteristics of *Glioblastoma multiforme*

1.1.1 Epidemiology and etiology

Although primary tumors of the brain and the central nervous system (CNS) only represent a small fraction (1.4%) of all new cancer cases in western countries in comparison with other tumors such as breast (15.5%) or lung cancers (13.5%), they show by far the highest death rate (70.5%) when diagnosed [American Cancer Society, 2018]. Strikingly, 74.5% of malignant primary brain and CNS tumors are classified as astrocytomas, a large group of tumors in which the most malignant form, termed *Glioblastoma multiforme* (GBM) has a global incidence rate of 2.98 newly diagnosed cases per 100,000 individuals per year [Ostrom et al., 2018, Leece et al., 2017]. Since 2016, the World Health Organization defines *Glioblastoma multiforme* as diffuse astrocytic grade IV tumor. In detail, the whole group of diffuse infiltrating astrocytic tumors are graded with increasing malignancy into diffuse astrocytoma grade II, anaplastic astrocytoma grade III, as well as oligodendroglioma grade II and III, and astrocytoma grade IV or glioblastomas [Louis et al., 2016]. Furthermore, the most malignant form, glioblastoma, is subcategorized into primary and secondary evolving tumors. While a primary glioblastoma is able to evolve *de novo* in patients within three to six months, a secondary one arises from low-grade astrocytomas of grade II or III during two to five years depending on the precursor [Pisapia, 2017, Ohgaki et al., 2004, Nobusawa et al., 2009]. Additionally, men have an 1.5 higher susceptibility for the development of glioblastomas compared to women and the mean age of diagnosis is 65. Despite the general possibility to treat glioblastoma patients with conventional therapies including surgical resection of tumor tissue and consecutive radio- and chemotherapy, only 5.6% of patients receiving this therapy survive more than five years after GBM diagnosis [Ostrom et al., 2018, Stupp et al., 2005]. This corresponds with an extremely low median progression-free survival of only eight months after surgery [Rapp et al., 2017]. By contrast, secondary gliomas are more frequent in women compared to men and arise more often in people of younger age (mean age: 45) [Ohgaki et al., 2004, Louis et al., 1993]. Differences in therapy efficiency between primary and secondary glioblastomas have not been proven [Hamisch et al., 2017].

1.1.2 Pathology

Besides environmental factors that were identified to affect glioma growth, such as ionizing radiation and the protecting effects of allergies, genetic factors play a more important role in glioma pathogensis and progression [Sadetzki et al., 2005, Amirian et al., 2016]. Although most cases of glioblastoma are sporadic, approximately 5% are

associated to be family-related [Wrensch et al., 1997]. In particular, distinct genetic abnormalities are associated to gliomagenesis and progression. Especially primary and secondary tumors show different genetic variations. An early event in gliomagenesis is the mutation of the *isocitrate dehydrogenase 1* (*IDH1*) gene which potentially determines whether a low-grade astrocytoma or a glioblastoma arises [Yan et al., 2009, Ichimura et al., 2009]. The question about the cell of origin for gliomagenesis is still not yet solved. Different evidences exist that astrocytomas may either develop from normal astrocytes, neural stem cells or oligodendrocyte precursor cells (for review see Zong et al. [2015]). Nevertheless, mutations in the *tumor protein 53* (*TP53*) gene are frequently observed in low-grade and secondary tumors. By contrast, loss of heterozygosity at 10q, *epidermal growth factor receptor* (*EGFR*) amplification, as well as mutations in the *phosphatase and tensin homolog* (*PTEN*) gene and *cyclin-dependent kinase inhibitor 2A* (*CDKN2A*) deletion, are predominantly found in primary glioblastomas, that develop *de novo*. During tumor progression, secondary glioblastomas are also able to acquire those genetic variations [Ohgaki et al., 2004].

1.1.3 Conventional therapy

The overall survival (OS) and the progression-free survival (PFS) of patients suffering from astrocytic tumors is mainly dependent on the grade of malignancy, age of the patient at diagnosis, the performance status and the extent of resection as uninfluencable factors [Li et al., 2011b]. After diagnosis by magnetic resonance imaging (MRI) and biopsy analysis, the first-line therapy starts with the fluorescence-guided maximal-safe surgical resection of the tumor followed by a concomitant radio- and chemotherapy with temozolomide (TMZ) [Stummer et al., 2006, Stupp et al., 2005]. The extent of resection is highly dependent on the location of the tumor, for that a gross total resection in eloquent areas, in which the removal would cause major disabilities, is difficult to achieve. In general, the gross total resection is preferable in comparison with a subtotal or incomplete one [Chaichana et al., 2014, McGirt et al., 2009a, Bette et al., 2018, Kreth et al., 2013, Li et al., 2011b], resembled by an increased OS of 17.1 months in cases of gross total resections compared to 11.8 months for incomplete resections [Stummer et al., 2008].
Other prognostic factors on the molecular level include the IDH status and the *6-O-methylguanine-deoxyribonucleic acid methyltransferase* (*MGMT*) promotor methylation. Especially IDH1-mutated tumors mainly appear in younger patients in line with low-grade astrocytomas or secondary glioblastomas as explained above. Therefore, they are associated with an enhanced OS for patients compared to the IDH-wildtype ones [Hartmann et al., 2010]. Moreover, methylation of the *MGMT* promotor leads to an epigenetic silencing of the corresponding gene, which is, in general, responsible for the de-methylation of the deoxyribonucleic acid (DNA) [Watts et al., 1997]. Since

the conventionally used chemotherapeutic TMZ alkylates DNA, thereby introducing double-strand breaks during DNA replication, active DNA methyltransferases, such as MGMT are able to remove such methyl residues and by this means impede the temozolomide's way of action [Zucchetti et al., 1989, Pieper et al., 1991]. Thus, patients with glioblastomas, that reveal a methylated *MGMT* promotor, profit far more from the TMZ therapy compared to those with tumors that show an unmethylated promotor [Hegi et al., 2005]. In summary, treatment regimens are adapted to prognostic values, which is illustrated in fig. 1.1. Moreover, additional treatment of the tumor with TMZ only yielded a slight increase in survival rates from 12 to 14.6 months [Stupp et al., 2005, 2009]. Alongside with manifold adverse effects of TMZ itself and its systemic administration [Trinh et al., 2009] and despite maximal surgical resection followed by an intense radiotherapy, the tumor tends to recur within a tumor margin zone of 2 cm length [Hochberg and Pruitt, 1980, Watanabe et al., 1992].

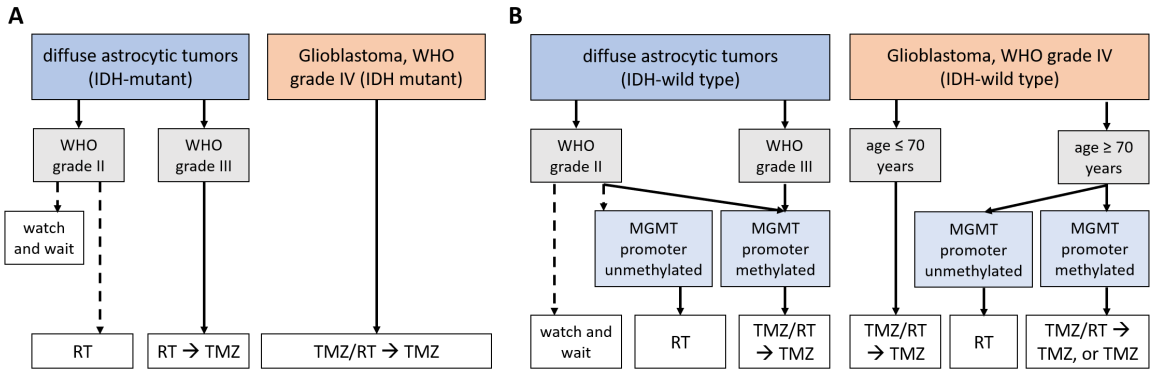

Figure 1.1: Current therapy for patients diagnosed with malignant astrocytomas. After a maximal safe resection of the tumor by surgery, patients with a tumor, characterized by an IDH-mutant status (**A**) as well as of low-grade, are treated either with radiotherapy (RT) alone or radiotherapy followed by chemotherapy with TMZ. By contrast, patients with IDH-mutant grade IV tumors receive combined radio- and chemotherapy followed by chemotherapy alone. In case of wild-type IDH tumors (**B**), the methylation status of the promotor of the *MGMT* gene is further analyzed. If unmethylated, patients obtain radiotherapy, while methylated tumors are treated with concomitant radio- and chemotherapy. Furthermore, the age of patients is crucial for the treatment of grade IV astrocytomas (The figure is based on Reifenberger et al. [2017]).

1.1.4 Therapy challenges

Manifested by the short OS and PFS of patients suffering from astrocytomas, the tumor cells acquire and develope several mechanisms to escape from or adapt to conventional treatment regimen. Those are either based on molecular differences of distinct cells gained during gliomagenesis, the molecular adaption on certain therapeutic or environmental stimuli or the close communication of tumor cells with their microenvironment.

1.1.4.1 Heterogeneity

As all genetic variabilities, described in chapter 1.1.2, are not ubiquitously found in glioblastomas but rather appear sporadically in different patients, the existence of distinct molecular subtypes becomes obvious. Therefore, the pioneers Godard et al. [2003] and Phillips et al. [2006] classified grade IV glioblastoma subgroups by their molecular patterns. Furtheron, Verhaak et al. [2010] performed a genome-wide microarray analysis of 202 patients and identified four distinct molecular subtypes with striking differences in gene expression profiles, mutations and copy number alterations. This was further correlated with corresponding variances in the metabolome of each subtype [Cuperlovic-Culf et al., 2012]. In accordance with The Cancer Genome Atlas (TCGA), the identified subtypes were termed proneural, neural, classical and mesenchymal associated to certain cell type properties of oligodendrocytes, neurons, astrocytes and cultured astroglia. The dominant differences between the subtypes are 1) the intense amplification of chromosome 7 and the concomitant higher *EGFR* expression, as well as the *CDKN2A* deletion in the classical subtype, 2) the hemizygous deletion of the long arm of chromosome 17 including *neurofibromin 1* (*NF1*) corresponding to the mesenchymal subtype and 3) the high amplification of *platelet-derived growth factor receptor A* (*PDGFRA*) and the IDH1 mutation within the proneural group. Recently, Wang et al. [2017b] postulated, that the neural subtype was only identified due to contaminations with normal neuronal cells of the brain. Therefore, the glioma subtypes were re-defined into three categories instead of four. As implicated, the distinct subtypes show different responses to therapy. For instance, the proneural subtype was predominantly observed in younger patients and is highly present in low-grade astrocytomas alongside with their IDH-mutation status, whereas recurrent tumors tend to switch to the mesenchymal subtype. Patients with proneural tumors have a better prognostic survival due to their IDH1 mutation, correlated with an increased production of 2-hydroxyglutarate resulting in an enhanced chemo- and radiosensitivity [Verhaak et al., 2010, Wood et al., 2016, Johnson et al., 2014, Bleeker et al., 2010]. Especially the tumor microenvironment, mainly consisting of tumor-associated immune cells (see chapter 1.1.4.3), drives glioblastoma subtyping and, thereby impacts the responsiveness to therapy [Wang et al., 2017b].

Further investigations revealed, that glioblastomas are described not only by those distinct molecular subtypes and their potential to change during tumor progression, but also by a pronounced intratumor heterogeneity. By a spatial collection of tumor samples and a single-cell analysis, Sottoriva et al. [2013] and Patel et al. [2014] displayed the presence of different molecular subtypes within one tumor. This corresponds with the finding of certain molecular and biological characteristics of cells depending on their location within the tumor mass affected by their environment. In detail, cells located in the tumor margin tend to show a pro-survival and infiltrative

phenotype, while high proliferation and inflammation strongly correspond to the core area [Aubry et al., 2015, Ross et al., 2017]. The highly infiltrative phenotype belongs to the most prominent characteristics of glioblastomas, as invasive cells use perivascular spaces around blood vessels and axons to migrate to distant areas into healthy brain parenchyma, first described by Hans-Joachim Scherer [Scherer, 1938]. The migratory phenotype is frequently induced by hypoxic conditions in the core area of the tumor. Those migrating cells are unaffected by surgery, thereby most likely causing fast recurrences in the tumor margin zone (reviewed in De Vleeschouwer [2017]). Beyond this, another cell subpopulation found in solid glioblastomas are cancer stem cells, that are very likely to be responsible for the tumor growth and maintenance [Singh et al., 2003, 2004]. Those glioma stem cells are thought to originate either from neuronal stem cells or by de-differentiation from normal brain cells [Schneider et al., 2016]. Moreover, glioma stem cells are also categorized either into a mesenchymal or a proneural subtype with a distinct responsiveness to therapy [Ricci-Vitiani et al., 2008]. Mesenchymal glioma stem cells are predominantly found in primary glioblastomas revealing a more aggressive and invasive phenotype, while proneural ones are mostly observed in grade III astrocytomas and are less resistant to treatment [Mao et al., 2013]. Especially mesenchymal glioma stem cells are characterized by a reversible non-proliferating or quiescent phenotype triggered by the tumor microenvironment. In particular, quiescent cancer stem cells have a high self-renewal capacity and are associated with a strong therapy resistance [Tejero et al., 2019].

1.1.4.2 Tumor dormancy

Besides the high invasive potential of tumor cells, aberrant self-renewal properties, as well as the genomic instability influencing the tumor progression and molecular subtyping, tumor dormancy was recently postulated to be a new hallmark of cancer, describing a certain state of tumor growth arrest [Yeh and Ramaswamy, 2015]. The clinical relevance is given, as the dormant tumor itself becomes and remains undetectable and unsusceptible for therapy for weeks, years or even decades, until a local relapse or metastatic disease emerges [Friedl and Herfarth, 1992, MacKie et al., 2003]. Tumor dormancy is divided into an immunogenic, angiogenic and cellular type (see fig. 1.2). In the immunogenic dormancy, the interplay between immune cells of the tumor microenvironment, that try to eliminate the tumor, and tumor cells, which block those cytostatic effects, reaches an equilibrium state. As the tumor is no longer susceptible to the immune surveillance, the tumor cells ultimately escape the immunogenic dormancy and start re-growth (reviewed by Mittal et al. [2014]). Beyond this, the tumor expansion relies on the availability of oxygen and nutrients provided by blood vessels. Thus, an avascularity results in an angiogenic dormancy, which is exited by an angiogenic switch established by the communication between the tumor and its

microenvironment [Naumov et al., 2006]. At least, single tumor cells are able to enter the cellular dormancy characterized by a reversible cell-cycle arrest [Hadfield, 1954, Naumov et al., 2002]. Elevated levels of mitogen-activated protein kinase (MAPK) p38 compared to reduced levels of the MAPK p42/44 (ERK) are essential factors in cellular dormancy [Aguirre-Ghiso et al., 2004].

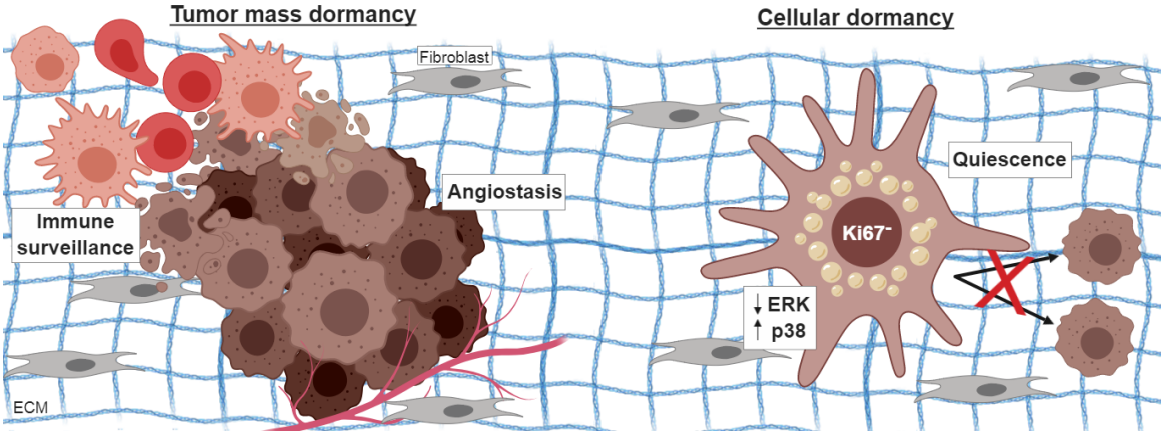

Figure 1.2: Tumor dormancy mechanisms. Tumors are prone to enter a resting state under specific circumstances that either lead to a so called tumor mass or cellular dormancy. Tumor mass dormancy is further classified into an immunogenic and angiogenic type. In the immunogenic dormancy, the elimination of the tumor by the immune system (orange and red cells), exemplified by (brown) apoptotic cells, and the proliferation of the other (brown) tumor cells reach an equilibrium state. By contrast, the angiogenic dormancy is driven by the limitation of nutrients and oxygen, until an angiogenic switch occurs that drives vascularization (red vessel). The least well-defined cellular dormancy is described as a quiescent, Ki67-negative state of the cell, in which the cell division is arrested but reversible, further characterized by an altered ratio of ERK and p38 levels.

This temporary mitotic arrest was first described by Hadfield [1954]. Apart from senescence, which represents a permanent loss of the proliferative potential [Demidenko et al., 2009], also quiescent cells persevere in a prolonged G0/G1 phase upon a withdrawal of growth factors and loss of adhesion molecules. By the addition of growth factors, those quiescent cells are able to re-enter proliferation (reviewed in Blagosklonny [2011]). Indeed, dormant cells seem to adapt mechanisms of quiescence. Thus, a connection between dormant and cancer stem cells becomes obvious. Endaya et al. [2016] observed the expression of typical stem cell markers in a non-proliferating, dormant subpopulation in glioblastomas and Deleyrolle et al. [2011], Zeng et al. [2016] identified a non-proliferative tumor-initiating subpopulation in glioblastomas. Furthermore, Hofstetter et al. [2012] demonstrated an induction of dormancy in tumor stem-like cells by certain signaling pathways triggered through the microenvironment. A closer look on dormant cells revealed the upregulation of a small gene set containing *ephrin type A receptor 5* (*EphA5*), *thrombospondin*, *angiomotin*, *insulin-like growth factor-binding protein 5* (*IGFBP5*) and *histone cluster 1 H2B family member K* (*H2BK*), that are exclusively expressed in dormant glioblastoma tumors compared to fast growing ones [Almog et al., 2009, Satchi-Fainaro et al., 2012]. Since many

experiments highlighted the correlation of cell cylce arrest and a reduced chemosensitivity [Naumov et al., 2003], it is of high interest, to understand the entrance and exit mechanisms of dormancy and dealing with dormant tumor cells.

1.1.4.3 Tumor microenvironment

As already briefly mentioned in several chapters before, the tumor microenvironment plays a crucial role in the development and the maintenance of important features of glioblastoma cells such as their self-renewal capacity, highly invasive phenotype, chemoresistance and distinct genetic profiles (for review see Zhang et al. [2019], Quail and Joyce [2017]). The tumor microenvironment consists of endothelial cells surrounding blood vessels, tumor-associated inflammatory cells, neurons as well as extracellular matrix proteins and other non-cellular factors (cf. fig. 1.3).

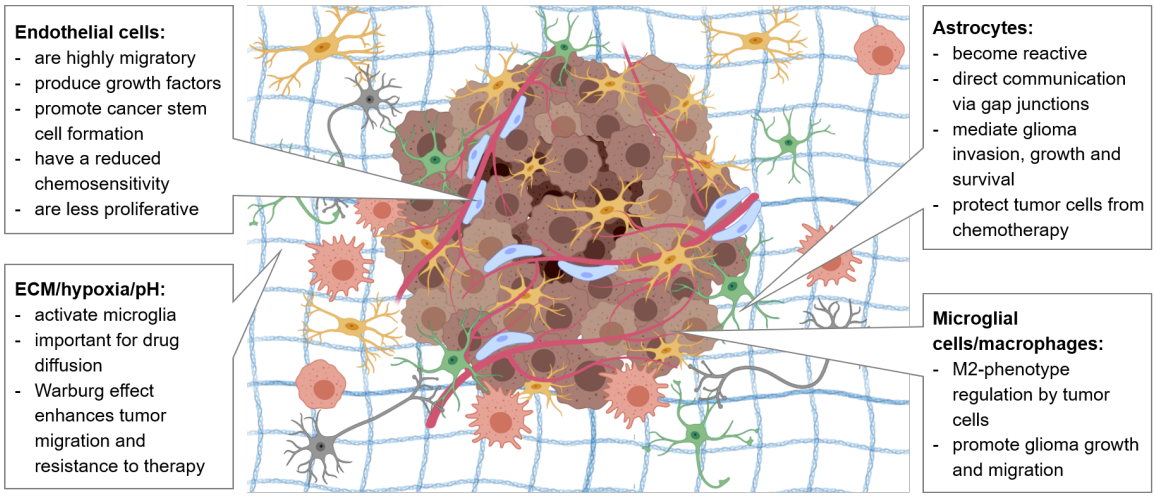

Figure 1.3: The tumor microenvironment. The interaction of tumor cells (brown) with their microenvironment is essential for the maintenance of the tumor. Especially, endothelial cells (blue), astrocytes (green), microglia (yellow) and tumor-associated macrophages (dark orange) as well as neurons (grey) and non-cellular factors such as the extracellular matrix and other molecules and environmental factors play crucial roles.

Endothelial cells associated to glioblastoma cells show distinct characteristics, like a faster migratory potential, a lower proliferation rate, a high production of growth factors and an increased chemoresistance, compared to their counterparts in normal brain [Charalambous et al., 2005, Hida et al., 2004]. In general, endothelial cells together with astrocytes and pericytes are critical for the maintenance of the blood-brain barrier (BBB). This barrier protects the brain from diseases and, therefore, prevents molecules such as anti-tumor agents to pass, which becomes a crucial problem in tumor therapy (reviewed by Muldoon et al. [2007]). Moreover, endothelial cells play an important role in the formation and the preservation of cancer stem cells by the secretion of factors such as chemokines [Calabrese et al., 2007]. In return, those cancer stem cells secrete angiogenic factors, that enhance the blood vessel construction [Bao

et al., 2006].
Beside endothelial cells, astrocytes are the most abundant cell population in the normal brain (reviewed in Farina et al. [2007]). Tumor cells activate astrocytes, which is described as cellular hypertrophy and genetic upregulation of the *glial fibrilliar acidic protein* (*GFAP*) gene [Le et al., 2003]. Additionally, astrocytes are able to de-differentiate into cancer-stem like cells, which is probably mediated by tumor cells [Moon et al., 2011]. Direct communication of glioma cells and astrocytes is guaranteed by the generation of gap junctions between adjacent cells [Lin et al., 2016]. Thereby, astrocytes moderate tumor invasion by microRNA signaling and activation of the matrix-metalloproteinase 2 [Oliveira et al., 2005, Hong et al., 2015, Le et al., 2003]. Moreover, by the additional release of growth factors and chemokines, reactive astrocytes maintain tumor cell survival and growth [Lin et al., 2016, Hoelzinger et al., 2007]. Recently, different experiments revealed, that the communication between glioblastoma cells and astrocytes reduced the responsiveness to chemotherapy of the tumor cells [Lin et al., 2016, Chen et al., 2015, Yang et al., 2014]. Thus, astrocyte-glioma cross-communication might play a pivotal role in the chemoresistance of tumors.
The majority of non-tumor cells in gliomas are tumor-associated or resident macrophages of the brain called microglia (for review see Charles et al. [2011]). In general, two different phenotypes of microglia and macrophages exist: M1, which is activated in an inflammatory surrounding and M2, which is observed under homeostatic conditions. Glioblastomas tend to secrete molecules such as the macrophage colony-stimulating factor (M-CSF) that drive macrophages towards the M2 phenotype leading to an enhanced tumor growth, in return. Therefore, the amount of microglia in the M2 phenotype positively correlates with tumor malignancy [Komohara et al., 2008, Wu et al., 2010]. The favoring of glioma invasion by microglial cells also contributes to the increased malignancy [Bettinger et al., 2002]. Enhanced numbers of microglial cells are correlated with poor survival of glioblastoma patients, since Lu-Emerson et al. [2013] postulated that those reduce the sensitivity of tumor cells to anti-angiogenic therapy.
Last but not least, non-cellular factors such as the extracellular matrix (ECM) play important roles in glioblastomas. For example, the ECM was shown to activate microglial cells resulting in the secretion of interleukin-18 (IL-18), which leads to an increased migration of tumor cells [Yeh et al., 2012]. Aside from that, the extracellular matrix represents a crucial factor in drug release and diffusion of molecules and particles, which has to be taken into account in therapy development [Kuppen et al., 2001]. Further non-cellular environmental factors are hypoxic and acidic conditions in the tumor area known as the Warburg effect [Warburg, 1956, Poteet et al., 2013]. An acidic pH and low oxygen levels potentially decrease the sensitivity of tumor cells to therapy and induce a shift to a more invasive phenotype in glioblastoma cells [Joseph

et al., 2015, Cairns et al., 2006]. Considering the influence of the tumor microenvironment in terms of understanding the tumor dynamics and invention of new therapies, the necessity is given to also consider effects on other than tumor cells and introduce multi-cell models, such as 2D and 3D co-culture models, tumor spheroids and ECM scaffolds (for reviews see Caragher et al. [2019], Lenting et al. [2017], Xiao et al. [2017]).

1.1.4.3.1 The role of chemokines

The classical role of chemotactic cytokines, also called chemokines, is the guidance of leukocytes to inflammatory regions [Hayashi, 1982]. In general, they are part of the cytokine family with chemoattractant properties. They obtained their name, since they induce directed migration in receptor-carrying cells along a gradient of the corresponding secreted ligands. All in all, the chemokine family contains approximately 50 ligands and 20 receptors, which reveals that one receptor is able to bind more than one ligand and *vice versa*. Furthermore, the chemokine group is divided into four different subgroups according to their chemokine domain, in which one or two disulfide bonds occur. They are named CXC, CC, C and CX3C, respectively. Signaling of chemokines is mediated by their corresponding G protein-coupled receptors with seven transmembrane helical domains found on the plasmamembrane of cells (summarized by Hughes and Nibbs [2018]). Usually, chemokine ligands are small molecules secreted into the extracellular region, where they bind to their individual receptors. The chemokines CXCL16 and CX3CL1 are an exception, since they possess an extra transmembrane domain followed by a mucin-like stalk in the extacellular lumen. Nevertheless, after cleavage by a disintegrin and metalloproteinase (ADAM) 10 and 17 between the plasmamembrane and the mucin-like region, both chemokines also exist as soluble forms and introduce signaling either as secreted or membrane-bound ligands (reviewed by Ludwig and Mentlein [2008]). Structural information of chosen chemokines and receptors are presented in fig. 1.4.

In particular, CXCL12, formally known as stromal-cell derived factor 1α (SDF1α) and one of its receptors, CXCR4, are expressed on glioblastoma cells and have firstly been detected adjacent to tumor necrosis in areas of a reduced oxygenation, where they are upregulated according to the hypoxic conditions or by stimulation with vascular endothelial growth factor (VEGF) [Rempel et al., 2000, Oh et al., 2001b, Zagzag et al., 2008]. Further, signaling through CXCR4 induces several mechanisms: 1) increase of glioma cell invasiveness, which is also partly mediated by autocrine stimulation of glioma cells themselves [Ehtesham et al., 2006], 2) induction of glioma angiogenesis by activation of hypoxia-inducible factor-1 (HIF-1) in an oxygen-deprived environment [Zagzag et al., 2008] and 3) stimulation of proliferation of glioblastoma cell progenitors, as well as mediation of tumor progression [Ma et al., 2008, Ehtesham et al.,

2009]. By contrast, signaling via the other CXCL12 receptor, CXCR7, is less well described but associated with tumor progression in accordance with apoptosis resistance in cells, tumor cell proliferation and, overall, reduced survival of patients [Deng et al., 2017, Flüh et al., 2016, Liu et al., 2015, Hattermann et al., 2012].

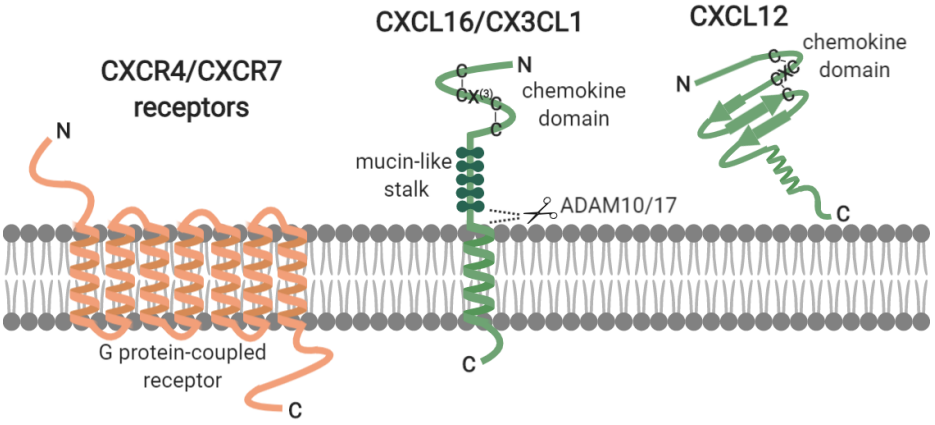

Figure 1.4: Structure of CXCR4, CXCR7, CXCL16, CXCL12 and CX3CL1 chemokines. Chemokine receptors are G protein-coupled receptors that contain seven transmembrane helices such as CXCR4 and the atypical chemokine receptor CXCR7. Ligands for such receptors are, in general, soluble molecules like CXCL12 with an conserved tertiar structure. Two exceptions are CXCL16 and CX3CL1 chemokines, that consist of an additional transmembrane region and a mucin-like stalk. Nevertheless, those chemokines are also able to function as soluble ligands after shedding between the plasmamembrane and mucin-like region is performed by ADAM10 and 17.

As opposed to this, CXCR6, the unique receptor for CXCL16, is detected on glioma cells with stem cell properties, whereas CXCL16 itself is strongly expressed in glioblastoma, microglial, endothelial cells and astrocytes [Hattermann et al., 2013, Ludwig et al., 2005]. Recent studies revealed, that microglial cells express CXCR6 and, thus, are modulated by CXCL16 release from tumor cells towards the anti-inflammatory phenotype [Lepore et al., 2018]. In connection to this, beside moderate expression of CX3CL1 in microglia [Hattermann et al., 2014], the CX3CL1/fractalkine receptor, CX3CR1, is exclusively found in microglial cells. Expression of CX3CL1 by tumor cells promotes recruitment of microglia, which ultimately results in an increased tumor invasion by the glial expression of matrix metalloproteinases [Held-Feindt et al., 2010]. In contrast, CX3CL1-CX3CR1 signaling in a restricted subset of tumor cells negatively regulates tumor invasion by tumor aggregation [Sciumè et al., 2010]. Recently, Hattermann et al. [2016b] introduced a novel signaling pathway of the transmembrane-localized forms of these chemokines via binding of their own soluble ligands. This inverse signaling yields an enhanced proliferation and rescue from apoptosis and thereby opens a new chapter in glioma biology regulation by CXCL16 and CX3CL1.

1.2 Alternative forms of therapy

1.2.1 Alternative therapeutics for GBM therapy

The first chemotherapeutics for glioblastomas, established in the early 70's, were nitrosoureas [Rosenblum et al., 1973]. The group of nitrosoureas is also known as first-generation DNA alkylating agents and includes, for instance, chloroethyl-cyclohexyl-nitrosourea (CCNU, "lomostine") and bischloroethyl-cyclohexyl-nitrosourea (BCNU, "carmustine") [Brisman et al., 1976]. Despite several observed severe side effects, both first-generation compounds are still in use, as lomostine is administered as systemic treatment option in recurrent glioblastomas [Batchelor et al., 2013] and carmustine for other alternative therapy approaches (discussed in chapter 1.2.2.2). In the end of the 90's, temozolomide, the second-generation of DNA alkylating agents, superseded BCNU, CCNU and others and became first-line chemotherapeutic for glioblastoma ever since [Yung et al., 1999]. As described previously, TMZ is not only characterized by many adverse effects, but it also only mildly improved survival of patients suffering from glioblastoma tumors. Therefore, sensitizing of glioma cells to current therapies is one great field of investigations.

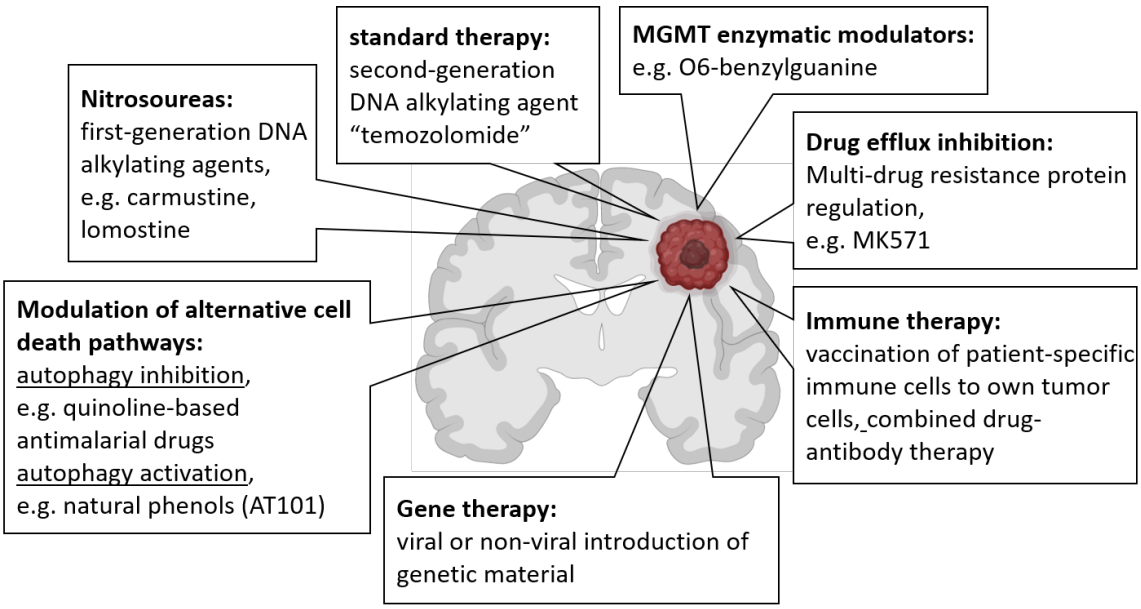

Figure 1.5: Alternative treatment approaches in GBM therapy. The current gold standard chemotherapy for patients suffering from GBM is DNA alkylation by temozolomide. Due to the poor improvement of patient's overall survival, various alternative therapeutic approaches have been developed, including MGMT enzymatic activity regulation and drug efflux inhibition, as well as immune and gene therapy attempts and addressing alternative cell death pathways.

In order to augment classical chemotherapy efficiency of TMZ, possible opportunities comprise the inactivation or modulation of the MGMT enzyme activity, as *MGMT* promotor silencing is associated with increased cytotoxic effect of TMZ [Pieper et al., 1991]. However, a clinical phase I trial with O6-benzylguanine in combination with

TMZ revealed limited use due to pronounced myelosuppression [Quinn et al., 2005, Lun et al., 2016]. Additionally, since multi-drug resistance proteins (MRPs), that are variously expressed in human glioma samples, are responsible for drug efflux into the extracellular lumen [Calatozzolo et al., 2005, Debenham et al., 1982, Kartner et al., 1983, Munoz et al., 2014], different attempts were made on the combined therapy of anti-cancer drugs and compounds inhibiting drug efflux *in vitro* [Peignan et al., 2011, Tivnan et al., 2015].
Further external factors addressed in GBM treatment are the innate and adaptive immune system as part of the tumor microenvironment by the use of certain antibodies [Presta et al., 1997, Sampson et al., 2008, Taube et al., 2014, Sangro et al., 2013]. However, clinical trials revealed an increase in PFS but no benefit in OS [Gilbert et al., 2014, Brandes et al., 2019]. Other approaches focus on patient-specific immune therapy, induction of natural killer (NK) cell cytotoxicity with natural killer-group 2D (NKG2D) receptors as well as viral and non-viral gene therapy (for reviews see Tivnan et al. [2017], Golán et al. [2018], Caffery et al. [2019]).
One major aspect in the induction of glioma cell death is the choice of the cell death pathway, e.g. apoptosis or autophagy. The current standard therapeutic TMZ influences both on different levels [De Salvo et al., 2011, Würstle et al., 2017, Kanzawa et al., 2003]. While cellular resistance to TMZ is associated with the activation of autophagy-related signaling pathways [Carmo et al., 2011], inhibition of autophagy resulted in enhanced cytotoxicity during TMZ administration [Liu et al., 2013]. Therefore, autophagy-inhibiting compounds, such as quinoline-based antimalarial drugs, e.g. (hydroxy)chloroquine and quinacrine, represent promising agents for glioblastoma therapy. Indeed, Golden et al. [2015, 2014] observed the improvement of TMZ cytotoxicity by co-administration of quinoline-based drugs *in vitro*, such as quinacrine and chloroquine, that blocked autophagy-dependent cell death and induced apoptosis. Lee et al. [2015b] additionally proved the chemosensitizing effect of chloroquine on TMZ-stimulated glioma cells. Both, chloroquine as well as its derivate hydroxychloroquine, which has similar anti-cancer effects but is less toxic than its counterpart [Gunja et al., 2009], were investigated in clinical trials in combination with standard therapy partly demonstrating increased survival rates for GBM patients [Sotelo et al., 2006, Briceno et al., 2007, Rosenfeld et al., 2014]. Another natural molecule, activating autophagy in glioblastomas by the inactivation of members of the B-cell lymphoma 2 (Bcl-2) family, is gossypol, a polyphenol from cottonseed oil, and its R-(-)-enantiomer AT101 [Keshmiri-Neghab et al., 2014, Voss et al., 2010]. Initially, gossypol was associated with great cytotoxic effects on solid tumor cell lines, including GBMs [Coyle et al., 1994]. Nevertheless, a first clinical trial with recurrent glioblastomas only revealed little response rates, but good tolerance of the drug [Bushunow et al., 1999]. However, Jarzabek et al. [2014] demonstrated synergistic effect of com-

bined TMZ/gossypol stimulation of GBM cells resulting in a decreased proliferation and invasion of tumor cells. In addition, advantages of gossypol and AT101 in tumorsphere and glioma stem-like cell treatment have recently been revealed [Park et al., 2018, Linder et al., 2019], thus, highlighting AT101 as a molecule of great interest in alternative GBM therapy. An overview of different alternative therapeutic applications for glioblastoma treatment is illustrated in fig. 1.5.

1.2.2 Alternative strategies

1.2.2.1 Nanomedicine

Beside the necessity of addressing other or multiple pathways in GBMs, another challenge in brain-tumor therapy is the limited passage of molecules across the blood-brain barrier. This barrier mainly consists of endothelial cells closely connected to perivascular cells like astrocytes and pericytes. In general, it is responsible for the prevention of the entrance of harmful molecules into the brain, which is maintained by transport, enzymatic, immunologic barriers and efflux transport systems (reviewed in Bernacki et al. [2008], Wilhelm et al. [2011]). Under tumor conditions, the blood-brain barrier becomes slightly leaky at highly angiogenic tumor sites resulting in an enhanced permeability and retention (EPR) effect [Matsumura and Maeda, 1986, Yuan et al., 1995, Ambruosi et al., 2006]. Nanocarriers as drug delivery system take advantage of this situation [Kreuter and Gelperina, 2008]. Such nanoparticles are composed of various molecular formulations and shapes either acting as therapeutic agents themselves or carrying respective compounds through encapsulation of or attachment to them (for review see Játiva and Ceña [2017]). Further reasons for the application of nanoparticles are their positive influences on drug bioavailability [Maincent et al., 1986] as well as the enhancement of the systemic circulation of the compound [Gao et al., 2015, Jain et al., 2016]. Moreover, encapsulation of chemicals prevents from biological degradation, reduces toxicity to healthy tissue and enhances water solubility (reviewed in García-Pinel et al. [2019]. Due to the EPR effect, passive targeting of nanoparticles of sizes between 20 and 200 nm in diameter after intravascular administration represents one option for the delivery of therapeutics to the brain. However, the possibility of active targeting of nanoparticles by surfarce functionalization with tumor-specific antibodies, peptides or aptamers is often favored [Lu et al., 1997, Monsky et al., 1999] (for review see Kobayashi et al. [2013], Wanjale and Kumar [2017]). In the case of glioblastomas, diverse approaches in the delivery of different substances, such as therapeutic compounds, nucleid acids and antibodies, by nanoparticles have been made so far. A selection of used nanoparticle systems in GBM therapy is displayed in fig. 1.6.

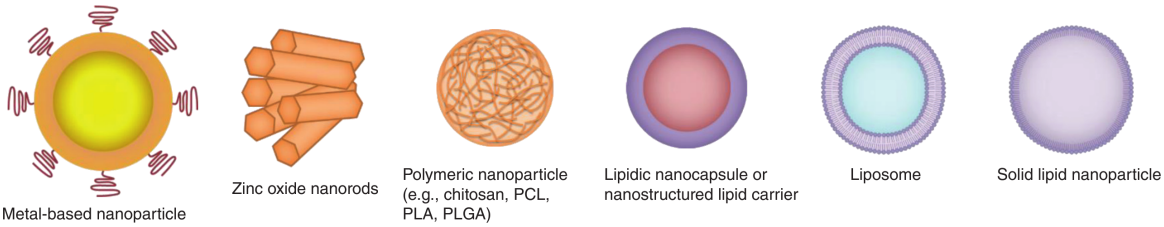

Figure 1.6: Selected formulations and shapes of nanoparticles used in GBM therapy (modified after Játiva and Ceña [2017]).

High interest is laid on solid nanoparticles made of metals due to their valuable effects concerning magnetic properties in case of iron oxide, structural variability regarding gold nanoparticle production and antimicrobial qualities of silver [Jordan et al., 2006, Jang et al., 2018, Aymonier et al., 2002] as well as self-mediation of toxicity by reactive oxygen species (ROS) production of silver and zinc oxide (ZnO) nanoparticles [Wu et al., 2016, Sruthi and Mohanan, 2015, Wahab et al., 2016]. Moreover, Ostrovsky et al. [2009] showed selective cell death initiation of ZnO nanoparticles in glioma cells compared to normal astrocytes. Further experiments revealed effects on migratory and invasive properties corresponding to the shape of ZnO nanoparticles [Wahab et al., 2016]. Thus, ZnO itself represents a promising alternative tool for glioblastoma therapy.

In addition to self-mediated toxicity of specific nanoparticle components, most particle formulations include either polymers or lipidic elements for their general use as vehicles for molecules. In case of polymeric applications in gliomas, among many other polymers, poly(ϵ-caprolactone) (PCL), in particular, as well as poly(dimethylsiloxane) (PDMS) were used for the delivery of drugs such as paclitaxel and doxorubicin [Xin et al., 2012, da Silveira et al., 2013, Gao et al., 2014, Figueiredo et al., 2016]. Regarding lipidic compositions of particles, mainly 1,2-distearoyl-sn-glycero-3-phosphoethanolamine (DSPE), poly(ethylene glycol) (PEG) and cholesterol are used for their application in glioblastomas (reviewed in [Játiva and Ceña, 2017]). As TMZ is the first-line chemotherapeutic for gliomas, some nanomedical attempts for TMZ have already been investigated. An aim was the increase of TMZ stability and half-life by its conjugation to chitosan and biotin molecules or poly(β-L-malic acid) [Fang et al., 2015, Patil et al., 2010], while others used either poly(D,L-lactide-co-glycolide) (PLGA) or mesoporous silica nanoparticles to encapsulate TMZ. However, despite an enhanced cellular uptake of TMZ-loaded PLGA particles, its cytotoxic effect was not improved [Jain et al., 2014, Ananta et al., 2016], only if co-administered with other molecules or therapeutics [Bertucci et al., 2015, Maggini et al., 2016].

Among several studies on the discovery of alternative therapeutics and strategies in gliomas, especially alternative drugs got into the focus of nanomedical research. Beside nanomedical approaches in various other cancers [Mezzaroba et al., 2013, Sleightholm

et al., 2017, Sun et al., 2015, Satapathy et al., 2018], in particular quinoline-based compounds like quinacrine or hydroxychloroquine were encapsulated in liposomes for a combined treatment of glioblastoma cells with other chemotherapeutics [Wang et al., 2018, Li et al., 2014, Wang et al., 2017c]. By contrast, gossypol-loaded nanoparticles have not been studied in glioblastomas, yet. However, Zhai et al. [2008] firstly encapsulated gossypol in liposomes, in order to use them as anti-cancer agents in breast and cervical cancer cells. Thereafter, various other approaches for prostate, breast, cervical, lung and ovarian tumors followed with focus on extended water solubility of the drug [Li et al., 2011a, Liu et al., 2014, Tomada et al., 2017] or multiple chemotherapeutic applications [Cho et al., 2013, Heleg-Shabtai et al., 2016, Shen et al., 2018]. Although an increase of the anti-tumor effect of encapsulated *versus* free gossypol was not observed, synergistic effects with other therapeutic compounds and sensitization to radiotherapy or goals in the pH-responsive and receptor-mediated drug release were achieved.

1.2.2.2 Local-therapy approaches

Another opportunity to circumvent the poor transfer of molecules across the blood-brain barrier is the local administration of therapeutic compounds into the tumor area or the implantation of therapeutical devices into the resection cavity after surgery. Several attempts regarding local administration of drugs and particularly nanocarriers were already tested. Intratumoral or intracerebral stereotactical injection represents the simplest method for direct administration of drugs. As a single application is not sufficient, storage of therapeutic compounds was achieved by using an Ommaya reservoir, for instance [Sheldon and Ommaya, 1963]. In this respect, an improvement of treatment outcome for glioblastoma patients was established by either direct application of nitrosoureas [Tator et al., 1977] or a combined therapy approach including systemic administration of TMZ and local delivery of mitoxantrone in recurrent GBMs [Boiardi et al., 2003, 2008]. However, this technique bears difficulties such as catheter obstruction by tissue adsorption [Prados et al., 2003, Fetell et al., 1990], variable positioning of the catheter and a limited dose distribution of drugs [Saw et al., 1989, Torres et al., 2008] as well as a propensity to infections [Fetell et al., 1990].
In order to overcome the limited distribution of chemicals, Bobo et al. [1994] invented the convection-enhanced delivery (CED), in principle, an extended version of the intratumoral-injection method. By this means, the applied therapeutical concentration was reduced due to a greater penetration plus a deeper distribution of the drug into the tumor area achieved by a pressure gradient [Sugiyama et al., 2007, Saito et al., 2004, Sampson et al., 2007]. Although many clinical trials were performed for brain-tumor administration (reviewed by Mehta et al. [2017]), constant physical limitations and adverse effects of CED are the backflow of therapeutics into unwanted

areas of the brain [Casanova et al., 2014, Sillay et al., 2014] as well as drug leakage into the subarachnoid space and ventricles [Varenika et al., 2008, Lidar et al., 2004] and heterogeneous distribution of the therapeutic due to the diverse structure of the tumor tissue [Groothuis et al., 1999, Raghavan et al., 2006].

Another local-treatment approach was first demonstrated by Brem et al. [1991], who used an polyanhydride biodegradable co-polymer made of a 20:80 ratio of 1,3-bis-(p-carboxyphenoxy)propane and sebacic acid to incorporate BCNU. After several clinical studies revealed a survival benefit of two months upon combined radio- plus wafer therapy compared to radiotherapy alone [Brem et al., 1995b,a, Westphal et al., 2003, 2006], the United States Food and Drug Administration (FDA) approved the use of these so called Gliadel® wafers for the treatment of recurrent glioblastomas in 1997 and of newly diagnosed gliomas in 2003. Since eight wafers are able to be placed into the resection cavity (depicted in fig. 1.7), a maximum of 60 mg BCNU is administered locally [Brem et al., 1995b]. Upon the degradation of the polymer matrix, the complete release of carmustine is attained after six to eight weeks [Wu et al., 1994]. Nevertheless, *in-vitro* and animal studies in monkeys revealed a maximum release of over 75% of the therapeutic within one week. Additionally, the drug penetration was restricted to a maximum of 6.1 mm distance from the polymer, thereby hardly crossing the 2 cm margin zone [Fung et al., 1998]. A comparison between a Gliadel® wafer implantation and the classical glioma therapy including radiotherapy plus concomitant TMZ administration exhibited unclear effects. On the one hand, McGirt et al. [2009b] showed no different effects in the OS between wafer plus radiotherapy-treated patients compared to those receiving classical therapy, but a significant increase in the OS of patients treated with BCNU-wafer as well as radio- plus concomitant chemotherapy with TMZ in comparison with classical therapy. On the other hand, Noël et al. [2012] had seen no differences between Gliadel® wafer plus radio-/TMZ therapy compared to the classical treatment. However, frequently reported adverse effects connected to Gliadel® wafers included myelosuppression, neurological deficits, healing abnormalities and seizures (literature review of Ashby et al. [2016]).

Figure 1.7: Gliadel® wafers implanted into a brain tumor resection cavity (from Wolinsky et al. [2012]).

As drug-releasing implants still represent an attractive way of local tumor therapy, more advanced approaches are currently emerging. Those include partly the further

development of the original Gliadel® wafer system containing classical or alternative drugs [Brem et al., 2007, Shapira-Furman et al., 2019, Harn et al., 2011] and partly the investigation of other systems based on hydrogels. Hydrogels basically consist of polymers, that are capable of absorbing a high amount of water in their 3D network due to their hydrophilic structure (reviewed in Ahmed [2015]). For glioma treatment, newly developed hydrogels, mainly built of PLGA, PEG or lipidic components, are equipped with various features like thermoreversability, photopolymerization or else [Vellimana et al., 2013, Ramachandran et al., 2017, Zhao et al., 2018, Bastiancich et al., 2018]. Nonetheless, despite individual promising *in-vitro* and *in-vivo* results, the research is still devoted to the invention of a device with a high loading capacity, slow release rates and long-term effectiveness, in order to improve brain-tumor treatment.

2 Aim of this study

After various treatment attempts in approximately 100 years of investigations since the first successful brain-tumor removal by surgery in 1879 (reviewed in Preul [2005]) and the first description of the brain tumor *Glioblastoma Multiforme* [Bailey and Cushing, 1928], the necessity of surgery as well as radiotherapy was proven to drastically increase the overall survival of patients suffering from such astrocytic tumors [Simpson et al., 1993, Miller et al., 1990]. However, only little proceedings were made so far in chemotherapeutic treatment, which to date only reveal a severely limited improvement of the patients' outcome. This insufficiency of treatment relies on the persistent unsatisfying knowledge about glioblastomas. On the one hand, the pronounced molecular heterogeneity of tumor cells [Verhaak et al., 2010, Wang et al., 2017b], which impedes addressing of different cell subpopulations by a restricted panel of chemicals, is hardly conceived. On the other hand, the ability of gliomas to develop escape mechanisms such as dormancy, to survive treatment regimen [Hadfield, 1954], is not yet comprehensively understood. In order to improve glioblastoma therapy, a deeper knowledge of the molecular pathways impacting tumor survival and therapy resistance is indispensable. To gain a closer insight into molecular processes, which affect therapy-escape mechanisms and thereby provide the basis for the development of suitable, revised therapy approaches, this project was divided into three major tracks:

1) For a comprehensive analysis of mechanisms that drive tumor-cell survival upon therapy, in particular, triggers of tumor dormancy have to be investigated. Hereby, *in-vitro* experiments under classical chemotherapeutic administration taking account of environmental circumstances such as inflammation should reveal relevant molecular pathways influencing dormancy entry and exit.

2) The improvement and adaption of the current standard therapeutics to different cell subpopulations considering therapy-escape mechanisms is mandatory. By this means, the introduction of different compounds, that mediate cell death via distinct pathways, as well as the application of various administration schemes should be evaluated in *in-vitro* tumor-cell systems. Consequently, not only responses of tumor but also normal brain cells should be taken into account by mono- and co-culture stimulation models.
3) An additional aspect of the failure of systemic chemotherapy is the limited access of molecules to brain-tumor cells depending on blood-brain barrier restrictions (reviewed in Bernacki et al. [2008]). Thus, treatment approaches improving blood-brain barrier passaging of drugs or local application attempts of therapeutic compounds in line with the reduction of systemic side effects are favorable. Therefore, based on obtained results of alternative theraputics and stimulations schemes, advanced therepy approach should be established in collaboratory work with materials scientists, in order to generate suitable drug carrier systems such as nanoparticles and devices for local implantation, that overcome therapy limitations. Such systems have to be tested and improved regarding their release kinetics and cytotoxic effects compared to free drug administration in *in-vitro* cellular systems, to build the basis for further *in-vivo* applications.

3 Material & Methods

3.1 Material

3.1.1 Chemicals and prepared solutions

Table 3.1: List of used chemicals.

Chemical	Provider
Acetone	Honeywell International, Charlotte, NC, USA
30% (w/v) Acrylamide/Bis Solution 29:1	Serva Electrophoresis GmbH, Heidelberg, DE
Ammonium persulfate (APS)	Carl Roth GmbH + Co. KG, Karlsruhe, DE
Agarose	Carl Roth GmbH + Co. KG
Bovine serum albumin (BSA) Fraction V	Serva Electrophoresis GmbH
Calcium chloride ($CaCl_2$)	Carl Roth GmbH + Co. KG
Casein	Carl Roth GmbH + Co. KG
D-(+)-Glucose	Carl Roth GmbH + Co. KG
Disodium phosphate (Na_2HPO_4)	Merck, Darmstadt, DE
Dithiothreitol (DTT)	Merck
Ethanol absolute 96%	Carl Roth GmbH + Co. KG
Ethylenediaminetetraacetic acid disodium salt dihydrate (EDTA)	Carl Roth GmbH + Co. KG
Glycerol	Carl Roth GmbH + Co. KG
Glycine	Carl Roth GmbH + Co. KG
Isopropyl alcohol	Merck
Magnesium chloride ($MgCl_2$)	Carl Roth GmbH + Co. KG
Methanol	Carl Roth GmbH + Co. KG
Monopotassium phosphate (KH_2PO_4)	Merck
N-2-Hydroxyethylpiperazine-N'-2-ethane sulfonic acid (HEPES)	Biomol GmbH, Hamburg, DE
Orthovanadate	Merck
Paraformaldehyde	Merck
Potassium chloride (KCl)	Merck
Sodium bicarbonate ($NaHCO_3$)	Carl Roth GmbH + Co. KG
Sodium chloride (NaCl)	Carl Roth GmbH + Co. KG
Sodium dodecyl sulfate (SDS)	Serva Electrophoresis GmbH
Sodium hydroxyde (NaOH)	Carl Roth GmbH + Co. KG
Tetramethylethylenediamine (TEMED)	Carl Roth GmbH + Co. KG

Trichlormethan/Chloroform	Carl Roth GmbH + Co. KG
Tris	Merck
Triton X-100	Merck
Trypsin from porcine pancreas	Merck
Tween-20	Merck

Table 3.2: Compositions of buffers and solutions.

Solution	Composition
Artificial cerebrospinal fluid (aCSF)	124 mM NaCl 5 mM KCl 26 mM $NaHCO_3$ 1.3 mM $MgCl_2$ 2 mM $CaCl_2$ 10 mM D-Glucose 0.05% (w/v) BSA in H_2O
Blocking buffer	0.1% (w/v) BSA 0.2% (w/v) Glycine in phosphate-buffered saline (PBS)
Dissociation solution	10 mM HEPES 5.4 mM EDTA 2 $\frac{g}{L}$ Trypsin in Dulbecco's Modified Eagle's Medium (DMEM)
Electrode buffer	25 mM Tris 192 mM Glycine 0.1% (w/v) SDS in H_2O (pH 8.3)
Lysis buffer	5 mM Tris 10 mM NaCl 0.1% (v/v) Triton X-100 0.2 mM EDTA 2 mM Orthovanadate in H_2O (pH 7.8)
PBS	137 mM NaCl 2.7 mM KCl 10 mM Na_2HPO_4 1.8 mM KH_2PO_4 in H_2O (pH 7.2)

Sample buffer	62.5 mM Tris 10% (v/v) Glycerol 2% (w/v) SDS 10 mM DTT in H_2O (pH 6.8)
Separating gel buffer	1.5 M Tris 0.4% (w/v) SDS in H_2O (pH 8.8)
Stacking gel buffer	0.5 M Tris 0.4% (w/v) SDS in H_2O (pH 6.8)
Transfer buffer	25 mM Tris 192 mM Glycine 10% (v/v) Methanol in H_2O (pH 9)
Tris-buffered saline (TBS)	20 mM Tris 0.14 mM NaCl 1 mM EDTA in H_2O (pH 7.5)
TBST	TBS + 0.1% (v/v) Tween-20

3.1.2 Biological Material

In this study, several tumor tissues from patients were processed and used for *in-vitro* experiments. Freshly dissected tissues were kindly provided by the director Prof. Dr. H. M. Mehdorn and afterwards Prof. Dr. M. Synowitz of the Department of Neurosurgery of the University Medical Center Schleswig-Holstein (UKSH, Kiel, DE) in accordance with the Helsinki Declaration of 1975 with approval of the ethics committee of the University of Kiel, DE (file reference: D536/15, D471/15 and D524/17). The patients were informed beforehand and consented the use of their tumor tissue for studies, respectively. Diagnosis was stated by the Department of Pathology (UKSH, Kiel, DE).

Table 3.3: Information about obtained tumor tissue from patients used for immunocytochemistry staining.

Name	Classification	Origin
Tissue 1	primary GBM WHO IV	49-year old man
Tissue 1.2	recurrent GBM WHO IV	50-year old man
Tissue 2	recurrent GBM WHO IV	71-year old woman

Table 3.4: Information about used immortalized cell lines and self-generated primary cultures.

Name	Classification	Source
A172	GBM, 53-year old man	ECACC, Salisbury, UK
HMC3	human embroyonic microglia	LGC Standards (ATCC), Wesel, DE
LN229	GBM, 60-year old woman	LGC Standards (ATCC)
SVGA	human astrocytes	Prof. Dr. Hanssen Rinaldo, University Hospital of North Norway [Henriksen et al., 2014]
U251MG	GBM, man	ECACC, Salisbury, UK
27/07	recurrent GBM WHO IV	38-year old woman
83/13	recurrent GMO WHO IV	52-year old man
116/14	primary GBM WHO IV	77-year old man
118/14	recurrent GBM WHO IV	65-year old man
124/15	primary GMO WHO IV	57-year old man
141/15	primary GMO WHO IV	45-year old man

3.1.3 Biochemicals

Table 3.5: List of CRIPSR/Cas9 plasmids used for gene knock-out in LN229 cells.

Name/Target	Provider
Control CRISPR/Cas9 Plasmid	Santa Cruz Biotechnology, Inc., Dallas, TX, USA
CXCL16 CRISPR/Cas9 KO Plasmid	Santa Cruz Biotechnology, Inc.
CXCR7 CRISPR/Cas9 KO Plasmid	Santa Cruz Biotechnology, Inc.
CX3CL1 CRISPR/Cas9 KO Plasmid	Santa Cruz Biotechnology, Inc.

Table 3.6: List of primary antibodies used for immunofluorescent staining (IF) of cells or tissue and Western Blot (WB).

Target	Host	Application	Provider	Catalog no.
β-Catenin	mouse	1:100(IF)	BD Biosciences, Franklin Lakes, NJ, USA	610153
CCL2	mouse	1:500(IF/WB)	ThermoFisher Scientific, Waltham, MA, USA	MA5-17040
CX3CL1	mouse	1:200(IF)	R&D Systems, Minneapolis, MN, USA	MAB3651
CXCL16	rabbit	1:100(IF)	PeproTech GmbH, Hamburg, DE	500-P200
CXCR7	mouse	1:100(IF)	R&D Systems	MAB42273
FSTL3	goat	1:20(WB)	ThermoFisher Scientific	PA5-47106
FSTL3	rabbit	1:100(IF)	Abgent, San Diego, CA, USA	AP12300b
GAPDH	rabbit	1:200(WB)	Santa Cruz Biotechnology, Inc.	sc-47724
pp38	rabbit	1:250(WB)	Cell Signaling Technology, Danvers, MA, USA	4511
pp42/44	rabbit	1:1000(WB)	Cell Signaling Technology	9101
SAA2	rabbit	1:200(IF/WB)	Proteintech Europe, Manchester, UK	13192-1-AP
THSD4	rabbit	1:500(IF/WB)	Proteintech Europe	20619-1-AP
VEGFC	mouse	1:200(IF/WB)	Abcam, Cambridge, UK	ab106512

Secondary antibodies were used either for immunofluorescent staining of proteins in cells or tissue or detection of proteins by Western Blot. Hereby, HRP-conjugated antibodies were provided by Santa Cruz Biotechnology, Inc., while Alexa Fluor antibodies were obtained from ThermoFisher Scientific.

Table 3.7: List of secondary antibodies used for immunofluorescent staining or Western Blot.

Target	Conjugation	Host	Application
α-goat IgG	HRP	donkey	1:100000(WB)
α-mouse IgG	HRP	donkey	1:30000(WB)
α-rabbit IgG	HRP	donkey	1:40000(WB)
α-mouse IgG	Alexa Fluor 488	donkey	1:1000(IF)
α-mouse IgG	Alexa Fluor 555	donkey	1:1000(IF)
α-rabbit IgG	Alexa Fluor 488	donkey	1:1000(IF)
α-rabbit IgG	Alexa Fluor 555	donkey	1:1000(IF)

Table 3.8: Analyzed genes and respective assay details for TaqMan™ primer-probes for qRT-PCR.

Gene	Interrogated Sequence	Assay location	Amplicon length
ACTB	NM_001101.3	53	171
CCL2	NM_002982.3	151	101
CDKN1A	NM_000389.4	566	66
	NM_001220777.1	511	66
	NM_001220778.1	676	66
	NM_001291549.1	718	66
	NM_078467.2	513	66
CX3CL1	NM_002996.4	183	72
CXCL16	NM_022059.3	893	62
	NM_001100812.1	893	62
CXCR4	NM_003467.2	107	78
CXCR7	NM_020311.2	564	73
FSTL3	NM_005860.2	540	84
GAPDH	NM_001289746.1	229	122
	NM_002046.5	243	122
MAP2	NM_001039538.1	1803	98
	NM_002374.3	5404	98
	NM_031845.2	1336	98
	NM_031847.2	1429	98
SAA2	NM_001127380.2	297	97
THSD4	NM_001286429.1	1035	73
	NM_024817.2	1986	73
VEGFC	NM_005429.4	981	66

3.2 Methods

3.2.1 Cell biological techniques

3.2.1.1 Cell cultivation

Many results shown in this thesis were obtained by *in-vitro* experiments on different immortalized cell lines and self-generated primary cultures (cf. tab. 3.4). For this purpose, all experiments were performed under sterile conditions using a work bench with an adjusted airflow (Heraeus GmbH, Hanau, DE) to prevent contaminations. Furthermore, cell lines and primary cultures were routinely checked for Mycoplasma contamination using the Venor®GeM OneStep Mycoplasma Detection Kit (Minerva

Biolabs, Berlin, DE) followed by gel electropheresis. Moreover, cell lines and primary cultures were regularly stained regarding cell-type specific markers.
If not declared elsewhere, cells were cultivated in T25 or T75 flasks with DMEM (ThermoFisher Scientific) containing 10% fetal bovine serum (FBS, Gibco® Qualified, ThermoFisher Scientific), 1% Penicillin-Streptomycin ($10,000\,\frac{\mathrm{U}}{\mathrm{ml}}$, ThermoFisher Scientific) and 2 mM L-Glutamine (ThermoFisher Scientific) at 37°C in an humidified atmosphere with 5% CO_2 in a HeraCell 240i CO_2 incubator (Heraeus GmbH). In the following, this particular medium composition is referred to as "culture medium". Depending on cell line or primary culture proliferation, cells were routinely passaged at $80-90\%$ layer density. For this purpose, the culture medium was carefully aspirated with a sterile glass pipette. Then, cells were washed with prewarmed PBS and detached with Trypsin-EDTA solution (Merck) for 5 min at 37°C/5% CO_2. Finally, cells were carefully resuspended in culture medium and transferred into a new flask. For experiments cells were counted prior to seeding.

3.2.1.1.1 Determination of viable cell numbers

For counting of viable cells, detached cells were either transferred into a Falcon™ tube or an Eppendorf tube®, depending on the used amount of culture medium for resuspension, and centrifugated at 300 g for 5 min. After centrifugation, the supernatant was carefully removed. Before counting, the cell pellet was resuspended in culture medium. To allow for identification of dead cells, 10 µl cell suspension were added to an equivalent volume of Trypan Blue solution (0.4%, Merck). Finally, this mixture was filled into a Neubauer counting chamber. Viable, unstained cells were counted and the amount of cells per ml was calculated with the formula

$$\frac{\text{cell no.}}{\text{ml}} = \frac{\text{counted cell no.} \cdot 10^4 \cdot \text{dilution factor}}{\text{number of counted squares}}\,. \tag{1}$$

3.2.1.2 CRISPR/Cas9 gene knock-out

The CRISPR/Cas9 genome editing system is a simple-to-use technique to knock out particular genes in mammalian cells. At first, $1.5 \cdot 10^5$ LN229 cells were seeded in a 6-well plate and cultivated over night at 37°C/5% CO_2. On the day of transfection, 1 µg of the respective CRISPR/Cas9 plasmid (listed in tab. 3.5) was diluted in Plasmid Transfection Medium (Santa Cruz Biotechnology, Inc.) to reach an overall volume of 150 µl. Simultaneously, 10 µl UltraCruz® Transfection Reagent (Santa Cruz Biotechnology, Inc.) was mixed with 140 µl Plasmid Transfection Medium. Both solutions were incubated for 5 min at room temperature (RT). Afterwards, the solutions were merged and further incubated for 20 min at RT. Meanwhile, the medium on the cells was aspirated, cells were washed with PBS and overlaid with 700 µl DMEM containing 10% FBS. Finally, the CRISPR/Cas9 plasmid solution was added dropwise to

the cells. Transfection was performed at 37°C/5% CO_2 over night. To ensure gene knock-out, successfully transfected clones were antibiotically selected based on their acquired Puromycin resistance. Thus, after the transfection, the medium was removed and cells were washed with PBS. Subsequently, transfected cells were cultivated in culture medium supplemented with 1 $\frac{\mu g}{ml}$ Puromycin (InvivoGen, San Diego, CA, USA) at 37°C/5% CO_2 for two to three days. After exchanging the antibiotic-containing medium to culture medium, single clones were picked, passaged and cultivated as described in chapter 3.2.1.1. Knock-out efficiency was analyzed by quantitative real-time polymerase chain reaction (qRT-PCR, chapter 3.2.4.3) and by immunocytochemistry (chapter 3.2.3.1) regarding the existence of the respective messenger ribonucleic acid (mRNA) or the corresponding protein.

3.2.1.3 Long-term stimulation

Glioblastoma cell lines were stimulated with the golden-standard therapeutic TMZ in a long-term stimulation model. For this purpose, $1.5 \cdot 10^5$ LN229 cells were seeded in 6-well culture plates and grown over night at 37°C/5% CO_2. On the next day, cells were stimulated with 500 μM TMZ (Merck) or 0.5% (v/v) Dimethyl sulfoxide (DMSO, Merck), respectively, in culture medium for ten days. Hereafter, the medium was changed and cells were cultivated for further 15 days without TMZ stimulation. In between, DMSO-stimulated cells were detached and re-seeded with $1.5 \cdot 10^5$ cells per well every third or fourth day. The medium on not-splitted cells was renewed, likewise.

Furthermore, the influence of inflammatory molecules on cytotoxic and subcellular effects during and after TMZ treatment was examined using the same long-term stimulation model as described above. Additional to TMZ, 2 nM CXCL12, CXCL16 and CX3CL1 (recombinant human proteins, PeproTech GmbH) were added individually or as a chemokine cocktail. Stimulation with single chemokines and with the cocktail was continued during the recovery period of 15 days after TMZ treatment. Moreover, investigated effects of single chemokines were proven by genetic CRIPSR/Cas9 knock-out of the gene encoding the corresponding protein, responsible for binding and activation of particular chemokine signaling cascades. In addition, CXCR4 signaling via CXCL12 binding was specificly inhibited by co-stimulation with 10 μM AMD3100 (CXCR4 inhibitor, Merck). Clones were stimulated as explained above. Regulation of mRNA expression and changes in the synthesis of the respective protein were analyzed after ten days of stimulation and further 15 days of recovery.

3.2.1.3.1 Vital staining of cells

Vital cell staining was used to determine cell division upon stimulation over a certain time frame, since dye molecules are equally distributed between daugther cells, which

ultimately reduces the intensity of the staining upon proliferation.
After three days of stimulation with TMZ ± chemokine cocktail (cf. chapter 3.2.1.3), cells were fluorescently stained with Vybrant™ DiO Cell-Labeling Solution (ThermoFisher Scientific) according to manufacturer's protocol for adherent cells. Briefly, cells were stained with DiO reagent (1:200 in culture medium) for 20 min at 37°C/5% CO_2. First pictures were taken after overall ten days of stimulation with the AxioObserver.Z1 microscope (Carl Zeiss AG, Oberkochen, DE) and the ZEN2 software (Carl Zeiss AG). Parameter settings were set as reference for further image acquisition. During recovery upon TMZ treatment, staining intensities were observed after seven and 15 days. Finally, the ratio of stained *versus* total amounts of cells was calculated based on pictures acquired at day 10, $10 + 7$, $10 + 15$.

3.2.1.4 Generation of primary cell cultures

To obtain primary cell cultures freshly resected tumor tissue was dissociated under sterile conditions. Initially, the dissected tumor tissue was washed in cold PBS, attached residues of vessels were removed and the tissue was roughly chopped with a scalpel. Next, crushed tissue was digested in 5 ml dissociation solution containing 10 $\frac{\mu g}{ml}$ Deoxyribonuclease (DNase) I from bovine pancreas (Merck) at 37°C for 30 min in a Hybridizer HB-1000 (Analytik Jena US LLC, Upland, CA) under continuous rotation. In between, after 15 min, the tissue residues were thoroughly resuspended and further digested. Finally, tissue leftovers were sedimented and the supernatant was carefully aspirated. The pellet was washed with 6 ml culture medium, which was discarded afterwards. In the end, primary cells grew from the tissue residuals in a T25 flask containing 10 ml culture medium. After two to three days bulk tissue pieces were removed by carefully washing the attached cells with PBS. Handling of primary cells was performed as described in sec. 3.2.1.1.

3.2.1.5 Cytotoxicity assay

Since this study deals with the improvement of therapy in GBMs, different therapeutic compounds and strategies were tested concerning their cytotoxic effect in GBM cell lines and primary cultures. To measure number of dead cells, the CytoTox-Fluor™ Cytotoxicity Assay (Promega) represented a suitable assay system, since alive cells attached to the culture plate were further analyzable after cytotoxicity measurement. For cytotoxic studies of different therapeutics, $1.5 \cdot 10^5$ LN229 or A172 cells were seeded in 6-well cultures plates and cultivated over night at 37°C/5% CO_2. On the day of stimulation, cells originally seeded in an extra well were firstly washed with PBS, detached with Trypsin-EDTA and counted as noted in chapter 3.2.1.1.1 to estimate the cell number on the day of stimulation. Then, cells seeded in 6-well culture plates were treated with with different concentrations ranging from 0.5 μM to 2 mM, depending

on substrate efficiency of TMZ, AT101 (Tocris Bioscience, Bristol, UK), Quinacrine (QXN, Merck), Chloroquine (CQ, Merck) and Hydroxychloroquine (HCQ, Tocris Bioscience) as well as Clomipramine (CIMP, Merck) and control stimulation with DMSO or without additive, respectively. Since phenol red as colored indicator interferes with assay measurement, DMEM without phenol red (Pan-Biotech GmbH, Aidenbach, DE) containing 10% FBS (Pan-Biotech), 1% Penicillin-Streptomycin ($10,000\,\frac{\mathrm{U}}{\mathrm{ml}}$) and 2 mM L-Glutamine served and is termed as stimulation medium in the following. After three days of treatment, 50 μl supernatant of each stimulation was transferred to an opaque 96-well plate in duplicates. Subsequently, 50 μl bis-alanyl-alanyl-phenylalanyl-rhodamine 110 (bis-AAF-R110) Substrate (1:1000 in Assay Buffer) were added to the samples. The bis-AAF-R110 Substrate is processed upon the presence of a certain enzyme in the supernatant, that is released upon loss of integrity of the cell membrane. After an incubation of 90 min at 37°C/5% CO_2, the fluorescent substrate conversion was measured with the GENios-Basic plate reader (Tecan Group, Männedorf, CH) at $485\,\mathrm{nm_{Ex}}/530\,\mathrm{nm_{Em}}$. For calculation of total numbers of dead cells in samples, different concentrations of dead cells ($25 \cdot 10^3 - 100 \cdot 10^3$ per ml) for each analyzed cell line were adjusted by treatment with 670 nM Digitonin (Merck) for 60 min at 37°C before actual assay preparation. Likewise, 50 μl of standard dead-cell amounts were mixed with 50 μl bis-AAF-R110 Substrate (1:1000 in Assay Buffer) in duplicates in the opaque 96-well plate and measured as described above. Furthermore, viable cells attached to the corresponding 6-well culture plate were washed with PBS once, detached with Trypsin-EDTA and counted as depicted in chapter 3.2.1.1.1. Percentages of dead cells were calculated by the following formula

$$\text{dead cells}_{\,3\mathrm{d}}\,[\%] = \frac{\text{amount of dead cells}_{\,3\mathrm{d}}}{\text{amount of dead cells}_{\,3\mathrm{d}} + \text{amount of viable cells}_{\,3\mathrm{d}}} \cdot 100\,. \qquad (2)$$

3.2.1.5.1 Cytotoxic effect of preincubated drugs

Besides therapeutic compound testing, experiments that needed to analyze cytotoxicity efficiency upon selected stimuli over a longer time frame were performed. For this purpose, $3 \cdot 10^4$ primary culture cells of GBM 116/14 and GBM 118/14 were seeded twice in 6-well culture plates and grown over night at 37°C/5% CO_2. Additionally, stimulation medium supplemented with 50 μM TMZ or 5 μM AT101 was prepared and incubated at 37°C/5% CO_2 24 h before stimulation. On the next day, the actual cell number was determined as described previously. Then, cells were stimulated with either with 50 μM TMZ or 5 μM AT101 freshly added to stimulation medium or with preincubated drugs. The cytotoxicity as well as the amount of viable cells was first measured after three days of stimulation as noted above. In the other batch, that was not used for cytotoxicity and viability measurements after three days, the medium was renewed containing either fresh or preincubated 50 μM TMZ or 5 μM

AT101 in stimulation medium. Ultimately, after further three days of stimulation, the cytotoxicity of therapeutics and proliferation of cells was analyzed according to the above-mentioned protocol. Percentages of dead cells after a total of six days of treatment were calculated by

$$\text{dead cells}_{\,6\text{d}}\,[\%] = \frac{\text{amount of dead cells}_{\,3\text{d}+6\text{d}}}{\text{amount of dead cells}_{\,3\text{d}+6\text{d}} + \text{amount of viable cells}_{\,6\text{d}}} \cdot 100\,. \quad (3)$$

3.2.1.5.2 Co-culture experiments

Glioblastoma tumor tissue does not only consist of tumor cells, but also other cells of the central nervous system are found to be associated to the tumor forming the tumor microenvironment. The majority of cells of the tumor microenvironment are glial cells representing about 30% of the total tumor mass. Glial cells are divided into tumor-associated microglia/macrophages and reactive astrocytes composing roughly 29% and 1%, respectively [Roggendorf et al., 1996, Zeiner et al., 2018] (reviewed by Matias et al. [2018], Guan et al. [2018]).

On that basis, an *in-vitro* co-culture resection model was established in collaboratory work with Christina Schmitt (Institute of Anatomy, Christian-Albrechts university (CAU), Kiel, DE). Since this model mimics the *in-vivo* situation after surgical resection of the tumor, it was furtheron used for cytotoxic studies on therapeutics and therapeutic combinations. Two different scenarios were assumed: (1) resection of the complete tumor, approximately, and (2) subtotal resection of the tumor termed "incomplete resection". Scenario (1) was extensively studied by Christina Schmitt (Institute of Anatomy), while scenario (2) is part of this thesis. To estimate the numbers of cells needed to mimic an incomplete resection *in vivo*, different assumptions were made. Presuming a typical tumor diameter of 3 cm [Murray, 2012, Bette et al., 2018, Kreth et al., 2013], the surface area and volume of the resection hole is calculated with the assumption of a spherical cavity by equations

$$\text{Surface area} = 4\pi \mathrm{r}^2 \quad (4)$$

and

$$\text{Volume} = \frac{4}{3}\pi \mathrm{r}^3\,. \quad (5)$$

Hence, within a spherical resection hole of 3 cm in diameter the surface area is determined to be 28.3 cm2 and 14.1 ml free volume are filled with liquor. Furthermore, the mean 2D-size of A172 and LN229 tumor cells, HMC3 microglia and SVGA astrocytes was determined by scaling of cells in phase-contrast images taken with an Axiovert200 microscope (Carl Zeiss AG) and the AxioVision 40 software (Carl Zeiss

AG). Cell numbers to be found on the surface area of the resection hole for the incomplete resection model were calculated (cf. tab. 3.9).

Table 3.9: Calculations on cells for the incomplete-resection co-culture model.

	tumor cells	astrocytes	microglia
mean cell size [cm^2]	$3.3 \cdot 10^{-5}$	$2.6 \cdot 10^{-5}$	$3.1 \cdot 10^{-5}$
number of cells (on 28.3 cm^2)	$6 \cdot 10^5$	10^4	$2.6 \cdot 10^5$
actual seeded number	$1.5 \cdot 10^5$	$3 \cdot 10^3$	$6 \cdot 10^4$

To create an *in-vitro* co-culture, different cell types had to be cultivated in one system, in which medium exchange but no direct cell contact was guaranteed. Otherwise, immune activation of cells might be triggered because of different human leukocyte antigen (HLA) clusters present on each cell type. Hence, tumor cells were seeded in 10 cm culture dishes, while SVGA and HMC3 cells were grown on cover slips in Millicell® cell culture inserts (0.4 μm, Merck) placed into the culture dish on top of tumor cells (illustrated in fig. 3.1). In this system cells were not able to migrate across the 0.4 μm pores, but molecules could be transferred. Overall, within the dish 10 ml and in the transwells 2 ml culture medium was added, yielding a total of 14 ml in the system, which resembles the free cavity volume to be filled with liquor after resection. Since cerebrospinal fluid (CSF) would continuously be exchanged in the cavity, which could not be achieved *in vitro*, seeded cell numbers were reduced likewise, to guarantee a longer availability of nutrients for the cells. Employing this co-culture system the cytotoxic effect of sequential treatment with therapeutics was investigated. For this purpose, tumor cells as well as SVGA and HMC3 were seeded in numbers as depicted in tab. 3.9 in culture medium to adhere over night at 37°C/5% CO_2. SVGA and HMC3 cells were first cultivated on cover slips (Ø 18 mm) in transwells in 30 μl for 3 h to allow adhesion. Afterwards, the transwell was equipped with 2 ml culture medium. As the cytotoxic effect of drugs was analyzed over six days, cells were seeded for the cytotoxicity assay after three and after six days, seperately. On the day of stimulation, the actual amount of cells was determined as noted previously. For treatment, the complete medium was exchanged with stimulation medium without phenol red plus culture ingredients supplemented with 50 μM TMZ and 2.5 μM AT101 or 0.0525% DMSO, respectively. After three days of stimulation, the CytoTox-Fluor™ Cytotoxicity Assay was performed according to the denoted protocol in chapter 3.2.1.5. In the special case of co-culture, 50 μl supernatant were taken from each compartment in duplicates, the culture dish and both transwells, in order to measure cytotoxicity for each cell type individually. Furthermore, viable cells were counted as mentioned in chapter 3.2.1.5 and 3.2.1.1.1. Thereafter, the medium on the other batch was changed to stimulation medium containing 2.5 μM AT101 for further treatment. Ulti-

mately, the cytotoxicity and cell proliferation were measured after three further days of stimulation as described above.

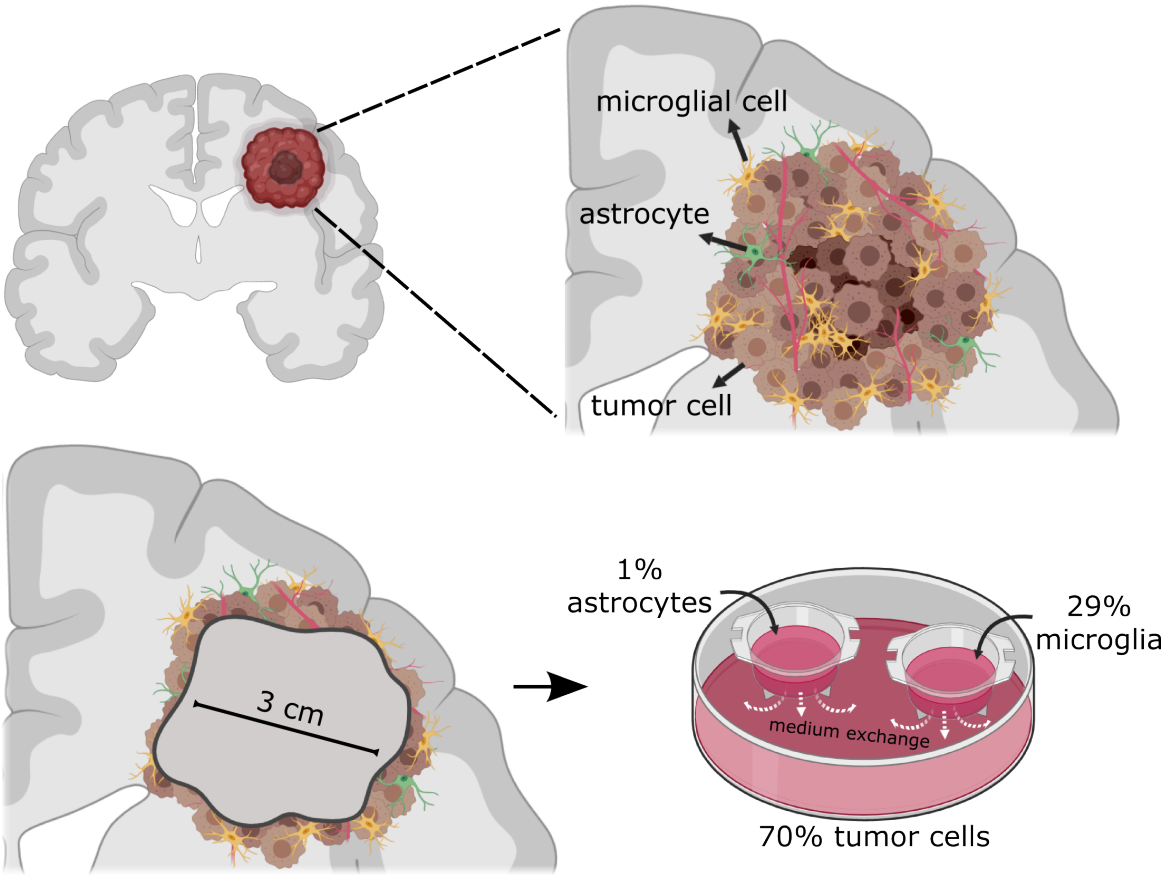

Figure 3.1: Illustration of established *in-vitro* co-culture model of a subtotal resection.

3.2.2 Materials scientific techniques

An aim of this study was the development of an implant material loaded with a therapeutic, which is continuously released, to use it as local device for glioblastoma therapy. Florian Rasch (Institute for Materials Science, CAU, Kiel, DE) contributed with his technical expertise in the field of materials science. In a collaborative approach scaffold materials, based on ZnO 3D-networks [Mishra et al., 2015, 2013], were produced and parameters improved in order to yield optimal drug release. Furthermore, in collaboratory work with Christina Schmitt (Institute of Anatomy) the administration of the material itself as well as material-drug combinations were investigated on tumor and normal brain cells.

In a second approach, advantages of nanoparticles were taken regarding drug bioavailability and stability enhancement. Thus, AT101, in particular, was encapsulated in cubosomal-structured nanoparticles in collaboratory work with Dr. ing. Dorota Flak (NanoBioMedical Centre, Adam Mickiewicz university, Poznań, Poland). Accordingly,

particles were characterized and cellular responses upon encapsulated compound were investigated.

3.2.2.1 Quantitative measurement of molecules in aqueous solutions

3.2.2.1.1 Zn^{2+} ion release

To estimate the release of Zn^{2+} ions from scaffold materials primarily used for drug loading and cell cytotoxicity analysis, a ZnO template was placed in a Millicell® cell culture insert into a 10 cm cell culture dish containing a total of 14.5 ml culture medium. Amounts of Zn^{2+} ions were measured in between one hour and six days of incubation at 37°C/5% CO_2. In these experiments, the colored complexation of Zn^{2+} with Zincon was used for quantitative, photometric measurement of Zn^{2+} ions. At first, 50 μl Zn^{2+}-containing solution to be analyzed were either immediately processed or stored at −30°C until measurement. For the reaction, the sample was diluted 1:500 in 5 mM Borax buffer (pH 9) containing 194 μM Zincon (Carl Roth GmbH + Co. KG) and 1.2 mM NaOH. After thorough mixing, the absorption of the complex was measured at $\lambda = 620$ nm with the Libra UV/Vis spectrophotometer S60. For quantification, a standard with defined Zn^{2+} concentrations was additionally prepared in ranges from 10 to 500 $\frac{\mu g}{ml}$ in culture medium. For this purpose, ZnO powder was initially dissolved in little amounts of 1 M HCl. After successful solvation, the solution was diluted 1:33 in deionized water.
For further analysis regarding chemical activity of the template and saturation of ions in solution, different attempts were made: 1) medium was exchanged after three days of incubation, 2) the template was exchanged after three days of stimulation. The concentration of Zn^{2+} ions in culture medium was determined as described above.

3.2.2.1.2 Drug release from bulk materials

In order to define release kinetics of drugs from scaffold materials, concentrations of therapeutics in aqueous solutions were quantitatively determined according to their photometric characteristics by ultraviolet/visible (UV/Vis) spectroscopy with the Libra UV/Vis spectrophotometer S60 (Biochrom GmbH, Berlin, DE) with QS High Precision Cell cuvettes (Hellma GmbH, Müllheim, DE). In detail, TMZ and AT101 distinct absorption peaks were identified in absorption spectra between 250 and 450 nm in aCSF.
Especially, AT101, diluted in an 1:2-mixture of aCSF-DMSO without supplemented BSA, was loaded on PDMS scaffolds with a cylindric shape (1 mm in height and 6 mm in diameter) by wet infiltration in collaboration with Florian Rasch (Institute for Materials Science). The rough structure inversely formed from the original 3D ZnO network is shown in fig. 3.2.

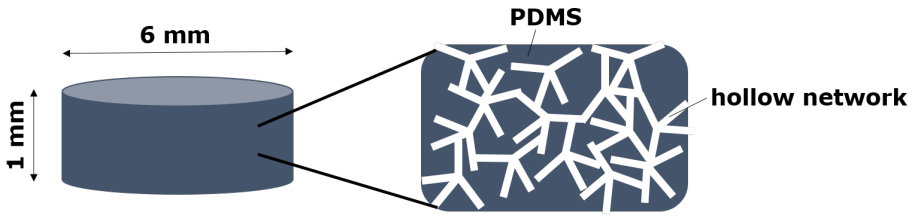

Figure 3.2: PDMS scaffold material used for drug loading.

To improve drug release, different approaches concerning material properties and loading amounts of AT101 were evaluated in cooperation with Florian Rasch (Institute for Materials Science) and Christina Schmitt (Institute of Anatomy). The release of the therapeutic was monitored under sterile conditions at 37°C/5% CO_2 for a maximum of three or six days. Equal distribution of drug in solution was assured by continuous planar rotation at 25 rpm with the KM CO2-FL small shaker (Edmund Bühler GmbH, Tübingen, DE). The AT101-loaded PDMS scaffold was put into a Millicell® cell culture insert containing 1.5 ml aCSF, which was placed in a 10 cm cell culture dish with 13 ml aCSF solution. The concentration of AT101 was analyzed spectrophotometrically at $\lambda = 289$ nm after different time periods ranging from 30 min to ultimately three days. For quantification, defined AT101 concentrations were freshly adjusted in aCSF solution, that was incubated at 37°C/5% CO_2 for the exact time periods just as the samples.

3.2.2.2 Production of blank and AT101-loaded nanoparticles

Cubosomes were prepared using the top-down approach [Ljusberg-Wahren et al., 1996, Akhlaghi et al., 2016] (reviewed by Guo et al. [2010]). Glyceryl monooleate (GMO) was used as structure-forming lipid and pluronic F-127 as surfactant stabilizing the cubosome dispersion.

For blank cubosomes, GMO (IOI Oleo GmbH, Hamburg, DE) was melted at 40°C and mixed with pluronic F-127 (Merck) in a 4:1 ratio at 40°C. In case of drug loading, AT101, diluted in ethanol, was added at 10% (w/w) to the mixture. Afterwards, ethanol was evaporated in vacuum over night. Next, prewarmed PBS was added to molten compounds to gain a concentration of 20 $\frac{\text{mg}}{\text{ml}}$ GMO in the solution. Afterwards the solution was mixed to reach a homogeneous state. Cubic gel was formed over night at RT. To obtain cubosomal dispersion, the cubic gel was sonicated with a Branson Sonifier 250 (Emerson Electric Company, St. Louis, MO, USA) at 60 W by 2 sec pulse and 2 sec pause for a total of 30 min including pulse and pause phases. Meanwhile, the solution was cooled by a jacketed vessel with water flux. On the next day, the cubosomal dispersion was transferred into a fresh tube and stored at RT.

3.2.2.3 Characterization of nanoparticles

3.2.2.3.1 Entrapment efficiency and drug loading capacity

Ultrafiltration centrifugation was performed prior to the determination of the entrapment efficiency and removal of unbound drug from cubosomal particles. 500 μl of drug-loaded cubosomes were filtrated through the Amicon® Ultra-0.5 or -15 Centrifugal Filter Device (10000 molecular weight cut-off (MWCO), Merck) at 14000 g for 30 min, according to the manufacturer's protocol. During the centrifugation, unbound AT101 was filtrated, while cubosomes remained on the filter membrane. To recover cubosomes, the filters were placed upside down into a fresh Eppendorf tube® and centrifugated at 1000 g for 2 min. The concentration of unbound AT101 within the filtrate was determined spectrophotometrically at $\lambda = 289$ nm with the LAMBDA 950 UV/Vis/NIR spectrophotometer (Perkin Elmer, Waltham, MA, USA). As a prove of principle, recovered cubosomes were disrupted with ethanol and the concentration of encapsulated AT101 was analyzed likewise. The entrapment efficiency (EE [%]) and the drug loading capacity (DLC [%]) were calculated by

$$\text{EE}\,[\%] = \frac{\text{amount of entrapped AT101}}{\text{total amount of AT101}} \cdot 100\,. \tag{6}$$

$$\text{DLC}\,[\%] = \frac{\text{mass of entrapped AT101}}{\text{total mass of cubosomes}} \cdot 100\,. \tag{7}$$

3.2.2.3.2 Particle size and morphologic analyses

Z-average, particle size distribution (by their number) along with polydispersity index (PDI) and the zeta potential ζ of prepared cubosomes, as well as their stability over a time and temperature, were measured on Zetasizer Nano-ZS (Malvern Instruments, Malvern, UK) based on non-invasive dynamic light scattering method (DLS) using an angle of 173° and electrophoretic light scattering (ELS), respectively. For measurements blank GMO cubosomes as well as AT101-loaded cubosomes were stored either at RT or 37°C. Measurements were performed for 40 $\frac{\mu g}{\text{ml}}$ cubosome dispersion diluted in distilled water at the 25°C and 37°C, respectively, and results are the mean ± standard deviation of three individual analyses. In order to investigate the stability of prepared cubosomes, measurements were performed at time intervals over a period of 17 days.

Moreover, particle size and morphology of particles were observed by cryogenic transmission electron microscopy (cryo-TEM) with a JEM-1400 transmission electron microscope (Jeol, Akishima, JPN) operating at 120000 V with a maximum resolution of 0.2 nm. For this purpose, samples were diluted in an 1:1 ratio with distilled water. Then, $3 - 4\,\mu$l sample suspension were deposited on a lacey/carbon grid (Ted

Pella, Inc., Redding, CA, USA) and freeze-dried at −170°C with the Cryoplunge 3 System (Gatan, Inc., Pleasanton, CA, USA). Cryo-TEM pictures were acquired with the DigitalMicrograph software (Gatan, Inc.).

3.2.2.3.3 Thermal stability measurements

To estimate the thermal stability and physical behavior of cubosomes upon AT101 loading, samples were analyzed by differential scanning calorimetry (DSC). This thermoanalytical technique provides information about phase transitions as well as structure decomposition by the analysis of absorbed and emitted heat within the sample upon heating and cooling cycles [Höhne et al., 2003]. Thus, 5-11 mg GMO lipids, GMO cubosomes and AT101-loaded GMO cubosomes were heated or cooled, respectively, in a nitrogen atmosphere from 15° to 80°C and cooled *vice versa* at a constant rate of 10°C per minute for three cycles with the DSC 8000 (Perkin Elmer). After each cycle the temperature was hold at 15°C for 2 min.

3.2.2.3.4 AT101 release

The release of AT101 from GMO cubosomes was determined by dialysis [Gupta et al., 1987]. For this purpose, 500 μl AT101-loaded cubosome dispersion were filled into a Spectra/Por® 2 Dialysis Membrane (12000 - 14000 MWCO, VWR International, Radnor, PA, USA), which was previously equilibrated with 0.1 M NaOH, then rinsed and stored in distilled water over night. Filled membrane was closed with bendable clips to form a dialysis bag. Next, this bag was placed into 20 ml aCSF solution at a temperature of 37°C and continuously stirred for 72 h. After 3, 6, 24, 48 and 72 h, 500 μl sample in aCSF solution was withdrawn and replaced with fresh one. The AT101 concentration in withdrawn samples was determined spectrophotometrically at $\lambda = 289$ nm with the LAMBDA 950 UV/Vis/NIR spectrophotometer.

3.2.2.4 Uptake of nanoparticles into cells

To demonstrate uptake, AT101-loaded cubosomes were fluorescently labelled in order to visualize their uptake into tumor cells. At first, 20 $\frac{\text{mg}}{\text{ml}}$ GMO cubosomes encapsulating AT101 were incubated with 5 $\frac{\mu\text{g}}{\text{ml}}$ Nile Red (Merck) at 37°C over night under continuous shaking at 300 rpm in the dark. After 24 h, unattached Nile Red molecules were removed by ultrafiltration centrifugation with Amicon® Ultra-4 Centrifugal Filter Devices (10000 MWCO), according to manufacturer's instructions. 250 μl stained cubosome dispersion were added onto the filter membrane and centrifugated at 3000 g for 30 min. Fluorescently labelled nanoparticles were recovered from the filter, redispersed in the PBS solution up to the initial volume of 250 μl and stored in a fresh Eppendorf tube®.

For visualization of nanoparticle uptake efficiency, $1.5 \cdot 10^5$ A172 and LN229 cells were

seeded onto coverslips and cultivated over night at 37°C/5% CO_2. Moreover, uptake of cubosomes in 3D tumor spheroids, reflecting a tumor environment, was investigated. For this purpose, 10^4 A172 and LN229 cells were cultivated as hanging drops on 6-well lids in 30 μl culture medium with 2 ml culture medium in the well underneath for two days at 37°C/5% CO_2. Afterwards, formed spheroids were transferred into 6-well plates covered with 1% agarose overlaid with 3 ml culture medium and grown for further six days at 37°C/5% CO_2. After stimulation with 26 $\frac{\mu g}{ml}$ fluorescently labelled AT101-loaded GMO cubosomes for 24 h at 37°C/5% CO_2 in culture medium, spheroids were stained with Alexa Fluor®-conjugated Concanavalin A (1:20 in PBS, ThermoFisher Scientific) for 30 min at 37°C after washing with prewarmed PBS, to allow for membrane identification. Subsequently, cells were washed with PBS for 3 min and the nuclei was fluorescently marked with Hoechst 33342 (1:100 in PBS, ThermoFisher Scientific) for 10 min at 37°C. Next, cells were washed three times with PBS, Live Cell Imaging Solution (ThermoFisher Scientific) was added and pictures were acquired immediately with the AxioObserver.Z1 microscope (Carl Zeiss AG) and the ZEN2 software (Carl Zeiss AG). By contrast, adherent native cells, stimulated with 26 $\frac{\mu g}{ml}$ fluorescently labelled AT101-loaded GMO cubosomes for 24 h, were fixed and permeabilized with 4% (w/v) paraformaldehyde in deionized water for 10 min at RT after washing with PBS once. Subsequently, cells were washed with PBS twice and the coverslip was treated with 0.1% (v/v) Triton X-100 in PBS for 5 min at RT. Unspecific binding sites were blocked with 1% (w/v) BSA in PBS after further three washing steps with PBS for 60 min at RT. Next, cells were stained with β-Catenin antibody (information in tab. 3.6) for 60 min at 37°C, to indirectly define the cell body. After three steps of washing with PBS, the secondary antibody was applied as noted in tab. 3.7 for 60 min at 37°C. Then, unbound secondary antibody was removed by washing with PBS three times. Finally, the nuclei were stained with Hoechst 33342 (1:100 in PBS) for 10 min at RT and fixed cells were embedded in Immu-Mount™ solution (ThermoFisher Scientific) on an object slide after washing with PBS three times and once with deionized water. Images were acquired with the AxioObserver.Z1 microscope (Carl Zeiss AG) and the ZEN2 software (Carl Zeiss AG). Further image editing was performed with GNU Image Manipulation Program (GIMP).

3.2.2.5 Determination of cell viability

3.2.2.5.1 Long-term viability analysis

The cell viability upon treatment with material and material-drug combinations based on ZnO 3D-networks was analyzed by a cell counting technique (cf. chapter 3.2.1.1.1). In a first approach, the biocompatibility of the material was analyzed in accordance

with DIN EN International Organization for Standardization (ISO) 10993-5. For this purpose, extract medium was generated by incubation of the material in culture medium under sterile conditions at 37°C/5% CO_2 for 72 h following DIN EN ISO 10993-12 standards. Afterwards, the release of Zn^{2+} ions into the medium was determined as described in chapter 3.2.2.1.1. Then, different concentrations of Zn^{2+} ions were adjusted in culture medium and tested regarding their effect on cells. $3 \cdot 10^4$ primary culture cells of GBM 27/07, 116/14 and 118/14 were seeded into 6-well plates and grown over night at 37°C/5% CO_2. On the next day, cell numbers were counted within an extra seeded well in a Neubauer counting chamber. Subsequently, cells were stimulated with different concentrations of Zn^{2+} ions with or without 2.5 μM AT101 for six days in culture medium. In between, the reagent-containing medium was renewed after three days of treatment. Cell numbers were counted after six days as noted above.

Secondly, the effect of indirect contact of drug-loaded material to cells was investigated. Thus, a ZnO 3D-network with cylindric shape (2 mm in height and 6 mm in diameter) was loaded with 193 μg AT101 included in poly(L-lactide-co-caprolactone) (PLCL). The scaffold material was infiltrated six times with 1 mM AT101-PLCL-DMSO solution and dried in between. $3 \cdot 10^4$ previously seeded primary culture cells of GBM 27/07 or 116/14 in 6-well plates were indirectly stimulated with this template. The template was placed in a Millicell® cell culture insert (0.4 μm) on top of the cell layer. The 6-well cavity was flooded with 2 ml and the transwell with 1 ml culture medium. Proliferation of cells as well as Zn^{2+} ion and AT101 release were analyzed after two, four and six days of stimulation (cf. chapter 3.2.1.1.1, 3.2.2.1.2, 3.2.2.1.1).

3.2.2.5.2 WST-1 assay

The effect of AT101-loaded GMO cubosomes on cells compared to free drug was evaluated in two different tumor cell lines (A172 and LN229), as well as normal cells of the central nervous system such as astrocytes (SVGA) and microglia (HMC3), by the determination of cell viability. For experiments, $6 \cdot 10^3$ cells were seeded into 96-well culture plates and grown over night at 37°C/5% CO_2. To firstly estimate the toxicity of blank GMO cubosomes, seeded cells were stimulated in triplicates with increasing concentrations from 20 to 200 $\frac{\mu g}{ml}$ GMO cubosomes in culture medium. Further, cells were treated with different concentrations of AT101-loaded GMO cubosomes in comparison to the corresponding free drug concentration in culture medium. After 72 h of stimulation, the cell viability was determined by the colorimetric assay based on enzymatically triggered conversion of the tetrazolium salt 4-[3-(4-Iodophenyl)-2-(4-nitrophenyl)-2H-5-tetrazolio]-1,3-benzene disulfonate (WST-1) by cellular dehydrogenases to formazan which can be detected spectrophotometrically [Peskin and Winter-

bourn, 2000]. In detail, stimulated cells were washed with PBS once and fresh culture medium was added to the wells. Subsequently, Cell Proliferation Reagent WST-1 (Hoffmann-La Roche, Basel, CH) was added at a volume ratio of 1:10 to all samples. After 90 min of incubation at 37°C/5% CO_2, the absorbance at $\lambda = 450$ nm compared to $\lambda = 595$ nm as reference was measured with the Infinite M Plex plate reader (Tecan Group). Prior to measurement, the plate was orbitally shaked for 50 sec.

3.2.2.6 Cytoskeletal rearrangement experiments

For further analysis of intracellular effects triggered by nanoparticle treatment, the cytoskeletal rearrangement upon stimulation with AT101-loaded GMO cubosomes was investigated on mRNA and protein level. Initially, $1.5 \cdot 10^5$ A172 and LN229 cells were seeded either onto coverslips or into 6-well culture plates and cultivated over night at 37°C/5% CO_2. On the next day, cells were stimulated with 26 $\frac{\mu g}{\text{ml}}$ blank and AT101-loaded GMO cubosomes as well as the respective concentration of free drug for six and 24 h in culture medium. Regarding the evaluation of regulations in cytoskeleton-associated gene expression, cells were harvested after 24 h and further processed as described in chapter 3.2.4.1.1 and the following. For fluorescent visualization of alterations in cytoskeletal structure, stimulated cells were washed with PBS once, then fixed and permeabilized with 4% paraformaldehyde in deionized water for 10 min at RT. Next, cells were washed with PBS twice and treated with 0.1% Triton X-100 in PBS for 5 min at RT. After three further washing steps with PBS, unspecific binding sites were blocked with 1% BSA in PBS for 20 min at RT. Then, actin filaments were stained with Phalloidin-Atto 488 (1:75 in 1% BSA in PBS, Merck) for 20 min at RT. Subsequently, cells were washed with PBS twice and nuclei were fluorescently marked with Hoechst 33342 (1:100 in PBS) for 10 min at RT. At last, cells were washed again with PBS three times, once with deionized water and finally embedded in Immu-Mount$^{\text{TM}}$ solution on an object slide. Fluorescent signals were studied with the AxioObserver.Z1 microscope and pictures were taken with the ZEN2 software. Further processing of images was done with GIMP software.

3.2.3 Protein biochemical techniques

3.2.3.1 Immunocytochemistry

To fluorescently visualize subcellular proteins, they are labeled with antibodies against a certain protein domain. To investigate the efficiency of genetic editing in CRISPR/Cas9-transfected cells, the knock-out was visualized by fluorescent staining of the corresponding protein. For this purpose, $1.5 \cdot 10^5$ CRISPR/Cas9-transfected cells were seeded onto a coverslip and grown over night at 37°C/5% CO_2. Before staining, cells were incubated in serum-reduced DMEM containing 0.5% FBS for 60 min in total. In between, after every 20 min, medium was aspirated, cells were washed with

PBS and fresh serum-reduced medium was added. For staining, cells were washed with PBS once, fixed onto the coverslip and permeabilized with an 1:1-mixture of methanol and acetone for 10 min at RT. Afterwards, cells were washed with PBS three times followed by a blocking step of unspecific binding sites with blocking buffer for at least 60 min at RT. After removal of blocking buffer, binding of antibody to the protein of interest was performed in a wet chamber in the dark over night at 4°C. Antibodies were diluted as noted in tab. 3.6 in PBS. To prove specificity of antibody binding, an IgG control antibody - either mouse IgG (R&D Systems MAB002) or rabbit IgG (R&D Systems AB-105-C) - was additionally used in the very same concentration as the respective antibody against the protein of interest. On the next day, unbound antibody was removed by three washing steps with PBS. Thereafter, bound antibody was stained with a fluorescence-conjugated secondary antibody diluted in PBS as depicted in tab. 3.7. The secondary antibody bound to the respective species of the primary antibody for 60 min in a wet chamber in the dark at 37°C. To dye the nucleus, after further three washing steps with PBS, cells were incubated with DNA-intercalating 4',6-diamidino-2-phenylindole (DAPI, 1:30000 in PBS, Merck) for at least 30 min at RT in a wet chamber in the dark. Finally, the coverslip was washed with PBS three times and once with deionized water followed by embedding in Immu-Mount^{TM} solution on an object slide. The fluorescent signal was observed with the AxioObserver.Z1 microscope and images were acquired and primary processed with ZEN2 software. Furthermore, editing of pictures was performed with GIMP software.

3.2.3.2 Immunohistochemistry of tumor tissue

For the analysis of presence, abundance and localization of proteins of interst in solid tumor tissue, proteins were fluorescently stained. Hereby, the staining procedures followed the general protocol described in chapter 3.2.3.1. Slight differences are pointed out in the further protocol. Initially, tissue sections already fixed on an object slide were encircled with a grease pencil. After fixation of cells, the object slide was washed three times with TBST for at least 5 min, which is the typical washing procedure in case of fluorescent staining of tumor tissue. In order to differentiate between single cells in tissue, before fluorescent labeling, lipids of the cell membrane were stained with Sudan black. Hence, tissue was primarily incubated in 20% ethanol for 2 min, then in 70% ethanol for 2 min, and finally in Sudan black solution (1% (w/v) in 70% ethanol, Carl Roth GmbH + Co. KG) for 10 min. Afterwards, the object slide was shortly washed in 70% ethanol for three times and in 20% ethanol for 2 min. Especially in tumor tissue, high interest was laid on co-staining of more than one protein. For this purpose, either the second primary antibody was added after fluorescent conjugation of the first one or, if the respective antibodies were originated from the same host animal, a F_{ab} fragment step - a complete blockage of unbound domains

of the respective host antibody - was introduced. After fluorescent conjugation of the first primary antibody, the object slide was washed with TBST three times and unbound domains were blocked with α-mouse or α-rabbit F_{ab} fragment (1:1000, donkey, Jackson ImmunoResearch, Cambridge, UK) for 60 min in a wet chamber at RT. Subsequently, the second primary antibody was applied as described previously. At last, prior to staining of the nuclei and embedding, the object slide was additionally washed in TBS and DAPI was diluted 1:30000 in TBS before use.

3.2.3.3 Preparation of cell lysates

After stimulation (cf. chapter 3.2.1.3), cells were washed with PBS once and stored in lysis buffer containing 1% (v/v) Halt™ Protease Inhibitor Cocktail (ThermoFisher Scientific) at −30°C until further processing. After thawing, cells were harvested with a scraper and centrifugated at 20000 g for 15 min at 4°C to pellet cell debris. The supernatant containing proteins was transferred into a fresh Eppendorf tube® and protein concentration was determined using the Bradford assay. For this purpose, after dilution of samples in deionized water, Protein Assay Dye Reagent Concentrate (Bio-Rad Laboratories Inc., Hercules, CA, USA) was added in an 1:5-ratio. To quantify protein concentration, a serial dilution of a BSA standard was prepared in deionized water, likewise. After an incubation for 20 min at RT, all samples were transferred in triplicates into a transparent 96-well plate and the absorbance at 595 nm was measured with the GENios-Basic plate reader (Tecan Group).

3.2.3.4 Sodium dodecyl sulfate polyacrylamide gel electrophoresis (SDS-PAGE)

After protein concentration measurement, samples were adjusted to equal amounts in lysis buffer. Subsequently, secondary and higher structures of proteins were denaturated in sample buffer at 95°C for 5 min. For optimal electrophoretic separation of proteins, different percentages of acrylamide in SDS gels were used, depending on the size of the protein of interest. Preparation of SDS gels is displayed in tab. 3.10. Separation itself was performed in electrode buffer at 35 mA per gel and 300 V by placing prepared gels into a Mini-PROTEAN Tetra System (Bio-Rad). Depending on the abundance of the respective protein to be detected, 3, 10, 12 or 30 μg whole protein lysate was loaded in each gel lane. For analysis of molecular weight of the protein of interest, the PageRuler™ Plus Prestained Protein Ladder (ThermoFisher Scientific) was carried along in each gel.

Table 3.10: Pipet scheme for SDS gels.

	10% gel	12.5% gel	15% gel	Stacking gel
30% acrylamide	3.33 ml	4.17 ml	5 ml	1.67 ml
Separating gel buffer	2.6 ml	2.6 ml	2.6 ml	
Stacking gel buffer				2.6 ml
deionized H_2O	4.03 ml	3.29 ml	2.46 ml	5.79 ml
APS (10% (w/v) in H_2O)	60 μl	60 μl	60 μl	60 μl
TEMED	30 μl	60 μl	60 μl	60 μl

3.2.3.5 Protein detection by semi-dry Western Blot

For immunodetection, separated proteins were transferred onto a Amersham™ Hybond™ PVDF blotting membrane (GE Healthcare, Chicago, IL, USA). Therefore, the semi-dry technique was applied. Prior to protein transfer at 25 V and 1 A for 30 min in the Trans-Blot® Turbo™ Transfer System (Bio-Rad), the PVDF membrane was shortly moistened in methanol, as well as the Whatman™ filter papers (GE Healthcare) were wetted in transfer buffer.

After blotting, the membrane was placed in a plastic box and incubated with TBST containing 5% BSA for at least 60 min. The primary antibody was diluted in the same solution or 2% casein in TBST in concentrations noted in tab. 3.6. Antibody binding to the protein of interest was performed over night at 4°C in a hermetic chamber. On the next day, unbound antibody was removed by washing with TBST for 15 min three times. Afterwards, the membrane was incubated with the corresponding secondary antibody, diluted in TBST plus 2% casein, for 60 min. Again, unbound antibody was removed by three washing steps with TBST for 15 min. Prior to immunodetection, the membrane was washed with TBS for 10 min once. The protein of interest was detected by chemiluminescent reaction with an 1:1 mixture of Immobilon™ Western luminol and peroxide solution (Merck) for 5 min. For documentation, chemiluminescent signals were visibly fixed on Amersham Hyperfilm™ ECL (GE Healthcare). Image processing and band intensity quantification was done with the ImageJ software.

To ensure loading of equal amounts of protein, the membrane was shortly washed in TBST and reblotted with an antibody detecting GAPDH as a loading control. For this purpose, bound antibody on the membrane was stripped with Re-Blot Plus stripping solution (Merck) for 15 min per side. Afterwards, the membrane was incubated in TBST containing 2% casein for at least 60 min. For immunoredetection, the protocol described above was performed except for chemiluminescent reaction, which was carried out with an 1:1 mixture of Amersham™ ECL Select™ Western Blotting Detection Reagents solution "A" and "B" (GE Healthcare).

3.2.4 Molecular biological techniques

3.2.4.1 RNA isolation

For several *in-vitro* experiments, mRNA expression of certain genes or alteration of mRNA expression upon certain stimuli was analyzed (in cases of chapter 3.2.1.2, 3.2.1.3). Depending on the available amount of (stimulated) cells, RNA was isolated either with the ARCTURUS® PicoPure® RNA Isolation Kit (for a maximum of $\sim 2.5 \cdot 10^5$ cells, ThermoFisher Scientific) or with TRIzol™ reagent (for higher cell amounts, ThermoFisher Scientific). After isolation, RNA concentration and purification were determined with the NanoDrop 2000c (ThermoFisher Scientific). Purification was defined by absorption ratios at 260/280 and 260/230. Isolated RNA was stored at −80°C.

3.2.4.1.1 Isolation with TRIzol™

This RNA isolation method is based on the guanidinium thiocyanate-phenol-chloroform extraction. At first, medium was aspirated from the cell layer. After washing with PBS, 1 ml TRIzol™ reagent was added and cells were either stored at −30°C or harvested immediately. Next, cell debris was pelleted at 12000 g for 10 min at 4°C. The supernatant was transferred into an new Eppendorf tube® and shortly incubated at RT for 5 min. After addition of 200 µl chloroform the sample was inverted 15 times and incubated at RT for 3 min. For phase separation of proteins, sugars and nucleic acids, the mixture was centrifugated at 12000 g for 15 min at 4°C. The entire upper phase was carefully transferred into a new Eppendorf tube®. After thorough mixing with ice-cold 500 µl isopropyl alcohol, the solution was incubated for at least 40 min at 4°C. Afterwards, RNA was pelleted at 12000 g for 10 min at 4°C and subsequently washed with 1 ml 75% ethanol absolute by vortexing. For drying, the RNA pellet was centrifugated at 7600 g for 5 min at 4°C, the supernatant almost completely removed and the RNA dried at RT. At last, depending on pellet size, RNA was solved in $20 - 100$ µl RNase-free water (Carl Roth GmbH + Co. KG) at 58°C for 10 min during slow shaking.

3.2.4.1.2 Isolation with the ARCTURUS® PicoPure® RNA Isolation Kit

If only small amounts of biological material was available, cells were firstly lyzed in $50 - 100$ µl Extraction buffer (provided by the kit) at 42°C for 30 min after washing with PBS once. Then, lyzed material was either stored at −80°C or RNA isolation was immediately performed according to the manufacturer's instructions of the ARCTURUS® PicoPure® RNA Isolation Kit. Ultimately, RNA was eluated from the column with 15 µl Elution buffer (provided by the kit).

3.2.4.2 Reverse transcription

Prior to the investigation of mRNA expression by qRT-PCR, isolated RNA was converted to complementary DNA (cDNA) by reverse transcription protocol. If possible, RNA concentration was adjusted to 1 μg in 7 μl RNase-free water. Otherwise, the maximal possible concentration of RNA in 7 μl was used. Residual DNA was digested by the addition of 1 μl RQ1 RNase-free DNase (1 $\frac{\text{U}}{\mu\text{l}}$, Promega) and 1 μl RQ1 DNase 10x Reaction Buffer (Promega) at 37°C for 15 min. Digestion was stopped with 2 mM EDTA at 65°C for 10 min. Breakage of secondary structures of RNA and followed primer annealing was assured by the addition of 200 ng pd(N)$_6$ Random Hexamer 5'-Phosphate Sodium Salt primers (GE Healthcare) at 70°C for 5 min. After cooling on ice, the following reagents were added to each RNA sample:

Table 3.11: Amounts of used reagents per one sample for reverse transcription protocol.

Volume	Reagent	Provider
4 μL	5x Reaction Buffer for RT	ThermoFisher Scientific
2 μL	10 mM dNTP mix	ThermoFisher Scientific
1 μL	RNase-free water	Carl Roth GmbH + Co. KG
1 μL	RevertAid H Minus Reverse Transcriptase, 200$\frac{\text{U}}{\mu\text{l}}$	ThermoFisher Scientific

After gentle mixing and centrifugation, the sample was initially incubated at 25°C for 10 min. Then, cDNA strands were synthesized at 42°C for 60 min. At last, the enzyme was denaturated at 70°C for 10 min. cDNA was stored at −30°C before further processing.

3.2.4.3 qRT-PCR

For the quantitative detection of mRNA, the TaqMan™ concept was used, which is based on fluorescence resonance energy transfer (FRET) [Förster, 1965]. In general, a fluorescent dye called 6-Carboxyfluorescein is quenched. Upon binding of the TaqMan™ probe to the respective gene sequence on the cDNA strand and primer binding to an adjacent region, the TaqMan™ polymerase is able to sequence the strand and removes the quencher via its 5'-3' exonuclease activity [Holland et al., 1991]. For this purpose, cDNA templates were mixed with reagents as depicted in tab. 3.12. Measurements were performed in technical duplicates in a 96-well plate sealed with a transparent foil. After sealing, the plate was shortly centrifugated in a mini plate spinner (Labnet International, Inc., Edison, NJ, USA) and the qRT-PCR protocol shown in tab. 3.13 was applied with a QuantStudio5 (ThermoFisher Scientific). To control for technical contaminations, a negative control lacking any cDNA was measured for every gene whenever analyzed. Moreover, mRNA expression

of Glycerinaldehyde 3−phosphate dehydrogenase (GAPDH), a housekeeping gene, served as a reference. Genes of interest and respective assay details of the TaqMan™ primer-probes (ThermoFisher Scientific) are depicted in tab. 3.8. The expression of the gene of interest was evaluated by the QuantStudio™ Design & Analysis software (ThermoFisher Scientific). Ultimately, the cycle-of-threshold (CT) value of the gene of interest was normalized to the GAPDH reference as follows:

$$\Delta CT_{\text{gene of interest}} = CT_{\text{gene of interest}} - CT_{\text{GAPDH}} \,. \tag{8}$$

Table 3.12: Pipet scheme for qRT-PCR.

Volume	Reagent	Provider
2 μl	10 ng cDNA	
1 μL	TaqMan™ primer-probe	ThermoFisher Scientific
7 μL	RNase-free water	Carl Roth GmbH + Co. KG
10 μL	TaqMan™ Gene Expression Master Mix	ThermoFisher Scientific

Table 3.13: qRT-PCR programm.

Time	Temperature	Cycles	Step
10 min	95°C	1	denaturation
15 sec	95°C	40	denaturation
1 min	60°C		elongation

3.2.5 Statistical analysis

The data were statistically analyzed using the GraphPad Prism 5 Software (GraphPad Software, San Diego, CA, USA). Depending on the experimental setup either a student's t-test, a one-way analysis of variances (ANOVA) or a two-way ANOVA was performed, as seperately annotated for each experiment. In general, the data are presented as mean ± standard deviation (SD). Statistical significance is marked with asterisks or hashtags depending on the p-value: */# $p \leq 0.05$, **/## $p \leq 0.01$, ***/### $p \leq 0.001$ and ****/#### $p \leq 0.0001$.

4 Results

4.1 Entry and exit mechanisms of dormancy in GBM cells

4.1.1 Chemotherapeutic-induced dormancy in GBM cells is associated with stem-like abilities

The primary brain tumor *Glioblastoma Multiforme* (GBM) is known to overcome and adapt to therapy regimen in order to survive the treatment. This is achieved through different mechanisms. On the one hand, the existence of cell subpopulations with different molecular profiles resembles the tumor heterogeneity [Verhaak et al., 2010, Wang et al., 2017b], for that chemical stimulation fails to address all tumor cells equally. On the other hand, stem cell abilities of so called glioma stem cells are responsible for tumor maintenance and progression after therapy [Singh et al., 2003, 2004]. Last but not least, the high migratory potential of a subset of tumor cells in line with chemoresistant features additionally accounts for surgical escape [Scherer, 1938, Claes et al., 2007]. Consecutively, the prognostic survival of patients is extremely short despite extensive therapy [American Cancer Society, 2018]. Another recently identified therapy-escape mechanism of cancer cells is dormancy, a state of tumor growth arrest [Yeh and Ramaswamy, 2015]. While tumor mass, especially angiogenic dormancy, in which the tumor persists in a dormant state due to avascularity, has been comprehensively studied in glioblastomas [Naumov et al., 2006, Almog et al., 2009, Satchi-Fainaro et al., 2012], dormancy on the cellular level and influences of therapy have not been described so far.

Thus, to primarily determine the abundance and location of dormant cells in solid GBM tumor samples, those were analyzed *ex vivo* concerning the expression of the known dormancy markers ephrin type A receptor 5 (EphA5), insulin-like growth factor-binding protein 5 (IGFBP5) and histone cluster 1 H2B family member K (H2BK) [Almog et al., 2009, Satchi-Fainaro et al., 2012]. Immunohistochemistry stainings and gene expression analysis revealed well-detectable amounts of such markers on mRNA and protein level regardless of the grade of malignancy in Kiel-67 (Ki67)-negative areas adjacent to blood vessels indicating a quiescent area of cells [Gerdes et al., 1984]. Furthermore, an investigation of the abundance of typical embryonal or neural stem cell markers like krüppel-like factor 4 (KLF4), octamer-binding transcription factor 4 (OCT4), sex-determining region Y-box 2 (SOX2) and musashi-1 (MSI1) [Brembeck and Rustgi, 2000, Nichols et al., 1998, Avilion et al., 2003, Sakakibara et al., 1996, Hattermann et al., 2016a] in solid GBM tissue revealed a partly co-staining with those dormancy markers. This pointed to a possible connection between dormancy features and stem cell abilities, which has also been postulated by others [Endaya et al., 2016, Deleyrolle et al., 2011].

Furthermore, in order to estimate the impact of classical therapy with temozolomide (TMZ) on dormancy induction, GBM cell lines and primary cultures with different molecular profiles (see supplementary fig. A.1) were stimulated with a subletal dose of TMZ for ten days. Indeed, GBM cell lines and primary cultures responded to different extents to TMZ treatment and surviving cells exhibited an extended cytoplasm. Additionally, vital-dyed cells, that were stimulated with TMZ, retained their staining over the stimulation period of ten days, while those, that were treated with DMSO, lost it rapidly due to cell division. This revealed a potential stop in proliferation of TMZ-treated cells (shown for cell lines in fig. 4.1A).
Known by literature, dormant cells are not only characterized by an enhanced expression of dormancy markers, but also by an increased signaling via p38 compared to decreased signaling through ERK [Aguirre-Ghiso et al., 2004]. Hence, to confirm the induction of cellular dormancy, further experiments on mitogen-activated protein kinase (MAPK) signaling-pathway induction and the expression of known dormancy markers revealed an upregulation of dormancy-associated genes as well as an altered signaling ratio for ERK/p38 MAP kinases (results regarding cell lines displayed in fig. 4.1B and C) concluding that tumor cells entered cellular dormancy upon TMZ treatment. Moreover, in a comparative analysis of DMSO- *versus* TMZ-pretreated LN229 cells, TMZ-pretreated cells showed a reduced sensitivity to further stimulation compared to the control representing a therapy resistance under dormant conditions. Due to a possible connection of dormancy and stem cell abilities, which was already indicated *ex vivo*, stem cell marker regulation was observed in line with dormancy marker induction in TMZ-treated GBM cell lines. Furthermore, LN229 cells, previously characterized by an augmented expression of dormancy-associated genes upon TMZ stimulation, exhibited an increased self-renewal capacity analyzed by an extreme limiting dilution analysis (ELDA) assay (fig. 4.1D) indicating the acquisition of stem cell features in association with dormancy entrance.
As previously mentioned, the extent of response to TMZ depended on the cell line or primary culture. Thus for quantification, the amount of dead cells upon administration of TMZ was determined in a time-dependent manner. In order to improve classical treatment, GBM cells were additionally treated with another therapeutic compound, AT101, acting on autophagy-related pathways [Voss et al., 2010] after six days of single TMZ stimulation. Interestingly, those cells, responding to a low extent to classical therapy such as A172, could be effectively targeted with TMZ plus AT101 as well as single AT101 treatment. In contrast, LN229 and U251MG cells did not reveal an increased cytotoxicity upon additional AT101 stimulation (cf. fig. 4.1E) and were moderately affected by single AT101 administration.

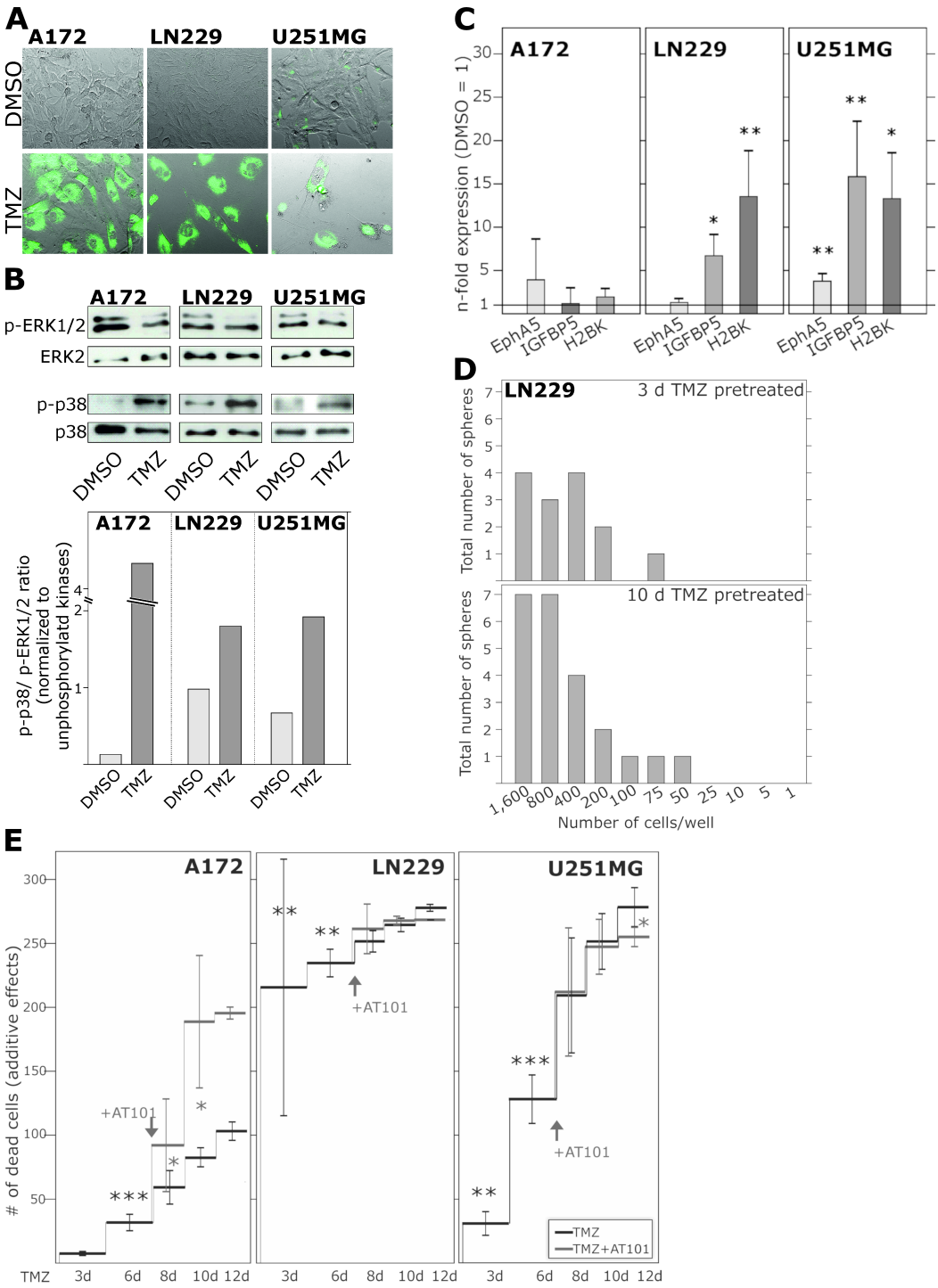

Figure 4.1: GBM cells show dormancy-like features, acquire stem cell abilities upon TMZ treatment and are differentially affected by additional AT101 stimulation. To generate dormant tumor cells *in vitro*, different GBM cell lines were stimulated with 500 μM TMZ or DMSO, respectively, for ten to twelve days. To allow for identification of non-proliferative cells, cells were stained with DiI after three days of TMZ stimulation. Pictures were acquired after ten days of stimulation (**A**). For further dormancy characterization, ERK/p38 signaling was analyzed in TMZ-treated cells by Western Blot (n=3, **B**) and the expression of dormancy-associated genes was determined by qRT-PCR (n=4, **C**). To draw connections between dormancy and self-renewal capacity, LN229 cells, stimulated with TMZ for either three or ten days, were seeded according to an ELDA assay (**D**). Since GBM cell lines responded differentially to TMZ treatment, exact numbers of dead cells were determined over certain intervals and the cytotoxic effect of another treatment schedule including TMZ $\pm$ 5 μM AT101 after six days of single TMZ application was examined (n=5, **E**). In all cases, statistical analysis was performed by paired student's t-test (adapted from Adamski et al. [2017a], attached in the appendix).

Taken together, these findings suggest that GBM cells entered cellular dormancy in order to survive classical treatment with TMZ. Moreover, entrance into dormancy seemed to correlate with the acquisition of stem cell abilities, thereby providing the basis for the re-induction of tumor growth afterwards. Apart from that, cell death initiation in tumor cells, that were less sensitive to classical treatment, was improved by the use of specific therapeutics, that mediate cell death through alternative pathways. In summary, inducing cell death through different pathways by multi-drug administration was more successful for tumor treatment (these results were published in Adamski et al. [2017a], which is attached in the appendix).

4.1.2 Entry and exit of dormancy is differentially regulated in tumor cells in an inflammatory environment

One major aspect, proven in chapter 4.1.1, unveiled that glioblastoma cells tended to escape classical treatment regimen by their entrance into a cell-cyle arrest. This arrest state was characterized by the upregulation of dormancy markers, suggesting that classical therapy with TMZ induced celluar dormancy in GBM cells. In principle, cellular dormancy is designated to be a reversible growth arrest [Yeh and Ramaswamy, 2015] (reviewed in Aguirre-Ghiso [2007]) implying that upon some trigger the cell starts to re-initiate proliferation. This was similarly shown in stem cells, that maintained a quiescent state and started differentiation in line with proliferation upon external stimuli [Scognamiglio et al., 2016]. So far, some individual mechanisms of dormancy entrance have been uncovered in different cancers [Hofstetter et al., 2012, Vera-Ramirez et al., 2018]. Despite some identified factors, pertinent to exit angiogenic dormancy [Almog et al., 2009], escape from cellular dormancy remains unclear. Thus, the established model for cellular dormancy (chapter 4.1.1) was extended, in order to observe re-initiation of cell division. For this purpose, LN229 cells, that have been stimulated with TMZ for ten days to enter cellular dormancy, were left untreated for further 15 days allowing for recovery upon chemotherapeutic treatment. Indeed, dormant GBM cells continued to die within the first week but started to proliferate again after 15 days when not targeted with TMZ (upper panel of fig. 4.2A) indicating for the reversibility of cellular dormancy.

Certainly, glioblastoma cells stay in close contact with their environment, that on cellular basis mainly consists of immune cells such as astrocytes and microglia, that facilitate tumor progression and maintenance (described in chapter 1.1.4.3). Beside immunogenic dormancy, that is explained by an equilibrium state between immune surveillance of immune cells and tumor cell-immune escape (see chapter 1.1.4.2), immune cell communication and response might also play a critical role in the chemotherapeutic-induced entrance and exit mechanisms of cellular dormancy. In fact, chemokines as inflammatory mediators were shown to affect metastatic breast-

cancer dormancy [Khazali et al., 2018, Nobutani et al., 2015, Clark et al., 2016] and distinct chemokines, in particular CXCL12, CXCL16 and CX3CL1, expressed either by glioblastoma cells themselves or astrocytes and microglia, are essential for tumor preservation by autocrine or paracrine signaling [Wang et al., 2012, Ludwig et al., 2005, Ludwig and Mentlein, 2008, Hattermann et al., 2014].

Based on the hypothesis that those chemokines have important functions in cellular dormancy, GBM cells were stimulated with TMZ alongside with a chemokine mix containing CXCL12, CXCL16 and CX3CL1 for ten days. After this period, TMZ treatment was stopped while stimulation with the above-mentioned chemokines was continued for additional 15 days. Interestingly, GBM cells showed in tendency a reduced sensitivity upon TMZ treatment when co-stimulated with chemokines. They did not initiate proliferation after 15 days without TMZ, though (fig. 4.2A). In order to verify and quantify the amount of cells, that entered cellular dormancy, after three days of TMZ administration, LN229 cells were stained with DiI. Indeed, less glioma cells retained the dye after ten days of treatment, but also less cells lost the dye during recovery when co-treated with chemokines (fig. 4.2B) indicating that less chemokine-stimulated cells enter and exit cellular dormancy. This was confirmed by a reduced increase of the p38/ERK signaling ratio upon treatment for ten days as well as a detectable shift of the p38/ERK signaling in chemokine-treated GBM cells, that recovered 15 days, which was not found in unstimulated, recovered cells (fig. 4.2C) [Aguirre-Ghiso et al., 2004].

Signaling of the chemokines CXCL12, CXCL16 and CX3CL1 is maintained either by their respective receptors, which are CXCR4 and CXCR7 in case of CXCL12 (reviewed by Hughes and Nibbs [2018]), or their transmembrane ligands themselves, known as inverse signaling, shown for CXCL16 and CX3CL1 [Hattermann et al., 2016b]. The receptors of CXCL16 (CXCR6) and CX3CL1 (CX3CR1) lack on GBM cells [Held-Feindt et al., 2010, Hattermann et al., 2013, Adamski et al., 2017b]. In fact, GBM cells did not only express the receptors and ligands, respectively, that are necessary for signaling in general, but those were also significantly upregulated upon TMZ stimulation (fig. 4.2D), thereby facilitating a possible signaling during treatment.

In summary, removal of TMZ yielded a start of proliferation in GBM cells after approximately ten to 15 days, whereas co-administration of chemokines CXCL12, CXCL16 and CX3CL1, that induce signaling via their upregulated receptors or ligands, resulted in both a delayed entry and delayed exit from therapeutical-induced cellular dormancy.

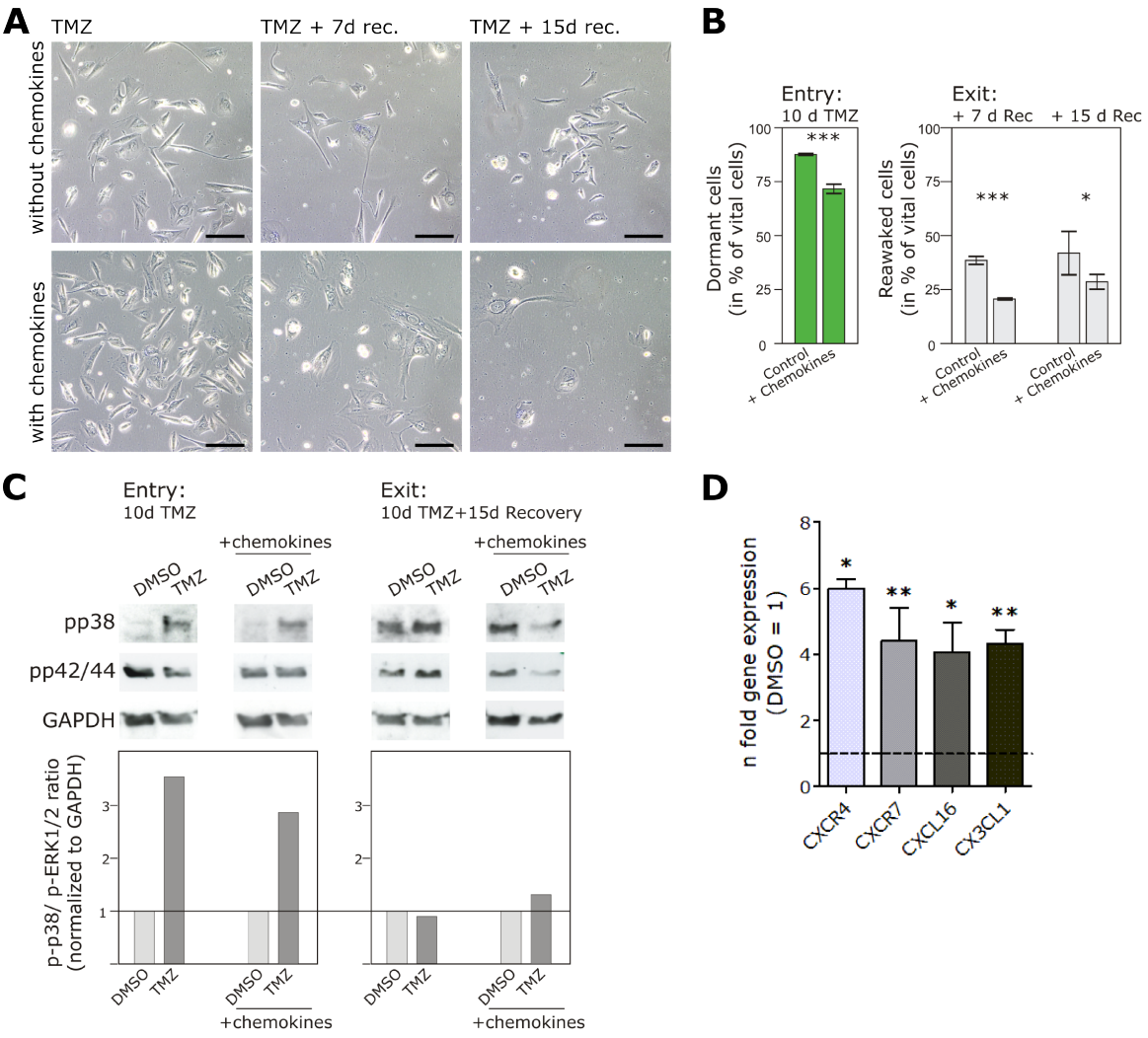

Figure 4.2: Inflammatory stimuli regulate entry into and exit from dormancy upon chemotherapeutic treatment in LN229 cells. To understand regulation of dormancy entry and exit mechanisms considering an inflammatory surrounding, LN229 cells were stimulated with 500 μM TMZ or DMSO, respectively, ± chemokine mix containing 2 nM CXCL12, CXCL16 and CX3CL1 for ten days, then, cells were left without chemotherapeutic but ± chemokine mix for further 15 days. Phase-contrast pictures were acquired after ten days of TMZ stimulation as well as after further seven and 15 days of recovery at the very same position. The black bar indicates 200 nm (**A**). To confirm these results by numbers, LN229 cells, stimulated with TMZ ± chemokine mix for three days, were stained with DiI. After ten days of chemotherapeutic treatment as well as after seven and 15 days without this stimulus, the amount of dye retaining cells compared to the whole cell amount was calculated (n=18, **B**). In addition, signaling via the p42/44 and p38 MAPK pathways was analyzed by Western Blot after ten days of TMZ ± chemokine mix and after further 15 days of recovery (n=4, **C**). Furthermore, the regulation of the gene expression of the respective chemokine receptors and ligands was investigated by qRT-PCR upon TMZ treatment for ten days (n=3, **D**). Statistical analysis concerning cell amount differences in dormancy entry was performed by unpaired student's t-test, whereas those in dormancy exit were analyzed by repeated two-way ANOVA with Bonferroni post test. Gene regulation upon TMZ stimulation was statistically interpreted by paired student's t-test (data shown in B, C and D were obtained with technical assistance and provided by Professor Dr. Dr. Janka Held-Feindt).

Since dormancy is one major process contributing to tumor malignancy, it is of high interest to identify those genes, that affect and are affected by dormancy. In line with other studies, that aimed at a comprehensive knowledge about dormancy entrance and

exit mechanisms [Tong et al., 2018, Magnus et al., 2014], a mRNA-microarray analysis of LN229 cells, that have been stimulated with a subletal dose of TMZ ± chemokine mix and afterwards recovered from treatment as previously described, was performed. The obtained information regarding selectively regulated genes in dormancy entrance and escape, that are additionally selectively modulated by chemokine stimulation, were provided by Professor Dr. Dr. Janka Held-Feindt for this project. In order to confirm a selective regulation of individual genes, LN229 cells were stimulated with TMZ ± CXCL12, CXCL16 and CX3CL1 for ten days followed by a recovery period of 15 days without chemotherapeutic treatment. Ultimately, the gene expression and protein synthesis of particular genes were analyzed after ten days of classical treatment (dormancy) as well as after further 15 days of recovery (reawakening) revealing that chemokine ligand CCL2 and serum amyloid A2 (SAA2) were upregulated upon classical therapy with TMZ for ten days, and follistatin-like 3 (FSTL3), vascular endothelial growth factor (VEGF) C as well as thrombospondin type-1 domain containing 4 (THSD4) after additional 15 days without TMZ stimulation (fig. 4.3). Moreover, this upregulation was decreased for all genes when cells were additionally stimulated with CXCL12, CXCL16 and CX3CL1.

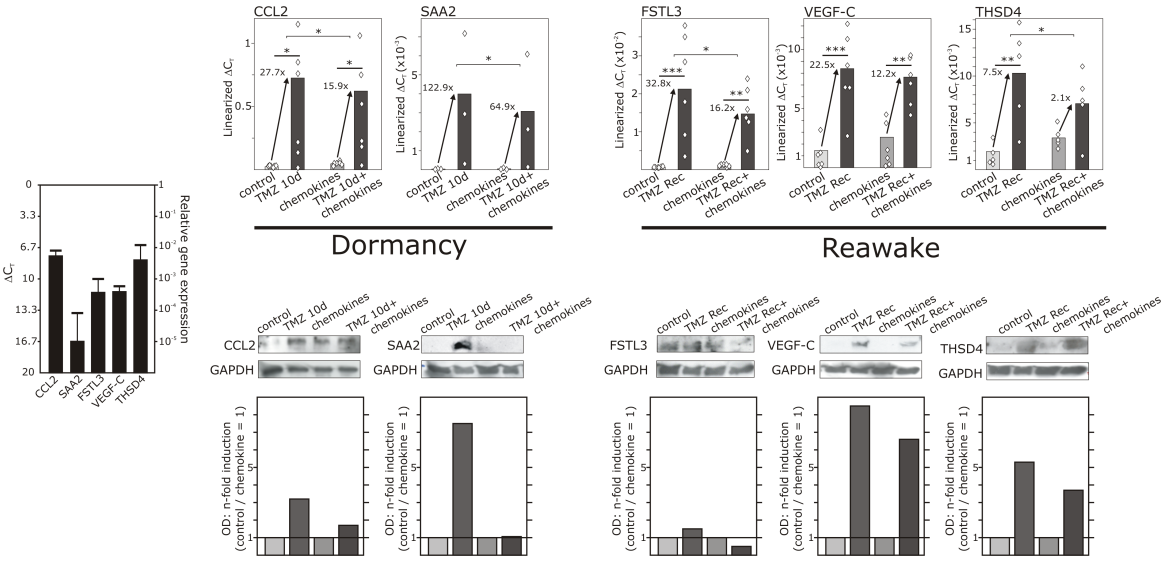

Figure 4.3: Regulation of dormancy entry and exit by inflammatory conditions is mimicked by the differential expression of certain genes. To verify the effect of inflammation on identified dormancy- and reawakening-related genes, at first, the basic gene expression levels were detected in LN229 by qRT-PCR (n=3). Additionally, tumor cells were treated with 500 μM TMZ or DMSO, respectively, ± chemokine mix including 2 nM CXCL12, CXCL16 and CX3CL1 for ten days followed by 15 days without chemotherapeutic but ± chemokine stimulation. Regulation of identified dormancy- and reawakening-associated genes was determined after ten and 25 days of stimulation by qRT-PCR and Western Blot (n=6, OD=optical density). Statistical analysis of gene regulation upon TMZ treatment was performed by repeated two-way ANOVA with Bonferroni post test, while comparison of effects with and without chemokines were analyzed by paired student's t test (data were obtained with technical assistance and provided by Professor Dr. Dr. Janka Held-Feindt).

Assuming that regulation of CCL2 and SAA2 plays an important function in dormancy entry and FSTL3, THSD4, VEGFC represent essential factors in the reawakening of tumor cells, the reduced increase of gene expression and protein synthesis upon chemokine administration contributed to the hypothesis, that dormancy entry as well as exit is delayed by CXCL12, CXCL16 and CX3CL1 signaling in glioblastoma cells.

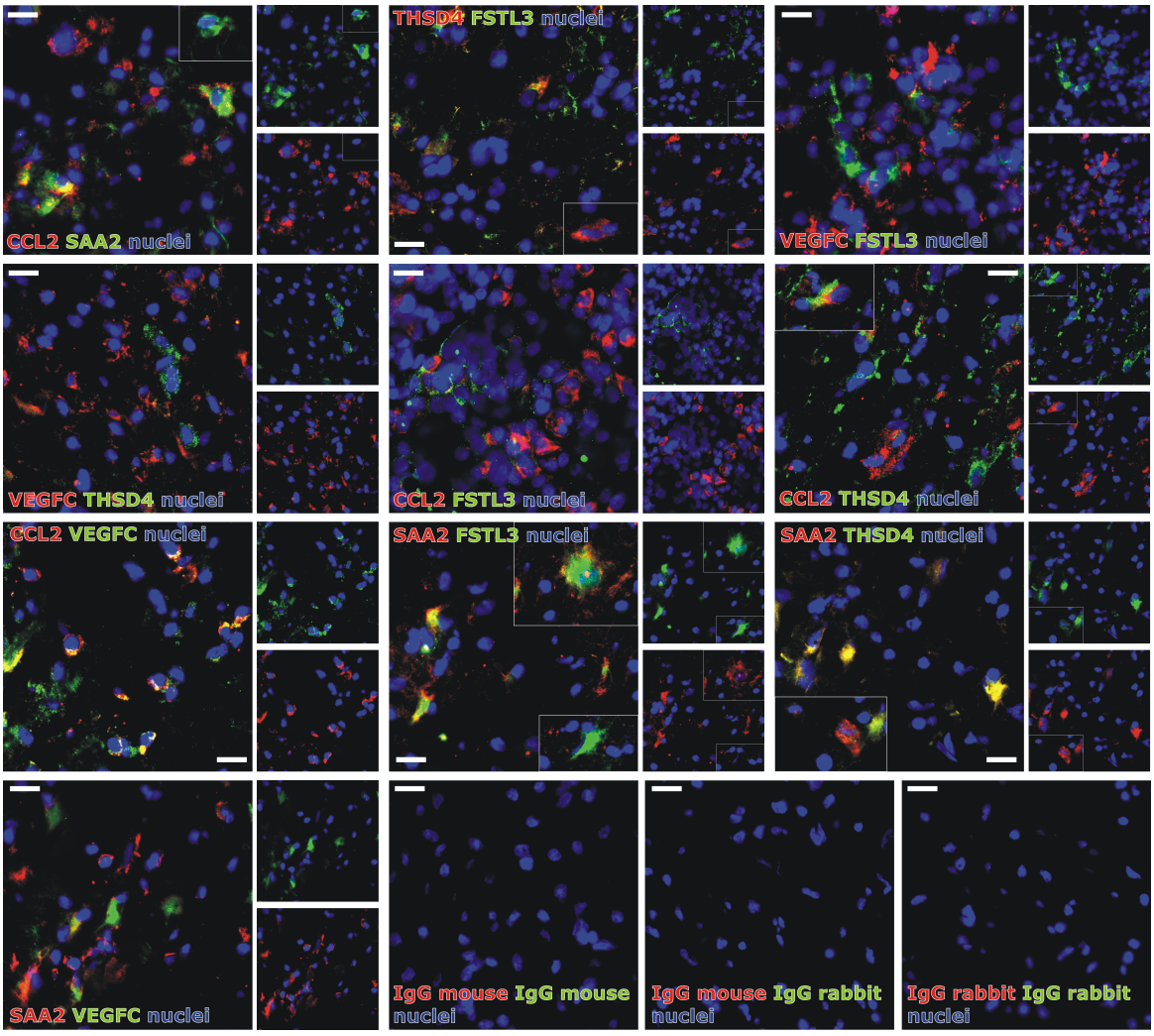

Figure 4.4: Dormancy- and reawakening-associated genes are expressed in solid GBM tumor samples. In order to strengthen the attributed roles of dormancy- and reawakening-relevant markers *ex vivo*, solid tumor sections of GBMs were stained by immunohistochemistry regarding the presence and co-staining of CCL2, SAA2, FSTL3, THSD4 and VEGFC proteins (green and red). Nuclei are depicted in blue. White bars indicate 20 μm.

In order to verify the appearance and distribution of the identified genes, that are pertinent to dormancy entry and exit, in tumor tissue, solid human glioblastoma sections of primary and recurrent tumors were fluorescently stained *ex vivo* by immunohistochemistry concerning the respective proteins. In fact, all proteins were abundantly found in both primary and relapsed glioblastomas. Interestingly, CCL2 and SAA2 as well as THSD4 and FSTL3 showed partial co-staining with each other, whereas

VEGFC revealed a unique staining without co-occurence of THSD4 or FSTL3. Furthermore, CCL2-positive cells showed a pronounced co-staining with VEGFC, in parts also for THSD4 but no co-staining with FSTL3. In contrast, SAA2 was almost exclusively co-stained with FSTL3 and THSD4 but only partially with VEGFC (fig. 4.4). Summarizing, the expression of identified dormancy-related and reawakening-associated markers was not restricted to dormant or respective recovered tumor cells and not particularly related to primary or recurrent tumors.

4.1.3 Identified dormancy- and reawakening-marker expression is distinctively modulated by single chemokines

The previous results revealed that upon an experimental induction of a pro-inflammatory tumor environment during chemotherapeutic treatment, mimicked by the simultaneous co-stimulation with the inflammatory chemokines CXCL12, CXCL16 and CX3CL1, LN229 cells showed a delayed entry into chemotherapeutically induced cellular dormancy as well as a delayed exit from dormancy. In connection to this, individual genes were identified, that were upregulated in dormancy entry and escape but less upregulated upon administration of the chemokine mix indicating for their relevance in dormancy mechanisms and supporting the hypothesis that inflammatory conditions modulate dormancy processes.

After it was proven, that the mixture of CXCL12, CXCL16 and CX3CL1 affected not only dormancy entry but also reawakening of glioma cells, in the following, it had to be clarified whether a single chemokine individually impacts on special dormancy or reawakening mechanisms. For this purpose, the influence of single chemokine treatment, co-administered to TMZ during dormancy and reawakening periods, was analyzed in glioma cells with respect to the denoted gene expression regulations, that played roles in dormancy entry and escape. To confirm the particular impact of individual chemokines upon dormancy/reawakening modifications, signaling was abolished either by CRISPR/Cas9 deletion [Jinek et al., 2012] of the receptor CXCR7 and the transmembrane ligands CXCL16 and CX3CL1 in GBM cells (success of transfection on mRNA and protein level is visualized in fig. 4.5A, B) or by co-stimulation with AMD3100, a specific inhibitor for CXCR4 signaling [Schols et al., 1997]. Interestingly, stimulation of untransfected LN229 cells with TMZ plus single chemokine application revealed no significant reduced regulation of *CCL2* or *SAA2* compared to TMZ application without chemokines (white bars, fig. 4.5C, D, E). Nonetheless, a significant decreased upregulation of *CCL2* and *SAA2* became visible when stimulating CXCR7-negative cells with CXCL12 indicating a relevance of CXCL12-CXCR4 signaling on the regulation of dormancy-associated gene expression (dark grey bars, fig. 4.5C). Further, the effects diminished in AMD3100 co-stimulated CRISPR/Cas9-CXCR7 cells (dark grey bars with stripes, fig. 4.5C). Since AMD3100 inhibits CXCR4

signaling, solely CXCL12-CXCR4 signaling seemed to be improtant for the regulation of *CCL2* and *SAA2*. In contrast, CXCL12 stimulation had no impact on the regulation of reawakening-related gene expression, neither via CXCL12-CXCR4 nor CXCL12-CXCR7 signaling, because untransfected cells, that were stimulated with AMD3100 concomitant to TMZ, showed no modulation of the analyzed gene expression (light grey bars with stripes, 4.5C). Thus, signaling via CXCR7 did not influence dormancy entry and exit at all (fig. 4.5C). Nevertheless, while CXCL16 and CX3CL1 showed no impact on the modification of dormancy entry, both affected the alteration of reawakening-associated gene expression. Both chemokines significantly reduced the upregulation of *THSD4* in control cells (white and light grey bars, fig. 4.5D, E). In conformity, no significant regulation was observed upon CXCL16 or CX3CL1 stimulation in cells with CXCL16- and CX3CL1-knock down (dark grey bars, fig. 4.5D, E). However, the modifications of *FSTL3* and *VEGFC* expression were ambiguous. Individual stimulation with both chemokines CXCL16 and CX3CL1 decreased the upregulation of *VEGFC* in untransfected, recovered LN229 cells (white bars, fig. 4.5D, E), whereas this effect became only slightly visible in CRISPR/Cas9-control transfected glioma cells, which was particularly more pronounced in case of CX3CL1 co-treatment (light grey bars, fig. 4.5D, E). Knock-down of CXCL16 or CX3CL1 led to no significant regulation of *VEGFC* expression compared to TMZ-treated cells (dark grey bars, fig. 4.5D, E). Interestingly, *FSTL3* expression was neither considerably modulated by singular CXCL16 nor CX3CL1 administration in control cells (white and light grey bars, fig. 4.5D, E). Also individual CXCL12 stimulation did not result in significant regulation of *FSTL3* via CXCR4 or CXCR7 or both (fig. 4.5C). Summarizing, the expression of the analyzed markers, that were associated to dormancy entry, was altered by CXCL12 but not CXCL16 or CX3CL1. Moreover, the regulation by CXCL12 was related to CXCR4 but not CXCR7 signaling. Thus, particular CXCL12-CXCR4 signaling might play an important role in the delay of dormancy entry, mimicked in the modulation of *CCL2* and *SAA2* expression. In addition, CXCR7 might overlay this effect, since cells, that had both receptors, did not show an alteration in the regulation of both analyzed genes. This proposed a relevant role of dormancy mechanisms concerning glioma stem cells, as those are characterized by an augmented CXCR4 expression [Ma et al., 2008, Ehtesham et al., 2009, Flüh et al., 2016]. Furthermore, CXCL12 was not attributed to the delay of reawakening of tumor cells, resembled by an altered modification of *VEGFC*, *FSTL3* and *THSD4* expression. In contrast, CXCL16 and CX3CL1 similarly contributed to the reduced upregulation of *THSD4*, while the modulation of FSTL3 seemed to rely on the co-stimulation of at least CXCL16 and CX3CL1 or all three chemokines, because individual chemokine stimulation did not result in a significant, different regulation of *FSTL3* expression. The modification of *VEGFC* expression was equally affected by

CXCL16 and CX3CL1 administration in untransfected cells but not in CRISPR/Cas9-control cells, suggesting an impact of transfection. Nevertheless, inverse signaling of CXCL16 and CX3CL1 might be important in the delay of reawakening of GBM cells.

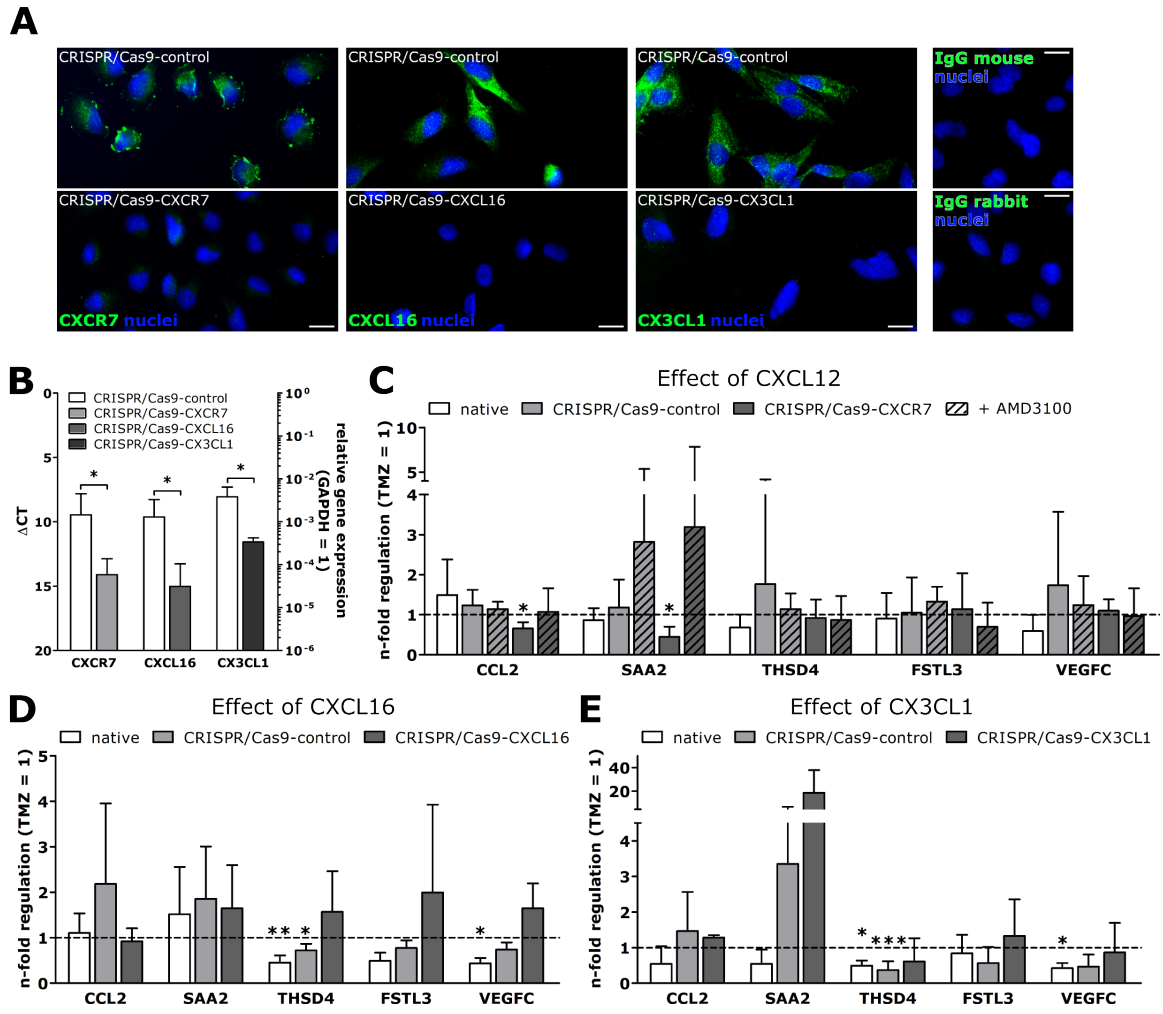

Figure 4.5: Particular gene regulation of dormancy- and reawakening-associated genes upon individual chemokine stimulation. For clear assignment of the identified gene regulation of dormancy and reawakening markers to stimulation of single chemokines, *CXCR7*, *CXCL16* and *CX3CL1* expression was modified by CRISPR/Cas9 knock-out of the respective genes in LN229 cells. To confirm the successful transfection, CRISPR/Cas9-transfected LN229 cells were stained by immunocytochemistry (n=2, **A**) as well as analyzed by qRT-PCR (n=3-7, **B**) regarding the expression of CXCR7, CXCL16 and CX3CL1. To identify specific gene regulation by single chemokine administration, native LN229 as well as LN229-CRISPR/Cas9-control and the corresponding CRISPR/Cas9-chemokine clones were stimulated with 500 μM TMZ ± 2 nM CXCL12 or CXCL16 or CX3CL1 for ten days with respect to the receptor or ligand, responsible for signaling. Additionally, LN229-CRISPR/Cas9-control and CRISPR/Cas9-CXCR7 cells were treated with 10 μM AMD3100 to inhibit CXCR4 signaling. Afterwards, pretreated cells were left without therapy with TMZ, but were further stimulated with 2 nM of the respective chemokine for 15 days. Ultimately, gene expression of *CCL2*, *SAA2*, *THSD4*, *FSTL3* and *VEGFC* was analyzed by qRT-PCR after ten or 25 days, respectively. The data are depicted as n-fold gene regulation by additional chemokine stimulation compared to single TMZ treatment (n=4-5, **C-E**). Statistical analysis of CRISPR/Cas9 transfection was performed by unpaired student's t test. Furthermore, differences according to distinct chemokine stimulation of native LN229 cells were analyzed by repeated one-way ANOVA with Dunnett post test, whereas regulations in CRISPR/Cas9-transfected cells concerning additional chemokine administration and superordinate comparisons between different clones were tested by paired student's t test.

4.2 Comparative analysis of alternative therapeutics and treatment schemes for GBM therapy

Concluding from the previous results, that glioblastoma cells tended to escape classical chemotherapy with temozolomide into cellular dormancy, having the ability to reawake and induce tumor growth, it is important to develop alternative treatments. Apparently, the introduction of other therapeutic compounds, that address cells in a different manner compared to TMZ or enhance TMZ sensitivity and multi-drug administrations, are attractive possibilities to avoid chemoresistance [Torres et al., 2011, Yu et al., 2015, Marinelli et al., 2018, Shao et al., 2019, Herrlinger et al., 2019]. In order to identify promising alternative compounds for GBM therapy and perform a comprehensive study on multi-drug application schemes, on the one hand, quinacrine (QXN), chloroquine (CQ) and its derivate hydroxychloroquine (HCQ) as autophagy inhibitors [Golden et al., 2015], showing beneficial cytotoxic effects in glioma studies [Rosenfeld et al., 2014, Sotelo et al., 2006], were chosen, since chemoresistance is partly attained by the induction of autophagy through TMZ [Lin et al., 2012]. On the other hand, due to its pro-apoptotic function by binding B-cell lymphoma (Bcl-)2 proteins [Kitada et al., 2003], the natural polyphenol AT101 has already been used in GBM therapy approaches [Bushunow et al., 1999, Jarzabek et al., 2014], revealing a higher cytotoxicity on tumor cells compared to gossypol, its racemic form [Varol et al., 2009, Blackstaffe et al., 1997].

In order to find suitable concentrations for long-term stimulation experiments, two different GBM cell lines with distinct molecular profiles (see supplementary fig. A.1) were stimulated with different amounts of the classical drug TMZ and the alternatives AT101, QXN, CQ and HCQ. The cytotoxic effect of each drug was determined by calculating the percentage of dead cells and the n-fold alive cells compared to control-stimulated cells after three days of treatment (fig. 4.6). Interestingly relatively high concentrations of TMZ were needed to achieve clear cytotoxic effects ($IC50_{A172}$=314 μM, $IC50_{LN229}$=137 μM), whereas AT101 and QXN were highly cytotoxic even at very low concentrations in both cell lines (AT101: $IC50_{A172}$=1.6 μM, $IC50_{LN229}$=3.2 μM and QXN: $IC50_{A172}$=1.4 μM, $IC50_{LN229}$=1.5 μM, fig. 4.6). CQ and HCQ revealed moderate effects on cytotoxicity, but heavily reduced the amount of alive cells with stronger effects of HCQ compared to CQ in LN229 cells (CQ: $IC50_{A172}$=13.9 μM, $IC50_{LN229}$=14.3 μM and HCQ: $IC50_{A172}$=16.5 μM, $IC50_{LN229}$=9.5 μM, fig. 4.6B). Although QXN and AT101 seemed to be the most promising candidates for alternative GBM therapy, comparative experiments with normal astrocytes (performed by Christina Schmitt, Institute of Anatomy) revealed that astrocytes were even more affected by QXN and CQ. Hence, beside the classical therapeutic TMZ, AT101 and HCQ were chosen for further studies and concentra-

tions were adjusted according to IC50 values and to liquor/plasma concentrations in treated patients [Ostermann et al., 2004, Zerp et al., 2015, Rosenfeld et al., 2014].

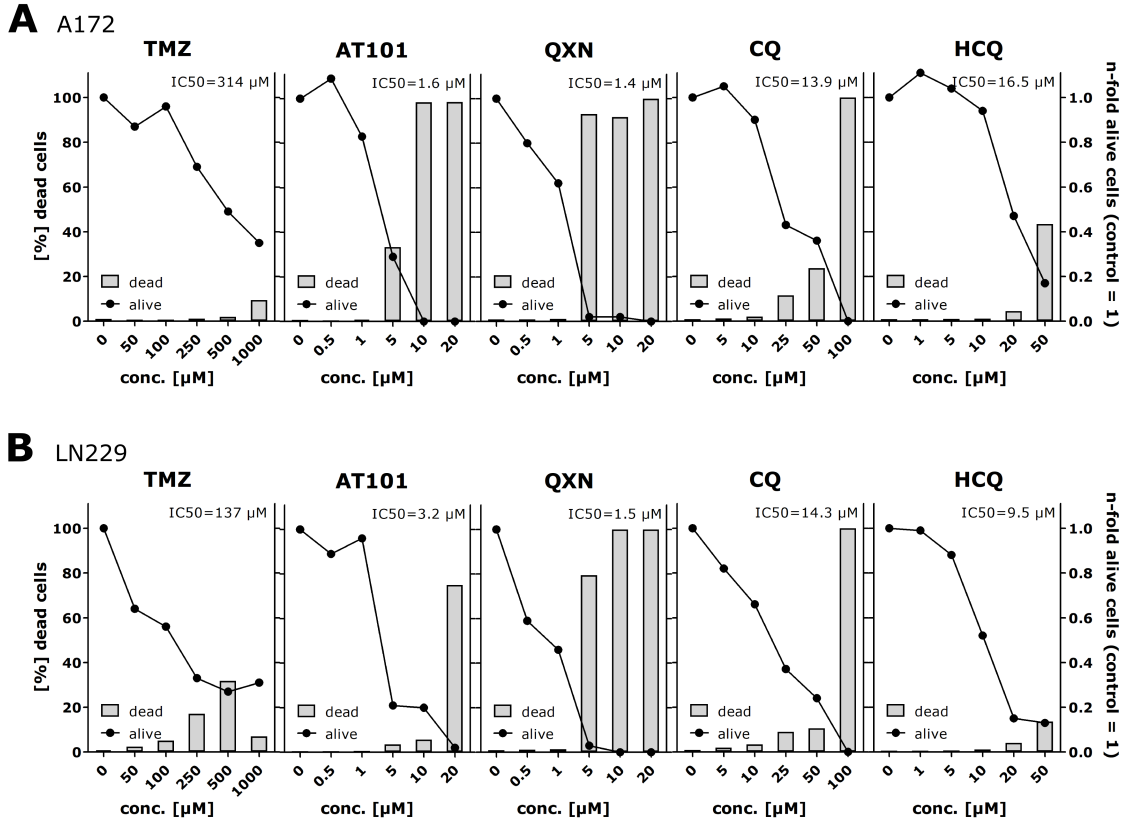

Figure 4.6: Cytotoxic effects of different concentrations of classical and alternative drugs on GBM cell lines. In order to establish suitable concentrations for further experiments regarding alternative treatments for glioblastomas, two distinct GBM cell lines, A172 (**A**) and LN229 (**B**), were stimulated with increasing concentrations of the classical therapeutic TMZ as well as alternative compounds such as AT101, QXN, CQ and HCQ for three days. The cytotoxic effect was determined by measurement of dead cells by CytoTox-Fluor^{TM} Cytotoxicity Assay and counting of alive cells. The data are displayed as percentage of dead cells compared to the whole cell number (bars) and n-fold viability compared to the control stimulation (dots and lines, n=1).

For the analysis of suitable drug-drug combinations and therapy schemes including the administration of alternative therapeutics (AT101, HCQ) additive to TMZ, a long-term stimulation model was applied, in which all stimulated cells including the control were cultivated for one week without detachment and re-seeding, thereby avoiding false positive cytotoxic results related to cell splitting. However, medium was exchanged after three days to allow for the constant availability of nutrients and re-application of therapeutics. Within this long-term stimulation, different drug-administration possibilities were employed including not only stimulations with each compound individually or in simultaneous combination with each other, but also sequential application of different drugs and drug combinations (all tested versions in time-dependent schemes are depicted in fig. 4.7A, B and C).

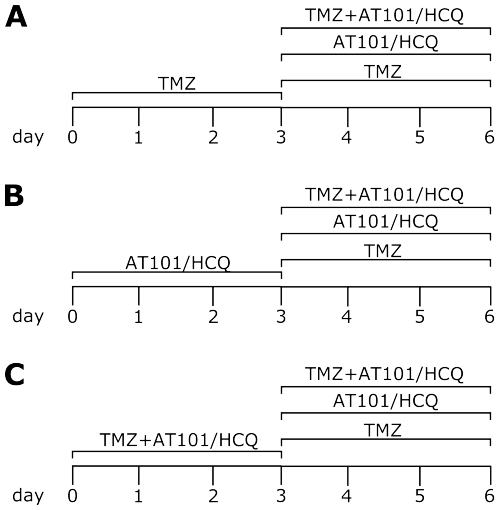

D

stimulus I	stimulus II	n-fold amount of dead cells (TMZ = 1) SVGA	A172	LN229	growth rate SVGA	A172	LN229
TMZ	TMZ	1.00	1.00	1.00	2.35	1.41	2.01
	HCQ	0.71	1.62	1.20	3.32	0.92	1.35
	TMZ+HCQ	1.16	1.39	1.83	1.79	1.17	1.25
HCQ	TMZ	0.54	0.23	0.31	2.65	3.25	2.40
	HCQ	0.29	0.21	0.20	3.20	5.57	2.88
	TMZ+HCQ	0.50	0.43	0.50	2.08	3.56	2.07
TMZ+HCQ	TMZ	1.62	1.26	2.11	1.60	1.01	0.90
	HCQ	1.68	2.30	1.86	1.20	0.84	0.89
	TMZ+HCQ	2.07	2.44	2.14	1.14	0.82	0.77
TMZ	TMZ	1.00	1.00	1.00	2.35	1.41	2.01
	AT101	0.84	1.64	1.67	4.14	1.57	1.84
	TMZ+AT101	0.67	2.59	1.70	3.92	1.10	1.93
AT101	TMZ	0.37	0.30	0.18	2.42	2.30	2.79
	AT101	0.38	0.25	0.42	4.04	3.71	2.19
	TMZ+AT101	0.50	0.67	0.60	2.89	1.98	1.93
TMZ+AT101	TMZ	0.84	1.38	1.41	3.57	1.51	1.80
	AT101	0.72	3.08	2.78	2.98	1.28	1.22
	TMZ+AT101	0.81	3.24	2.85	2.18	1.19	1.08

Figure 4.7: Cytotoxic effects of various treatment schemes with classical and alternative drugs on GBM cells and astrocytes. After determining suitable alternative drugs and concentrations for glioblastoma treatment, two different glioma cell lines, A172 and LN229, were stimulated according to various treatment schemes with 50 μM TMZ and 2.5 μM AT101 or 6 μM HCQ, respectively, for six days. Treatment regimen included either an initial stimulation with TMZ for three days followed by a further therapy with TMZ, an alternative drug or a combination of classical and alternative drug for additional three days (**A**), a first stimulation with an alternative compound and the subsequent treatment with the alternative, the classical or the combination of both drugs (**B**) or starting with a combined treatment with TMZ plus AT101 or HCQ, progressing with this combination or single drug administration (**C**). The cytotoxicity including n-fold percentage of dead cells and the growth rate was studied after three and six days of stimulation. For comparison, beside GBM cell stimulation, normal astrocytes (SVGA) were treated likewise by Christina Schmitt (Institute of Anatomy). Summarized results are depicted in a heatmap (**D**), in which the standard therapy (TMZ for six days) is colored yellow. Accordingly, a higher amount of dead cells as well as lower proliferation rates compared to standard treatment (augmented cytotoxic effect of the drug) are depicted in green colors in case of glioma cells and *vice-versa* conditions in deeper shades of red. As opposed to this, a lower amount of dead cells and higher growth rates of astrocytes (less harmful for SVGA) are colored in green and the opposite in red (n=3-4, adapted from Adamski et al. [2018], attached in the appendix).

To discover the best therapeutic scheme, that could also operate *in vivo*, not only two GBM cell lines, A172 and LN229, but also a normal astrocytic cell line, SVGA, (performed by Christina Schmitt, Institute of Anatomy) were treated with the evaluated strategies. Furthermore, both the amount of dead and of alive cells were measured after three and after six days of treatment in order to determine the toxic effect with respect to relative numbers of dead cells and growth rates of cells as the balance of dying and dividing cells is important when estimating drug cytotoxicity. Since the improvement of the classical GBM chemotherapy with TMZ was focussed, all results were compared to the effect of single TMZ treatment for the whole stimulation period. In detail, less harmful effects of the treatment regimen on SVGA (astrocytes) compared to TMZ administration, displayed as enhanced growth rates and lower amounts of dead cells, are colored green. Accordingly, an increased cytotoxicity of the therapy scheme on glioma cells, depicted as decreased growth rates and a higher amount of dead cells, are also visualized in green. In fact, the individual application of alterna-

tive drugs showed enhanced growth rates and less toxicity on SVGA (green colors) compared to TMZ treatment, but did not yield increased cytotoxicity in GBM cells (red colors, fig. 4.7D). In contrast, especially simultaneous multi-drug administration of TMZ and HCQ severely affected glioma cells (green), but also SVGA (red). Interestingly, simultaneous co-stimulation with TMZ and AT101 yielded promising effects for GBM cells as well as astrocytes (green colors). Moreover, sequential therapy, in which TMZ was only applied during the first three days but AT101 the whole six days, was less harmful for astrocytes compared to simultaneous treatment, while the increased cytotoxicity in glioma cell lines was maintained (fig. 4.7D). Equally, sequential application of TMZ for three days, then HCQ for further three days, represented the most promising stimulation scheme concerning TMZ and HCQ administration. In conclusion, multi-drug administration was favorable in comparison with single drug treatment. However, especially sequential treatment schemes were more protective for normal brain cells but remained cytotoxic for tumor cells, thereby representing the most beneficial way of therapy (these results were published in Adamski et al. [2018], which is attached in the appendix).
Besides, in order to estimate influence of inflammation on investigated therapy schemes, GBM cells were co-stimulated with CXCL12 as an inflammatory mediator during the whole stimulation period. Indeed, no remarkable differences were measured upon CXCL12 co-administration regarding cytotoxic effects of therapeutics and therapeutic combinations in A172 and LN229 cells (supplementary fig. A.2).

4.2.1 Co-culturing of GBM and normal brain cells resulted in different cytotoxic effects of a selected, sequential stimulation scheme compared to mono-culturing

Although CXCL12 administration, resembling an inflammatory environment common in GBMs [Stevens et al., 1988], did not show any effect on the investigated stimulation strategies, it is highly relevant to consider the tumor microenvironment into GBM therapy. Hereby, beside endothelial cells of tumor vessels in particular astrocytes and microglia play important roles as those cells are most abundant in GBM microenvironment [Calabrese et al., 2007, Roggendorf et al., 1996, Zeiner et al., 2018, Morantz et al., 1979, Rossi et al., 1967]. On one side, considering targets for treatment beside tumor cells also normal brain cells are affected by therapeutic compounds. On the other side, especially astrocytes and microglia impact chemoresistance and therapy outcome [Yang et al., 2014, Komohara et al., 2008, Bettinger et al., 2002]. Especially after a subtotal resection of the tumor, depending on tumor location, age of patient and medical performance [Kreth et al., 1994, Byun et al., 2019], the influence of cells different from tumor cells becomes critical. Therefore, an incomplete-resection co-culture model was established (described in 3.2.1.5.2) including a defined ratio of

70% primary tumor cells (116/14, 118/14), 29% microglia (HMC3) and 1% astrocytes (SVGA).

To determine differences in the treatment efficiency on mono- and co-culture, those cells were co-cultured with indirect contact to each other across membranes with pores and mono-cultured with respect to same cell densities in culture dishes in line with the co-culture. As shown before (chapter 4.2), sequential treatment approaches were prefered over single or combined applications of classical (TMZ) and alternative drugs (AT101, HCQ). Hence, the efficiency of the particular, promising sequential administration of TMZ for the first three days and AT101 for the whole stimulation period (TMZ+AT101/AT101) was analyzed in co- and mono-cultures.

Indeed, GBM primary cultures with different molecular profiles (see supplementary fig. A.1), 116/14 and 118/14, were heavily affected even though to different extents by the treatment regardless of culture conditions shown by increased amounts of dead cells (fig. 4.8A, C) and also stagnating (118/14) or even decreasing (116/14) growth rates (fig. 4.8B, D). Interestingly, the efficiency of stimulation was slightly reduced in GBM primary cultures after six days with respect to percentage of dead cells, when co-cultured with astrocytes and microglia (fig. 4.8A, C) suggesting a protective role of normal brain cells in tumor therapy. Furthermore, in particular the growth of primary culture 116/14 was significantly augmented under mono- compared to co-culture conditions (fig. 4.8B). Concerning normal brain cells, microglia revealed no notable differences in cytotoxicity with respect to the sequential treatment scheme for mono- and co-culture situations concerning both primary cultures (fig. 4.8). However, microglia grew faster if co-cultured with 118/14, which was independent of stimulus (fig. 4.8D). In contrast to this, astrocytes were significantly affected by the treatment to a lower extent compared to tumor cells, though. Nevertheless, this effect was elevated under co-culture conditions, especially with 118/14 cells regarding amounts of dead cells (fig. 4.8A, C). Surprisingly, although control-stimulated astrocytes proliferated better if co-cultured (fig. 4.8B), numbers of dead cells were also increased without the sequential application of TMZ and AT101 in a co-culture situation (fig. 4.8A, C).

In conclusion, astrocytes and microglia seemed to tendencially protect GBM cells from therapy mimicked in slightly reduced percentages of dead cells in primary cultures. As opposed to this, the presence of glioma cells not only increased cell death in astrocytes resembled by a higher degree of dead cells in the DMSO-stimulated co-culture compared to the respective mono-culture, but also severely affected the sensitivity of astrocytes to treatment. Microglia were not harmed differently in a co-culture situations.

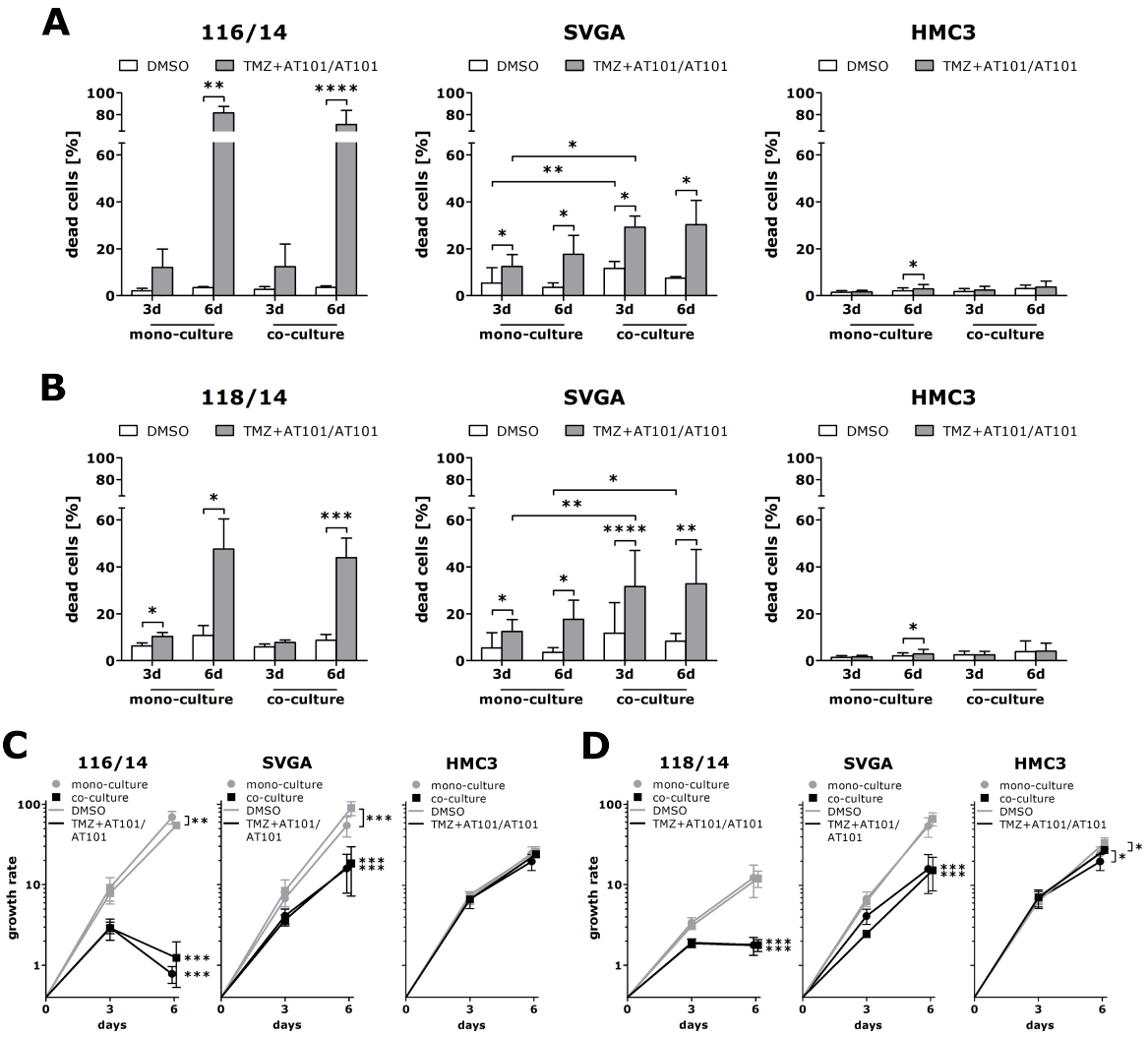

Figure 4.8: Cytotoxic effects of sequential application of TMZ and AT101 in an incomplete-resection co-culture model. Two distinct GBM primary cultures, 116/14 (**A**, **C**) and 118/14 (**B**, **D**), were stimulated according to a previously evaluated, promising sequential application scheme with 50 μM TMZ for the first three days and 2.5 μM AT101 during the whole stimulation period of six days (see chapter 4.2) or DMSO, respectively. Simultaneously, normal astrocytes (SVGA) and microglia (HMC3) were co-cultivated with each primary culture as described in chapter 3.2.1.5.2 and therefore, were also treated regarding this sequential strategy. For comparison, mono-cultures of tumor and normal brain cells were stimulated, respectively. After three and six days of treatment, the amount of dead and alive cells were measured (n=3). The data are depicted as percentage of dead cells (**A**, **B**) and growth rates of cells (**C**, **D**) for mono- (dots) and co-cultures (squares). To compare percentage of dead cells in mono-cultures concerning the treatment, statistical analysis was performed by paired student's t test for each day, while treatment significance in co-cultures was analyzed by repeated two-way ANOVA with Bonferroni post-test for each day. Furthermore, mono-*versus* co-culture effects were compared by repeated two-way ANOVA with Bonferroni post-test for each day. Growth rates for every cell type were statistically analyzed by a repeated two-way ANOVA with Bonferroni post-test.

4.3 Conquer blood-brain barrier restrictions

Beside the introduction of alternative therapeutics for GBM therapy, one major challenge of therapeutic compounds is their passaging across the blood-brain barrier in order to reach the tumor cells. Indeed, under tumor conditions the blood-brain barrier

becomes slightly leaky at angiogenic sites, therefore passaging of molecules is enhanced [Yuan et al., 1995]. However, since drugs are classically administered orally like TMZ [Newlands et al., 1992], only small amounts of drugs reach the brain tissue or liquor but they are rather efficiently eliminated in the body [Baker et al., 1999, Ostermann et al., 2004]. To conquer the blood-brain barrier, different attempts were pursued in this study including drug encapsulation in nanoparticles and the development of a drug-loaded 3D network for its use as local implant.

4.3.1 TMZ is processed in water-based solutions resulting in reduced cytotoxic effects in GBM cells

Taking account of TMZ as classical therapeutic and AT101 as promising compound for GBM therapy (cf. chapter 4.2), their application in alternative treatment approaches like nanomedicine and local administration was considered. Once present in the brain, drugs circulate in the cerebrospinal fluid and diffuse in brain tissue, where they reach their destination (reviewed in Hendricks et al. [2015]). As circulation and diffusion are time-dependent factors, it is highly important that drugs are chemically stable in brain liquor and retain their cytotoxic effect under *in-vivo* conditions.
The chemical stability of TMZ and AT101 was determined by their photometric activity in artificial cerebrospinal fluid (aCSF) solution containing small amounts of proteins (cf. tab. 3.2). A freshly prepared solution of TMZ showed a specific absorption spectrum between $250 - 450\,\text{nm}$ with a maximum at $\lambda = 330\,\text{nm}$ in line with literature values [Andrasi et al., 2011] (black line, fig. 4.9A, top). However, upon incubation at 37°C/5% CO_2 for 24 h, the absorption spectrum of TMZ in aCSF changed dramatically and the maximum shifted to approx. $\lambda = 265\,\text{nm}$ (red, green and blue lines, fig. 4.9A, top) indicating a processing of TMZ. In fact, temozolomide is rapidly metabolized in solutions with neutral to basic pH to 3-methyl-(triazen-1-yl)imidazole-4-carboxamide (MTIC), its active form, and further hydrolyzed to 5-amino-imidazole-4-carboxamide (AIC) [Denny et al., 1994, Andrasi et al., 2010, Lopes et al., 2013].
As opposed to this, AT101 absorption spectra differed only to a minor degree regarding the incubation time of the drug in solution at 37°C/5% CO_2 for 24, 48 and 72 h (fig. 4.9A bottom) suggesting a higher chemical stability of AT101 in an aqueous solution at body temperature compared to TMZ. The common absorption maximum at $\lambda = 373\,\text{nm}$ [Marciniak et al., 1989, Adams and Kirkpatrick, 1938, Frampton et al., 1948] was shifted to approx. $\lambda = 390\,\text{nm}$ and showed little decrease in intensity upon the period of incubation (red, green and blue lines, fig. 4.9A, bottom). In fact, the exact value for the absorption maximum between $357 - 393\,\text{nm}$ is dependent on the solvent [Marciniak et al., 1989]. Nevertheless, the other common absorption maximum at $\lambda = 289\,\text{nm}$ [Marciniak et al., 1989, Adams and Kirkpatrick, 1938, Frampton et al., 1948] was overlaid by another broad absorption peak but the absorption intensity was

stable during the incubation period. Additionally, increasing concentrations of AT101 showed a linear dependency at $\lambda = 289\,\text{nm}$ (fig. 4.9A, in-picture).

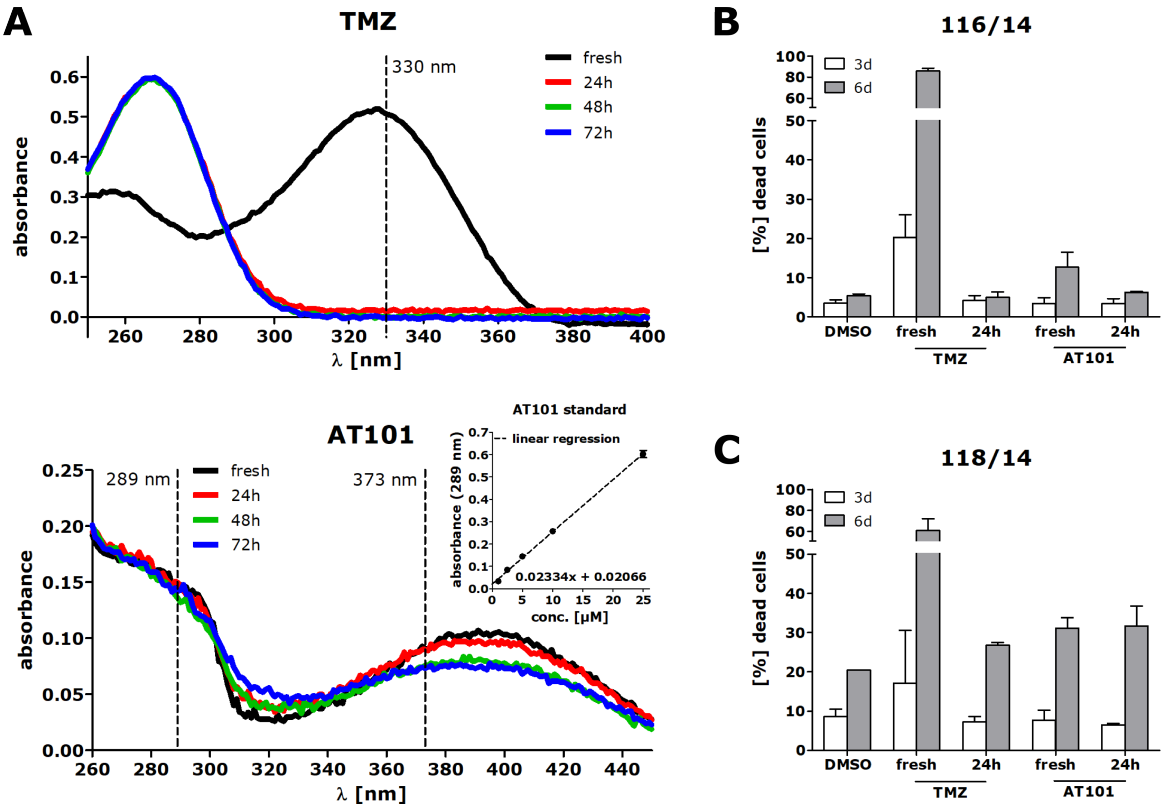

Figure 4.9: Cytotoxic effect of pre-incubated drugs in water-based solutions. To establish whether TMZ and AT101 are quantitatively detectable via UV/Vis spectroscopy in water-based solutions, 50 μM TMZ and 5 μM AT101 were diluted in aCSF solution and UV/Vis spectra from $250 - 450\,\text{nm}$ were measured immediately (black lines, **A**) and after 24 (red), 48 (green) and 72 h (blue) of incubation at 37°C/5% CO_2. Additionally, different concentrations of AT101 were adjusted in aCSF solution and a linear regression was calculated based on absorbance values at 289 nm (in-picture, **A**, n=4). Furthermore, in order to estimate cytotoxic effects of pre-incubated drugs, 50 μM TMZ as well as 5 μM AT101 were diluted in stimulation medium and incubated at 37°C/5% CO_2 for 24 h. Subsequently, GBM primary cultures, 116/14 (**B**) and 118/14 (**C**), were treated with 50 μM TMZ or 5 μM AT101, either freshly diluted in stimulation medium or pre-incubated for 24 h or DMSO, respectively. Numbers of dead and alive cells were determined after three and six days of treatment (n=2).

In compliance with previous results from GBM cell lines (cf. chapter 4.2), freshly prepared solutions of TMZ and AT101 yielded high (TMZ) and moderate (AT101) amounts of dead cells in GBM primary cultures 116/14 (fig. 4.9B) and 118/14 (fig. 4.9C), that show distinct molecular patterns (supplementary fig. A.1), in a long-term stimulation model. Interestingly, pre-incubation of TMZ at cell-culture conditions for 24 h led to a reduction of its cytotoxicity to levels comparable with DMSO-stimulated cells. In contrast, pre-incubation of AT101 yielded different effects. While the percentage of dead 116/14 cells was decreased to 6.31% (12.7% in case of fresh AT101) after six days of treatment (fig. 4.9B), the amount of dead 118/14 cells remained stable (fig. 4.9C).

Summarizing, TMZ was quickly processed in water-based solutions with physiological pH, leading to an almost complete omission of its cytotoxicity in glioma primary cultures, whereas no hint for metabolization was given and only minor variances in cytotoxicity were observed regarding AT101.

4.3.2 Nanoparticle production to improve bioavailability and cytotoxicity of AT101

After discovering the instability of TMZ in salt solutions of physiological pH resulting in its inability to induce cell death in primary glioma cells, AT101 was chosen for further studies on alternative routes of therapy, while oral TMZ administration additional to alternative strategies with other compounds was considered to be sufficient. In general, AT101 had a high cytotoxicity on GBM cells of different molecular expression profiles at relatively low concentrations ($5 - 10\,\mu$M) compared to other therapeutics (cf. chapter 4.2). However, experiments on normal brain cells, such as astrocytes and microglia, that were performed by Christina Schmitt (Institute of Anatomy) revealed a critial response of both cell lines to such amounts of AT101. In contrast, lower concentrations ($2.5\,\mu$M) were less harmful for normal brain cells but hardly attacked the glioma cell viability when applied singularily (cf. chapter 4.2, Adamski et al. [2018]). Considering other side effects, gossypol was also shown to have severe impacts on the hepatic system in treated patients [Bushunow et al., 1999] and is rapidly eliminated within the body [Wu et al., 1986, Jia et al., 2008]. In fact, nanoparticles, in particular cubosomes, qualified by a high potential of loading of various drugs [Wyatt and Dorschel, 1992, Changm and Bodmeier, 1997], partly based on their highly ordered cubic structure, which is spontaneously formed [Lutton, 1965, Larsson, 1983], represent a promising device in order to overcome the limited bioavailability of AT101 and increase its cytotoxicity on glioma cells. Further advantage is taken of the ability of nanoparticles to increase the amount of drug, that passes the blood-brain barrier [Kreuter and Gelperina, 2008] and to prevent AT101 from binding to e.g. blood-plasma proteins or else [Cater and Lyman, 1969, Dabrowski et al., 2001]. Hence, 10% (w/w) AT101 was encapsulated into cubosomes made of glyceryl monooleate (GMO) and pluronic F-127 yielding a high entrapment efficiency (EE [%], $97.7\% \pm 1.8$) and a drug loading capacity of $9.9\% \pm 0.05$. Cubosome preparation and characterization was performed in cooperation with the NanoBioMedical Centre of the Adam Mickiewicz University in Poznań (Poland). Visualization of blank cubosomes by cryo-transmission electron microscopy (cyro-TEM) revealed the cubosomal structure of particles of roughly 150 nm in diameter. Indeed, AT101 loading yielded smaller cubosomes and some additional liposomal-shaped particles (fig. 4.10). Interestingly, the characterization of blank and AT101-loaded cubosomes by dynamic light scattering (DLS) confirmed the assumption that GMO-AT101 nanoparticles were smaller in

size compared to unloaded particles (tab. 4.1). Additionally, the ζ or electrokinetic potential, describing the electrostatic repulsion between neighbored colloidal particles [Hunter et al., 2013], was significantly reduced upon AT101 loading in cubosomes (p=0.002, n=3), while other factors, such as z-average size, the intensity-weighted average particle size, and the polydispersity index (PDI), defining the heterogeneity of the sizes of particles (ISO 22412:2017), did not differ between both samples (tab. 4.1).

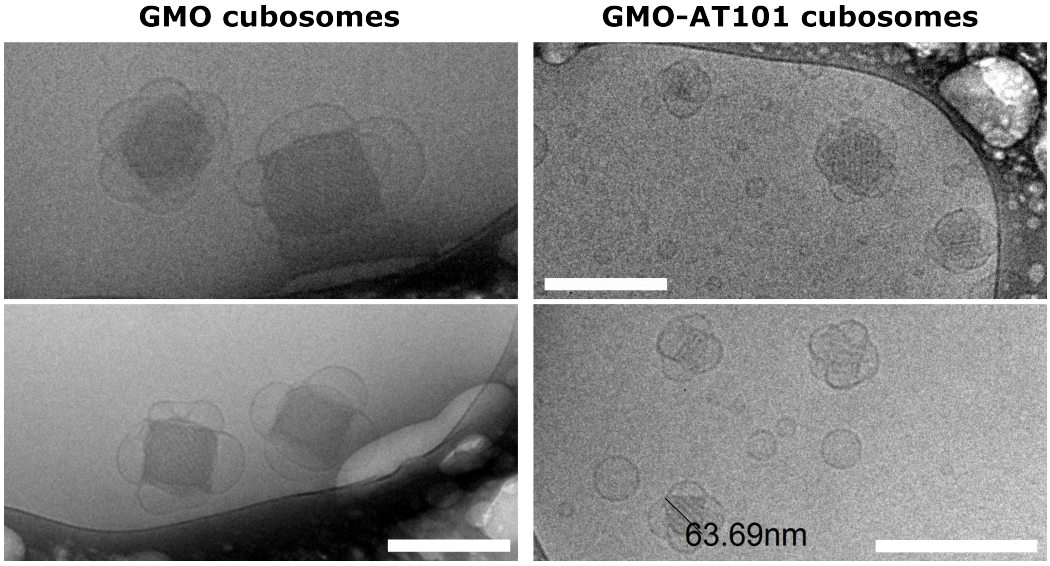

Figure 4.10: Morphologic analysis of blank and AT101-loaded GMO nanoparticles by cryo-TEM. The white bars indicate 200 nm.

Table 4.1: Characterization of blank and AT101-loaded GMO nanoparticles by DLS.

	Z-average size [nm]	PDI	Size [nm]	ζ potential [mV]
GMO	129.5 ± 14.2	0.167 ± 0.012	74.1 ± 10.0	-18.6 ± 1.6
GMO-AT101	120.3 ± 6.2	0.183 ± 0.021	65.3 ± 8.2	-33.7 ± 3.5

4.3.2.1 AT101 enhances the stability of cubosomal-structured nanoparticles

In fact, the ζ potential correlates with the stability of colloidal particles in suspension [Joffe and Mudd, 1935, Heiati et al., 1998] as the electrical repulsion of adjacent particles indicates the possibility of aggregation of those. Thus, a ζ potential above ± 30 mV implies good stability (reviewed in Wissing et al. [2004]) assuming that GMO-AT101 cubosomes were more stable than unloaded ones (tab. 4.1). To confirm this hypothesis, long-term stability of AT101-loaded and unloaded GMO cubosomes at room (25°C) and body temperature (37°C) was investigated by DLS measurements for at total of 17 days. Indeed, no changes of the PDI and the ζ potential were observed neither regarding the time nor concerning the storage temperature (fig. 4.11A).

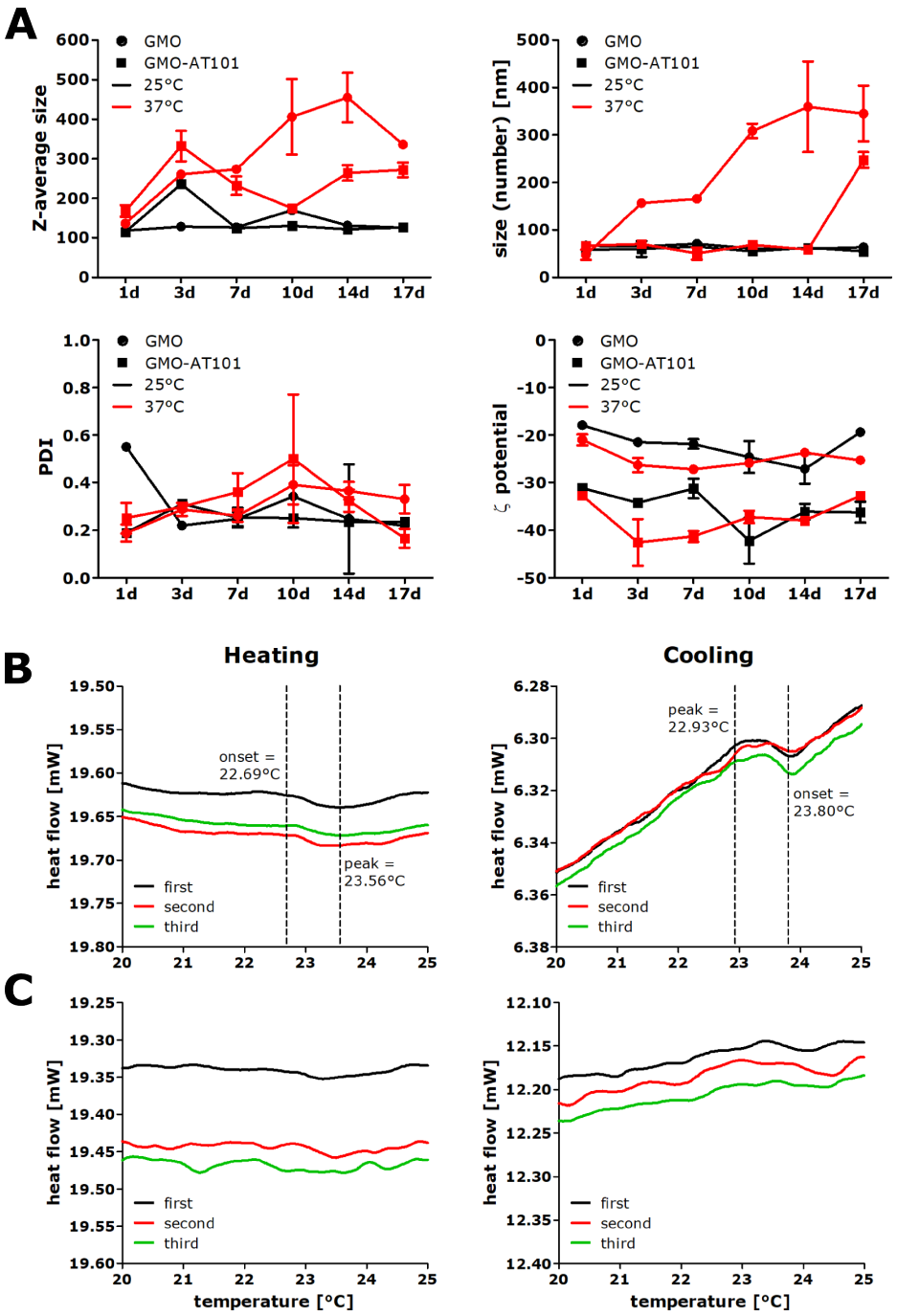

Figure 4.11: Stability measurements of blank and AT101-loaded GMO cubosomes. In order to estimate changes in the long-term stability upon AT101 loading, GMO (spheres) and GMO-AT101 cubosomes (squares) were stored either at 25°C (black) or 37°C (red) for 17 days. In between, characterization of nanoparticles concerning the z-average size, the polydispersity index, particle size by number and ζ potential was performed by DLS measurements after one, three, seven, ten, 14 and 17 days (**A**, n=3). Furthermore, thermal stability and physical behavior of GMO (**B**) and GMO-AT101 (**C**) nanoparticles were determined by differential scanning calorimetry (DSC) measurements.

However, the z-average size of GMO unloaded particles was notably enhanced after ten days of storage at 37°C, whereas the z-average size of GMO-AT101 cubosomes fluctuated during the whole storage period but did not strikingly change during the time period of 17 days (fig. 4.11A). This effect was even more prominent when an-

alyzing the size distribution calculated by the number, in which they appear. Here, blank GMO cubosomes increased in size already after three days of storage at 37°C. In contrast, AT101 loading into GMO nanoparticles resulted in a delayed expansion in size not before 17 days of storage at 37°C compared to their unloaded counterparts (fig. 4.11A).
Furthermore, GMO and GMO-AT101 cubosomes were analyzed regarding their stability at a working temperature range between 15°C and 80°C by DSC measurements. In general, GMO cubosomal systems show no phase transition within this temperature range, while the lipid itself does (supplementary fig. A.3, Bei et al. [2010], Shi et al. [2017]). This indicated for the stability of those colloidal particles since no melting or crystallization process was measured. Nevertheless, by having a closer look on the spectra of unloaded GMO cubosomes, a slight transition between 22°C and 24°C became obvious (fig. 4.11B). Intriguingly, this transition was not visible in GMO-AT101 particles (fig. 4.11C). In conclusion, AT101 loading into GMO cubosomes yielded an increased stability of nanoparticles.

4.3.2.2 AT101 encapsulation into cubosomes increases its cytotoxicity in GBM cells

Increasing the drug stability and bioavailability as well as the possibility to improve the cytotoxic effect of AT101 on glioma cells were purposes for the encapsulation of AT101 into GMO cubosomal-structured nanoparticles. A controlled release of the drug from cubosomes was essential in order to obtain drug-related cytotoxic effects. Thus, as cells in the brain are surrounded by fluctuating CSF (see review of Hendricks et al. [2015]), release measurements were performed at physicologic conditions (37°C, continuous stirring) in artificial CSF solution for 72 h. Indeed, approx. 20% AT101 of the whole encapsulated amount were released from GMO cubosomes within the first 24 h. Then, the release was decelerated but constant, reaching an average of 34.79% after 72 h (fig. 4.12, left), thereby guaranteeing AT101 to attack cells. The release kinetic was best defined by the Higuchi model by plotting the cumulative amount of released AT101 *versus* the square root of the time [Higuchi, 1961, 1963].
As glioma tumors are not planar, two-dimensional layers of cells, but rather three-dimensional clusters or tumor spheroids [Rubinstein et al., 1973, Bailey and Cushing, 1928], the ability of particles to penetrate into 3D tumor spheroids was of high importance. To visualize the uptake efficiency of GMO-AT101 cubosomes in 3D glioma spheroids as well as into the cell body, those were stained with Nile Red and spheroid margins were defined by Concanavalin A respective β-Catenin in the case of 2D cell layers. In fact, GMO-AT101 showed a high penetration into LN229 as well as A172 spheroids after 24 h of stimulation (fig. 4.13A, B, left). Moreover, a closer look on 2D cell layers also revealed a good uptake of GMO-AT101 cubosomes into single glioma

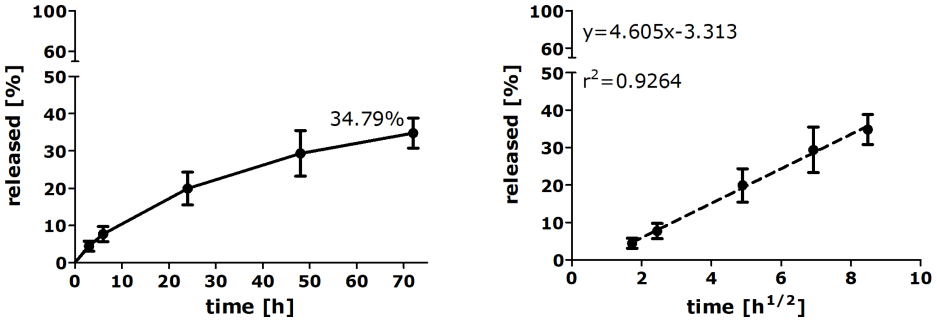

Figure 4.12: AT101 release from GMO cubosomes. To calculate the release kinetic of AT101-loaded cubosomes at physiologic conditions, 500 μl GMO-AT101 cubosome dispersion were filled into a dialysis bag, which was placed in 20 ml aCSF solution. The amount of released AT101 was determined spectrophotometrically at $\lambda = 289$ nm after 3, 6, 24, 48 and 72 h of continuous stirring at 37°C (left, n=3). To define the release kinetic, the Higuchi model, in which the cumulative release is plotted against the square root of the time, was applied (right).

cells (fig. 4.13A, B, right, indicated by white arrows). This direct transfer into cells might improve the cytotoxicity of AT101.

In general, GMO cubosomes are known to be biocompatible at low concentrations [Abdel-Bar and El Basset Sanad, 2017]. Thus, the cytotoxicity of unloaded GMO cubosomes was evaluated in two different GBM cell lines (LN229, A172) with distinct molecular profiles (supplementary fig. A.1), human astrocytes (SVGA) and microglia (HMC3). Hereby, blank/empty or unloaded GMO cubosomes revealed the highest cytotoxicity on HMC3 cells ($IC50_{HMC3}$=32.5 $\frac{\mu g}{ml}$, fig. 4.13C). In contrast, LN229, A172 and SVGA cells were less affected by GMO treatment ($IC50_{LN229}$=54.8 $\frac{\mu g}{ml}$, $IC50_{A172}$=64.5 $\frac{\mu g}{ml}$, $IC50_{SVGA}$=51.7 $\frac{\mu g}{ml}$, fig. 4.13C). Therefore, the biocompatibility of blank GMO cubosomes was also limited to low concentrations. Hence, for the following experiments, AT101 was encapsulated at 10% (w/w) into GMO cubosomes in order to reach a maximal applied concentration of 19.5 $\frac{\mu g}{ml}$ particles, which was almost tolerable for all cells but to aim therapeutically relevant concentrations of AT101 (2.5 and 3.75 μM).

The cytotoxic effects of different concentrations of encapsulated AT101 in GMO cubosomes compared to equal concentrations of free AT101 in solution and blank cubosomes, respectively, was investigated in LN229 as well as A172 GBM cells and human astrocytes and microglia after 72 h of stimulation. Hereby, low concentrations of free AT101 in solution had no (2.5 μM) or only small (3.75 μM AT101) cytotoxic effects on GBM cell lines (fig. 4.13D, left) but showed a somewhat higher impact on the viability of astrocytes and microglia (fig. 4.13D, right). However, by the encapsulation of AT101 into cubosomes, the cytotoxicity was significantly increased in LN229 cells compared to DMSO-stimulated cells but also to 2.5 μM freely applied AT101 (fig. 4.13D, left). This effect was less pronounced at a concentration of 3.75 μM free or encapsulated AT101. In addition, same amounts of blank GMO cubosomes were not toxic to LN229, thereby underlining the improvement of the cytotoxic effect of

AT101 upon encapsulation. In conformity albeit less strikingly, similar results were obtained with A172 cells (fig. 4.13D, left). Interestingly, although the administration of free AT101 reduced the viability of SVGA and HMC3 cells to a small degree, no significant enhancement of this effect but rather a slightly less toxic response, in particular in case of astrocytes, was observed with GMO-AT101 cubosomes (fig. 4.13D, right). Nevertheless, at higher concentrations of cubosomes themselves, corresponding to 3.75 μM AT101, the viability of HMC3 was somewhat affected (fig. 4.13D, right), which is explained by their stronger response to empty cubosomes shown in fig. 4.13C.

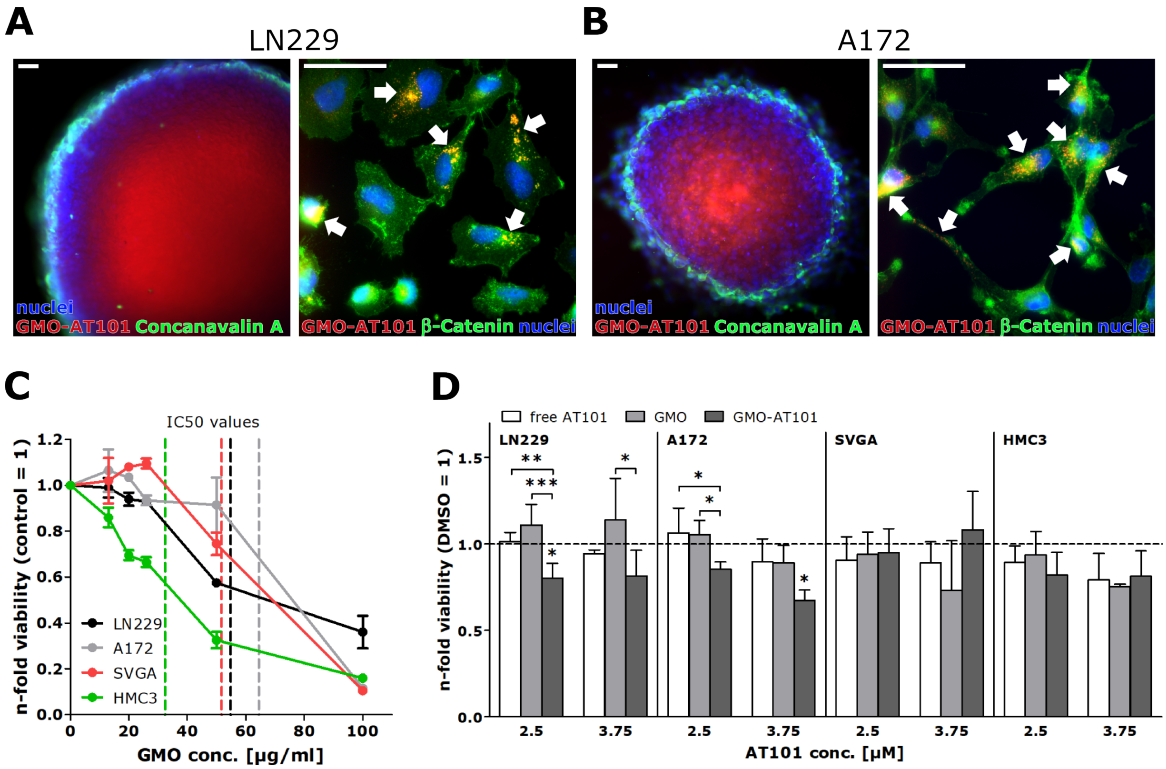

Figure 4.13: Cytotoxic efficiency of AT101 encapsulation on GBM cells, astrocytes and microglia. In order to prove the uptake of particles, AT101-loaded GMO cubosomes were stained with Nile Red 24 h before stimulation. Afterwards, LN229 (**A**) and A172 (**B**) native cells as well as spheroids, made by cultivation on agarose for six days, were stimulated with stained GMO-AT101 nanoparticles for 24 h. Then, spheroids were further stained with Concanavalin A (green) to allow for cell membrane identification. Furthermore, native cells fixed on a cover slip were stained with β-Catenin (green) to define the cell body. The nuclei were marked in blue, white bars indicate 50 μm (n=2). To estimate the biocompatibility of blank GMO cubosomes, two different GBM cell lines, LN229 and A172, as well as human astrocytes (SVGA) and microglia (HMC3) were stimulated with increasing concentrations from 13 $\frac{\mu g}{ml}$ to 100 $\frac{\mu g}{ml}$ cubosomes for 72 h. The amount of alive cells was measured by WST-1 assay and the data are plotted as n-fold viability compared to the unstimulated control (**B**, n=3). In addition, the cytotoxic efficiency of encapsulated AT101 *versus* free drug and blank cubosomes, respectively, was determined in GBM and normal brain cells by WST-1 assay after 72 h of stimulation with two different concentrations of AT101 (2.5 μM and 3.75 μM, **D**, n=3-4). Statistical analysis was performed by repeated one-way ANOVA followed by Tukey post-test for each concentration.

In summary, AT101-loaded GMO cubosomal-structured nanoparticles showed a great penetration efficiency in 3D tumor spheroids and were well taken up by single cells. Moreover, AT101 was continuously released at physiologic conditions. Upon encapsulation, the cytotoxic effect of AT101 on GBM cells was increased compared to directly applied drug. As opposed to this, normal brain cells were equally or slightly less affected compared to free drug administration.

To further underline the enhanced efficiency of encapsulated AT101 in comparison with the free application, GBM cell lines (LN229 and A172) were analyzed regarding their time-dependent cytoskeletal rearrangement for at total of 24 h on protein and mRNA level. During the execution phase of apoptosis, the cytoskeleton has to reorganize to ensure the induction of the typically known features of an apoptotic cell including cell contraction, plasma membrane blebbing and else [Kerr et al., 1972, Laster and Mackenzie, 1996]. Besides microtubules and intermediate filaments, actin rearrangement and shortening of fibers is essential for nuclear fragmentation and membrane blebbing [Coleman et al., 2001, Wickman et al., 2013, Seo and Rhee, 2018]. Actin fibers are bound by Phalloidin, a fluorescently-marked toxin from the death cap mushroom [Lengsfeld et al., 1974], of which was taken advantage for visualization of actin remodelling upon stimulation of cells with free AT101, GMO-AT101 and the respective controls.

Remarkably, a network of actin fibers was still visible after six hours of treatment with free AT101 in LN229 cells and in controls, respectively, while GMO-AT101 administration yielded slight condensation of actin fibers at poles accompanied by decreased intensity of stained actin (fig. 4.14A, bottom). After 24 h of stimulation, condensation of fibers became visible with free AT101 treatment as well (fig. 4.14A, bottom). The impact on actin was not only observed on protein but also on mRNA level as *β-actin* (*ACTB*) was significantly downregulated in cells stimulated with free and encapsulated AT101 for 24 h (fig. 4.14A, top). Interestingly, *cyclin-dependent kinase inhibitor 1A* (*CDKN1A*), which is associated with microtubule integrity [Stewart et al., 1999, Mantel et al., 2002, Blajeski et al., 2002, Lee and Helfman, 2004], was highly upregulated upon treatment with free AT101. However, this increased expression was not observed in GMO-AT101-stimulated cells (fig. 4.14A, top). Moreover, a further protein associated with microtubule function, microtubule-associated protein 2 (MAP2) [Herzog and Weber, 1978, Kim et al., 1979, Zhang and Dong, 2012, Uzdensky et al., 2012], was not transcriptionally regulated in AT101-stimulated GBM cells but significantly downregulated upon the administration of GMO-AT101 cubosomes compared to DMSO stimulation, noting that blank GMO cubosomes also showed an impact on the regulation albeit not significant (fig. 4.14A, top).

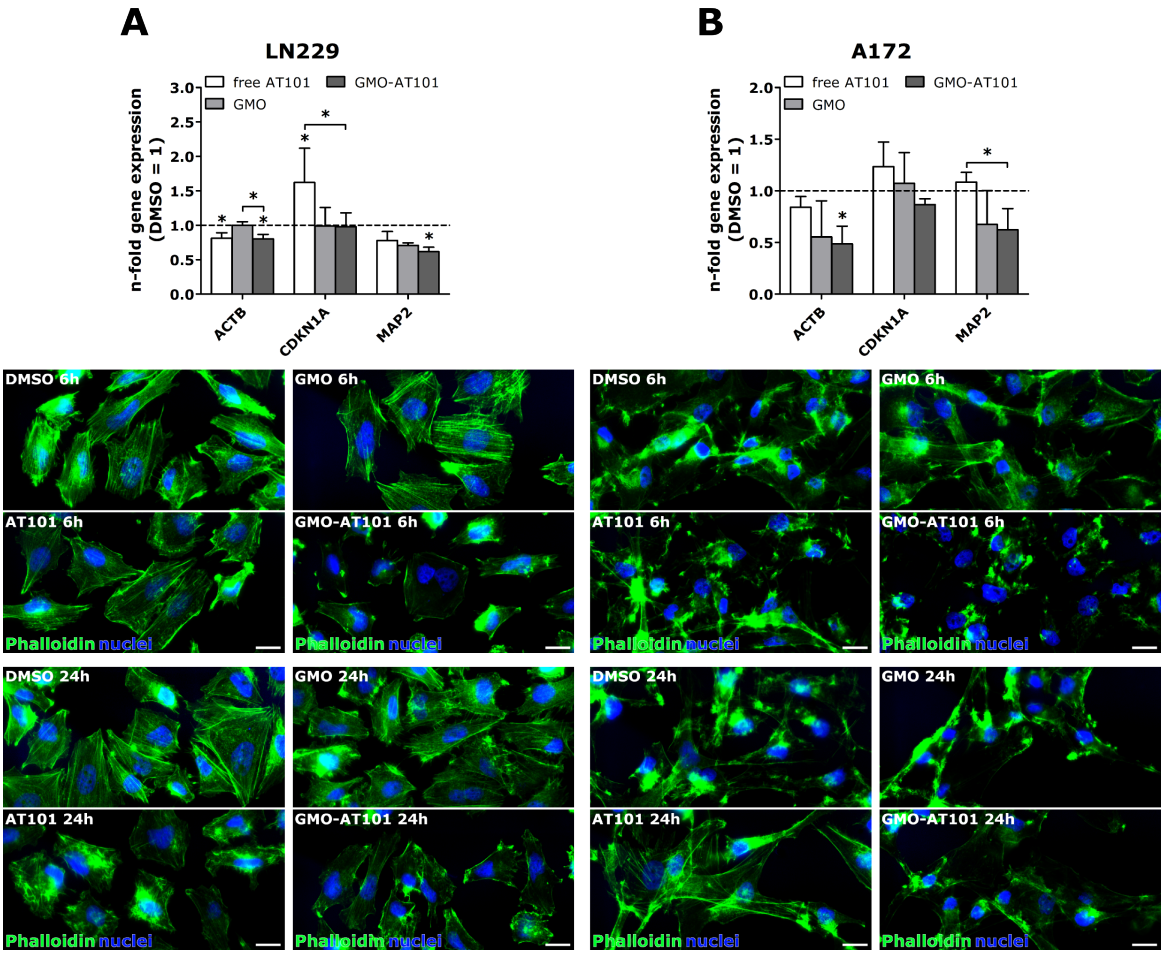

Figure 4.14: Cytoskeletal changes mediated by GMO-AT101 compared to free AT101 in glioma cells. Upon stimulation of LN229 (**A**) and A172 (**B**) cells with 26 $\frac{\mu g}{ml}$ GMO-AT101 or 5 μM AT101, respectively, cytoskeletal rearrangement occured after 6 and 24 h. In more detail, after stimulation, cells were either stained with Phalloidin (green) to visualize the cytoskeleton (bottom, n=2) or harvested and the transcriptional regulation of *ACTB*, *CDKN1A* and *MAP2* was determined after 24 h (top, n=3). The white bars indicate 20 μm, the nuclei were stained in blue. Gene expression was statistically analyzed by repeated one-way ANOVA followed by Tukey post-test for each gene.

Indeed, in case of A172 cells the alteration of the actin fiber network upon treatment with GMO-AT101 was less pronounced compared to LN229 cells. While controls and AT101-treated cells showed an indifferent staining of actin in the cell body, some areas of condensed actin were observed upon GMO-AT101 stimulation after six hours (fig. 4.14B, bottom). After 24 h, the intensity of actin decreased even more in GMO-AT101-treated A172, whereas a more condensed staining of actin was visible in controls (fig. 4.14B, bottom). Nevertheless, on transcriptional level *ACTB* was clearly downregulated upon GMO-AT101 treatment but not in case of free AT101 administration (fig. 4.14B, top). Furthermore, no regulation of *MAP2* was detected in AT101-treated A172 cells, while the expression was significantly decreased when stimulated with GMO-AT101 indicating for a change in the microtubule network (fig. 4.14B, top).

In conclusion, administration of AT101, encapsulated in GMO cubosomes, resulted in

an earlier rearrangement of actin cytoskeleton and a partial downregulation of *ACTB* compared to free AT101 treatment suggesting an earlier entry into apoptosis. In addition, the expression of other cytoskeletal markers associated to microtubule formation was significantly altered upon GMO-AT101 compared to free AT101 stimulation also pointing to a dysregulation of the cytoskeleton. This might underline the improved cytotoxicity of GMO-AT101 compared to free AT101 application shown in fig. 4.13D.

4.3.3 Development of a suitable device for local GBM therapy

As mentioned before, advantages of the encapsulation of AT101 into nanoparticles for its use in brain-tumor therapy are, besides others, the potential shielding of the drug from its metabolization or chemical reactivity [Kenar, 2006] and binding to plasma particles [Cater and Lyman, 1969, Dabrowski et al., 2001] as well as a possible increase of its limited bioavailability [Jia et al., 2008]. Although nanoparticles generally profit from an enhanced passive passaging through the blood-brain barrier compared to unencapsulated molecules [Kreuter and Gelperina, 2008], another apparent opportunity to bypass blood-brain barrier restrictions and reduce foreign-body side effects of therapeutics is to develop implant materials for local administration of therapeutics. In the following, different material approaches were developed in collaboratory work with material scientists and tested regarding their applicability for local GBM therapy.

4.3.3.1 Released Zn^{2+} ions from scaffolds in combination with AT101 show heterogenous cytotoxic effects in GBM cells

In order to find an appropriate template with a high drug-loading capacity, that is easy to manufacture and variable in size guaranteeing an improved, prolonged release of therapeutic compared to already locally used Gliadel® wafers [Brem et al., 1991], different approaches were followed in the first case. Hereby, a network of ZnO tetrapods represented the best suited device due to its simple production and tunability as well as its high surface-to-volume ratio and great free-volume space ($> 90\%$ porosity), which causes its drug-loading potential [Mishra et al., 2015, 2013, Hölken et al., 2016]. This tetrapodal ZnO network was produced by Florian Rasch (Institute for Materials Science) and provided for *in-vitro* experiments for this project. The network of ZnO tetrapods was successfully fabricated by the interconnection of single arms of ZnO tetrapods on a microscale leading to a large free-volume space and a great surface-to-volume ratio with a porosity of 94.7% (fig. 4.15A). In order to estimate the biocompatibility of the ZnO template, at first, the potential release of Zn^{2+} ions from the bulk material was investigated by incubation of the template in culture medium at 37°C/5% CO_2 for six days. The quantitative determination of the Zn^{2+} ions at different time points revealed a continuous release of Zn^{2+}, which was

kinetically described by the Higuchi model within the first 48 h (fig. 4.15B, black line). After 72 h of incubation, the Zn^{2+} concentration reached an averaged maximum of 15.12 $\frac{\mu g}{ml}$, which was almost stable until the sixth day of further analysis. This maximal measured concentration was linked to a saturation of Zn^{2+} ions in the culture medium rather than a gained inactivity of the template as an exchange of the template after 72 h did not lead to a further, significant increase of Zn^{2+} concentration (16.68 $\frac{\mu g}{ml}$, fig. 4.15B, red line). In contrast, exchanging the culture medium but retaining the ZnO template again resulted in the release of Zn^{2+} ions to a maximum of 14.49 $\frac{\mu g}{ml}$ after further 72 h (fig. 4.15B, green line).

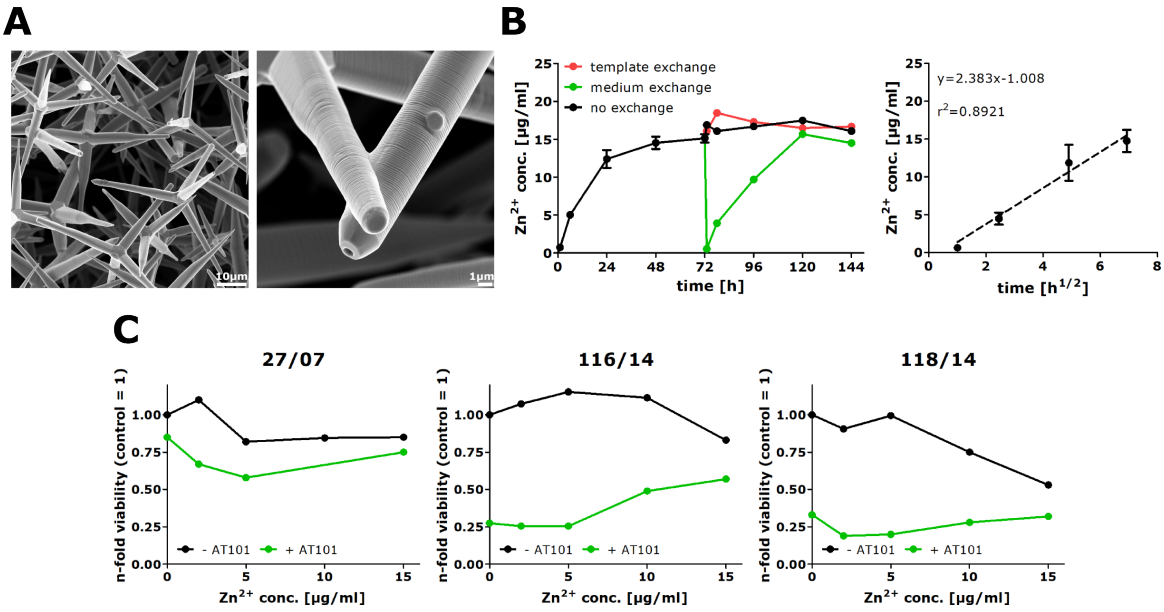

Figure 4.15: Combined-treatment effect of Zn^{2+} ions released from tetrapodal ZnO networks plus AT101 on primary GBM cells. 3D tetrapodal ZnO-network templates were produced in collaboration with Florian Rasch (Institute for Materials Science), who also provided scanning electron microscopy (SEM) pictures (**A**). The release of Zn^{2+} ions from such templates was measured spectrophotometrically via Zincon complexation at $\lambda = 620$ nm under cell-culture conditions in culture medium at 37°C/5% CO_2 over six days (**B**, left, black line). In between, either the template (red line) or the medium (green line) was exchanged after three days of incubation. To define the release kinetic, the Higuchi model, in which the cumulative release is plotted against the square root of the time, was used for the first 48 h (**B**, right). According to DIN EN ISO 10993-12, conditioned Zn^{2+}-culture medium was prepared and tested for *in-vitro* cytotoxicity following DIN EN ISO 10993-5 regulations. GBM primary cultures 27/07, 116/14 and 118/14 were stimulated with increasing concentrations of Zn^{2+} in medium either with (green line) or without (black line) 2.5 μM AT101. After six days, the n-fold viability of cells was determined by standard cell-counting technique (**C**).

In a next step, the biocompatibility of the tetrapodal ZnO network was examined focussing on its *in-vitro* cytotoxicity on three primary glioma cultures of different gene expression profiles (supplementary fig. A.1). Accordingly, normal brain cells (astrocytes and microglia) were tested likewise by Christina Schmitt (Institute of Anatomy). For this purpose, conditioned medium was prepared in accordance with DIN EN ISO 10993-12 by incubation at 37°C/5% CO_2 for 72 h. Then, the viability of primary GBM

cells, stimulated with increasing concentrations of Zn^{2+} ions in culture medium for six days, was determined following DIN EN ISO 10993-5 regulations. Interestingly, the primary glioma cultures 27/07 and 116/14 were almost not affected by cumulating amounts of Zn^{2+} ions, while the viability of 118/14 cells was markedly reduced with 10 and 15 $\frac{\mu g}{ml}$ Zn^{2+} ions in the medium (fig. 4.15C, black lines). As the tetrapodal ZnO networks potentially served as scaffolds to use them as drug-loading devices for local application releasing AT101 as promosing candidate for alternative GBM therapy accompanied by systemic TMZ administration (cf. chapters 4.2, 4.3.1, 4.3.2), the combined cytotoxic effect of increasing amounts of released Zn^{2+} ions plus 2.5 μM AT101 was investigated. Indeed, the primary GBM cultures differentially responsed to single AT101 treatment with 27/07 showing the highest viability, whereas 116/14 and 118/14 were heavily affected by AT101 (fig. 4.15C, green lines). However, the cytotoxic effect of AT101 was either not changed or slightly antagonized with increasing Zn^{2+} concentrations (fig. 4.15C, green lines).
In summary, Zn^{2+} ions were continuously released from tetrapodal ZnO networks until their saturation in cell-culture medium. In case of primary GBM cells, ZnO itself showed no cytotoxicity except for 118/14 cells but negatively influenced the cytotoxic effect of AT101 at higher Zn^{2+} concentrations, though. Moreover, a closer look on the response of normal brain cells on Zn^{2+} ions revealed a relatively high potential of Zn^{2+} to reduce the viability of astrocytes and microglia at 10$\frac{\mu g}{ml}$ (SVGA) and only 5 $\frac{\mu g}{ml}$ (HMC3). When co-administering AT101, the viability of astrocytes and microglia was even more decreased (data provided by Christina Schmitt (Institute of Anatomy)).
Nevertheless, in a second attempt, the drug-loading capacity and release potential of the tetrapodal ZnO network was investigated. Therefore, a high amount of AT101 was loaded onto the template by wet infiltration. In order to guarantee a homogeneous distribution of AT101 across the ZnO network, it was mixed with poly(L-lactide-co-caprolactone) (PLCL) solution, which was shown to homogeneously cover the tetrapodal ZnO structures beforehand (data owned by Florian Rasch (Institute for Materials Science)). Indeed, PLCL shows a great biocompatibility, therefore it is widely used for tissue engineering [Jeong et al., 2004, Vaquette et al., 2008]. It was also taken advantage of its slow biodegradability [Hiljanen-Vainio et al., 1997], thereby potentially slowly releasing the trapped AT101. Coverage performance of AT101-PLCL was visualized by SEM imaging carried out by Florian Rasch (Institute for Materials Science). The polymer was recognized as undulated layer on the tetrapodal arms of ZnO (fig. 4.16A). In line with previous findings, Zn^{2+} was released at an average of 8 to 10 $\frac{\mu g}{ml}$ over 48 h under cell-culture conditions in the presence of primary GBM cells, which continued for six days with an exchange of medium after every measurement (fig. 4.16B, left). However, AT101 release was characterized by a burst effect within the first two days reaching a mean concentration of 32.9 μM between both primary

cells, an almost 13-fold higher amount of AT101 compared to the previously used, therapeutically relevant concentration. This release was rapidly decreasing after the following four days to 7.1 μM and 1.3 μM, respectively, to less therapeutically relevant concentrations (fig. 4.16B, right).

Beside the analysis of the Zn^{2+} and AT101 release from the template in the presence of cells, its cytotoxic effect on two primary GBM cells was determined during six days of indirect incubation. For this purpose, primary GBM cells were stimulated via indirect contact with the ZnO-AT101-PLCL template across a Millicell® cell culture insert membrane for six days. During the first four days of stimulation, the template showed a good tumor growth control of 27/07 and 116/14 primary glioma cells. Nevertheless, tumor cells tended to re-initate proliferation between day 4 and 6, which was even more prominent in 27/07 cells (fig. 4.16C).

Summarizing, Zn^{2+} ions were continuously released from ZnO networks covered with AT101-PLCL every 48 h comparable to previous findings. In contrast, AT101 release was described by a burst effect with rapidly decreasing concentrations thereafter leading to an initial tumor growth control of primary GBM cells, that were able to recover afterwards. In conclusion, the tetrapodal ZnO network was characterized by a great drug-loading potential. However, on the one hand, the drug release had to be adjusted to lower, more constant levels. On the other hand, the amount of released Zn ions was slightly cytotoxic for astrocytes and microglia. Thus, the use of ZnO as template material was ineligible.

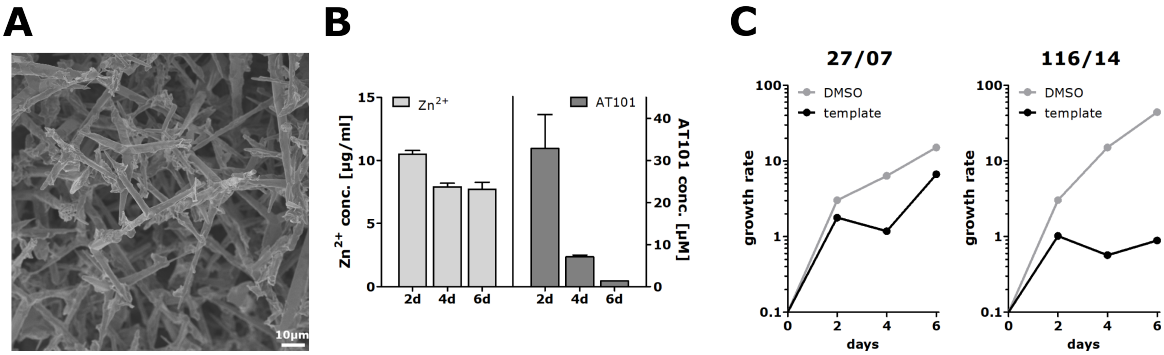

Figure 4.16: Indirect stimulation of primary GBM cells with an AT101-PLCL-covered ZnO-network template. The ZnO-network template was infiltrated six times with 1 mM AT101-PLCL-DMSO solution and dried in between, guaranteeing homogeneous distribution of AT101-PLCL on the ZnO network (**A**, kindly provided by Florian Rasch (Institute of Materials Science)). GBM primary cultures 27/07 and 116/14 were indirectly stimulated with this ZnO-AT101-PLCL template for six days at 37°C/5% CO_2. The release of Zn^{2+} ions was determined spectrophotometrically via Zincon complexation at $\lambda = 620$ nm after two, four and six days (**B**). Furthermore, AT101 release was measured spectrophotometrically at $\lambda = 289$ nm likewise (**B**). Every second day the medium was renewed and cell amounts were counted after two, four and six days of stimulation. The data are plotted as growth rates of cells (**C**).

4.3.3.2 Adjustment of the release of AT101 from a three-dimensional PDMS network

To overcome potentially unwanted side effects of released Zn^{2+} ions from tetrapodal ZnO networks but to retain the advantage of such networks with respect to high drug-loading capacities, biocompatibility, mechanical stability, technical variability and chemical resistance, in collaboratory work with Christina Schmitt (Institute of Anatomy) and Florian Rasch (Institute for Materials Science) different approaches were investigated. At first, the ZnO network was loaded with drug (AT101) diluted in PLCL-DMSO solution to guarantee a homogeneous distribution of the therapeutic on the tetrapodal network as well as to impede a burst release of AT101 (described in the previous chapter 4.3.3.1, illustrated in fig. 4.17A). Nevertheless, ZnO was only moderately biocompatible in case of astrocytes and microglia and AT101 was rapidly released despite PLCL. Therefore, in a second attempt, ZnO was replaced by poly(dimethylsiloxane) (PDMS), a biocompatible, under physiological conditions non-degradable, elastic polymer (for review see Belanger and Marois [2001]). For this purpose, the free volume of the ZnO network was filled with wax. Then, the ZnO was etched out by acetic acid leaving a hollow channel network, that was filled with PDMS. Afterwards, the wax was removed by melting at 40°C (fig. 4.17B). However, although PDMS is known to be insoluble in DMSO [Lee et al., 2003], after infiltration of AT101-PLCL-DMSO solution, the network collapsed probably caused by too high shear forces between tetrapodal arms. The last followed attempt included the coverage of the ZnO network by PDMS. In accordance with the previous approach, the ZnO was etched out by acetic acid yielding a PDMS sponge with a tetrapodal channel network (fig. 4.17C). Additionally, outer channels were uncovered by a short treatment with hexane to ensure proper drug loading and release.

The visualization of the surface of the PDMS template by SEM displayed many open holes representing entrances into the channel network in the inside of the sponge (fig. 4.18A). In a next step, AT101 was loaded into this network by vacuum infiltration within distinct AT101 concentrations in an 1:2 ratio of aCSF-DMSO solution without supplemented BSA in aCSF to avoid AT101-binding to serum proteins. In order to develop a device with a high drug-loading capacity and an optimal, continuous release of therapeutically relevant concentrations over a long-time period as well as an almost linear release kinetic of the drug, different parameters were changed and adjusted. The criteria for assessment of adjusted parameters was the release of AT101 in aCSF solution at 37°C/5% CO_2 under continuous shaking for three days.

In the first place, the influence of the channel density (porosity) of the PDMS network on the AT101 release was investigated. For this purpose, different amounts of ZnO tetrapods were pressed into the template structure to form ZnO networks of different channel densities, which were, in turn, inherited by the PDMS channel network.

Afterwards, all different channel properties were filled with 5 mM AT101 stock solution and analyzed regarding their drug release after 24, 48 and 72 h. Interestingly, only 0.5 μM AT101 was released from 0.9 $\frac{g}{cm^3}$-channel density networks after 24 h, that were not re-detected after 48 and 72 h depicting the detection range of AT101 in the solution (fig. 4.18B, white columns). In fact, by increasing the channel density to 1.2 or 1.5 $\frac{g}{cm^3}$, more stable concentrations were measured, that hardly reached therapeutically relevant concentrations (approx. 1.3 μM AT101). However, no significant difference was observed between 1.2 and 1.5 $\frac{g}{cm^3}$ channel densities (fig. 4.18B, grey columns). By ultimately duplicating the channel density to 2.7 $\frac{g}{cm^3}$, the release of AT101 was continuously increasing during the measurement period up to 2.1 μM at day 3, thereby nearly reaching therapeutically relevant concentrations for *in-vitro* experiments with GBM cells (fig. 4.18B, black column).

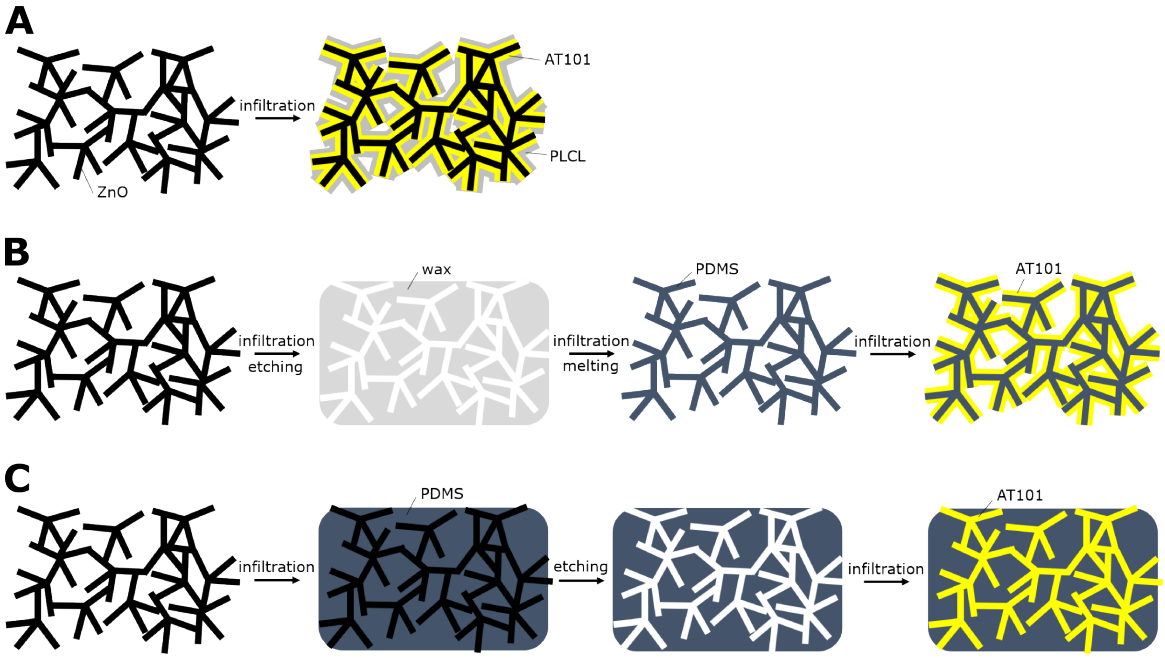

Figure 4.17: Different approaches of 3D networks for local glioma therapy. In collaboration with Florian Rasch (Institute for Materials Science) and Christina Schmitt (Institute of Anatomy) different templates for their use in local glioma therapy were produced. In a first attempt, a tetrapodal ZnO network was infiltrated with a solution of AT101-PLCL in DMSO (cf. chapter 4.3.3.1, **A**). Second, the tetrapodal ZnO network was covered with wax. Afterwards, ZnO was etched out leaving hollow channels in wax, that were filled with PDMS. The wax was removed by melting. Ultimately, the tetrapodal PDMS network was infiltrated with AT101 solution (**B**). In a third approach, the tetrapodal ZnO network was embedded in PDMS and etched out subsequently. Then, the tetrapodal, hollow channels in PDMS were filled with AT101 solution (**C**).

In order to enhance the release of AT101 in smaller networks (1.5 $\frac{g}{cm^3}$), the PDMS channels were coated with graphene oxide, which also shows *in-vitro* biocompatibility (Unagolla and Jayasuriya [2019], for reviews see Gurunathan and Kim [2016], Liao et al. [2018]), thus taking advantage of the potential repulsive effect of graphene oxide on the hydrophobic compound AT101 [Zou et al., 2017] and disturbing the potential

strong interaction between hydrophobic AT101 and hydrophobic PDMS. Nevertheless, the addition of a graphene layer onto the PDMS channels did not yield a relevant increase in the release of AT101 after 72 h of incubation (fig. 4.18C).

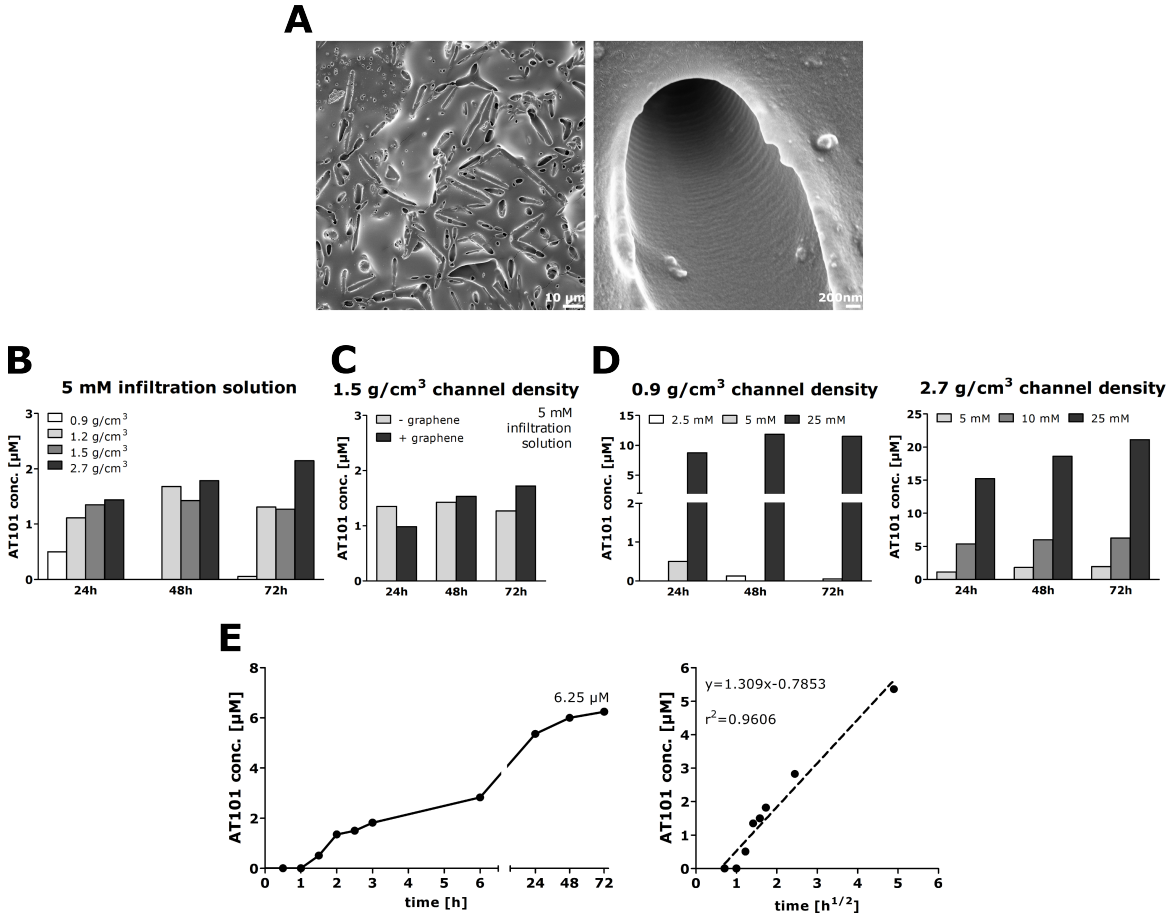

Figure 4.18: Adjustment of different parameters and their effect on AT101 release from PDMS scaffolds. PDMS scaffolds were produced on the basis of tetrapodal ZnO networks in collaboration with Florian Rasch (Institute for Materials Science) resulting in a PDMS template with a tetrapodal channel network (cf. fig. 4.17C, **A**, kindly provided by Florian Rasch (Institute for Materials Science)). Next, the PDMS scaffold was filled with AT101 solution. To achieve an optimal release of AT101 from PDMS scaffolds in aCSF solution under cell-culture conditions, different parameters such as various channel densities (**B**), coating with graphene (**C**) and increasing concentrations of AT101 for the infiltration of different channel densities ($0.9\,\frac{\mathrm{g}}{\mathrm{cm}^3}$ or $2.7\,\frac{\mathrm{g}}{\mathrm{cm}^3}$, **D**) were adjusted. Finally, the release kinetic of AT101 with respect to the identified, best-working parameters was determined using the Higuchi model, plotting the cumulative release against the square root of the time, within the first 24 h (**E**, data were obtained with technical assistance of the master's student Rieke Johanna Meyer).

Finally, the concentration of AT101 in the infiltration solution was comparatively adjusted for 0.9 and $2.7\,\frac{\mathrm{g}}{\mathrm{cm}^3}$-channel densities, in order to achieve higher release rates. In fact, increasing the amount of AT101 captured inside the PDMS channels heavily influenced the released concentration. While an infiltration with 5 mM AT101 in $0.9\,\frac{\mathrm{g}}{\mathrm{cm}^3}$-density networks only yielded maximal released concentrations of $0.5\,\mu$M, infiltrating the 5-fold amount of AT101 led to a release of over $11.5\,\mu$M after 72 h (fig. 4.18D, left). In comparison, by the infiltration of 25 mM AT101 solution in networks

of 2.7 $\frac{g}{cm^3}$ density, the release was even doubled to 21.1 μM after 72 h, additionally revealing a continuous increase of the AT101 concentration between 24 and 72 h (fig. 4.18D, right). However, therapeutically relevant concentrations were best obtained with 2.7 $\frac{g}{cm^3}$-channel density and 10 mM AT101 in the infiltration solution resulting in a constant release of drug within 24 h, then reaching a plateau with a maximum of 6.25 μM after 72 h (fig. 4.18E, left). The release kinetic was best described by the Higuchi model during the first 24 h (fig. 4.18E, right).

In summary, the PDMS template with a tetrapodal channel network showed great drug-loading capacity. By adjusting different parameters, such as channel density and the amount of infiltrated AT101, the release of the therapeutic compound was variously triggered. In this case, the optimal fitting parameters for *in-vitro* application were a channel density of 2.7 $\frac{g}{cm^3}$ and an infiltration with 10 mM AT101. Nevertheless, astrocytes and especially microglia were shown to be heavily affected by 5 μM AT101 and above, that were released using such parameters. Therefore, lower amounts of AT101 have to be loaded into the PDMS sponge. After fine-tuning, this device represents the basis for initial *in-vitro* experiments for GBM therapy and advancement of the controlled, long-term drug release.

5 Discussion

Glioblastoma Multiforme represents one of the most aggressive primary brain tumors with by far the highest death rate among all other tumor types in western countries [American Cancer Society, 2018]. Surgical resection and concomitant radio- and chemotherapy fail to control tumor re-growth, therefore the median progression-free survival only reaches eight months [Rapp et al., 2017]. Additionally, on average more than 94 of 100 patients die within five years after a distressing period of repeated surgeries and weakening therapy [Ostrom et al., 2018]. The reasons behind the insufficient response of the tumor to therapy causing the poor prognosis for patients and the high mortality rate are not yet comprehensively understood. The tumor heterogeneity, expressed by the existence of cell subpopulations with distinct abilities [Wang et al., 2017b, Aubry et al., 2015, Singh et al., 2003, Claes et al., 2007] and the close communication of the tumor with its microenvironment (reviewed by Quail and Joyce [2017]) embody two identified aspects impeding GBM therapy. Hence, this study was devoted to unveil the key aspects and their relative impact on glioma therapy, in order to overcome the current limitations of treatment and improve the patients' outcome by the development of new approaches and the introduction of alternatives of therapy.

5.1 Tumor dormancy as therapy-escape mechanism

A key role of high importance in the tumor's development of therapy-escape mechanisms is tumor dormancy, that has recently been defined as new hallmark of cancer [Yeh and Ramaswamy, 2015]. Dormancy explains a state, in which the tumor remains occult and not expanding for a long time period [MacKie et al., 2003]. This has mainly been investigated and reviewed for metastatic breast cancer and melanoma [Senft and Ronai, 2016, Dittmer, 2017], but also contributes to the poor therapy outcome in glioblastomas [Tong et al., 2018]. Concerning breast and melanoma cancers, especially circulating tumor cells (CTCs), orignated from the primary tumor, that entered the circulation to disseminate and persist in foreign tissues until their metastatic progression, were typically known as dormant cancer cells (reviewed by Dasgupta et al. [2017]). Although only very rare cases of extracranial metastases of glioblastomas have been observed [Zhen et al., 2010, Tanaka et al., 2014], Müller et al. [2014] were the first, who proved the existence of glioma CTCs. However, local recurrences of gliomas within the primary tumor-margin zone and beyond represent the common problems of therapy [Hochberg and Pruitt, 1980, Watanabe et al., 1992]. Relapses evolve from a solitary group of cells, that have resisted classical therapy regimen. Therefore, the characterization of those persisting tumor cells was part of this project.

In general, it is distinguished between cellular and tumor-mass dormancy, which is

divided in an angiogenic and immunogenic type [Naumov et al., 2002, 2006, Koebel et al., 2007]. While angiogenic dormancy has already been studied several times in regard to glioblastomas by Naumov et al. [2002, 2006], Almog et al. [2009], Satchi-Fainaro et al. [2012], Tiram et al. [2018], the focus of this study was laid on the cellular dormancy of GBM tumors, in which individual cells enter a temporary cell-cycle arrest [Hadfield, 1954]. Indeed, a long-term treatment with a subletal dose of the classic chemotherapeutic temozolomide (TMZ) partly induced cellular dormancy *in vitro* in GBM cell lines. Dormancy entrance was dependent on the responsiveness of the glioma cell line to TMZ, wherefore those cells, that were heavily affected by TMZ stimulation, escaped into cellular dormancy and those, that were only moderately affected, did not show a dormant phenotype (fig. 4.1, Adamski et al. [2017a]). Intriguingly, these distinct sensitivities to therapy were accompanied with the different molecular expression of *EGFR*, *PDGFRA*, *NF1* and *CDKN1A* of the glioma cell lines associated to glioblastoma subtypes (supplementary fig. A.1, Verhaak et al. [2010]). In fact, resistance to TMZ has already been linked to the induction of a G2-M cell-cycle arrest, in which *growth arrest and DNA damage-inducible protein 45* α (*GADD45*α) upregulation as well as the activation of Wnt/β-Catenin and Akt signaling pathways were relevant factors [Hirose et al., 2001, Yi et al., 2016, Wang et al., 2017a]. Beyond that, the expression of the dormancy-related genes *H2BK*, *IGFBP5* and *EphA5* was elevated in those TMZ-treated, unproliferative glioma cells indicating a link of the cell-cycle arrest induced by TMZ to cellular dormancy (fig. 4.1, Adamski et al. [2017a]).

Besides the induction of the expression of dormancy-associated markers, GBM cell lines additionally upregulated typical stem cell markers such as *MSI1*, *KLF4* and *OCT4* and the ability of spheroid formation was increased upon TMZ stimulation, thereby pointing to a connection between dormancy and self-renewal abilities (fig. 4.1, Adamski et al. [2017a]). Indeed, TMZ resistance has already been linked to an augmented expression of *cluster of differentiation 133* (*CD133*), a common stem cell marker [Perazzoli et al., 2015]. *Vice versa*, quiescence, an unproliferative state induced by growth factor depletion (reviewed in Blagosklonny [2011]), is a general feature of many stem cells of different tissues, but was also attributed to tumor stem cells, especially those in GBM [Deleyrolle et al., 2011, Zeng et al., 2016, Endaya et al., 2016]. Besides the correlation of stem cell properties with glioma CTCs [Liu et al., 2018], unproliferative glioma cells are capable of tumor initiation or reactivation *in vivo* and show an enhanced TMZ resistance as well as a high self-renewal capacity [Zeng et al., 2016, Tejero et al., 2019, Galvao et al., 2014], thus contributing to the overall glioblastoma's aggressiveness [Campos et al., 2014]. In conclusion, glioma cells were differently affected by classic chemotherapeutic treatment with TMZ. Further, those GBM cells, showing a strong responsiveness to TMZ, escaped into cellular dor-

mancy. Additionally, those dormant glioma cells were also equipped with an increased self-renewal property, which might facilitate the re-growth of the tumor later on. Indeed, a molecular-profiling study of Kwon et al. [2015] revealed that recurrent glioblastomas noticeably express stemness-related genes and upregulated DNA-repair genes hinting to the therapy-resistent, stem-like phenotype of reawaked tumors. While chemotherapy seems to induce dormancy entry of tumor cells, those triggers, that drive tumor reawakening, have not been identified, yet. A look on prokaryotes reveals that persistent bacteria exit the dormant state when the environmental conditions are favorable again, e.g. by the addition of growth factors into the medium [Jõers et al., 2010] indicating that the environment seems to play a pivotal role in tumor dormancy and reawakening mechanisms, which has also been adressed by Magnus et al. [2014] in case of GBMs. The tumor microenvironment of gliomas is highly important for the tumor maintenance and progression as it not only directly shields the tumor from therapy-induced cell death [Zhang et al., 2019, Lin et al., 2016, Chen et al., 2015, Yang et al., 2014], but also provides pro-survival and pro-migratory factors [Ross et al., 2017, Le et al., 2003, Oliveira et al., 2005, Bettinger et al., 2002, Yeh et al., 2012]. In general, tumor-associated cells such as microglia, astrocytes and other immune cells are responsible for the induction of an inflammatory response to attack tumor cells. However, during immunosurveillance, tumor cells, which evaded their elimination by immune cells, start growing contributing to tumor progression (reviewed in Dunn et al. [2012]). Meanwhile, tumor-associated immune cells secrete inflammatory molecules like chemokines, that, in turn, influence tumor progression in terms of rescue from apoptosis and promoting invasive properties and tumor-cell proliferation [Ehtesham et al., 2006, Hattermann et al., 2012, 2016b]. Beside the communication between glioma and immune cells, also autocrine and paracrine signaling of chemokines between tumor cells are highly relevant in glioma cell biology [Ludwig et al., 2005, Hattermann et al., 2010, Held-Feindt et al., 2010, Hattermann et al., 2012, 2013, Flüh et al., 2016]. However, the impact of chemokines on dormancy and reawakening mechanisms in GBM tumors has not been elucidated, yet. In particular CXCR4, CXCR7, CXCL16 and CX3CL1 have been already attributed to rescue from apoptosis and proliferation of tumor cells [Hattermann et al., 2010, 2012, 2013, 2016b] and were highly upregulated upon TMZ stimulation, thus potentially impacting tumor dormancy (fig. 4.2D). Indeed, by generating an inflammatory surrounding through stimulation with the chemokines CXCL12, CXCL16 and CX3CL1, dormancy entry and exit regulation of TMZ-treated glioblastoma cells was altered in comparison with normal conditions. On the one hand, those inflammatory mediators delayed the entry of glioma cells into cellular dormancy induced by chemotherapeutic treatment. On the other hand, the reawakening process of dormant tumor cells, that were no longer stimulated with TMZ, was also delayed in an inflammatory environment

(fig. 4.2A-C). Interestingly, the influence of some chemokines on dormancy-related pathways have been partly studied in other tumors such as breast cancers. De Cock et al. [2016] showed that inflammation triggered the escape of metastatic breast-cancer cells from a dormant phase in lung parenchyma. Accordingly, Tivari et al. [2018] and Khazali et al. [2018] demonstrated that reawakening of dormant breast-cancer cells is dependent on the signaling of the inflammatory markers IL-6, IL-8 and transforming growth factor $\beta 1$ (TGFβ1). Contrary to these findings, a downregulation of CXCR4 in metastatic breast-cancer cells has been linked to a restrained proliferation, thus indicating that CXCR4 signaling is relevant for maintaining tumor cells in a proliferative state prior to dormancy entry [Nobutani et al., 2015].

A closer look on the transcriptional and translational changes, that occured upon dormancy entry and reawakening of GBM cells, revealed the discrete upregulation of *CCL2* and *SAA2* in dormant cells, which were significantly less upregulated under pro-inflammatory conditions. Likewise, reawakening of glioma cells was connected to an augmented expression of *FSTL3*, *VEGFC* and *THSD4*, while the administration of the inflammatory mediators reduced the extent of upregulation (fig. 4.3). Thus, those genes seem to be relevant for the maintenance of dormancy or reawakening, respectively.

Intriguingly, CXCL12-CXCR4 but not CXCL12-CXCR7 signaling was particularly assigned to delay the entry into dormancy, since single CXCL12 stimulation of LN229 cells with CXCR7-knock down led to a significant, reduced upregulation of *CCL2* and *SAA2*. Interestingly, this effect was only observed when signaling via CXCR7 was abolished by downregulation of the receptor (fig. 4.5C) indicating a special role of CXCR4 in glioma stem cells, in which CXCR4 is more abundant than CXCR7 [Ehtesham et al., 2009, Flüh et al., 2016]. In contrast, CXCL16 and CX3CL1 inverse signaling also had no influence (fig. 4.5D, E). Indeed, Goffart et al. [2017] and Hattermann et al. [2013] associated the CXCL12-CXCR4 signaling axis to an increased resistance of glioblastoma-stem cells to radiotherapy and chemotherapy with TMZ. As opposed to this, particularly *CXCR7* expression is correlated with an enhanced chemoresistance of colon-cancer cells co-stimulated with CXCL12 [Heckmann et al., 2014], which was neither relevant for the modification of the dormancy entrance nor reawakening of GBM cells in this study, though (fig. 4.5). In fact, CCL2 expression is correlated with tumor progression of glioblastomas [Desbaillets et al., 1994, Bowman and Joyce, 2014]. In connection to that, CCL2 secretion induces the recruitment of microglia/macrophage and T cells [Platten et al., 2003, Chang et al., 2016], that enhance the expression of pro-invasive metalloproteinases, thereby promoting tumor invasiveness [Zhang et al., 2012, Hussain et al., 2006]. Beyond that, Oh et al. [2001a] observed an increased expression of *CCL2* in glioma cells upon stimulation with CXCL12, thus assuming a potential role of CXCR4-induced upregulation of CCL2 in inflammation

and angiogenesis. Moreover, beside others, CXCR4 and CCL2 have been identified as differentially expressed genes in colon cancer metastases [Chu et al., 2017]. Besides its additional pro-inflammatory effect on microglia, autocrine SAA2 stimulation of GBM cells supports resistance to TMZ and induces stem cell marker expression *in vivo* [Facci et al., 2018, Hasan et al., 2019]. Moreover, the migratory behavior of glioma cell lines is differentially affected by long-term TMZ treatment [Adamski et al., 2017c] and CXCR4 signaling contributes to the glioma invasiveness via autocrine activation [Ehtesham et al., 2006]. Hence, along with CXCR4, CCL2 and SAA2 might regulate tumor invasiveness and also immunoediting during unfavorable conditions concerning tumor-mass expansion (fig. 5.1).

In contrast to that, inverse signaling of CXCL16 and CX3CL1 was important in the delayed exit from dormancy, shown by the decreased upregulation of *THSD4* and partly *VEGFC* (fig. 4.5D, E). Intriguingly, significant FSTL3 regulation was dependent on stimulation with all three chemokines. Although inverse signaling has been associated with enhanced proliferation and rescue from apoptosis [Hattermann et al., 2016b], CXCL16 and CX3CL1 might facilitate the plasticity of dormant tumor cells, thus contributing to the tumor's aggressiveness. An awakening or proliferation initiation of GBM cells represents an *in-vitro* model for the development of tumor recurrences *in vivo*. In quiescent GBM stem-like cells lymphangiogenic factors such as VEGFC are downregulated [Fiscon et al., 2018]. Moreover, to escape angiogenic dormancy, a persistent state of tumor growth induced by avascularity, the tumor undergoes an angiogenic switch characterized by upregulation of vessel formation (reviewed in Almog [2010]). For example, the upregulation of the vascular endothelial growth factors like VEGFA, which are essential for angiogenesis [Connolly et al., 1989, Leung et al., 1989], contribute to tumor reawakening [Tabouret et al., 2015]. Therefore, VEGFC might play similar roles. Interestingly, CX3CL1 has been described as an inflammatory mediator of angiogeneis [Szewczyk et al., 2013]. Stimulation of macrophages with CX3CL1 results in a reduced expression of *VEGFA* [Chen et al., 2018] and VEGFC as well as CX3CL1 are upregulated in spine-derived metastatic lung cancer cells [Cai et al., 2015]. Contrary to VEGFC induction, repression of thrombospondin-1 activity induces angiogenesis and proliferation in persistent tumors [Tiram et al., 2018]. Indeed, THSD4 is a protease also known as an ADAM with thrombospondin motifs-like (ADAMTSL) 6, that was upregulated in tumor reawakening (fig. 4.3). However, other ADAMs with thrombospondin motifs (ADAMTS4, ADAMTS5) positively impact the proliferation of glioma cells *in vitro* and potentially promote their invasion by cleavage of brevican, a major component of brain tissue [Held-Feindt et al., 2006, Nakada et al., 2005]. Apart from that, FSTL3 is overexpressed in invasive breast cancers [Bloise et al., 2009] and upregulation of FSTL1, a homolog, increases the TMZ resistance of GBM cells due to an enhanced expression of *MGMT* [Nie et al.,

2019] and is correlated with proliferation and colony formation [Jin et al., 2017]. Nonetheless, no correlation between CXCL16, CX3CL1 or CXCL12-CXCR4-CXCR7 and THSD4 or FSTL3 has been described, yet. Summarizing, distinct functions of VEGFC, THSD4 and FSTL3 reveal their roles in tumor progression and proliferation (fig. 5.1). Therefore, especially angiogenic factors seem to be suitable candidates for therapy improvement. Hence, different studies aim to use anti-angiogenic therapeutics like specific inhibitors and certain antibodies in order to increase the patients' survival [Okuda et al., 2017, Solecki et al., 2019]. However, a comprehensive literature research of Ameratunga et al. [2018] has revealed that anti-angiogenic therapy neither shows significant survival benefits for newly diagnosed GBM patients nor for recurrent glioblastomas compared to conventional chemotherapy. At least, the authors have claimed that treatment with the anti-angiogenic drug bevacizumab increased the progression-free survival of patients.

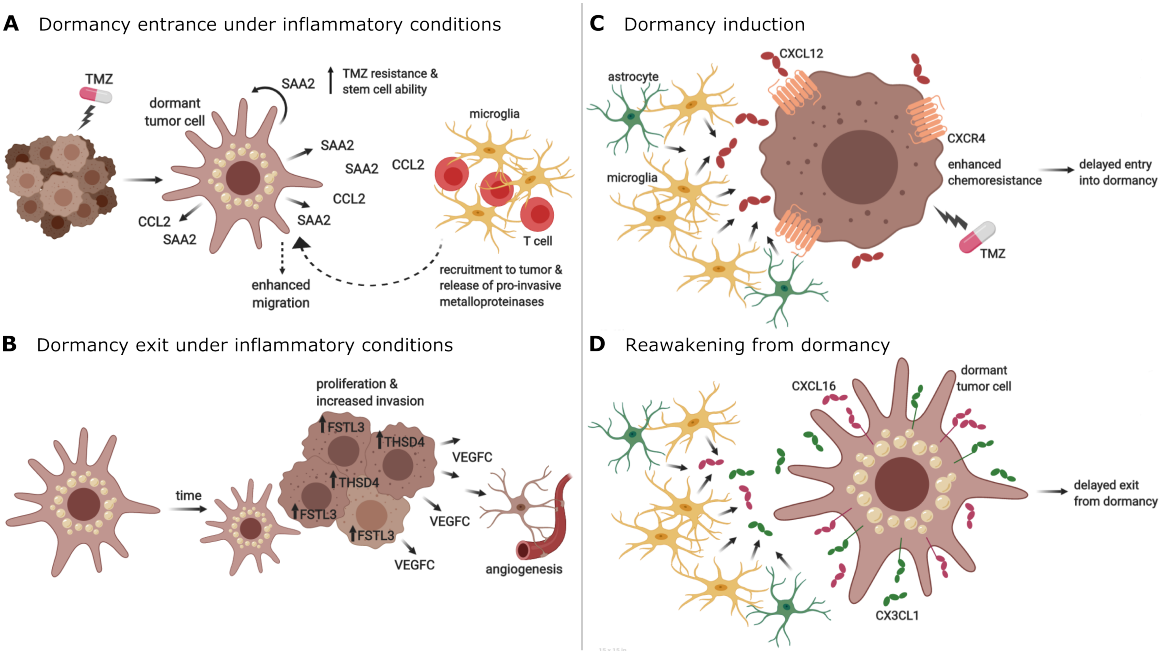

Figure 5.1: Overview about mechanisms that characterize and regulate dormancy entry and exit. The induction of dormancy is associated with increased expression of *CCL2* and *SAA2*, that recruite immune cells, which, in turn, promote tumor migration in an unproliferative state (**A**). When left untreated, persistent glioma cells start to re-initiate proliferation, which is characterized by the induction of *THSD4*, *VEGFC* and *FSTL3* supporting further proliferation and invasion as well as angiogenesis (**B**). Dormancy entry by TMZ stimulation and exit of glioma cells is modulated by the supply of chemokines by the immunological microenvironment, e.g. microglia (yellow) and astrocytes (green) (**C** and **D**).

Dormancy entrance is not restricted to classical therapy with TMZ or radiation but rather a general mechanism to adapt to various treatment regimen [Simon et al., 2018]. Furthermore, since co-stimulation with inflammatory chemokines has revealed that dormancy is also affected by the tumor microenvironment, simple *in-vitro* experiments fail to provide reliable information about therapy-escape mechanisms *in*

vivo. Therefore, new, complex systems have to be developed to give valid data about tumor dormancy. However, in the end one question remains: How to deal with tumor dormancy? In fact, different options exist: 1) Killing of all tumor cells without giving them the opportunity to enter a dormant state is almost unachievable, since tumor cells are extremely prone to adapt to environmental changes and, therefore likely escape therapy. 2) Actively inducing dormancy in tumor cells by therapy but keeping them in a dormant state as long as possible might represent an attractive possibility, since dormant tumors are not clinically relevant. Albeit some scientists have already aimed to use dormancy by hyperthermia to delay the evolving of GBM relapses [Wion, 2017], too little is known about those factors that suppress reawakening in order to successfully keep tumors in the dormant state over a long time period. 3) Actively awakening of tumor cells or reprogramming of dormancy-related pathways, in order to improve the susceptibility of tumor cells to therapy, has been intitally investigated by Tiram et al. [2018]. Nevertheless, the possibility, that the tumor progresses after dormancy entry and exit, is quite high. Hence, classical therapy might fail to successfully kill tumor cells afterwards. In conclusion, a detailed understanding of the driving forces of therapy-escape mechanisms is of high necessity and the introduction of alternative therapy approaches might improve the tumor-growth control.

5.2 Alternative chemotherapeutic approaches in a tumor model system

The general therapy for glioblastomas following maximal-safe surgical resection of the tumor involves radiation and concomitant chemotherapy with temozolomide [Stupp et al., 2005]. As stated above and by others, especially chemotherapy fails to successfully kill residual tumor cells, since the improvement of applying chemotherapy to radiotherapy with respect to the median survival of patients comprises only 2.5 months [Stupp et al., 2009].

Tumor cells are prone to adapt to therapy regimen as shown in chapter 4.1.1 and the following, e.g. by entering a resting state called cellular dormancy. Beside apoptosis [Hirose et al., 2001], another mechanism of therapy response of tumor cells includes autophagy [Paglin et al., 2001]. In fact, the induction of autophagy upon TMZ administration has already been proven by Kanzawa et al. [2004] and Carmo et al. [2011], who have further claimed that inhibiting autophagy potentially improves the sensitivity of glioma cells to TMZ. When activating autophagy, un- or misfolded proteins, that e.g. accumulate upon apoptosis induction, are cleared (for review see Lee et al. [2015c]), therefore autophagy has the potential to protect tumor cells from apoptotic cell death. In conclusion, the inhibition of autophapy-related pathways increases the sensitivity of GBM cells to TMZ, which has been already shown by Liu et al. [2013].

Hence, therapeutic compounds such as quinoline-based drugs, that act by autophagy blockage (reviewed by Solomon and Lee [2009]), e.g. by inhibiting the activity of heat shock protein family A member 5 (HSPA5) [Golden et al., 2014], a key regulator of the unfolded protein response, which is highly upregulated in glioblastomas [Lee et al., 2008], represent potential alternative targets for glioma therapy. To comprehensively study the sensitizing effects of different autophagy inhibitors, two GBM cell lines with distinct extents of the susceptibility to TMZ were chosen. Despite their distinct levels of TMZ sensitivity, both cell lines (A172 and LN229) seemed to be similarly responsive for single quinacrine, chloroquine (CQ) or hydroxychloroquine (HCQ) treatment albeit to varying degrees regarding the different drugs themselves. Quinacrine was most effective, followed by hydroxychloroquine and chloroquine (fig. 4.6). However, in order to estimate the drugs' toxicity on normal brain cells, the very same experiment was performed with astrocytes by Christina Schmitt (Institute of Anatomy) revealing a high cytotoxicity of quinacrine on astrocytes. Thus, HCQ superior to CQ was chosen for further studies. In the following, various combinatory treatment schemes of TMZ and HCQ administrations were investigated concerning their cytotoxic effects and tumor-growth control on the different chemosensitive glioma cell lines in a long-term stimulation model of three plus three days of treatment (fig. 4.7A, B, C). Comparing all results to the standard therapy with TMZ revealed a much lower cytotoxic profile of those treatment schemes, that began with HCQ. In contrast, especially treatment regimens, that started with the combined application of TMZ+HCQ followed by single TMZ or HCQ or even continued combined stimulation, were most favorable in terms of GBM cytotoxicity (fig. 4.7D). Single HCQ treatment of GBM cells was propitious to no or control stimulation, in line with results from Golden et al. [2015] but not to single TMZ application. In comparison, Golden et al. [2014] have obtained similar results for TMZ+CQ administration. Intriguingly, a clinical trial of an initial HCQ administration, followed by a combined dose-intense TMZ+HCQ treatment in advanced solid tumors has revealed a good tolerance of the therapy in patients. However, assorting to the reduced cytotoxicity of therapy schemes, that start with HCQ application (fig. 4.7D), only moderate improvements of progression-free survival have been observed [Rangwala et al., 2014]. Besides, a phase I/II trial with a combined TMZ+HCQ therapy with low doses of HCQ including radiation has exhibited an improvement in the median overall survival of two months of patients younger than 70 years compared to classical therapy regimen. As opposed to this, high doses of HCQ lead to severe side effects [Rosenfeld et al., 2014]. This implies, that toxic effects on normal tissue have to be taken into account as well when analyzing drug efficiency on tumor cells. In fact, normal astrocytes well tolerated a sequential treatment regimen of TMZ at first, followed by HCQ but not the combined application of TMZ+HCQ, that was, in turn, more promising for GBM cytotoxicity.

Moreover, all therapy schemes with an initial combined administration of TMZ+HCQ were unfavorable for astrocytes (fig. 4.7D). Therefore, the sequential approach of TMZ accompanied by HCQ treatment was determined as most beneficial in this case (fig. 5.2).

In fact, sensitization of GBM cells to chemotherapeutic treatment is not only possible through the inhibition of autophagy-related pathways, but also through the activation of autophagy-dependent apoptosis [Torres et al., 2011, Shao et al., 2019]. Since the inactivation of anti-apoptotic Bcl-2 is a crucial step in autophagic cell death [McCullough et al., 2001], AT101, which acts as a Bcl-2 homolog domain 3 (BH3) mimetic, binds and, thereby blocks Bcl-2 activation [Kitada et al., 2003]. Hence, it was chosen for further alternative chemosensitizing studies. Interestingly, AT101 exhibited high cytotoxic effects at low concentrations on both glioma cell lines, while an even greater harmful effect was observed in A172 cells, which were less sensitive to TMZ compared to LN229 cells (fig. 4.6). Moreover, an experiment with normal brain cells, performed by Christina Schmitt (Institute of Anatomy), noteworthy revealed a low cytotoxicity of AT101 on normal astrocytes. In fact, a less harmful impact on astrocytes in comparison with GBM cells has been already explored according to low concentrations of ABT-737, another inhibitor of Bcl-2 proteins [Vidomanova et al., 2016]. Thus, different therapy schemes of AT101 and TMZ were applied to both GBM cell lines according to the profiles used with HCQ and TMZ (fig. 4.7A, B, C). Intriguingly, similar effects to HCQ treatment were observed regarding those stimulation schemes, that started with AT101. In detail, single AT101 treatment as well as initial AT101 administration followed by TMZ or a combined stimulation of TMZ+AT101 affected GBM cells less than the standard TMZ application. Contrarily, first stimulating glioma cells with TMZ+AT101 accompanied by single AT101 or continued combined treatment yielded a greater cytotoxicity and better tumor-growth control compared to single TMZ stimulation. Furthermore, the therapy regimen, which began with TMZ at first, then continued with TMZ+AT101 application, was also beneficial (fig. 5.2). Interestingly, LN229 cells, more sensitive to TMZ, were less affected by this treatment scheme compared to A172, that are less sensitive to TMZ (fig. 4.7D). Accordingly, in another study, that focussed on overcoming therapy escape of glioma cells induced by TMZ, the amount of dead cells of those glioma cells, that responded to TMZ treatment to high degrees, was not increased upon co-stimulation of TMZ+AT101 after an initial period with TMZ. In contrast, A172, that were less affected by initial TMZ administration, were effectively addressed by the combined concomitant therapy of TMZ+AT101 (fig. 4.1, Adamski et al. [2017a]). Besides some trials have emphasized cytotoxic effects and molecular alterations due to singular administration of AT101 in glioma cells and tumor-stem cells [Coyle et al., 1994, Keshmiri-Neghab et al., 2014, Antionetti et al., 2017, Warnsmann et al., 2018, Meyer et al., 2018, Park

et al., 2018, Linder et al., 2019], others confirmed the sensitizing effect of AT101 to TMZ-induced cell death upon a combined application of both drugs [Voss et al., 2010, Jarzabek et al., 2014]. Intriguingly, Jarzabek et al. [2014] have reported no beneficial reduction in tumor volumes of AT101-treated mice compared to controls, which was mimicked *in vitro* by the long-term stimulation model (fig. 4.7D). However, they also have not observe a significant decrease of the tumor volume concerning TMZ+AT101 therapy compared to TMZ-treated mice but higher necrosis and reduced proliferation of cells [Jarzabek et al., 2014]. Probably, a significant effect might become visible after a longer time period as three days of administration of TMZ+AT101 did also not show any significant increase of the n-fold amount of dead glioma cells *in vitro*, while six days did (fig. 4.7D). Indeed, an initial clinical trial with recurrent glioblastoma has revealed good tolerance of AT101 therapy but only little benefits concerning tumor-growth control [Bushunow et al., 1999], which is similar to the observed poor response of both glioma cell lines to single AT101 treatment (fig. 4.7D). As AT101 represents a promising alternative therapeutic for GBM therapy, other clinical studies, that either re-investigate the effect of AT101 therapy in recurrent glioblastomas (phase II: NCT00540722) or focus on AT101 treatment additional to standard care (phase I: NCT00390403), are currently taking place. In terms of other tumors, such as small-cell lung, prostate and head and neck cancer and cortical carcinomas, AT101 administration with or without other drugs seldomly show an improvement of therapy outcome [Schelman et al., 2014, Stein et al., 2016, Swiecicki et al., 2016, Xie et al., 2019].

		n-fold amount of dead cells (TMZ = 1)			*growth rate*		
stimulus I	*stimulus II*	SVGA	A172	LN229	SVGA	A172	LN229
TMZ	TMZ	1.00	1.00	1.00	2.35	1.41	2.01
	HCQ	0.71	1.62	1.20	3.32	0.92	1.35
TMZ	TMZ	1.00	1.00	1.00	2.35	1.41	2.01
	AT101	0.84	1.64	1.67	4.14	1.57	1.84
	TMZ+AT101	0.67	2.59	1.70	3.92	1.10	1.93
TMZ+AT101	AT101	0.72	3.08	2.78	2.98	1.28	1.22

Figure 5.2: Most beneficial treatment schemes with TMZ and AT101/HCQ. A172 and LN229 glioblastoma cell lines were stimulated with TMZ and AT101 or HCQ according to various treatment schemes displayed in fig. 4.7A, B, C. Moreover, astrocytes (SVGA) were stimulated accordingly by Christina Schmitt (Institute of Anatomy). Ultimately, the n-fold cytotoxicity compared to TMZ stimulation and the growth rate were determined after six days of treatment. Benefical effects regarding tumor cells (high cytotoxicity and low growth rate) are depicted in green compared to TMZ (yellow). Likewise, favorable effects for astrocytes (low cytotoxicity and high growth rate) were colored in green compared to TMZ (yellow). Thus, the best treatment regimen is depicted in overall green colors (modified after Adamski et al. [2018]).

In fact, the most experiments focusing on cytotoxicity of drugs include stimulation of tumor cells for a maximum of 96 h without their validation in normal brain cells [Golden et al., 2015, Voss et al., 2010, Park et al., 2018, Keshmiri-Neghab et al., 2014,

Jarzabek et al., 2014]. Besides the usual administration of one drug or a combination of two ore more, that are applied simultaneously, some scientists have also investigated sequential treatment schemes [Lee et al., 2015a, Roy et al., 2015] and some extended cytotoxic studies on cells to ten and even 15 days [Lee et al., 2015a, Coyle et al., 1994, Jarzabek et al., 2014]. However, many attempts fail to reliably predict the drugs' effect on tumors *in vivo* or in patients. Therefore, the development and use of suitable drug-screening models is of high importance. Since immortalized GBM cell lines hardly resemble the multifaceted phenotypes of GBM tumors [Lee et al., 2006, Allen et al., 2016], an adaption to a more patient-derived model is the use of primary GBM cells, that originate from extracted tumor tissue from patients. Nevertheless, as GBM tumors are not only composed of tumor cells but also tumor-associated immune cells such as microglia and astrocytes, that affect each others behavior (reviewed in Quail and Joyce [2017]), co-culture systems of glioma cells, astrocytes and microglia are preferable. Besides the employment of cell-conditioned medium on other cell cultures providing cell-specific, released factors [Oliveira et al., 2017], transwell or boyden chamber experiments [Rath et al., 2015, Kenig et al., 2010], in which different cell types are co-cultivated with indirect contact to each other model cell communication more effectively if direct co-cultivation is difficult to achieve due to different HLA profiles of cells.

In order to test the appropriate sequential drug-stimulation scheme (simultaneous application of TMZ+AT101 for three days followed by single AT101 treatment), that has been evaluated most promising for two GBM cell lines and astrocytes before (fig. 4.7, 5.2, Adamski et al. [2018]), *in vitro* closer to *in-vivo* conditions, a co-culture model with primary GBM cells, microglia and astrocytes was established. Hereby, the cell-to-cell ratios were calculated according to assessed data about tumor sizes, cell compositions in glioblastomas and grade of resection (cf. chapter 3.2.1.5.2, Murray [2012], Roggendorf et al. [1996], Zeiner et al. [2018], Bette et al. [2018], Kreth et al. [2013]). In general, the applied sequential drug-stimulation scheme was efficient in killing of tumor cells and in tumor-growth control with respect to both primary cultures (fig. 4.8). Intriguingly, both primary GBM cells were associated to distinct molecular profiles, that are related to the mesenchymal and proneural GBM subtype (supplementary fig. A.1, Verhaak et al. [2010]) and both reacted to different degrees to the treatment. Comparing mono-culture to co-culture results revealed a slight reduction albeit not significant in the percentage of dead primary GBM cells when co-cultivated with astrocytes and microglia, hinting to a protective effect of astrocytes and microglia concerning therapy cytotoxicity on glioblastomas (fig. 4.8A, B). Indeed, the tumor microenvironment not only promotes tumor invasion, growth and progression [Oliveira et al., 2005, Hoelzinger et al., 2007, Bettinger et al., 2002], but also either directly or indirectly contributes to the resistance of tumor cells to

therapy. In particular, co-culture experiments with astrocytes have revealed that the cross-communication between astrocytes and GBM cells, especially via gap junctions [Lin et al., 2016], decreases the sensitivity of tumor cells to chemo- and radiotherapy [Chen et al., 2015, Yang et al., 2014, Rath et al., 2015]. In addition, a study with microglia-conditioned medium has shown an increased chemo-radioresistance of glioma cells by creating a glioma stem cell niche [Hide et al., 2018], while the reduction of the recruitment of microglia to tumors *in vivo* decreases radioresistance of glioblastomas [Chiblak et al., 2019]. A closer look on cell-death initiation in normal brain cells showed, that mono-cultured astrocytes were moderately affected by the applied treatment regimen. Interestingly, the percentage of dead cells was significantly elevated by co-cultivation with tumor and microglial cells not only regarding the chemotherapeutic stimulation but also in controls (fig. 4.8A, B). This implies that gliomas cells might not only be protected against therapy by astrocytes and microglia, but also, in turn, affect the viability of astrocytes, in general, and especially during drug administration. In fact, glioblastoma cells activate astrocytes to acquire a reactive phenotype, which is advantageous for tumor invasion and growth [Le et al., 2003, Taheri et al., 2018]. Hence, in case of an incomplete resection of the tumor with many residual tumor cells, the progression-free and overall survival of patients is considerably lower than in terms of a complete resection [Bette et al., 2018, Kreth et al., 2013, Chaichana et al., 2014]. Furthermore, Tang et al. [2019] have observed an improved progression-free survival and seizure control after surgery in low-grade glioblastomas based on the extent of resection implicating that remaining tumor cells might have a bystander effect on resident astrocytes manifested in the patients performance. Accordingly, the progression-free survival is associated to the distance of the re-emerging tumor from the original tumor margin zone [Rapp et al., 2017]. This bystander effect has been also observed *in vitro* in terms of an increased amount of double-strand breaks in astrocytes, that have been incubated with conditioned medium from previously-irradiated glioma cells [Burdak-Rothkamm et al., 2007]. In conclusion, the co-cultivation of primary GBM cells with astrocytes and microglia revealed an enhanced chemoresistance of glioblastoma cells mediated by the presence of these two cell types. *Vice versa*, the existence of tumor cells facilitated cell death of astrocytes, especially with respect to therapy (fig. 5.3).

The co-culture model used in this study includes the communication of different cell types in a surgical-relevant manner, which better predicts *in vivo* responses compared to mono-culture systems. However, when investigating new treatment approaches, the way of application of drugs plays an important role. In order to reach those concentrations of therapeutics, that are toxic to tumor cells *in vitro*, in the tumor tissue *in vivo*, much higher amounts of drugs have to be administered since the blood-brain barrier heavily restricts molecules from their entrance into the brain (reviewed in

[Bernacki et al., 2008, Wilhelm et al., 2011]). In order to estimate or circumvent the limitation of blood-brain barrier transport for drugs, either complex tumor models have to be used [Zhang et al., 2016, Brown et al., 2016, Wang et al., 2017d] or other drug application systems have to be chosen.

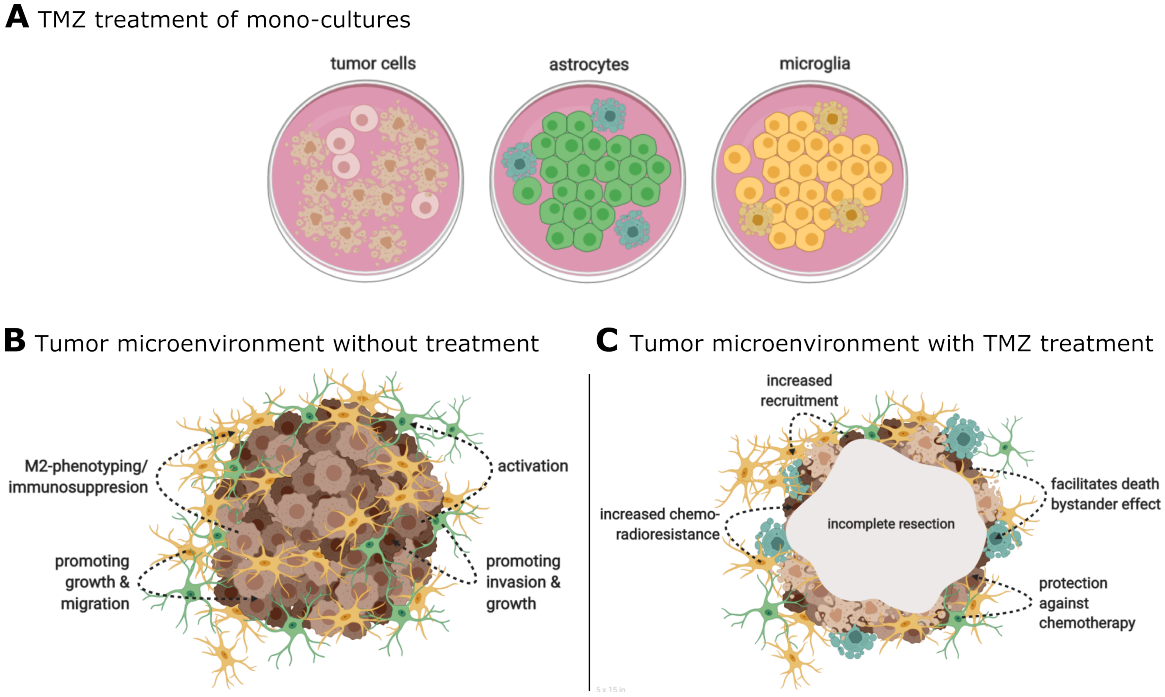

Figure 5.3: Applicability of the co-culture model: Cross-influences of tumor cells, astrocytes and microglia. When treated with TMZ as standard chemotherapeutic, tumor cells react to a high degree in mono-culture systems. Compared to this, astrocytes and microglia are moderately or or slighty affected (**A**). However, the tumor cells, astrocytes and microglia influence each other by different mechanisms (**B**). Upon the application of the chemotherapeutic the tumor cells promote an increased cell death of astrocytes compared to mono-culture systems. Moreover, astrocytes and microglia contribute to the protection of the tumor cells against chemotherapy (**C**).

5.3 Nanoparticles as drug stabilizers and therapy improvement

As described above, a major limitation in GBM treatment is the blood-brain barrier, that regulates the passaging of molecules. Hence, and due to a typically significant clearance of the therapeutic, a high amount of drug has to be administered systemically, in order to reach cytotoxic concentrations in the brain. This, in turn, often leads to severe side effects, as described for TMZ [Trinh et al., 2009]. Temozolomide is given orally at initial concentrations of 75 $\frac{\text{mg}}{\text{m}^2}$ per day accompanied by radiotherapy. Afterwards, patients receive $150 - 200\,\frac{\text{mg}}{\text{m}^2}$ per day without radiation [Stupp et al., 2005]. Despite such high doses, a measurement of the TMZ concentration in the CSF has revealed that only 1 $\frac{\mu\text{g}}{\text{ml}}$ reach the tumor cells, while a concentration of up to 14 $\frac{\mu\text{g}}{\text{ml}}$ was measured in blood plasma [Ostermann et al., 2004]. In order to increase the transport of therapeutic molecules across the blood-brain barrier and potentially influence the drug diffusion in brain tissue, encapsulation of drugs into nanoparticles represents an

useful opportunity [Ahirrao and Shrotriya, 2017, Zhu et al., 2019, Nance et al., 2012]. In the case of glioblastoma therapy, manifold approaches regarding nanoparticle application have been already clinically investigated. On the one hand, the toxicity and pharmacokinetics have been assessed in patients with recurrent glioblastomas intravenously receiving irinotecan encapsulated in liposomes yielding no unexpected toxic profiles upon intravenous administration [Clarke et al., 2017]. Equally, liposomal irinotecan has been applied by convection-enhanced delivery in order to analyze the safety and efficiency of this application technique [Butowski et al., 2014]. However, final results have not been provided, yet. Beyond that, a clinical phase II trial has been performed in patients with newly-diagnosed GBMs, who have been treated by classical radio- and chemotherapy plus PEGylated liposomes encapsulating doxorubicin. Albeit only a slight increase in the overall survival (17.6 months) has been observed compared to the conventional therapy, the treatment has been well tolerated [Beier et al., 2009], thus underlining the potential of the use of nanoparticles for GBM treatment.

Besides the applicability of nanoparticles for an improved passaging of drugs across the blood-brain barrier, in particular highly-ordered, cubic nanostructures called cubosomes display advantages in stabilization of chemically instable molecules as well as in enhancement of bioavailability of the drug [Ali et al., 2017, 2016]. This is especially relevant in terms of TMZ and AT101 for therapeutic use. Indeed, TMZ is a pro-drug, that is rapidly metabolized to its active form, MTIC, by hydrolysis at neutral to basic pH [Denny et al., 1994, Andrasi et al., 2010, Lopes et al., 2013]. A chemical change of the molecule was visualized spectrophotometrically by a shift of the absorption maximum (fig. 4.9A). Surprisingly, chemically altered TMZ had almost no cytotoxic effect on primary GBM cells, while freshly supplied TMZ greatly induced cell death in primary GBM cells (fig. 4.9B, D). In fact, after oral administration of TMZ, it is processed to MTIC within 2 h [Lopes et al., 2013]. Moreover, MTIC is known to be poorly able to cross the blood-brain barrier [Meer et al., 1986], which is explained by a low affinity of MTIC to biological membranes, therefore passaging across the blood-brain barrier is restricted [Ramalho et al., 2019]. Assuming that TMZ was processed to MTIC might also clarify the decreased cytotoxic effect of metabolized TMZ on primary GBM cells, as the converted form might not able to be taken up by cells anymore. Several attempts have been made by other researchers to prolong the stability of TMZ using nanoparticles without clinically relevant approaches, yet [Nordling-David et al., 2017, Appel et al., 2012].

In contrast, AT101 is not further converted at physiological conditions (fig. 4.9C, Jia et al. [2008]) and the cytotoxicity of preincubated AT101 on primary GBM cells could be partly sustained (fig. 4.9B, D). The slight reduction of its cytotoxicity on 116/14 cells might be explained by the high affinity of AT101 to bind to blood-plasma pro-

teins [Dabrowski et al., 2001, Cater and Lyman, 1969] since the cultivation medium, in which AT101 was preincubated, contained carbohydrates, peptides, vitamins and fetal bovine serum (cf. chapter 3.2.1.1). This potentially resulted in a reduced uptake into 116/14 cells or a decreased ability to initiate cell death. Beyond that, AT101 is rapidly eliminated in the body when applied orally or intravenously [Wu et al., 1986]. On that basis, nanocarrier systems, especially cubosomes, have the potential not only to improve blood-brain barrier passaging, but also to inhibit binding of AT101 to proteins and increase its low bioavailability and solubility in aqueous solutions.
Accordingly, AT101 was encapsulated in cubosomes to 10% (w/w) using glyceryl monooleate (GMO) and pluronic F-127 and the top-down approach described by Ljusberg-Wahren et al. [1996], Akhlaghi et al. [2016]. Besides the high loading capacity of this system for AT101 in comparison with other attempts [Ali et al., 2016, 2017], the entrapment efficiency of AT101 was over 97%, which was comparable to other approaches using GMO cubosomes incorporating hydrophobic drugs [Ahirrao and Shrotriya, 2017, Badie and Abbas, 2018, Ali et al., 2017, Elnaggar et al., 2015], while encapsulation of hydrophilic compounds yields lower entrapment efficiencies [Nasr et al., 2015]. In comparison to other nanoparticle formulations, loading of AT101 was quite efficient [Zhai et al., 2008, Li et al., 2011a, Jin et al., 2015], thus providing the basis for the beneficial use of nanocarrier systems in AT101 application. However, as it is not clear, whether AT101 is actually trapped in the lipid bilayer of GMO cubosomes or only attached to the particle's surface, further experiments including nuclear magnetic resonance (NMR), self-diffusion analysis and small angle X-ray scattering (SAXS) and others might unveil the binding or entrapment character. Intriguingly, loading of AT101 led to a structural change in GMO cubosomes showing that AT101-loaded nanoparticles were smaller in size compared to unloaded counterparts (fig. 4.10). This was additionally confirmed by DLS measurements. Nevertheless, the small polydispersity index, indicative for homogeneous particles in solution, was comparable to other studies [Ahirrao and Shrotriya, 2017, Abdelrahman et al., 2015]. On top of that, initially indicated by the decreased ζ potential of AT101-loaded cubosomes compared to blank ones (tab. 4.1), those nanoparticles, that encapsulated AT101, showed a long-term stability at 37°C for 17 days, whereas blank cubosomes changed in size and Z-average already after three days of storage at 37°C (fig. 4.11A). Assuming that AT101 directly or indirectly interacts with the monooleate chains, which potentially leads to a structural change, thereby presenting more negatively charged side chains on the outer surface of cubosomes, might explain the lower ζ potential. As the ζ potential is a parameter for the repulsion of neighbored particles [Joffe and Mudd, 1935, Heiati et al., 1998], clustering of highly charged cubosomes is relatively uncommon, thus the overall structure and distribution of the nanocarriers in solution was stable. Interestingly, a high negative charge

of nanoparticles loaded with AT101 as well as an increase in stability due to AT101 encapsulation has been also observed by others [Liu et al., 2014, Zhai et al., 2008, Shen et al., 2018]. Based on this, the DSC thermogram of blank GMO cubosomes showed no significant phase transition between 15°C and 80°C, in general, but a closer look revealed a very small peak between 22°C and 24°C, which disappeared in the thermogram of GMO-AT101 cubosomes (fig. 4.11B, C). This also hinted at the stabilization of cubosomes upon AT101 loading. Nonetheless, it has to be elucidated, which portion of the blank GMO cubosomes sample melts or crystallizes at approx. 23°C. In summary, the GMO-cubosome system is characterized by a high stability in solutions, in general [Ali et al., 2016, Badie and Abbas, 2018], which was even enhanced upon AT101 loading, thereby representing a suitable system for tumor therapy.
To allow for cell-death initiation by the therapeutic compound, the release kinetic was determined in artificial CSF solution resembling the brain liquor. Up to 34.79% of AT101 was released over 72 h, which followed the Higuchi release kinetic (fig. 4.12). Especially in liposomes and micelles, incorporating AT101, higher release rates have been often described [Zhai et al., 2008, Cho et al., 2013, Liu et al., 2014]. Compared to cubosomes loaded with other contents, the release of components also was noteably higher than with GMO-AT101 particles [Elnaggar et al., 2015, Badie and Abbas, 2018, Ali et al., 2016, Ahirrao and Shrotriya, 2017]. However, slow release of therapeutics is prefered, as those nanocarriers are generally administered orally or intravenously, at first, circulating through the blood until they reach their destination, at which a sustained and prolonged release of drug has to be guaranteed. Besides an improved transport across the blood-brain barrier, nanoparticles, especially cubosomes, show a good brain tissue penetration [Ahirrao and Shrotriya, 2017, Zhu et al., 2019, Nance et al., 2012]. In line with that, GMO-AT101 cubosomes exhibited a good uptake in 3D glioma spheroids and also in 2D cell layers (fig. 4.13A, B). Finally, cytotoxic studies on glioma and normal brain cells revealed interesting effects of GMO-AT101 cubosomes compared with freely administered AT101. In terms of two glioblastoma cell lines, encapsulation of AT101 was beneficial for cell-death initiation as low concentrations of GMO-AT101 significantly decreased the n-fold viability of tumor cells compared to free AT101 treatment of two different glioma cell lines (fig. 4.13D). Based on this, an earlier induction of cytoskeletal rearrangement, indicated by actin agglomerisation and reduction of actin filaments, upon GMO-AT101 stimulation compared to free AT101 was observed within the first six hours (fig. 4.14) suggesting apoptosis induction. On mRNA level, *ACTB* downregulation was confirmed after 24 h of GMO-AT101 administration (fig. 4.14). Indeed, free AT101 application also yielded decreased expression of *ACTB* in LN229, which was associated to actin filament condensation observed on protein level (fig. 4.14A). Moreover, *MAP2* downregulation of GMO-AT101-stimulated cells (fig. 4.14) demonstrated a disruption of microtubule structures

[Zhang and Dong, 2012], thereby probably indirectly indicating cell-death initiation [Uzdensky et al., 2012]. Stimulation with blank cubosomes also led to reduced levels of *MAP2* and *ACTB* (in case of A172 cells), though. Thus, transcriptional changes of cytoskeleton-associated genes might be influenced by nanoparticles themselves, while relevant rearrangement of the cytoskeleton due to treatment of cells with encapsulated AT101 might only occur on protein level. Furthermore, *CDKN1A* was upregulated in AT101-stimulated LN229 cells but not with GMO-AT101 treatment. Nonetheless, elevated expression of *CDKN1A* is associated to therapeutic-induced cell-cycle arrest in glioma and lymphoma cells (supplementary fig. A.4, Hirose et al. [2001], Marches et al. [1998, 1999]), which has been already observed in AT101-treated melanoma cells [Jang and Lee, 2014]. Thus, encapsulation of AT101 might trigger cell death differently, circumventing a potential dormancy entry via CDKN1A. Interestingly, nanoparticle approaches of AT101 in liposomes, micelles and polymeric capsules have not shown increased cytotoxic effects of encapsulated AT101 *in vitro* [Jin et al., 2015, Zhai et al., 2008, Liu et al., 2014, Cho et al., 2013], so far. At least tumor-growth control has been established by multi-drug loading and functionalization of particles [Heleg-Shabtai et al., 2016, Shen et al., 2018, Liu et al., 2014, Cho et al., 2013]. However, no experiments with healthy tissue have been performed *in vitro*. With this nanoparticle formulaton, the viability of astrocytes (SVGA) and microglia (HMC3) was retained when treated with GMO-AT101 compared to controls (fig. 4.13D). In general, the cellular uptake of those cubosomes in astrocytes and microglia was assumed to be similar. Nevertheless, the interaction of GMO cubosomes is dependent on the lipid character of the membrane [Jablonowska et al., 2016], which is certainly different in normal brain from those in glioma cells [Slagel et al., 1967, Martin et al., 1996]. Hence, nanoparticle uptake might be impaired in astrocytes and microglia. Furthermore, albeit AT101 was continuously released from nanoparticles outside of the cells, some cubosomes were internalized into cells, thereby probably improving the cytotoxic effect of AT101 in case of GBM cells. The internalization of cubosomes is associated to endocytic pathways [Abdel-Bar and El Basset Sanad, 2017]. Thus, detailed studies on the uptake mechanism of GMO-AT101 cubosomes into normal brain cells might give insights into the uptake efficiency of such nanoparticles in astrocytes and microglia. In brief, GMO-AT101 cubosomes showed an augmented cytotoxic effect on glioma cells, while astrocytes and microglia were less harmed. Therefore, they represent a promising basic tool for an alternative GBM therapy.

For the application of such nanoparticles in glioblastomas, different attempts have been investigated so far. In general, passive targeting of nanoparticles of approx. 100 nm size is guaranteed by the enhanced permeability and retention effect in tumor tissue due to an abnormal vasculature (reviewed by Maeda et al. [2013]). In conformity, an improved uptake of cubosomes with different loads has been observed using

an *in-situ* gel and intranasal application [Ahirrao and Shrotriya, 2017, Patil et al., 2018]. Moreover, the incorporation of Tween-80 into cubosomes not only stabilizes those [Azhari et al., 2016], but also augments the transfer of compounds to the brain [Kreuter et al., 2003, Abdelrahman et al., 2015, Elnaggar et al., 2015], thereby representing an active-targeting tool for drug delivery. In fact, active targeting upon functionalization of nanoparticles is often favored. However, a comprehensive literature report of Wilhelm et al. [2016] about the overall efficiency of nanoparticle application *in vivo* concerning solid tumor therapy has shown that less than 1% of particles on average independent of tumor type and functionalization are effectively delivered. Hence, new targets and more detailed experiments are necessary to achieve the clinically relevant use of nanoparticles.

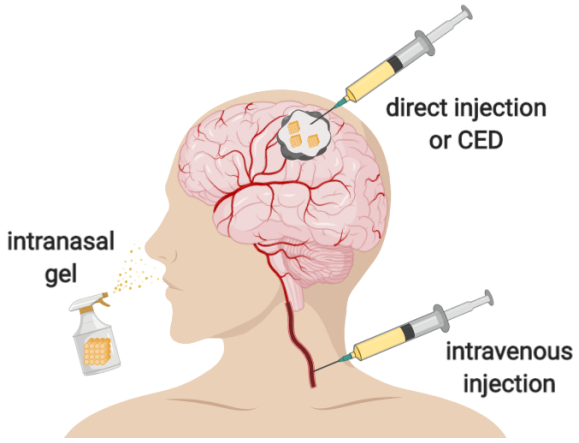

Figure 5.4: Application routes for produced AT101 nanoparticles (CED = convection-enhanced delivery).

5.4 Implant development for local GBM-therapy application

In order to circumvent the limited transport efficiency of molecules to the tumor tissue, several methods have been developed for local application of therapeutic compounds and also nanocarriers. Beside the direct injection of therapeutics into the ventricles via catheter implants, that carry many disadvantages [Fetell et al., 1990, Torres et al., 2008, Saw et al., 1989], a pressure-driven direct application of compounds including nanoparticles has been preclinically tested e.g. with liposomal TMZ [Nordling-David et al., 2017] or cisplatin-loaded polypeptides [Zhang et al., 2017]. A clinical trial with carboplatin has shown an improvement of the therapy outcome in patients with recurrent GBM using convection-enhanced delivery [Barua et al., 2016]. Nevertheless, backflow causing neurotoxicity and drug leakage with a rate of approx. 20% are common adverse effects of using CED [Kunwar et al., 2007, Varenika et al., 2008]. Therefore, the surgical implantation of devices releasing therapeutics in a controlled manner into the tumor cavity seems to be a promising approach, in order to avoid side effects of catheter-based techniques.

In 1991, Brem et al. [1991] have introduced a polyanhydride co-polymer incorporating BCNU, that has been FDA approved for the treatment of recurrent and primary glioblastomas in 1997 and 2003. The sustained release of the drug is guaranteed by the degradation of the polymer. In monkeys, cytotoxic levels of carmustine have been detected for at least 21 days including a burst release of over 75% within the first seven days [Fung et al., 1998]. This and the poor distribution of drug into the surrounding tissue [Fung et al., 1998] might have caused the reported, ambiguous effects in patients receiving standard radio- and chemotherapy plus implantation of the BCNU wafer [McGirt et al., 2009b, Noël et al., 2012].
Nonetheless, implantation of materials with a degradation-dependent drug release is still an appealing technique to overcome mentioned limitations of drug delivery. Additionally, Brem et al. [2007] have demonstrated that the local application of TMZ by polymer wafers reduces its plasma concentration compared to oral administration of TMZ, thus guaranteeing a better control of side effects. Indeed, manifold formulations of polymers and liposomes have been investigated aiming at a controlled and sustained drug release superior to the approved Gliadel® wafers. Especially hydrogels have been used according to their variable characteristics including thermoreversability, which makes it easy to implant those hydrogels, as they just solidify at body temperature, e.g. ReGel™ (Arai et al. [2010], reviewed in Elstad and Fowers [2009]). Other approaches involve distinct compositions of one or more polymers forming fibers, that are ultimately pressed into discs, sheets or wafers. Upon further processing, the drug release is adjusted in terms of a sustained release for up to 80 days *in vitro*, respectively 30 days *in vivo* with a moderate burst effect, depending on the applied polymer [Ranganath and Wang, 2008, Ramachandran et al., 2017]. Despite innovative ideas, for example to grow the hydrogel within the tumor cavity upon photopolymerization, release measurements have revealed a continuous release over just one week [Zhao et al., 2018]. Moreover, almost all promising attempts have shown an improved tumor-growth control compared to untreated or resected control animals [Bastiancich et al., 2018, Zhao et al., 2018, Arai et al., 2010, Ranganath and Wang, 2008, Ramachandran et al., 2017], but a comparative analysis to standard therapy including radio- plus concomitant chemotherapy is missing. Apart from this, a paclitaxel-loaded thermosensitive hydrogel called OncoGel™ maintains the drug release for 50 days *in vitro* and demonstrats a great benefit in the overall survival of unresected gliosarcoma-bearing rats compared to radiation and classical chemotherapy [Zentner et al., 2001, Vellimana et al., 2013]. An additional, local application of TMZ in dextran carriers (Temodex) to standard radio- and chemotherapy yields an enhanced survival of patients in a phase II clinical trial [Karlsson et al., 2019]. However, as those polymer approaches rely on the degradation-dependent release of therapeutics, their long-term applicability is limited. Furthermore, a comparison

between hydrogel implantation and standard therapy is often lacking, hypothesizing that those local approaches might not be favorable against oral TMZ administration. Hence, alternative devices for local GBM therapy have to be developed.

Beside the mentioned polymer-based approaches used in glioblastoma research, especially pure metals and metal alloys containing e.g. gold, silver, titanium or zinc are used for biomedical engineering. In particular zinc-based materials are applied for vascular stents or medical sutures due to their biocompatibility, low reactivity and slow degradation rate (reviewed by [Seitz et al., 2015, Mostaed et al., 2018]). On top of that, zinc oxide cements are routinely used in dentistry, displaying a long-term stability without medical complications [Woelber et al., 2016]. Therefore, a 3D network build of ZnO tetrapods was provided by Florian Rasch (Institute for Materials Science, fig. 4.15A) and loaded with different compositions containing AT101 as a promising alternative therapeutic for glioblastoma therapy as shown in previous experiments (cf. chapters 4.2, 4.3.2). The template was composed of an interconnected tetrapodal ZnO network and characterized by a high drug-loading capacity due to its great surface-to-volume ratio and large free-volume space with 94.7% porosity [Mishra et al., 2015, 2013]. Upon exposure of the ZnO template to cultivation medium for 72 h at 37°C/5% CO_2, Zn^{2+} ions were rapidly released until a saturated concentrations of approx. $15\,\frac{\mu g}{ml}$ was reached (fig. 4.15B). The release of Zn^{2+} ions from pure Zn materials, Zn alloys and ZnO-based devices [Towler et al., 2004] upon corrosion is a common effect associated to the biodegradability of such implants (reviewed in Seitz et al. [2015], Mostaed et al. [2018]). Thereupon, comparable results have been published by Choi et al. [2015], who have observed a burst release of $8 - 20\,\frac{\mu g}{ml}$ Zn^{2+} ions after 24 h from ZnO thin films of different thicknesses. While Choi et al. [2015] have reported no influence of released Zn^{2+} on the proliferation of glioma cells after 48 h of stimulation, a slight dose-dependent effect on the viability of primary GBM 118/04 cells was observed after six days of administration of conditioned medium from ZnO templates but not on 116/14 and 27/07 cells (fig. 4.15C). Indeed, ZnO nanostructures have been diversively tested for their applicability in GBM therapy. Even though some studies on ZnO nanoparticles of different architecture have revealed cell-selective cytotoxicity of ZnO with a high sensitivity on glioma cells compared to astrocytes or fibroblasts [Sruthi and Mohanan, 2015, Wahab et al., 2016, Ostrovsky et al., 2009, Akhtar et al., 2012], Kim et al. [2014] and Papavlassopoulos et al. [2014] have claimed, that the cytotoxic effect of ZnO nanoparticles is associated to the particles themselves but not to Zn^{2+} ions as stimulation with zinc cloride ($ZnCl_2$) has a lower or even no effect on the cell viability of GBM cells and fibroblasts. Accordingly, Haase and Beyersmann [1999] have proven that the uptake of Zn(II) did not necessarily correlate with an increased cell death in rat glioma cells. Hence, singular stimulation with ZnO might not be

sufficient for GBM treatment. However, the tetrapodal ZnO network was initially established for its use as drug-loadable scaffold with AT101. Thus, the effect of ZnO-conditioned medium plus direct AT101 application was investigated, revealing slight synergistic, cytotoxic effects on primary GBM cells at low Zn^{2+} concentrations ($< 5\,\frac{\mu g}{ml}$). Surprisingly, at higher concentrations of Zn^{2+}, the cytotoxic effect of AT101 was reduced (fig. 4.15C). In fact, Zn(II) abolishes apoptotic cell-death initiation induced by Cadmium and irradiation at concentrations around $10\,\frac{\mu g}{ml}$ [Sellins and Cohen, 1987, Ishido et al., 1995]. In case of AT101 co-application, complexation or other chemical reactions with Zn as catalyst might cause the impaired biological activity of AT101 [Pasha et al., 2010, Kenar, 2006]. Hence, in order to decrease the release of Zn^{2+}, the ZnO template was covered by a biocompatible PLCL film, which is often used in tissue engineering [Jeong et al., 2004, Vaquette et al., 2008]. Additionally, AT101 was incorporated into this film to allow for a homogeneous distribution of the drug across the scaffold and to initially determine the drug release from such a 3D network (fig. 4.16A). However, the reduction of Zn^{2+} release was barely successful, since approx. $8 - 10\,\frac{\mu g}{ml}$ Zn^{2+} were detected every 48 h (fig. 4.16B). On top of that, an extreme burst release of AT101 ($32.9\,\mu$M) was observed within the first 48 h, rapidly decreasing to $7.1\,\mu$M and $1.3\,\mu$M afterwards (fig. 4.16B). The burst concentration exceeded the therapeutically relevant concentration of AT101 by 13-fold, whereas $1.3\,\mu$M, measured after six days, was only half of the anti-tumorigenic concentration. Accordingly, stimulation of primary glioblastoma cells by indirect contact to the ZnO-AT101-PLCL template only yielded a moderate tumor-growth control, as large proportions of the cells heavily died after 48 and 96 h but slightly recovered thereafter (fig. 4.16C). In comparison to that, Zheng et al. [2018] have also reported little or no improvement of the cytotoxicity of TMZ when loaded onto ZnO nanoparticles on human glioma cells. In conclusion, the effect of Zn was controversial not only because of its ambiguous cytotoxic effect on glioma cells, but also due to a reported high toxicity on e.g. fibroblasts, smooth muscle cells and aortic endothelial cells [Shearier et al., 2016, Wang et al., 2014, Sharma et al., 2017] as well as astrocytes and microglia at low concentrations. As decreasing the release of Zn^{2+} ions, in order to simply use it as scaffold for drug loading without additionaly therapeutic relevance, was not successful, the tetrapodal ZnO network was not used furtheron.

Nevertheless, the ZnO template display superior physicochemical properties advantageous for drug delivery due to the interconnected arms of the ZnO tetrapods. As demonstrated by Florian Rasch (Institute for Materials Science, unpublished), the porous structure was retainable by covering of the ZnO network with different polymer solutions (already shown for carbon nanotubes [Schütt et al., 2017] and silicon [Hölken et al., 2016]). Therefore, in order to create a porous scaffold out of

a non-biodegradable material for long-term stability, the free volume of the ZnO network was filled with PDMS and the ZnO was etched out, leaving a PDMS template with hollow channels (performed by Florian Rasch, Institute for Materials Science, fig. 4.18A). In fact, 3-dimensional networks are propitious for controlled drug-release studies. Even though many approaches are based on different biodegradable polymers forming hydrogels or nanofibers [Zhao et al., 2018, Ramachandran et al., 2017, Ranganath and Wang, 2008], porous networks and grids of cross-linked filaments or sheets of PDMS have been already produced by either 3D printing or chemical approaches for drug delivery and tissue engineering [Holländer et al., 2017, Wrzeszcz et al., 2014, Pedraza et al., 2013, Varshney et al., 2019]. To estimate the drug-loading capacity and control the drug release, the porosity of the sample is an important factor. With the approach of Florian Rasch (Institute for Materials Science) various porosities were easy to establish, since they only depended on the amount of ZnO tetrapods used to fabricate the template. By this means, different channel densities or porosities of the PDMS channels were tested regarding their drug-loading capability and release kinetics with the focus to achieve therapeutic relevant concentrations for *in-vitro* experiments, that were determined before (cf. chapters 4.2, 4.3.2). Noting that the detection limit of AT101 laid at approx. $1\,\mu$M, reliable results were only obtained with respect to high channel densities ($> 1.2\,\frac{\mathrm{g}}{\mathrm{cm}^3}$). In case of low channel densities ($< 1.5\,\frac{\mathrm{g}}{\mathrm{cm}^3}$), high concentrations of AT101 in the stock solution ($> 5\,$mM) had to be used to gain reliable data. Indeed, therapeutically relevant concentrations were measured 72 h regarding $2.7\,\frac{\mathrm{g}}{\mathrm{cm}^3}$-channel density loaded with 5 to 10 mM AT101 (fig. 4.18D, E). However, almost 40% of the drug were already released concerning 5 mM infiltration solution and $2.7\,\frac{\mathrm{g}}{\mathrm{cm}^3}$-channel density (supplementary fig. A.5) indicating a short-term availability of the drug. Loading of higher amounts of AT101 (10 and 25 mM) yielded even higher release rates (67% and 90%, respectively, supplementary fig. A.5, left), which resulted in AT101 concentrations, that are known to be toxic for healthy brain tissue (fig. 4.18B, right and chapter 4.3.2). Since decreasing the channel density did not lead to a slower release of the drug, but was rather associated with a great burst effect followed by plateau (supplementary fig. A.5, right), controlling the release in networks with $2.7\,\frac{\mathrm{g}}{\mathrm{cm}^3}$-channel density by alterations of the surface of the scaffold is favorable. Moreover, those are also characterized by a great drug-loading potential, as they have the highest porosity (48.1%). In fact, other techniques, e.g. 3D printing of layers, are used to achieve long-term release of drugs from PDMS scaffolds, that are crosslinked by UV light, leading to 20% release of prednisolone within 28 days [Holländer et al., 2017]. Furthermore, solvent casting and leaching methods yield 85% porosities and a prolonged release of dexamethasone for 30 days [Jiang et al., 2017, Pedraza et al., 2013]. However, burst effects and stucked release has not been prevented [Frei et al., 2018]. In fact, the restrained release of gossypol

from a chitosan-coated nanofibrous poly(L-lactide-co-D,L-lactide) implant after 7 h (15%) has been adjusted by introducing PEG into the matrix (55%). Nevertheless, the maximal release of 15% or respective 55% is already reached after approx. $2-4$ h accompanied by a plateau [Ignatova et al., 2012, 2014]. As burst effects are also common in case of degradable polymer implants including the Gliadel® wafer [Zhao et al., 2018, Menei et al., 2005, Fung et al., 1998, Ranganath and Wang, 2008], release control still represents a major obstacle. In terms of PDMS filaments, Wrzeszcz et al. [2014] have been able to reduce an initial burst of dexamethasone by coating their cochlear implant with a biodegradable hydrogel. Additionally, the hydrogel coating or surface modifications prevents cell and protein adhesion, thereby minimizing the possibility for an inflammatory reaction and increasing the biocompatibility of the scaffold [Wrzeszcz et al., 2014, Dalu et al., 2000, Xue et al., 2017]. In conclusion, homogeneous PDMS networks with a high drug-loading capacity (48.1% porosity) and a short-term drug delivery were successfully produced. Beyond that, several coatings e.g. with hydrogels, degradable polymer barriers or closing of open pores within the PDMS matrix might prolong the drug release.

In summary, this study provided insights into chemotherapeutic-related resistance mechanisms of glioblastomas called tumor dormancy, that might play an important role in the tumor aggressiveness and the progression of tumor recurrences after treatment. In fact, GBM cells were shown to adapt to administration of TMZ by entering a resting state (dormancy) waiting to reawake and develop a tumor relapse. Hereby, specific markers were identified, that characterized dormancy entry and exit. Especially, knowledge about the triggers for dormancy escape would offer new treatment strategies for glioblastomas, that might consider tumor-growth control by the suppression of tumor reawakening over an extended time period. As this study revealed that inflammatory molecules cause a delayed entry into and exit from dormancy and since the tumor microenvironment is essential for tumor maintenance, progression and also forces the acquisition of chemoresistance, uncovering the distinct roles of non-tumorous cells in terms of therapy-escape mechanisms, e.g. by *in-vitro* co-culture models, might help to develop new treatment approaches.
In addition, multi-drug administration represents an appealing option in order to increase the efficiency of treatment and overcome therapy-escape mechanisms of tumor cells. Nevertheless, most studies neglect the effect of simultaneous multi-drug application on healthy brain tissue, which is, in most cases, considerably harmed, as shown in this project. Hence, albeit it is of high necessity to address glioblastomas with different therapeutic compounds, that trigger cell death via various pathways, sequential treatment schedules are superior to simultaneous ones. Nonetheless, side effects are caused by the systemic administration of high amounts of drugs, resulting

from the rapid clearance of agents and the poor passaging of therapeutics across the blood-brain barrier. Therefore, overcoming the limitations of blood-brain molecule transport would improve the therapy outcome for patients. In this regard, the development of locally-placed implants with longevity and sustained, controllable drug release into the surrounding tissue of the tumor-resection cavity is of great interest. Although the elaboration of devices with a long-term, constant drug release remains challenging, the focus should be laid on multi-drug administration in a sequential way. Indeed, an initial trial regarding a combined release of drugs from implants in a small cohort of patients has revealed severe brain-edema outcome [von Eckardstein et al., 2005], while other studies in animals have displayed promising results in case of rat gliosarcomas [Shapira-Furman et al., 2019] but another has led to brain atrophy in healthy animals [Tseng et al., 2017]. Furthermore, a comprehensive analysis of new approaches compared to standard GBM therapy is often missing. In order to intially overcome simultaneous multi-drug release from devices but rather sequentially apply different therapeutics, the local, delayed release of alternative agents from an implant into the brain tissue during or after oral TMZ administration represents an preliminary opportunity to improve GBM therapy (fig. 5.5). After a comprehensive, *in-vitro* study with co-culture and tumor models, *in-vivo* experiments and clinical trials have to examine the applicability of this treatment model.

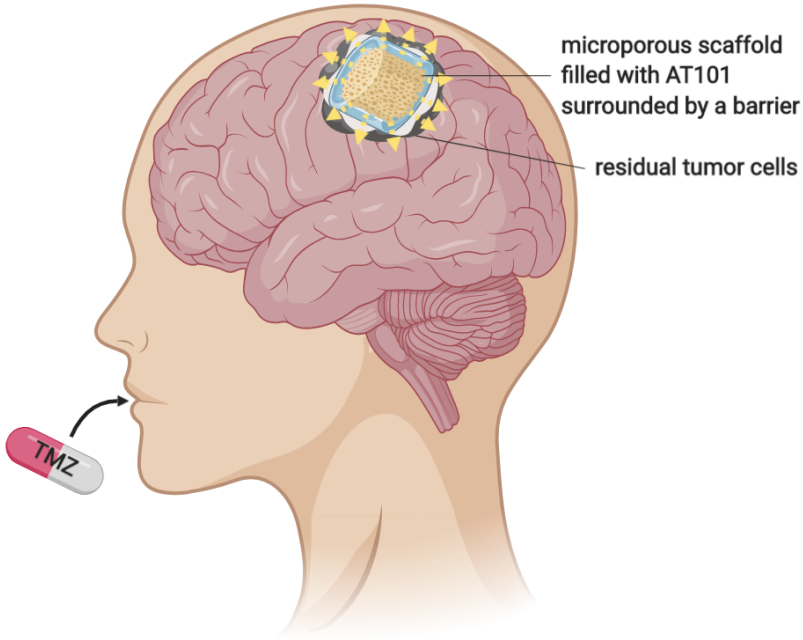

Figure 5.5: Treatment schedule for GBM patients optimized upon obtained results from this study. At first, patients, suffering from glioblastomas, undergo maximal-safe surgery. After removal of the tumor, an implant built of a microporous scaffold, that incorporates AT101, is placed in the tumor cavity. Thereafter, standard radio- and concomitant chemotherapy with TMZ are applied. The local release of AT101 is triggered with a slight delay upon a barrier layer covering the implant, thus guaranteeing a sequential application of TMZ first, then TMZ+AT101.

References

HM Abdel-Bar and RA El Basset Sanad. Endocytic pathways of optimized resveratrol cubosomes capturing into human hepatoma cells. *Biomed Pharmacother*, 93:561–569, 2017. doi: 10.1016/j.biopha.2017.06.093.

FE Abdelrahman, I Elsayed, MK Gad, A Badr, and MI Mohamed. Investigating the cubosomal ability for transnasal brain targeting: In vitro optimization, ex vivo permeation and in vivo biodistribution. *Int J Pharm*, 490:281–291, 2015. doi: 10.1016/j.ijpharm.2015.05.064.

R Adams and EC Kirkpatrick. Structure of Gossypol. XI. Absorption Spectra of Gossypol, its Derivatives and of Certain Dinaphthalene Compounds. *J Am Chem Soc*, 60:2180–2184, 1938.

V Adamski, A Hempelmann, C Flüh, R Lucius, M Synowitz, K Hattermann, and J Held-Feindt. Dormant glioblastoma cells acquire stem cell characteristics and are differentially affected by Temozolomide and AT101 treatment. *Oncotarget*, 8: 108064–108078, 2017a. doi: 10.18632/oncotarget.22514.

V Adamski, R Mentlein, R Lucius, M Synowitz, J Held-Feindt, and K Hattermann. The Chemokine Receptor CXCR6 Evokes Reverse Signaling via the Transmembrane Chemokine CXCL16. *Int J Mol Sci*, 18:E1468, 2017b. doi: 10.3390/ijms18071468.

V Adamski, AD Schmitt, C Flüh, M Synowitz, K Hattermann, and J Held-Feindt. Isolation and Characterization of Fast-Migrating Human Glioma Cells in the Progression of Malignant Gliomas. *Oncol Res*, 25:341–353, 2017c. doi: 10.3727/096504016X14737243054982.

V Adamski, C Schmitt, F Ceynowa, R Adelung, R Lucius, M Synowitz, K Hattermann, and J Held-Feindt. Effects of sequentially applied single and combined temozolomide, hydroxychloroquine and AT101 treatment in a long-term stimulation glioblastoma in vitro model. *J Cancer Res Clin Oncol*, 144:1475–1485, 2018. doi: 10.1007/s00432-018-2680-y.

JA Aguirre-Ghiso. Models, mechanisms and clinical evidence for cancer dormancy. *Nat Rev Cancer*, 7:834–846, 2007.

JA Aguirre-Ghiso, L Ossowski, and SK Rosenbaum. Green fluorescent protein tagging of extracellular signal-regulated kinase and p38 pathways reveals novel dynamics of pathway activation during primary and metastatic growth. *Cancer Res*, 64: 7336–7345, 2004.

M Ahirrao and S Shrotriya. In vitro and in vivo evaluation of cubosomal in situ nasal gel containing resveratrol for brain targeting. *Drug Dev Ind Pharm*, 43:1686–1693, 2017. doi: 10.1080/03639045.2017.1338721.

EM Ahmed. Hydrogel: Preparation, characterization, and applications: A review. *J Adv Res*, 6:105–121, 2015. doi: 10.1016/j.jare.2013.07.006.

SP Akhlaghi, IR Ribeiro, BJ Boyd, and W Loh. Impact of preparation method and variables on the internal structure, morphology, and presence of liposomes in

phytantriol-Pluronic F127 cubosomes. *Colloids Surf B Biointerfaces*, 145:845–853, 2016. doi: 10.1016/j.colsurfb.2016.05.091.

MJ Akhtar, M Ahamed, S Kumar, MM Khan, J Ahmad, and SA Alrokayan. Zinc oxide nanoparticles selectively induce apoptosis in human cancer cells through reactive oxygen species. *Int J Nanomedicine*, 7:845–857, 2012. doi: 10.2147/IJN.S29129.

MA Ali, S Noguchi, Y Iwao, T Oka, and S Itai. Preparation and Characterization of SN-38-Encapsulated Phytantriol Cubosomes Containing α-Monoglyceride Additives. *Chem Pharm Bull (Tokyo)*, 64:577–584, 2016. doi: 10.1248/cpb.c15-00984.

MA Ali, N Kataoka, AH Ranneh, Y Iwao, S Noguchi, T Oka, and S Itai. Enhancing the Solubility and Oral Bioavailability of Poorly Water-Soluble Drugs Using Monoolein Cubosomes. *Chem Pharm Bull (Tokyo)*, 65:42–48, 2017. doi: 10.1248/cpb.c16-00513.

M Allen, M Bjerke, H Edlund, S Nelander, and B Westermark. Origin of the U87MG glioma cell line: Good news and bad news. *Sci Transl Med*, 8:354re3, 2016. doi: 10.1126/scitranslmed.aaf6853.

N Almog. Molecular mechanisms underlying tumor dormancy. *Cancer Lett*, 294: 139–146, 2010. doi: 10.1016/j.canlet.2010.03.004.

N Almog, L Ma, R Raychowdhury, C Schwager, R Erber, S Short, L Hlatky, P Vajkoczy, PE Huber, J Folkman, and A Abdollahi. Transcriptional switch of dormant tumors to fast-growing angiogenic phenotype. *Cancer Res*, 69:836–844, 2009. doi: 10.1158/0008-5472.CAN-08-2590.

A Ambruosi, AS Khalansky, H Yamamoto, SE Gelperina, DJ Begley, and J Kreuter. Biodistribution of polysorbate 80-coated doxorubicin-loaded [14C]-poly(butyl cyanoacrylate) nanoparticles after intravenous administration to glioblastoma-bearing rats. *J Drug Target*, 14:97–105, 2006.

M Ameratunga, N Pavlakis, H Wheeler, R Grant, J Simes, and M Khasraw. Anti-angiogenic therapy for high-grade glioma. *Cochrane Database Syst Rev*, 11: CD008218, 2018. doi: 10.1002/14651858.CD008218.pub4.

Inc. American Cancer Society. Cancer Facts & Figures 2018. Technical report, Atlanta: American Cancer Society, 2018.

ES Amirian, R Zhou, MR Wrensch, SH Olson, ME Scheurer, D Il'yasova, D Lachance, GN Armstrong, LS McCoy, CC Lau, EB Claus, JS Barnholtz-Sloan, J Schildkraut, F Ali-Osman, S Sadetzki, C Johansen, RS Houlston, RB Jenkins, JL Bernstein, RT Merrell, FG Davis, R Lai, S Shete, CI Amos, BS Melin, and ML Bondy. Approaching a Scientific Consensus on the Association between Allergies and Glioma Risk: A Report from the Glioma International Case-Control Study. *Cancer Epidemiol Biomarkers Prev*, 25:282–290, 2016. doi: 10.1158/1055-9965.EPI-15-0847.

JS Ananta, R Paulmurugan, and TF Massoud. Temozolomide-loaded PLGA nanoparticles to treat glioblastoma cells: a biophysical and cell culture evaluation. *Neurol Res*, 38:51–59, 2016. doi: 10.1080/01616412.2015.1133025.

M Andrasi, R Bustos, A Gaspar, FA Gomez, and A Klekner. Analysis and stability study of temozolomide using capillary electrophoresis. *J Chromatogr B Analyt Technol Biomed Life Sci*, 878:1801–1808, 2010. doi: 10.1016/j.jchromb.2010.05.008.

M Andrasi, B Toerzoek, A Klekner, and A Gaspar. Determination of temozolomide in serum and brain tumor with micellar electrokinetic capillary chromatography. *J Chromatogr B Analyt Technol Biomed Life Sci*, 879:2229–2233, 2011. doi: 10.1016/j.jchromb.2011.06.005.

P Antionetti, B Linder, S Hehlgans, IC Mildenberger, MC Burger, S Fulda, JP Steinbach, F Gessler, F Rödel, M Mittelbronn, and D Kögel. Interference with the HSF1/HSP70/BAG3 Pathway Primes Glioma Cells to Matrix Detachment and BH3 Mimetic-Induced Apoptosis. *Mol Cancer Ther*, 16:156–168, 2017. doi: 10.1158/1535-7163.MCT-16-0262.

EA Appel, MJ Rowland, XJ Loh, RM Heywood, C Watts, and OA Scherman. Enhanced stability and activity of temozolomide in primary glioblastoma multiforme cells with cucurbit[n]uril. *Chem Commun (Camb)*, 48:9843–9845, 2012. doi: 10.1039/c2cc35131e.

T Arai, O Benny, T Joki, LG Menon, M Machluf, T Abe, RS Carroll, and PM Black. Novel local drug delivery system using thermoreversible gel in combination with polymeric microspheres or liposomes. *Anticancer Res*, 30:1057–1064, 2010.

LS Ashby, KA Smith, and B Stea. Gliadel wafer implantation combined with standard radiotherapy and concurrent followed by adjuvant temozolomide for treatment of newly diagnosed high-grade glioma: a systematic literature review. *World J Surg Oncol*, 14:225, 2016. doi: 10.1186/s12957-016-0975-5.

M Aubry, M de Tayrac, A Etcheverry, A Clavreul, S Saikali, P Menei, and J Mosser. From the core to beyond the margin: a genomic picture of glioblastoma intratumor heterogeneity. *Oncotarget*, 6:12094–12109, 2015. doi: 10.18632/oncotarget.3297.

AA Avilion, SK Nicolis, LH Pevny, L Perez, N Vivian, and R Lovell-Badge. Multipotent cell lineages in early mouse development depend on SOX2 function. *Genes Dev*, 17:126–140, 2003.

C Aymonier, U Schlotterbeck, L Antonietti, P Zacharias, R Thomann, JC Tiller, and S Mecking. Hybrids of silver nanoparticles with amphiphilic hyperbranched macromolecules exhibiting antimicrobial properties. *Chem Commun (Camb)*, 21: 3018–3019, 2002.

H Azhari, M Strauss, S Hook, BJ Boyd, and SB Rizwan. Stabilising cubosomes with Tween 80 as a step towards targeting lipid nanocarriers to the blood-brain barrier. *Eur J Pharm Biopharm*, 104:148–155, 2016. doi: 10.1016/j.ejpb.2016.05.001.

H Badie and H Abbas. Novel small self-assembled resveratrol-bearing cubosomes and hexosomes: preparation, charachterization, and ex vivo permeation. *Drug Dev Ind Pharm*, 44:2013–2025, 2018. doi: 10.1080/03639045.2018.1508220.

P Bailey and H Cushing. *A Classification of the Tumors of the Glioma Group on a Histogenetic Basis with a Correlated Study of Prognosis*. JB Lippincott, Philadelphia, 1928.

SD Baker, M Wirth, P Statkevich, P Reidenberg, K Alton, SE Sartorius, M Dugan, D Cutler, V Batra, LB Grochow, RC Donehower, and EK Rowinsky. Absorption, metabolism, and excretion of 14C-temozolomide following oral administration to patients with advanced cancer. *Clin Cancer Res*, 5:309–317, 1999.

S Bao, Q Wu, RE McLendon, Y Hao, Q Shi, AB Hjelmeland, MW Dewhirst, DD Bigner, and JN Rich. Glioma stem cells promote radioresistance by preferential activation of the DNA damage response. *Nature*, 444:756–760, 2006.

NU Barua, K Hopkins, M Woolley, S O'Sullivan, R Harrison, RJ Edwards, AS Bienemann, MJ Wyatt, A Arshad, and SS Gill. A novel implantable catheter system with transcutaneous port for intermittent convection-enhanced delivery of carboplatin for recurrent glioblastoma. *Drug Deliv*, 23:167–173, 2016. doi: 10.3109/10717544.2014.908248.

C Bastiancich, L Lemaire, J Bianco, F Franconi, F Danhier, V Préat, G Bastiat, and F Lagarce. Evaluation of lauroyl-gemcitabine-loaded hydrogel efficacy in glioblastoma rat models. *Nanomedicine (Lond)*, 13:1999–2013, 2018. doi: 10.2217/nnm-2018-0057.

TT Batchelor, P Mulholland, B Neyns, LB Nabors, M Campone, A Wick, W Mason, T Mikkelsen, S Phuphanich, LS Ashby, J Degroot, R Gattamaneni, L Cher, M Rosenthal, F Payer, JM Jürgensmeier, RK Jain, AG Sorensen, J Xu, Q Liu, and M van den Bent. Phase III randomized trial comparing the efficacy of cediranib as monotherapy, and in combination with lomustine, versus lomustine alone in patients with recurrent glioblastoma. *J Clin Oncol*, 31:3212–3218, 2013. doi: 10.1200/JCO.2012.47.2464.

D Bei, T Zhang, JB Murowchick, and BB Youan. Formulation of dacarbazine-loaded cubosomes. Part III. Physicochemical characterization. *AAPS PharmSciTech*, 11: 1243–1249, 2010. doi: 10.1208/s12249-010-9496-7.

CP Beier, C Schmid, T Gorlia, C Kleinletzenberger, D Beier, O Grauer, A Steinbrecher, B Hirschmann, A Brawanski, C Dietmaier, T Jauch-Worley, O Koelbl, T Pietsch, M Proescholdt, P Ruemmele, A Muigg, G Stockhammer, M Hegi, U Bogdahn, and P Hau. RNOP-09: pegylated liposomal doxorubicine and prolonged temozolomide in addition to radiotherapy in newly diagnosed glioblastoma–a phase II study. *BMC Cancer*, 9:308, 2009. doi: 10.1186/1471-2407-9-308.

MC Belanger and Y Marois. Hemocompatibility, biocompatibility, inflammatory and in vivo studies of primary reference materials low-density polyethylene and polydimethylsiloxane: a review. *J Biomed Mater Res*, 58:467–477, 2001.

J Bernacki, A Dobrowolska, K Nierwinska, and A Malecki. Physiology and pharmacological role of the blood-brain barrier. *Pharmacol Rep*, 60:600–622, 2008.

A Bertucci, EA Prasetyanto, D Septiadi, A Manicardi, E Brognara, R Gambari, R Corradini, and L De Cola. Combined Delivery of Temozolomide and Anti-miR221 PNA Using Mesoporous Silica Nanoparticles Induces Apoptosis in Resistant Glioma Cells. *Small*, 11:5687–5695, 2015. doi: 10.1002/smll.201500540.

S Bette, M Barz, B Wiestler, T Huber, J Gerhardt, N Buchmann, SE Combs, F Schmidt-Graf, C Delbridge, C Zimmer, JS Kirschke, B Meyer, YM Ryang, F Ringel, and J Gempt. Prognostic Value of Tumor Volume in Glioblastoma Patients: Size Also Matters for Patients with Incomplete Resection. *Ann Surg Oncol*, 25:558–564, 2018. doi: 10.1245/s10434-017-6253-0.

I Bettinger, S Thanos, and W Paulus. Microglia promote glioma migration. *Acta Neuropathol*, 103:351–355, 2002.

L Blackstaffe, MD Shelley, and RG Fish. Cytotoxicity of gossypol enantiomers and its quinone metabolite gossypolone in melanoma cell lines. *Melanoma Res*, 7:364–372, 1997.

MV Blagosklonny. Cell cycle arrest is not senescence. *Aging (Albany NY)*, 3:94–101, 2011.

AL Blajeski, VA Phan, TJ Kottke, and SH Kaufmann. G(1) and G(2) cell-cycle arrest following microtubule depolymerization in human breast cancer cells. *J Clin Invest*, 110:91–99, 2002.

FE Bleeker, NA Atai, S Lamba, A Jonker, D Rijkeboer, KS Bosch, W Tigchelaar, D Troost, WP Vandertop, A Bardelli, and CJ Van Noorden. The prognostic IDH1(R132) mutation is associated with reduced NADP+-dependent IDH activity in glioblastoma. *Acta Neuropathol*, 119:487–494, 2010. doi: 10.1007/s00401-010-0645-6.

E Bloise, HL Couto, L Massai, P Ciarmela, M Mencarelli, LE Borges, M Muscettola, G Grasso, VF Amaral, GD Cassali, F Petraglia, and FM Reis. Differential expression of follistatin and FLRG in human breast proliferative disorders. *BMC Cancer*, 9:320, 2009. doi: 10.1186/1471-2407-9-320.

RH Bobo, DW Laske, A Akbasak, PF Morrison, RL Dedrick, and EH Oldfield. Convection-enhanced delivery of macromolecules in the brain. *Proc Natl Acad Sci U S A*, 91:2076–2080, 1994.

A Boiardi, M Eoli, A Salmaggi, E Lamperti, A Botturi, G Broggi, M Bartolomei, and A Silvani. New approach in delivering chemotherapy: locoregional treatment for recurrent glioblastoma (rGBM). *J Exp Clin Cancer Res*, 22:123–127, 2003.

A Boiardi, A Silvani, M Eoli, E Lamperti, A Salmaggi, P Gaviani, A Fiumani, A Botturi, C Falcone, A Solari, G Filippini, F Di Meco, and G Broggi. Treatment of recurrent glioblastoma: can local delivery of mitoxantrone improve survival? *J Neurooncol*, 88:105–113, 2008. doi: 10.1007/s11060-008-9540-6.

RL Bowman and JA Joyce. Therapeutic targeting of tumor-associated macrophages and microglia in glioblastoma. *Immunotherapy*, 6:663–666, 2014. doi: 10.2217/imt.14.48.

AA Brandes, M Gil-Gil, F Saran, AF Carpentier, AK Nowak, W Mason, V Zagonel, F Dubois, G Finocchiaro, G Fountzilas, DM Cernea, O Chinot, R Anghel, F Ghiringhelli, P Beauchesne, G Lombardi, E Franceschi, M Makrutzki, C Mpofu,

HJ Urban, and J Pichler. A Randomized Phase II Trial (TAMIGA) Evaluating the Efficacy and Safety of Continuous Bevacizumab Through Multiple Lines of Treatment for Recurrent Glioblastoma. *Oncologist*, 24:521–528, 2019. doi: 10.1634/theoncologist.2018-0290.

H Brem, MS Jr Mahaley, NA Vick, KL Black, SC Jr Schold, PC Burger, AH Friedman, IS Ciric, TW Eller, JW Cozzens, and JN Kenealy. Interstitial chemotherapy with drug polymer implants for the treatment of recurrent gliomas. *J Neurosurg*, 74: 441–446, 1991.

H Brem, MG Ewend, S Piantadosi, J Greenhoot, PC Burger, and M Sisti. The safety of interstitial chemotherapy with BCNU-loaded polymer followed by radiation therapy in the treatment of newly diagnosed malignant gliomas: phase I trial. *J Neurooncol*, 26:111–123, 1995a.

H Brem, S Piantadosi, PC Burger, M Walker, R Selker, NA Vick, K Black, M Sisti, S Brem, G Mohr, P Muller, R Morawetz, and SC Schold. Placebo-controlled trial of safety and efficacy of intraoperative controlled delivery by biodegradable polymers of chemotherapy for recurrent gliomas. The Polymer-brain Tumor Treatment Group. *Lancet*, 345:1008–1012, 1995b.

S Brem, B Tyler, K Li, G Pradilla, F Legnani, J Caplan, and H Brem. Local delivery of temozolomide by biodegradable polymers is superior to oral administration in a rodent glioma model. *Cancer Chemother Pharmacol*, 60:643–650, 2007.

FH Brembeck and AK Rustgi. The tissue-dependent keratin 19 gene transcription is regulated by GKLF/KLF4 and Sp1. *J Biol Chem*, 275:28230–28239, 2000.

E Briceno, A Calderon, and J Sotelo. Institutional experience with chloroquine as an adjuvant to the therapy for glioblastoma multiforme. *Surg Neurol*, 67:388–391, 2007.

R Brisman, EM Housepian, C Chang, P Duffy, and E Balis. Adjuvant nitrosourea therapy for glioblastoma. *Arch Neurol*, 33:745–750, 1976.

JA Brown, SG Codreanu, M Shi, SD Sherrod, DA Markov, MD Neely, CM Britt, OS Hoilett, RS Reiserer, PC Samson, LJ McCawley, DJ Webb, AB Bowman, JA McLean, and JP Wikswo. Metabolic consequences of inflammatory disruption of the blood-brain barrier in an organ-on-chip model of the human neurovascular unit. *J Neuroinflammation*, 13:306, 2016. doi: 10.1186/s12974-016-0760-x.

S Burdak-Rothkamm, SC Short, M Folkard, K Rothkamm, and KM Prise. ATR-dependent radiation-induced gamma H2AX foci in bystander primary human astrocytes and glioma cells. *Oncogene*, 26:993–1002, 2007.

P Bushunow, MM Reidenberg, J Wasenko, J Winfield, B Lorenzo, S Lemke, B Himpler, R Corona, and T Coyle. Gossypol treatment of recurrent adult malignant gliomas. *J Neurooncol*, 43:79–86, 1999.

N Butowski, K Bankiewicz, A Kells, A Martin, M Berger, M Aghi, M Prados, S Chang, and J Clarke. A phase I study of convection-enhanced delivery of liposomal-irinotecan using real-time imaging with gadolinium in patients with recurrent high grade glioma. *Neuro Oncol*, 16:iii13–iii13, 2014. doi: 10.1093/neuonc/nou206.46.

J Byun, YH Kim, SJ Nam, JE Park, YH Cho, HS Kim, SH Hong, JH Kim, SJ Kim, and CJ Kim. Comparison of Survival Outcomes Between Partial Resection and Biopsy for Primary Glioblastoma: A Propensity Score-Matched Study. *World Neurosurg*, 121:e858–e866, 2019. doi: 10.1016/j.wneu.2018.09.237.

B Caffery, JS Lee, and AA Alexander-Bryant. Vectors for Glioblastoma Gene Therapy: Viral & Non-Viral Delivery Strategies. *Nanomaterials (Basel)*, 9:E105, 2019. doi: 10.3390/nano9010105.

X Cai, J Luo, X Yang, H Deng, J Zhang, S Li, H Wei, C Yang, L Xu, R Jin, Z Li, W Zhou, J Ding, J Chu, L Jia, Q Jia, C Tan, M Liu, and J Xiao. In vivo selection for spine-derived highly metastatic lung cancer cells is associated with increased migration, inflammation and decreased adhesion. *Oncotarget*, 6:22905–22917, 2015. doi: 10.18632/oncotarget.4416.

R Cairns, I Papandreou, and N Denko. Overcoming physiologic barriers to cancer treatment by molecularly targeting the tumor microenvironment. *Mol Cancer Res*, 4:61–70, 2006.

C Calabrese, H Poppleton, M Kocak, TL Hogg, C Fuller, B Hamner, EY Oh, MW Gaber, D Finklestein, M Allen, A Frank, IT Bayazitov, SS Zakharenko, A Gajjar, A Davidoff, and RJ Gilbertson. A perivascular niche for brain tumor stem cells. *Cancer Cell*, 11:69–82, 2007.

C Calatozzolo, M Gelati, E Ciusani, FL Sciacca, B Pollo, L Cajola, C Marras, A Silvani, L Vitellaro-Zuccarello, D Croci, A Boiardi, and A Salmaggi. Expression of drug resistance proteins Pgp, MRP1, MRP3, MRP5 and GST-pi in human glioma. *J Neurooncol*, 74:113–121, 2005.

B Campos, Z Gal, A Baader, T Schneider, C Sliwinski, K Gassel, J Bageritz, N Grabe, A von Deimling, P Beckhove, C Mogler, V Goidts, A Unterberg, V Eckstein, and C Herold-Mende. Aberrant self-renewal and quiescence contribute to the aggressiveness of glioblastoma. *J Pathol*, 234:23–33, 2014. doi: 10.1002/path.4366.

S Caragher, AJ Chalmers, and N Gomez-Roman. Glioblastoma's Next Top Model: Novel Culture Systems for Brain Cancer Radiotherapy Research. *Cancers (Basel)*, 11:E44, 2019. doi: 10.3390/cancers11010044.

A Carmo, H Carvalheiro, I Crespo, I Nunes, and MC Lopes. Effect of temozolomide on the U-118 glioma cell line. *Oncol Lett*, 2:1165–1170, 2011. doi: 10.3892/ol.2011.406.

F Casanova, PR Carney, and M Sarntinoranont. Effect of needle insertion speed on tissue injury, stress, and backflow distribution for convection-enhanced delivery in the rat brain. *PLoS One*, 9:e94919, 2014. doi: 10.1371/journal.pone.0094919.

CM Cater and CM Lyman. Reaction of gossypol with amino acids and other amino compounds. *J Am Oil Chem' Soc*, 46:649–653, 1969.

KL Chaichana, I Jusue-Torres, R Navarro-Ramirez, SM Raza, M Pascual-Gallego, A Ibrahim, M Hernandez-Hermann, L Gomez, X Ye, JD Weingart, A Olivi, J Blakeley, GL Gallia, M Lim, H Brem, and A Quinones-Hinojosa. Establishing percent

resection and residual volume thresholds affecting survival and recurrence for patients with newly diagnosed intracranial glioblastoma. *Neuro Oncol*, 16:113–122, 2014. doi: 10.1093/neuonc/not137.

AL Chang, J Miska, DA Wainwright, M Dey, CV Rivetta, D Yu, D Kanojia, KC Pituch, J Qiao, P Pytel, Y Han, M Wu, L Zhang, CM Horbinski, AU Ahmed, and MS Lesniak. CCL2 Produced by the Glioma Microenvironment Is Essential for the Recruitment of Regulatory T Cells and Myeloid-Derived Suppressor Cells. *Cancer Res*, 76:5671–5682, 2016.

CN Changm and R Bodmeier. Swelling of and drug release from monoglyceride-based drug delivery systems. *J Pharm Sci*, 86:747–752, 1997.

C Charalambous, FM Hofman, and TC Chen. Functional and phenotypic differences between glioblastoma multiforme-derived and normal human brain endothelial cells. *J Neurosurg*, 102:699–705, 2005.

NA Charles, EC Holland, R Gilbertson, R Glass, and H Kettenmann. The brain tumor microenvironment. *Glia*, 59:502–514, 2011. doi: 10.1002/glia.21136.

L Chen, GQ Liu, HY Wu, J Jin, X Yin, D Li, and PR Lu. Monocyte chemoattractant protein 1 and fractalkine play opposite roles in angiogenesis via recruitment of different macrophage subtypes. *Int J Ophthalmol*, 11:216–222, 2018. doi: 10.18240/ijo.2018.02.06.

W Chen, D Wang, X Du, Y He, S Chen, Q Shao, C Ma, B Huang, A Chen, P Zhao, X Qu, and X Li. Glioma cells escaped from cytotoxicity of temozolomide and vincristine by communicating with human astrocytes. *Med Oncol*, 32:43, 2015. doi: 10.1007/s12032-015-0487-0.

S Chiblak, Z Tang, D Lemke, M Knoll, I Dokic, R Warta, M Moustafa, W Mier, S Brons, C Rapp, S Muschal, P Seidel, M Bendszus, S Adeberg, OD Wiestler, U Haberkorn, J Debus, C Herold-Mende, W Wick, and A Abdollahi. Carbon irradiation overcomes glioma radioresistance by eradicating stem cells and forming an antiangiogenic and immunopermissive niche. *JCI Insight*, 4:123837, 2019. doi: 10.1172/jci.insight.123837.

H Cho, TC Lai, and GS Kwon. Poly(ethylene glycol)-block-poly(ϵ-caprolactone) micelles for combination drug delivery: evaluation of paclitaxel, cyclopamine and gossypol in intraperitoneal xenograft models of ovarian cancer. *J Control Release*, 166:1–9, 2013. doi: 10.1016/j.jconrel.2012..005.

WJ Choi, J Jung, S Lee, YJ Chung, CS Yang, YK Lee, YS Lee, JK Park, HW Ko, and JO Lee. Effects of substrate conductivity on cell morphogenesis and proliferation using tailored, atomic layer deposition-grown ZnO thin films. *Sci Rep*, 5:9974, 2015. doi: 10.1038/srep09974.

S Chu, H Wang, and M Yu. A putative molecular network associated with colon cancer metastasis constructed from microarray data. *World J Surg Oncol*, 15:115, 2017. doi: 10.1186/s12957-017-1181-9.

A Claes, AJ Idema, and P Wesseling. Diffuse glioma growth: a guerilla war. *Acta Neuropathol*, 114:443–458, 2007.

AM Clark, SE Wheeler, CL Young, L Stockdale, J Shepard Neimann, W Zhao, Stolz DB, R Venkataramanan, D Lauffenburger, L Griffith, and A Wells. A liver microphysiological system of tumor cell dormancy and inflammatory responsiveness is affected by scaffold properties. *Lab Chip*, 17:156–168, 2016. doi: 10.1039/c6lc01171c.

JL Clarke, AM Molinaro, JR Cabrera, AA DeSilva, JE Rabbitt, J Prey, DC Drummond, J Kim, C Noble, JB Fitzgerald, SM Chang, NA Butowski, JW Taylor, JW Park, and MD Prados. A phase 1 trial of intravenous liposomal irinotecan in patients with recurrent high-grade glioma. *Cancer Chemother Pharmacol*, 79: 603–610, 2017. doi: 10.1007/s00280-017-3247-3.

ML Coleman, EA Sahai, M Yeo, M Bosch, A Dewar, and MF Olson. Membrane blebbing during apoptosis results from caspase-mediated activation of ROCK I. *Nat Cell Biol*, 3:339–345, 2001.

DT Connolly, DM Heuvelman, R Nelson, JV Olander, BL Eppley, JJ Delfino, NR Siegel, RM Leimgruber, and J Feder. Tumor vascular permeability factor stimulates endothelial cell growth and angiogenesis. *J Clin Invest*, 84:1470–1478, 1989.

T Coyle, S Levante, M Shetler, and J Winfield. In vitro and in vivo cytotoxicity of gossypol against central nervous system tumor cell lines. *J Neurooncol*, 19:25–35, 1994.

M Cuperlovic-Culf, D Ferguson, A Culf, P Jr Morin, and M Touaibia. 1H-NMR metabolomics analysis of glioblastoma subtypes: correlation between metabolomics and gene expression characteristics. *J Biol Chem*, 287:20164–20175, 2012. doi: 10.1074/jbc.M111.337196.

EF da Silveira, JM Chassot, FC Teixeira, JH Azambuja, G Debom, FT Beira, FA Del Pino, A Lourenco, AP Horn, L Cruz, RM Spanevello, and E Braganhol. Ketoprofen-loaded polymeric nanocapsules selectively inhibit cancer cell growth in vitro and in preclinical model of glioblastoma multiforme. *Invest New Drugs*, 31: 1424–1435, 2013. doi: 10.1007/s10637-013-0016-y.

K Dabrowski, KJ Lee, J Rinchard, A Ciereszko, JH Blom, and JS Ottobre. Gossypol isomers bind specifically to blood plasma proteins and spermatozoa of rainbow trout fed diets containing cottonseed meal. *Biochim Biophys Acta*, 1525:37–42, 2001.

A Dalu, BS Blaydes, LG Lomax, and KB Delclos. A comparison of the inflammatory response to a polydimethylsiloxane implant in male and female Balb/c mice. *Biomaterials*, 21:1947–1957, 2000.

A Dasgupta, AR Lim, and CM Ghajar. Circulating and disseminated tumor cells: harbringer or initiators of metastasis? *Mol Oncol*, 11:40–61, 2017. doi: 10.10002/1878-0261.12022.

JM De Cock, T Shibue, A Dongre, Z Keckesova, F Reinhardt, and RA Weinberg. Inflammation Triggers Zeb1-Dependent Escape from Tumor Latency. *Cancer Res*, 76:6778–6784, 2016. doi: 10.1158/0008-5472.CAN-16-0608.

M De Salvo, G Maresca, I D'agnano, R Marchese, A Stigliano, R Gagliassi, E Brunetti, GH Raza, U De Paula, and B Bucci. Temozolomide induced c-Myc-mediated apoptosis via Akt signalling in MGMT expressing glioblastoma cells. *Int J Radiat Biol*, 87:518–533, 2011. doi: 10.3109/09553002.2011.556173.

S De Vleeschouwer. *Glioblastoma*. Codon Publications, Brisbane, Australia, 2017. doi: http://dx.doi.org/10.15586/codon.glioblastoma.2017.

PG Debenham, N Kartner, L Siminovitch, JR Riordan, and V Ling. DNA-mediated transfer of multiple drug resistance and plasma membrane glycoprotein expression. *Mol Cell Biol*, 2:881–889, 1982.

LP Deleyrolle, A Harding, K Cato, FA Siebzehnrubl, M Rahman, H Azari, S Olson, B Gabrielli, G Osborne, A Vescovi, and BA Reynolds. Evidence for label-retaining tumour-initiating cells in human glioblastoma. *Brain*, 134:1331–1343, 2011. doi: 10.1093/brain/awr081.

ZN Demidenko, SG Zubova, EI Bukreeva, VA Pospelov, TV Pospelova, and MV Blagosklonny. Rapamycin decelerates cellular senescence. *Cell Cycle*, 8:1888–1895, 2009.

L Deng, W Zheng, X Dong, J Liu, C Zhu, D Lu, J Zhang, L Song, Y Wang, and D Deng. Chemokine receptor CXCR7 is an independent prognostic biomarker in glioblastoma. *Cancer Biomark*, 20:1–6, 2017. doi: 10.3233/CBM-151430.

BJ Denny, RT Wheelhouse, MF Stevens, LL Tsang, and JA Slack. NMR and molecular modeling investigation of the mechanism of activation of the antitumor drug temozolomide and its interaction with DNA. *Biochemistry*, 33:9045–9051, 1994.

I Desbaillets, M Tada, N De Tribolet, AC Diserens, MF Hamou, and EG Van Meir. Human astrocytomas and glioblastomas express monocyte chemoattractant protein-1 (MCP-1) in vivo and in vitro. *Int J Cancer*, 58:240–247, 1994.

J Dittmer. Mechanisms governing metastatic dormancy in breast cancer. *Semin Cancer Biol*, 44:72–82, 2017. doi: 10.1016/j.semcancer.2017.03.006.

GP Dunn, PE Fecci, and WT Curry. Cancer immunoediting in malignant glioma. *Neurosurgery*, 71:201–222, 2012. doi: 10.1227/NEU.0b013e31824f840d.

M Ehtesham, JA Winston, P Kabos, and RC Thompson. CXCR4 expression mediates glioma cell invasiveness. *Oncogene*, 25:2801–2806, 2006.

M Ehtesham, KY Mapara, CB Stevenson, and RC Thompson. CXCR4 mediates the proliferation of glioblastoma progenitor cells. *Cancer Lett*, 274:305–312, 2009. doi: 10.1016/j.canlet.2008.09.034.

YS Elnaggar, SM Etman, DA Abdelmonsif, and OY Abdallah. Novel piperine-loaded Tween-integrated monoolein cubosomes as brain-targeted oral nanomedicine in Alzheimer's disease: pharmaceutical, biological, and toxicological studies. *Int J Nanomedicine*, 10:5459–5473, 2015. doi: 10.2147/IJN.S87336.

NL Elstad and KD Fowers. OncoGel (ReGel/paclitaxel)–clinical applications for a novel paclitaxel delivery system. *Adv Drug Deliv Rev*, 61:785–794, 2009. doi: 10.1016/j.addr.2009.04.010.

BB Endaya, PY Lam, AC Meedeniya, and J Neuzil. Transcriptional profiling of dividing tumor cells detects intratumor heterogeneity linked to cell proliferation in a brain tumor model. *Mol Oncol*, 10:126–137, 2016. doi: 10.1016/j.molonc.2015.09.001.

L Facci, M Barbierato, M Zusso, SD Skaper, and P Giusti. Serum amyloid A primes microglia for ATP-dependent interleukin-1β release. *J Neuroinflammation*, 15:164, 2018. doi: 10.1186/s12974-018-1205-6.

C Fang, K Wang, ZR Stephen, Q Mu, FM Kievit, DT Chiu, OW Press, and M Zhang. Temozolomide nanoparticles for targeted glioblastoma therapy. *ACS Appl Mater Interfaces*, 7:6674–6682, 2015. doi: 10.1021/am5092165.

C Farina, F Aloisi, and E Meinl. Astrocytes are active players in cerebral innate immunity. *Trends Immunol*, 28:138–145, 2007.

MR Fetell, EM Housepian, MW Oster, DN Cote, MB Sisti, SG Marcus, and PB Fisher. Intratumor administration of beta-interferon in recurrent malignant gliomas. A phase I clinical and laboratory study. *Cancer*, 65:78–83, 1990.

P Figueiredo, V Balasubramanian, MA Shahbazi, A Correia, D Wu, CG Palivan, JT Hirvonen, and HA Santos. Angiopep2-functionalized polymersomes for targeted doxorubicin delivery to glioblastoma cells. *Int J Pharm*, 511:794–803, 2016. doi: 10.1016/j.ijpharm.2016.07.066.

G Fiscon, F Conte, and P Paci. SWIM tool application to expression data of glioblastoma stem-like cell lines, corresponding primary tumors and conventional glioma cell lines. *BMC Bioinformatics*, 19:436, 2018. doi: 10.1186/s12859-018-2421-x.

C Flüh, K Hattermann, HM Mehdorn, M Synowitz, and J Held-Feindt. Differential expression of CXCR4 and CXCR7 with various stem cell markers in paired human primary and recurrent glioblastomas. *Int J Oncol*, 48:1408–1416, 2016. doi: 10.3892/ijo.2016.3354.

VL Frampton, JD Jr. Edwards, and HR Henze. The ultraviolet absorption spectrum of gossypol. *J Am Chem Soc*, 70:3944, 1948.

AW Frei, Y Li, K Jiang, P Buchwald, and CL Stabler. Local delivery of fingolimod from three-dimensional scaffolds impacts islet graft efficacy and microenvironment in a murine diabetic model. *J Tissue Eng Regen Med*, 12:393–404, 2018. doi: 10.1002/term.2464.

W Friedl and C Herfarth. The long-term prognosis of breast cancer. Retrospective study of 973 patients. *Langenbecks Arch Chir*, 377:168–173, 1992.

LK Fung, MG Ewend, A Sills, EP Sipos, R Thompson, M Watts, OM Colvin, H Brem, and WM Saltzman. Pharmacokinetics of interstitial delivery of carmustine, 4-hydroperoxycyclophosphamide, and paclitaxel from a biodegradable polymer implant in the monkey brain. *Cancer Res*, 58:672–684, 1998.

T Förster. *Delocalized excitation and excitation transfer. Modern Quantum Chemistry Vol. 3.* Academic Press Inc., New York, 1965.

RP Galvao, A Kasina, RS McNeill, JE Harbin, O Foreman, RG Verhaak, A Nishiyama, CR Miller, and H Zong. Transformation of quiescent adult oligodendrocyte precursor cells into malignant glioma through a multistep reactivation process. *Proc Natl Acad Sci U S A*, 111:E4214–4223, 2014. doi: 10.1073/pnas.1414389111.

H Gao, Y Xiong, S Zhang, Z Yang, S Cao, and X Jiang. RGD and interleukin-13 peptide functionalized nanoparticles for enhanced glioblastoma cells and neovasculature dual targeting delivery and elevated tumor penetration. *Mol Pharm*, 11: 1042–1052, 2014. doi: 10.1021/mp400751g.

J Gao, Z Wang, H Liu, L Wang, and G Huang. Liposome encapsulated of temozolomide for the treatment of glioma tumor: preparation, characterization and evaluation. *Drug Discov Ther*, 9:205–212, 2015. doi: 10.5582/ddt.2015.01016.

B García-Pinel, C Porras-Alcalá, A Ortega-Rodríguez, F Sarabia, J Prados, C Melguizo, and JM Lopez-Romero. Lipid-Based Nanoparticles: Application and Recent Advances in Cancer Treatment. *Nanomaterials (Basel)*, 9:E638, 2019. doi: 10.3390/nano9040638.

J Gerdes, H Lemke, H Baisch, HH Wacker, U Schwab, and H Stein. Cell cycle analysis of a cell proliferation-associated human nuclear antigen defined by the monoclonal antibody Ki-67. *J Immunol*, 133:1710–1715, 1984.

MR Gilbert, JJ Dignam, TS Armstrong, JS Wefel, DT Blumenthal, MA Vogelbaum, H Colman, A Chakravarti, S Pugh, M Won, R Jeraj, PD Brown, KA Jaeckle, D Schiff, VW Stieber, DG Brachman, M Werner-Wasik, IW Tremont-Lukats, EP Sulman, KD Aldape, WJ Jr Curran, and MP Mehta. A randomized trial of bevacizumab for newly diagnosed glioblastoma. *N Engl J Med*, 370:699–708, 2014. doi: 10.1056/NEJMoa1308573.

S Godard, G Getz, M Delorenzi, P Farmer, H Kobayashi, I Desbaillets, M Nozaki, AC Diserens, MF Hamou, PY Dietrich, L Regli, RC Janzer, P Bucher, R Stupp, N de Tribolet, E Domany, and ME Hegi. Classification of human astrocytic gliomas on the basis of gene expression: a correlated group of genes with angiogenic activity emerges as a strong predictor of subtypes. *Cancer Res*, 63:6613–6625, 2003.

N Goffart, A Lombard, F Lallemand, J Kroonen, J Nassen, E Di Valentin, S Berendsen, M Dedobbeleer, E Willems, P Robe, V Bours, D Martin, P Martinive, P Maquet, and B Rogister. CXCL12 mediates glioblastoma resistance to radiotherapy in the subventricular zone. *Neuro Oncol*, 19:66–77, 2017. doi: 10.1093/neuonc/now136.

EB Golden, HY Cho, A Jahanian, FM Hofman, SG Louie, AH Schönthal, and TC Chen. Chloroquine enhances temozolomide cytotoxicity in malignant gliomas by blocking autophagy. *Neurosurg Focus*, 37:E12., 2014. doi: 10.3171/2014.9.FOCUS14504.

EB Golden, HY Cho, FM Hofman, SG Louie, AH Schönthal, and TC Chen. Quinoline-based antimalarial drugs: a novel class of autophagy inhibitors. *Neurosurg Focus*, 38:E12, 2015. doi: 10.3171/2014.12.FOCUS14748.

I Golán, L Rodríguez de la Fuente, and JA Costoya. NK Cell-Based Glioblastoma Immunotherapy. *Cancers (Basel)*, 10:E522, 2018. doi: 10.3390/cancers10120522.

DR Groothuis, S Ward, AC Itskovich, C Dobrescu, CV Allen, C Dills, and RM Levy. Comparison of 14C-sucrose delivery to the brain by intravenous, intraventricular, and convection-enhanced intracerebral infusion. *J Neurosurg*, 90:321–331, 1999.

X Guan, MN Hasan, S Maniar, W Jia, and D Sun. Reactive Astrocytes in Glioblastoma Multiforme. *Mol Neurobiol*, 55:6927–6938, 2018. doi: 10.1007/s12035-018-0880-8.

N Gunja, D Roberts, D McCoubrie, P Lamberth, A Jan, DC Simes, P Hackett, and NA Buckley. Survival after massive hydroxychloroquine overdose. *Anaesth Intensive Care*, 37:130–133, 2009.

C Guo, J Wang, F Cao, RJ Lee, and G Zhai. Lyotropic liquid crystal systems in drug delivery. *Drug Discov Today*, 15:1032–1040, 2010. doi: 10.1016/j.drudis.2010.09.006.

PK Gupta, CT Hung, and DG Perrier. Quantitation of the release of doxorubicin from colloidal dosage forms using dynamic dialysis. *J Pharm Sci*, 76:141–145, 1987.

S Gurunathan and JH Kim. Synthesis, toxicity, biocompatibility, and biomedical applications of graphene and graphene-related materials. *Int J Nanomedicine*, 11: 1927–1945, 2016. doi: 10.2147/IJN.S105264.

H Haase and D Beyersmann. Uptake and intracellular distribution of labile and total Zn(II) in C6 rat glioma cells investigated with fluorescent probes and atomic absorption. *Biometals*, 12:247–254, 1999.

G Hadfield. The dormant cancer cell. *Br Med J*, 2:607–610, 1954.

C Hamisch, M Ruge, S Kellermann, AC Kohl, I Duval, R Goldbrunner, and SJ Grau. Impact of treatment on survival of patients with secondary glioblastoma. *J Neurooncol*, 133:309–313, 2017. doi: 10.1007/s11060-017-2415-y.

HJ Harn, SZ Lin, PC Lin, CY Liu, PY Liu, LF Chang, SY Yen, DK Hsieh, FC Liu, DF Tai, and TW Chiou. Local interstitial delivery of z-butylidenephthalide by polymer wafers against malignant human gliomas. *Neuro Oncol*, 13:635–648, 2011. doi: 10.1093/neuonc/nor021.

C Hartmann, B Hentschel, W Wick, D Capper, J Felsberg, M Simon, M Westphal, G Schackert, R Meyermann, T Pietsch, G Reifenberger, M Weller, M Loeffler, and A von Deimling. Patients with IDH1 wild type anaplastic astrocytomas exhibit worse prognosis than IDH1-mutated glioblastomas, and IDH1 mutation status accounts for the unfavorable prognostic effect of higher age: implications for classification of gliomas. *Acta Neuropathol*, 120:707–718, 2010. doi: 10.1007/s00401-010-0781-z.

T Hasan, SP Caragher, JM Shireman, CH Park, Fa Atashi, S Baisiwala, G Lee, D Guo, JY Wang, M Dey, M Wu, MS Lesniak, CM Horbinski, CD James, and AU Ahmed. Interleukin-8/CXCR2 signaling regulates therapy-induced plasticity and enhances tumorigenicity in glioblastoma. *Cell Death Dis*, 10:292, 2019. doi: 10.1038/s41419-019-1387-6.

K Hattermann, J Held-Feindt, R Lucius, SS Müerköster, ME Penfold, TJ Schall, and R Mentlein. The chemokine receptor CXCR7 is highly expressed in human glioma cells and mediates antiapoptotic effects. *Cancer Res*, 70:3299–3308, 2010. doi: 10.1158/0008-5472.CAN-09-3642.

K Hattermann, R Mentlein, and J Held-Feindt. CXCL12 mediates apoptosis resistance in rat C6 glioma cells. *Oncol Rep*, 27:1348–1352, 2012. doi: 10.3892/or.2012.1674.

K Hattermann, J Held-Feindt, A Ludwig, and R Mentlein. The CXCL16-CXCR6 chemokine axis in glial tumors. *J Neuroimmunol*, 260:47–54, 2013. doi: 10.1016/j.jneuroim.2013.04.006.

K Hattermann, S Sebens, O Helm, AD Schmitt, R Mentlein, HM Mehdorn, and J Held-Feindt. Chemokine expression profile of freshly isolated human glioblastoma-associated macrophages/microglia. *Oncol Rep*, 32:270–276, 2014. doi: 10.3892/or.2014.3214.

K Hattermann, C Flüh, D Engel, HM Mehdorn, M Synowitz, R Mentlein, and J Held-Feindt. Stem cell markers in glioma progression and recurrence. *Int J Oncol*, 49: 1899–1910, 2016a. doi: 10.3892/ijo.2016.3682.

K Hattermann, H Gebhardt, S Krossa, A Ludwig, R Lucius, J Held-Feindt, and R Mentlein. Transmembrane chemokines act as receptors in a novel mechanism termed inverse signaling. *Elife*, 5:e10820, 2016b. doi: 10.7554/eLife.10820.

H Hayashi. A review on the natural mediators of inflammatory leucotaxis. *Acta Pathol Jpn*, 32:271–284, 1982.

D Heckmann, P Maier, S Laufs, L Li, JP Sleeman, MJ Trunk, JH Leupold, F Wenz, WJ Zeller, S Fruehauf, and H Allgayer. The disparate twins: a comparative study of CXCR4 and CXCR7 in SDF-1α-induced gene expression, invasion and chemosensitivity of colon cancer. *Clin Cancer Res*, 20:604–616, 2014. doi: 10.1158/1078-0432.CCR-13-0582.

ME Hegi, AC Diserens, T Gorlia, MF Hamou, N de Tribolet, M Weller, JM Kros, JA Hainfellner, W Mason, L Mariani, JE Bromberg, P Hau, RO Mirimanoff, JG Cairncross, RC Janzer, and R Stupp. MGMT gene silencing and benefit from temozolomide in glioblastoma. *N Engl J Med*, 352:997–1003, 2005.

H Heiati, R Tawashi, and NC Phillips. Drug retention and stability of solid lipid nanoparticles containing azidothymidine palmitate after autoclaving, storage and lyophilization. *J Microencapsul*, 15:173–184, 1998.

J Held-Feindt, EB Paredes, U Blömer, C Seidenbecher, AM Stark, HM Mehdorn, and R Mentlein. Matrix-degrading proteases ADAMTS4 and ADAMTS5 (disintegrins and metalloproteinases with thrombospondin motifs 4 and 5) are expressed in human glioblastomas. *Int J Cancer*, 118:55–61, 2006.

J Held-Feindt, K Hattermann, SS Mueerkoester, H Wedderkopp, F Knerlich-Lukoschus, H Ungefroren, HM Mehdorn, and R Mentlein. CX3CR1 promotes recruitment of human glioma-infiltrating microglia/macrophages (GIMs). *Exp Cell Res*, 316:1553–1566, 2010. doi: 10.1016/j.yexcr.2010.02.018.

V Heleg-Shabtai, R Aizen, E Sharon, YS Sohn, A Trifonov, N Enkin, L Freage, R Nechushtai, and I Willner. Gossypol-Capped Mitoxantrone-Loaded Mesoporous SiO2 NPs for the Cooperative Controlled Release of Two Anti-Cancer Drugs. *ACS Appl Mater Interfaces*, 8:14414–14422, 2016. doi: 10.1021/acsami.6b03865.

BK Hendricks, AA Cohen-Gadol, and JC Miller. Novel delivery methods bypassing the blood-brain and blood-tumor barriers. *Neurosurg Focus*, 38:E10, 2015. doi: 10.3171/2015.1.FOCUS14767.

S Henriksen, GD Tylden, A Dumoulin, BN Sharma, HH Hirsch, and C Hanssen Rinaldo. The human fetal glial cell line SVG p12 contains infectious BK polyomavirus. *J Virol*, 88:7556–7568, 2014. doi: 10.1128/JVI.00696-14.

U Herrlinger, T Tzaridis, F Mack, JP Steinbach, U Schlegel, M Sabel, P Hau, RD Kortmann, D Krex, O Grauer, R Goldbrunner, O Schnell, O Bähr, M Uhl, C Seidel, G Tabatabei, T Kowalski, F Ringel, F Schmidt-Graf, B Suchorska, S Brehmer, A Weyerbrock, M Renovanz, L Bullinger, N Galldiks, P Vajkoczy, M Misch, H Vatter, M Stuplich, N Schäfer, S Kebir, J Weller, C Schaub, W Stummer, JC Tonn, M Simon, VC Keil, M Nelles, H Urbach, M Coenen, W Wick, M Weller, R Fimmers, M Schmid, E Hattingen, T Pietsch, C Coch, M Glas, and Neurooncology Working Group of the German Cancer Society. Lomustine-temozolomide combination therapy versus standard temozolomide therapy in patients with newly diagnosed glioblastoma with methylated MGMT promotor (CeTeG/NOA-09): a randomised, open-label, phase 3 trial. *Lancet*, 393:678–688, 2019. doi: 10.1016/S0140-6736(18)31791-4.

W Herzog and K Weber. Fractionation of brain microtubule-associated proteins. Isolation of two different proteins which stimulate tubulin polymerization in vitro. *Eur J Biochem*, 92:1–8, 1978.

K Hida, Y Hida, DN Amin, AF Flint, D Panigrahy, CC Morton, and M Klagsbrun. Tumor-associated endothelial cells with cytogenetic abnormalities. *Cancer Res*, 64: 8249–8255, 2004.

T Hide, Y Komohara, Y Miyasato, H Nakamura, K Makino, M Takeya, JI Kuratsu, A Mukasa, and S Yano. Oligodendrocyte Progenitor Cells and Macrophages/Microglia Produce Glioma Stem Cell Niches at the Tumor Border. *EBioMedicine*, 30:94–104, 2018. doi: 10.1016/j.ebiom.2018.02.024.

T Higuchi. Rate of release of medicaments from ointment bases containing drugs in suspension. *J Pharm Sci*, 50:874–875, 1961.

T Higuchi. Mechanisms of sustained action mediation. Theoretical analysis of rate of release of solid drugs dispersed in solid matrices. *J Pharm Sci*, 52:1145–1149, 1963.

MP Hiljanen-Vainio, PA Orava, and JV Seppaelae. Properties of epsilon-caprolactone/DL-lactide (epsilon-CL/DL-LA) copolymers with a minor epsilon-CL content. *J Biomed Mater Res*, 34:39–46, 1997.

Y Hirose, MS Berger, and RO Pieper. p53 effects both the duration of G2/M arrest and the fate of temozolomide-treated human glioblastoma cells. *Cancer Res*, 61: 1957–1963, 2001.

FH Hochberg and A Pruitt. Assumptions in the radiotherapy of glioblastoma. *Neurology*, 30:907–911, 1980.

DB Hoelzinger, T Demuth, and ME Berens. Autocrine factors that sustain glioma invasion and paracrine biology in the brain microenvironment. *J Natl Cancer Inst*, 99:1583–1593, 2007.

CP Hofstetter, JK Burkhardt, BJ Shin, DB Gürsel, L Mubita, R Gorrepati, C Brennan, EC Holland, and JA Boockvar. Protein phosphatase 2A mediates dormancy of glioblastoma multiforme-derived tumor stem-like cells during hypoxia. *PLoS one*, 7:e30059, 2012. doi: 10.1371/journal.pone.0030059.

PM Holland, RD Abramson, R Watson, and DH Gelfand. Detection of specific polymerase chain reaction product by utilizing 5'-3' exonuclease activity of Thermus aquaticus DNA polymerase. *Proc Natl Acad Sci U S A*, 88:7276–7280, 1991.

J Holländer, R Hakala, J Suominen, N Moritz, J Yliruusi, and N Sandler. 3D printed UV light cured polydimethylsiloxane devices for drug delivery. *Int J Pharma*, 544: 433–442, 2017. doi: 10.1016/j.ijpharm.2017.11.016.

X Hong, WC Sin, AL Harris, and CC Naus. Gap junctions modulate glioma invasion by direct transfer of microRNA. *Oncotarget*, 6:15566–15577, 2015. doi: 10.18632/oncotarget.3904.

CE Hughes and RJB Nibbs. A guide to chemokines and their receptors. *FEBS J*, pages 2944–2971, 2018. doi: 10.1111/febs.14466.

RJ Hunter, RH Ottewill, and RL Rowell. *Zeta Potential in Colloid Science: Principles and Applications*. Elsevier Science, 2013. ISBN 9781483214085.

SF Hussain, D Yang, D Suki, K Aldape, E Grimm, and AB Heimberger. The role of human glioma-infiltrating microglia/macrophages in mediating antitumor immune response. *Neurooncology*, 8:261–279, 2006.

GWH Höhne, WF Hemminger, and HJ Flammersheim. *Differential Scanning Calorimetry*. Springer Verlag, Berlin, Heidelberg, 2003.

I Hölken, G Neubüser, V Postica, L Bumke, O Lupan, M Baum, YK Mishra, L Kienle, and R Adelung. Sacrificial Template Synthesis and Properties of 3D Hollow-Silicon Nano- and Microstructures. *ACS Appl Mater Interfaces*, 8:20491–20498, 2016. doi: 10.1021/acsami.6b06387.

K Ichimura, DM Pearson, S Kocialkowski, LM Bäcklund, R Chan, DT Jones, and VPC Collins. IDH1 mutations are present in the majority of common adult gliomas but rare in primary glioblomastas. *Neuro Oncol*, 11:341–347, 2009. doi: 10.1215/15228517-2009-025.

M Ignatova, N Manolova, R Toshkova, I Rashkov, E Gardeva, L Yossifova, and M Alexandrov. Quaternized chitosan-coated nanofibrous materials containing gossypol: preparation by electrospinning, charachterization and antiproliferative activity towards HeLa cells. *Int J Pharm*, 436:10–24, 2012. doi: 10.1016/j.ijpharm.2012.06.035.

M Ignatova, K Kalinov, N Manolova, R Toshkova, I Rashkov, and M Alexandrov. Quaternized chitosan-coated nanofibrous implants loaded with gossypol prepared by electrospinning and their efficacy against Graffi myeloid tumor. *J Biomater Sci Polym Ed*, 25:287–306, 2014. doi: 10.1080/09205063.2013.857543.

M Ishido, ST Homma, PS Leung, and C Tohyama. Cadmium-induced DNA fragmentation is inhibitable by zinc in porcine kidney LLC-PK1 cells. *Life Sci*, 56:351–356, 1995.

E Jablonowska, E Nazaruk, D Matyszewska, C Speziale, R Mezzenga, EM Landau, and R Bilewicz. Interactions of Lipidic Cubic Phase Nanoparticles with Lipid Membranes. *Langmuir*, 32:9640–9648, 2016. doi: 10.1021/acs.langmuir.6b01746.

D Jain, A Bajaj, R Athawale, S Shrinkhande, PN Goel, Y Nikam, R Gude, S Patil, and P Prashant Raut. Surface-coated PLA nanoparticles loaded with temozolomide for improved brain deposition and potential treatment of gliomas: development, characterization and in vivo studies. *Drug Deliv*, 23:999–1016, 2016. doi: 10.3109/10717544.2014.926574.

DS Jain, RB Athawale, AN Bajaj, SS Shrikhande, PN Goel, Y Nikam, and RP Gude. Unraveling the cytotoxic potential of Temozolomide loaded into PLGA nanoparticles. *Daru*, 22:18, 2014. doi: 10.1186/2008-2231-22-18.

GH Jang and M Lee. BH3-mimetic gossypol-induced autophagic cell death in mutant BRAF melanoma cells with high expression of p21Cip1. *Life Sci*, 102:41–48, 2014. doi: 10.1016/j.lfs.2014.02.036.

Y Jang, N Lee, JH Kim, YI Park, and Y Piao. Shape-Controlled Synthesis of Au Nanostructures Using EDTA Tetrasodium Salt and Their Photothermal Therapy Applications. *Nanomaterials (Basel)*, 8:E252, 2018. doi: 10.3390/nano8040252.

MA Jarzabek, V Amberger-Murphy, JJ Callanan, C Gao, AM Zagozdzon, L Shiels, J Wang, KL Ligon, BE Rich, P Dicker, WM Gallagher, JH Prehn, and AT Byrne. Interrogation of gossypol therapy in glioblastoma implementing cell line and patient-derived tumour models. *Br J Cancer*, 111:2275–2286, 2014. doi: 10.1038/bjc.2014.529.

SI Jeong, BS Kim, SW Kang, JH Kwon, YM Lee, SH Kim, and YH Kim. In vivo biocompatibility and degradation behavior of elastic poly(L-lactide-co-epsilon-caprolactone) scaffolds. *Biomaterials*, 25:5939–5946, 2004.

L Jia, LC Coward, CD Kerstner-Wood, RL Cork, GS Gorman, PE Noker, S Kitada, M Pellecchia, and JC Reed. Comparison of pharmacokinetic and metabolic profiling among gossypol, apogossypol and apogossypol hexaacetate. *Cancer Chemother Pharmacol*, 61:63–73, 2008.

K Jiang, JD Weaver, Y Li, X Chen, J Liang, and CL Stabler. Local release of dexamethasone from macroporous scaffolds accelerates islet transplant engraftment by promotion of anti-inflammatory M2 macrophages. *Biomaterials*, 114:71–81, 2017. doi: 10.1016/j.biomaterials.2016.11.004.

CL Jin, ML Chen, Y Wang, XC Kang, GY Han, and SL Xu. Preparation of novel (-)-gossypol nanoparticles and the effect on growth inhibition in human prostate cancer PC-3 cells in vitro. *Exp Ther Med*, 9:675–678, 2015. doi: 10.3892/etm.2015.2172.

X Jin, E Nie, X Zhou, A Zeng, T Yu, T Zhi, K Jiang, Y Wang, J Zhang, and Y You. Fstl1 Promotes Glioma Growth Through the BMP4/Smad1/5/8 Signaling Pathway. *Cell Physiol Biochem*, 44:1616–1628, 2017. doi: 10.1159/000485759.

M Jinek, K Chylinski, I Fonfara, M Hauer, JA Doudna, and E Charpentier. A programmable dual-RNA-guided DNA endonuclease in adaptive bacterial immunity. *Science*, 337:816–821, 2012. doi: 10.1126/science.1225829.

EW Joffe and S Mudd. A Paradoxical Relation between Zeta Potential and Suspension Stability in S and R Variants of Intestinal Bacteria. *J Gen Physiol*, 18:599–613, 1935.

BE Johnson, T Mazor, C Hong, M Barnes, K Aihara, CY McLean, SD Fouse, S Yamamoto, H Ueda, K Tatsuno, S Asthana, LE Jalbert, SJ Nelson, AW Bollen, WC Gustafson, E Charron, WA Weiss, IV Smirnov, JS Song, AB Olshen, S Cha, Y Zhao, RA Moore, AJ Mungall, SJM Jones, M Hirst, MA Marra, N Saito, H Aburatani, A Mukasa, MS Berger, SM Chang, BS Taylor, and JF Costello. Mutational analysis reveals the origin and therapy-driven evolution of recurrent glioma. *Science*, 343:189–193, 2014. doi: 10.1126/science.1239947.

A Jordan, R Scholz, K Maier-Hauff, FK van Landeghem, N Waldoefner, U Teichgraeber, J Pinkernelle, H Bruhn, F Neumann, B Thiesen, A von Deimling, and R Felix. The effect of thermotherapy using magnetic nanoparticles on rat malignant glioma. *J Neurooncol*, 78:7–14, 2006.

JV Joseph, S Conroy, K Pavlov, P Sontakke, T Tomar, E Eggens-Meijer, V Balasubramaniyan, M Wagemakers, WF den Dunnen, and FA Kruyt. Hypoxia enhances migration and invasion in glioblastoma by promoting a mesenchymal shift mediated by the HIF1α-ZEB1 axis. *Cancer Lett*, 359:107–116, 2015. doi: 10.1016/j.canlet.2015.01.010.

P Játiva and V Ceña. Use of nanoparticles for glioblastoma treatment: a new approach. *Nanomedicine (Lond)*, 12:2533–2554, 2017. doi: 10.2217/nnm-2017-0223.

A Jõers, N Kaldalu, and T Tenson. The frequency of persisters in Escherichia coli reflects the kinetics of awakening from dormancy. *J Bacteriol*, 192:3379–3384, 2010. doi: 10.1128/JB.00056-10.

T Kanzawa, J Bedwell, Y Kondo, S Kondo, and IM Germano. Inhibition of DNA repair for sensitizing resistant glioma cells to temozolomide. *J Neurosurg*, 99:1047–1052, 2003.

T Kanzawa, IM Germano, T Komata, H Ito, Y Kondo, and S Kondo. Role of autophagy in temozolomide-induced cytotoxicity for malignant glioma cells. *Cell Death Differ*, 11:448–457, 2004.

I Karlsson, D Veevnik, A Fedulov, N Yurkshtovich, T Yurkshtovich, G Pejler, and I Lokot. Local delivery of temozolomide via a biologically inert carrier (Temodex) prolongs survival in glioma patients, irrespectively of the methylation status of MGMT. *Neoplasma*, 66:288–293, 2019. doi: 10.4149/neo_2018_180613N393.

N Kartner, JR Riordan, and V Ling. Cell surface P-glycoprotein associated with multidrug resistance in mammalian cell lines. *Science*, 221:1285–1288, 1983.

JA Kenar. Reaction chemistry of gossypol and its derivatives. *J Am Oil Chem' Soc*, 83:269–302, 2006. doi: 10.1007/s11746-006-1203-1.

S Kenig, MB Alonso, MM Mueller, and TT Lah. Glioblastoma and endothelial cells cross-talk, mediated by SDF-1, enhances tumour invasion and endothelial proliferation by increasing expression of cathepsins B, S, and MMP-9. *Cancer Lett*, 289: 53–61, 2010. doi: 10.1016/j.canlet.2009.07.014.

JF Kerr, AH Wyllie, and AR Currie. Apoptosis: a basic biological phenomenon with wide-ranging implications in tissue kinetics. *Br J Cancer*, 26:239–257, 1972.

H Keshmiri-Neghab, B Goliaei, and A Nikoofar. Gossypol enhances radiation induced autophagy in glioblastoma multiforme. *Gen Physiol Biophys*, 33:433–442, 2014. doi: 10.4149/gpb_2014017.

AS Khazali, AM Clark, and A Wells. Inflammatory cytokine IL-8/CXCL8 promotes tumour escape from hepatocyte-induced dormancy. *Br J Cancer*, 118:566–576, 2018. doi: 10.1038/bjc.2017.414.

H Kim, LI Binder, and JL Rosenbaum. The periodic association of MAP2 with brain microtubules in vitro. *J Cell Biol*, 80:266–276, 1979.

JE Kim, H Kim, SS An, EH Maeng, MK Kim, and YJ Song. In vitro cytotoxicity of SiO2 or ZnO nanoparticles with different sizes and surface charges on U373MG human glioblastoma cells. *Int J Nanomedicine*, 9:235–241, 2014. doi: 10.2147/IJN.S57936.

S Kitada, M Leone, S Sareth, D Zhai, JC Reed, and M Pellecchia. Discovery, characterization, and structure-activity relationships studies of proapoptotic polyphenols targeting B-cell lymphocyte/leukemia-2 proteins. *J Med Chem*, 46:4259–4264, 2003.

H Kobayashi, R Watanabe, and PL Choyke. Improving conventional enhanced permeability and retention (EPR) effects; what is the appropriate target? *Theranostics*, 11:81–89, 2013. doi: 10.7150/thno.7193.

CM Koebel, W Vermi, JB Swann, N Zerafa, SJ Rodig, LJ Old, MJ Smyth, and RD Schreiber. Adaptive immunity maintains occult cancer in an equilibrium state. *Nature*, 450:903–907, 2007.

Y Komohara, K Ohnishi, J Kuratsu, and M Takeya. Possible involvement of the M2 anti-inflammatory macrophage phenotype in growth of human gliomas. *J Pathol*, 216:15–24, 2008. doi: 10.1002/path.2370.

FW Kreth, PC Warnke, and CB Ostertag. The limited value of cytoreductive surgery in elderly patients with malignant gliomas. *Neurosurgery*, 35:344–345, 1994.

FW Kreth, N Thon, M Simon, M Westphal, G Schackert, G Nikkhah, B Hentschel, G Reifenberger, T Pietsch, M Weller, JC Tonn, and German Glioma Network. Gross total but not incomplete resection of glioblastoma prolongs survival in the era of radiochemotherapy. *Ann Oncol*, 24:3117–3123, 2013. doi: 10.1093/annonc/mdt388.

J Kreuter and S Gelperina. Use of nanoparticles for cerebral cancer. *Tumori*, 94: 271–277, 2008.

J Kreuter, P Ramge, V Petrov, S Hamm, SE Gelperina, B Engelhardt, R Alyautdin, H von Briesen, and DJ Begley. Direct evidence that polysorbate-80-coated poly(butylcyanoacrylate) nanoparticles deliver drugs to the CNS via specific mechanisms requiring prior binding of drug to the nanoparticles. *Pharm Res*, 20:409–416, 2003.

S Kunwar, MD Prados, SM Chang, MS Berger, FF Lang, JM Piepmeier, JH Sampson, Z Ram, PH Gutin, RD Gibbons, KD Aldape, DJ Croteau, JW Sherman, RK Puri, and Cintredekin Besudotox Intraparenchymal Study Group. Direct intracerebral delivery of cintredekin besudotox (IL13-PE38QQR) in recurrent malignant glioma: a report by the Cintredekin Besudotox Intraparenchymal Study Group. *J Clin Oncol*, 25:837–844, 2007.

PJ Kuppen, MM van der Eb, LE Jonges, M Hagenaars, ME Hokland, U Nannmark, RH Goldfarb, PH Basse, GJ Fleuren, RC Hoeben, and CJ van de Velde. Tumor structure and extracellular matrix as a possible barrier for therapeutic approaches using immune cells or adenoviruses in colorectal cancer. *Histochem Cell Biol*, 115: 67–72, 2001.

SM Kwon, SH Kang, CK Park, S Jung, ES Park, JS Lee, SH Kim, and HG Woo. Recurrent Glioblastomas Reveal Molecular Subtypes Associated with Mechanistic Implications of Drug-Resistance. *PLoS One*, 10:e0140528, 2015. doi: 10.1371/journal.pone.0140528.

K Larsson. Two cubic phases in monoolein-water system. *Nature*, 304:664, 1983.

SM Laster and JM Jr Mackenzie. Bleb formation and F-actin distribution during mitosis and tumor necrosis factor-induced apoptosis. *Microsc Res Tech*, 34:272–280, 1996.

DM Le, A Besson, DK Fogg, KS Choi, DM Waisman, CG Goodyer, B Rewcastle, and VW Yong. Exploitation of astrocytes by glioma cells to facilitate invasiveness: a mechanism involving matrix metalloproteinase-2 and the urokinase-type plasminogen activator-plasmin cascade. *J Neurosci*, 23:4034–4043, 2003.

HK Lee, C Xiang, S Cazacu, S Finniss, G Kazimirsky, N Lemke, NL Lehmann, SA Rempel, T Mikkelsen, and C Brodie. GRP78 is overexpressed in glioblastomas and regulates glioma growth and apoptosis. *Neuro Oncol*, 10:236–243, 2008. doi: 10.1215/15228517-2008-0006.

J Lee, S Kotliarova, Y Kotliarov, A Li, Q Su, NM Donin, S Pastorino, BW Purow, N Christopher, W Zhang, JK Park, and HA Fine. Tumor stem cells derived from glioblasotmas cultured in bFGF and EGF more closely mirror the phenotype and genotype of primary tumors than do serum-cultured cell lines. *Cancer Cell*, 9: 391–403, 2006.

JN Lee, C Park, and GM Whitesides. Solvent compatibility of poly(dimethylsiloxane)-based microfluidic devices. *Anal Chem*, 75:6544–6554, 2003.

S Lee and DM Helfman. Cytoplasmic p21Cip1 is involved in Ras-induced inhibition of the ROCK/LIMK/cofilin pathway. *J Biol Chem*, 279:1885–1891, 2004.

SW Lee, HK Kim, NH Lee, HY Yi, HS Kim, SH Hong, YK Hong, and YA Joe. The synergistic effect of combination temozolomide and chloroquine treatment is dependent on autophagy formation and p53 status in glioma cells. *Cancer Lett*, 360:195–204, 2015a. doi: 10.1016/j.canlet.2015.02.012.

SW Lee, HK Kim, NH Lee, HY Yi, HS Kim, SH Hong, YK Hong, and YA Joe. The synergistic effect of combination temozolomide and chloroquine treatment is dependent on autophagy formation and p53 status in glioma cells. *Cancer Lett*, 360:195–204, 2015b. doi: 10.1016/j.canlet.2015.02.012.

WS Lee, WH Yoo, and HJ Chae. ER Stress and Autophagy. *Curr Mol Med*, 15: 735–745, 2015c.

R Leece, J Xu, QT Ostrom, Y Chen, C Kruchko, and JS Barnholtz-Sloan. Global incidence of malignant brain and other central nervous system tumors by histology, 2003-2007. *Neuro Oncol*, 19:1553–1564, 2017. doi: 10.1093/neuonc/nox091.

AM Lengsfeld, I Loew, T Wieland, P Dancker, and W Hasselbach. Interaction of phalloidin with actin. *Proc Natl Acad Sci U S A*, 71:2803–2807, 1974.

K Lenting, R Verhaak, M Ter Laan, P Wesseling, and W Leenders. Glioma: experimental models and reality. *Acta Neuropathol*, 133:263–282, 2017. doi: 10.1007/s00401-017-1671-4.

F Lepore, G D'Alessandro, F Antonangeli, A Santoro, V Esposito, C Limatola, and F Trettel. CXCL16/CXCR6 Axis Drives Microglia/Macrophages Phenotype in Physiological Conditions and Plays a Crucial Role in Glioma. *Front Immunol*, 9:2750, 2018. doi: 10.3389/fimmu.2018.02750.

DW Leung, G Cachianes, WJ Kuang, DV Goeddel, and N Ferrara. Vascular endothelial growth factor is a secreted angiogenic mitogen. *Science*, 246:1306–1309, 1989.

H Li, L Piao, P Xu, W Ye, S Zhong, SH Lin, SK Kulp, Y Mao, Y Cho, LJ Lee, RJ Lee, and YC Lin. Liposomes containing (-)-gossypol-enriched cottenseed oil

suppress Bcl-2 and Bcl-xL expression in breast cancer cells. *Pharm Res*, 28:3256–3264, 2011a. doi: 10.1007/s11095-011-0498-2.

J Li, M Wang, M Won, EG Shaw, C Coughlin, WJ Jr Curran, and MP Mehta. Validation and simplification of the Radiation Therapy Oncology Group recursive partitioning analysis classification for glioblastoma. *Int J Radiat Oncol Biol Phys*, 81:623–630, 2011b. doi: 10.1016/j.ijrobp.2010.06.012.

XT Li, RJ Ju, XY Li, F Zeng, JF Shi, L Liu, CX Zhang, MG Sun, JN Lou, and WL Lu. Multifunctional targeting daunorubicin plus quinacrine liposomes, modified by wheat germ agglutinin and tamoxifen, for treating brain glioma and glioma stem cells. *Oncotarget*, 5:6497–6511, 2014. doi: 10.18632/oncotarget.2267.

C Liao, Y Li, and SC Tjong. Graphene Nanomaterials: Synthesis, Biocompatibility, and Cytotoxicity. *Int J Mol Sci*, 19:E3564, 2018. doi: 10.3390/ijms19113564.

Z Lidar, Y Mardor, T Jonas, R Pfeffer, M Faibel, D Nass, M Hadani, and Z Ram. Convection-enhanced delivery of paclitaxel for the treatment of recurrent malignant glioma: a phase I/II clinical study. *J Neurosurg*, 100:472–479, 2004.

CJ Lin, CC Lee, YL Shih, TY Lin, SH Wang, YF Lin, and CM Shih. Resveratol enhances the therapeutic effect of temozolomide against malignant glioma in vitro and in vivo by inhibiting autophagy. *Free Radic Biol Med*, 52:42998, 2012. doi: 10.1016/j.freeradbiomed.2011.10.487.

CY Lin, RJ Li, CY Huang, KC Wei, and PY Chen. Controlled release of liposome-encapsulated temozolomide for brain tumour treatment by convection-enhanced delivery. *J Drug Target*, 26:325–332, 2018. doi: 10.1080/1061186X.2017.1379526.

Q Lin, Z Liu, F Ling, and G Xu. Astrocytes protect glioma cells from chemotherapy and upregulate survival genes via gap junctional communication. *Mol Med Rep*, 13: 1329–1335, 2016. doi: 10.3892/mmr.2015.4680.

B Linder, A Wehle, S Hehlgans, F Bonn, I Dikic, F Roedel, V Seifert, and D Kögel. Arsenic Trioxide and (-)-Gossypol Synergistically Target Glioma Stem-Like Cells via Inhibition of Hedgehog and Notch Signaling. *Cancers (Basel)*, 11:E350, 2019. doi: 10.3390/cancers11030350.

H Liu, K Li, L Lan, J Ma, Y Zeng, L Xu, and D Wu. Double-layered hyaluronic acid/stearic acid-modified polyethylenimine nanoparticles encapsulating (-)-gossypol: a nanocarrier for chiral anticancer drugs. *J Mater Chem B*, 2: 5238–5248, 2014. doi: 10.1039/C4TB00539B.

T Liu, H Xu, M Huang, W Ma, D Saxena, RA Lustig, M Alonso-Basanta, Z Zhang, DM O'Rourke, L Zhang, Y Gong, GD Kao, JF Dorsey, and Y Fan. Circulating Glioma Cells Exhibit Stem Cell-like Properties. *Cancer Res*, 78:6632–6642, 2018. doi: 10.1158/0008-5472.CAN-18-0650.

XY Liu, L Zhang, J Wu, L Zhou, YJ Ren, WQ Yang, ZJ Ming, B Chen, J Wang, Y Zhang, and JM Yang. Inhibition of elongation factor-2 kinase augments the antitumor activity of Temozolomide against glioma. *PLoS One*, 8:e81345, 2013. doi: 10.1371/journal.pone.0081345.

Y Liu, E Carson-Walter, and KA Walter. Targeting chemokine receptor CXCR7 inhibits glioma cell proliferation and mobility. *Anticancer Res*, 35:53–64, 2015.

H Ljusberg-Wahren, L Nyberg, and K Larsson. Dispersion of the cubic liquid crystalline phase - Structure, preparation and functionality aspects. *Chim Oggi*, 14:40, 1996.

IC Lopes, SCB de Oliveira, and AM Oliveira-Brett. Temozolomide chemical degradation to 5-aminoimidazole-4-carboxamide - Electrochemical study. *J Electroanalytical Chemistry*, 704:183–189, 2013. doi: 10.1016/j.jelechem.2013.07.011.

DN Louis, A Deimling, RY Chung, MP Rubio, JM Whaley, RH Eibl, H Ohgaki, OD Wiestler, AD Thor, and BR Seizinger. Comparative study of p53 gene and protein alterations in human astrocytic tumors. *J Neuropathol Exp Neurol*, 52: 31–38, 1993.

DN Louis, A Perry, G Reifenberger, A von Deimling, D Figarella-Branger, WK Cavenee, H Ohgaki, OD Wiestler, P Kleihues, and DW Ellison. The 2016 World Health Organization Classification of Tumors of the Central Nervous System: a summary. *Acta Neuropathol*, 131:803–820, 2016. doi: 10.1007/s00401-016-1545-1.

DR Lu, SC Mehta, and W Chen. Selective boron drug delivery to brain tumors for boron neutron capture therapy. *Adv Drug Deliv Rev*, 26:231–247, 1997.

C Lu-Emerson, M Snuderl, ND Kirkpatrick, J Goveia, C Davidson, Y Huang, L Riedemann, J Taylor, P Ivy, DG Duda, M Ancukiewicz, SR Plotkin, AS Chi, ER Gerstner, AF Eichler, J Dietrich, AO Stemmer-Rachamimov, TT Batchelor, and RK Jain. Increase in tumor-associated macrophages after antiangiogenic therapy is associated with poor survival among patients with recurrent glioblastoma. *Neuro Oncol*, 15: 1079–1087, 2013. doi: 10.1093/neuonc/not082.

A Ludwig and R Mentlein. Glial cross-talk by transmembrane chemokines CX3CL1 and CXCL16. *J Neuroimmunol*, 198:92–97, 2008. doi: 10.1016/j.jneuroim.2008.04.024.

A Ludwig, A Schulte, C Schnack, C Hundhausen, K Reiss, N Brodway, J Held-Feindt, and R Mentlein. Enhanced expression and shedding of the transmembrane chemokine CXCL16 by reactive astrocytes and glioma cells. *J Neurochem*, 93:1293–1303, 2005.

X Lun, JC Wells, N Grinshtein, JC King, X Hao, NH Dang, X Wang, A Aman, D Uehling, A Datti, JL Wrana, JC Easaw, A Luchman, S Weiss, JG Cairncross, DR Kaplan, SM Robbins, and DL Senger. Disulfiram when Combined with Copper Enhances the Therapeutic Effects of Temozolomide for the Treatment of Glioblastoma. *Clin Cancer Res*, 22:3860–3875, 2016. doi: 10.1158/1078-0432.CCR-15-1798.

ES Lutton. Phase behavior of aqueous systems of monoglycerides. *J Am Oil Chem Soc*, 42:1068–1070, 1965.

YH Ma, R Mentlein, F Knerlich, ML Kruse, HM Mehdorn, and J Held-Feindt. Expression of stem cell markers in human astrocytomas of different WHO grades. *J Neurooncol*, 86:31–45, 2008.

RM MacKie, R Reid, and B Junor. Fatal melanoma transferred in a donated kidney 16 years after melanoma surgery. *N Engl J Med*, 348:567–568, 2003.

H Maeda, H Nakamura, and J Fang. The EPR effect for macromolecular drug delivery to solid tumors: Improvement of tumor uptake, lowering of systemic toxicity, and distinct tumor imaging in vivo. *Adv Drug Deliv Rev*, 65:71–79, 2013. doi: 10.1016/j.addr.2012.10.002.

L Maggini, I Cabrera, A Ruiz-Carretero, EA Prasetyanto, E Robinet, and L De Cola. Breakable mesoporous silica nanoparticles for targeted drug delivery. *Nanoscale*, 8: 7240–7247, 2016. doi: 10.1039/c5nr09112h.

N Magnus, D Garnier, B Meehan, S McGraw, TH Lee, M Caron, G Bourque, C Milsom, N Jabado, J Trasler, R Pawlinski, N Mackman, and J Rak. Tissue factor expression provokes escape from tumor dormancy and leads to genomic alterations. *Proc Natl Acad Sci U S A*, 111:3544–3549, 2014. doi: 10.1073/pnas.1314118111.

P Maincent, R Le Verge, P Sado, P Couvreur, and JP Devissaguet. Disposition kinetics and oral bioavailability of vincamine-loaded polyalkyl cyanoacrylate nanoparticles. *J Pharm Sci*, 75:955–958, 1986.

CR Mantel, VM Gelfano, YJ Kim, A McDaniel, Y Lee, HS Boswell, and HE Broxmeyer. P21waf-1-Chk1 pathway monitors G1 phase microtubule integrity and is crucial for restriction point transition. *Cell Cycle*, 1:327–336, 2002.

P Mao, K Joshi, J Li, SH Kim, P Li, L Santana-Santos, S Luthra, UR Chandran, PV Benos, L Smith, M Wang, B Hu, SY Cheng, RW Sobol, and I Nakano. Mesenchymal glioma stem cells are maintained by activated glycolytic metabolism involving aldehyde dehydrogenase 1A3. *Proc Natl Acad Sci U S A*, 110:8644–8649, 2013. doi: 10.1073/pnas.1221478110.

R Marches, RH Scheuermann, and JW Uhr. Cancer dormancy: role of cyclin-dependent kinase inhibitors in induction of cell cycle arrest mediated via membrane IgM. *Cancer Res*, 58:691–697, 1998.

R Marches, R Hsueh, and JW Uhr. Cancer dormancy and cell signaling: induction of p21(waf1) initiated by membrane IgM engagement increases survival of B lymphoma cells. *Proc Natl Acad Sci U S A*, 96:8711–8715, 1999.

B Marciniak, H Kozubek, J Koput, and S Paszyc. Spectroscopic and Photochemical Studies of Gossypol in Solution. Technical report, Faculty of Chemistry, A. Mickiewicz University, Poznan, Poland, 1989.

A Marinelli, G Lamberti, L Cerbone, N Cordua, C Buonerba, G Peluso, G Di Lorenzo, and S De Placido. High-dose fotemustine in temozolomide-pretreated glioblastoma multiforme patients: A phase I/II trial. *Medicine(Baltimore)*, 97:e11254, 2018. doi: 10.1097/MD.0000000000011254.

DD Martin, ME Robbins, AA Spector, BC Wen, and DH Hussey. The fatty acid composition of human gliomas differs from that found in nonmalignant brain tissue. *Lipids*, 31:1283–1288, 1996.

D Matias, J Balça-Silva, GC da Graça, CM Wanjiru, LW Macharia, CP Nascimento, NR Roque, JM Coelho-Aguiar, CM Pereira, MF Dos Santos, LS Pessoa, FRS Lima, A Schanaider, VP Ferrer, Tania Cristina Leite de Sampaio e Spohr, and V Moura-Neto. Microglia/Astrocytes-Glioblastoma Crosstalk: Crucial Molecular Mechanisms and Microenvironmental Factors. *Front Cell Neurosci*, 3:235, 2018. doi: 10.3389/fncel.2018.00235.

Y Matsumura and H Maeda. A new concept for macromolecular therapeutics in cancer chemotherapy: mechanism of tumoritropic accumulation of proteins and the antitumor agent smancs. *Cancer Res*, 46:6387–6392, 1986.

KD McCullough, JL Martindale, LO Klotz, TY Aw, and NJ Holbrook. Gadd153 sensitizes cells to endoplasmatic reticulum stress by down-regulating Bcl2 and pertubing the cellular redox state. *Mol Cell Biol*, 21:1249–1259, 2001.

MJ McGirt, KL Chaichana, M Gathinji, FJ Attenello, K Than, A Olivi, JD Weingart, H Brem, and Quiñones-Hinojosa AR. Independent association of extent of resection with survival in patients with malignant brain astrocytoma. *J Neurosurg*, 110:156–162, 2009a. doi: 10.3171/2008.4.17536.

MJ McGirt, KD Than, JD Weingart, KL Chaichana, FJ Attenello, A Olivi, J Laterra, LR Kleinberg, SA Grossman, H Brem, and A Quinones-Hinojosa. Gliadel (BCNU) wafer plus concomitant temozolomide therapy after primary resection of glioblastoma multiforme. *J Neurosurg*, 110:583–588, 2009b. doi: 10.3171/2008.5.17557.

L Meer, RC Janzer, P Kleihues, and GF Kolar. In vivo metabolism and reaction with DNA of the cytostatic agent, 5-(3,3-dimethyl-1-triazeno)imidazole-4-carboxamide (DTIC). *Biochem Pharmacol*, 35:3243–3247, 1986.

AM Mehta, AM Sonabend, and JN Bruce. Convection-Enhanced Delivery. *Neurotherapeutics*, 14:358–371, 2017. doi: 10.1007/s13311-017-0520-4.

P Menei, L Capelle, J Guyotat, S Fuentes, R Assaker, B Bataille, P Francois, D Dorwling-Carter, P Paguis, L Bauchet, F Parker, J Sabatier, N Faisant, and JP Benoit. Local and sustained delivery of 5-fluorouracil from biodegradable microspheres for the radiosensitization of malignant glioma: a randomized phase II trial. *Neurosurgery*, 56:242–248, 2005.

N Meyer, S Zielke, JB Michaelis, B Linder, V Warnsmann, S Rakel, HC Osiewacz, S Fulda, M Mittelbronn, C Münch, C Behrends, and D Kögel. AT 101 induces early mitochondrial dysfunction and HMOX1 (heme oxygenase 1) to trigger mitophagic cell death in glioma cells. *Autophagy*, 14:1693–1709, 2018. doi: 10.1080/15548627.2018.1476812.

N Mezzaroba, S Zorzet, E Secco, S Biffi, C Tripodo, M Calvaruso, R Mendoza-Maldonado, S Capolla, M Granzotto, R Spretz, G Larsen, S Noriega, M Lucafò, E Mansilla, C Garrovo, GH Marin, G Baj, V Gattei, G Pozzato, L Núñez, and P Macor. New potential therapeutic approach for the treatment of B-Cell malignancies using chlorambucil/hydroxychloroquine-loaded anti-CD20 nanoparticles. *PLoS Once*, 8:e74216, 2013. doi: 10.1371/journal.pone.0074216.

PJ Miller, RS Hassanein, PG Giri, BF Kimler, P O'Boynick, and RG Evans. Univariate and multivariate statistical analysis of high-grade gliomas: the relationship of radiation dose and other prognostic factors. *Int J Radiat Oncol Biol Phys*, 19: 275–280, 1990.

YK Mishra, S Kaps, A Schuchardt, I Paulowicz, X Jin, D Gedamu, S Freitag, M Claus, S Wille, A Kovalev, SN Gorb, and R Adelung. Fabrication of Macroscopically Flexible and Highly Porous 3D Semiconductor Networks from Interpenetrating Nanostructures by a Simple Flame Transport Approach. *Part Part Syst Char*, 30:775–783, 2013. doi: 10.1002/ppsc.201300197.

YK Mishra, G Modi, V Cretu, V Postica, O Lupan, T Reimer, I Paulowicz, V Hrkac, W Benecke, L Kienle, and R Adelung. Direct Growth of Freestanding ZnO Tetrapod Networks for Multifunctional Applications in Photocatalysis, UV Photodetection, and Gas Sensing. *ACS Appl Mater Interfaces*, 7:14303–14316, 2015. doi: 10.1021/acsami.5b02816.

D Mittal, MM Gubin, RD Schreiber, and MJ Smyth. New insights into cancer immunoediting and its three component phases–elimination, equilibrium and escape. *Curr Opin Immunol*, 27:16–25, 2014. doi: 10.1016/j.coi.2014.01.004.

WL Monsky, D Fukumura, T Gohongi, M Ancukiewcz, HA Weich, VP Torchilin, F Yuan, and RK Jain. Augmentation of transvascular transport of macromolecules and nanoparticles in tumors using vascular endothelial growth factor. *Cancer Res*, 59:4129–4135, 1999.

JH Moon, S Kwon, EK Jun, A Kim, KY Whang, H Kim, S Oh, BS Yoon, and S You. Nanog-induced dedifferentiation of p53-deficient mouse astrocytes into brain cancer stem-like cells. *Biochem Biophys Res Commun*, 412:175–181, 2011. doi: 10.1016/j.bbrc.2011.07.070.

RA Morantz, GW Wood, M Foster, M Clark, and K Gollahon. Macrophages in experimental and human brain tumors. Part 2: studies of the macrophage content of human brain tumors. *J Neurosurg*, 50:305–311, 1979.

E Mostaed, M Sikora-Jasinska, JW Drelich, and M Vedani. Zinc-based alloys for degradable vascular stent applications. *Acta Biomater*, 71:1–23, 2018. doi: 10.1016/j.actbio.2018.03.005.

LL Muldoon, C Soussain, K Jahnke, C Johanson, T Siegal, QR Smith, WA Hall, K Hynynen, PD Senter, DM Peereboom, and EA Neuwelt. Chemotherapy delivery issues in central nervous system malignancy: a reality check. *J Clin Oncol*, 25: 2295–2305, 2007.

JL Munoz, V Rodriguez-Cruz, SJ Greco, V Nagula, KW Scotto, and P Rameshwar. Temozolomide induces the production of epidermal growth factor to regulate MDR1 expression in glioblastoma cells. *Mol Cancer Ther*, 13:2399–23411, 2014. doi: 10.1158/1535-7163.MCT-14-0011.

JD Murray. Glioblastoma brain tumours: estimating the time from brain tumour initiation and resolution of a patient survival anomaly after similar treatment protocols. *J Biol Dyn*, 6:118–127, 2012.

C Müller, J Holtschmidt, M Auer, E Heitzer, K Lamszus, A Schulte, J Matschke, S Langer-Freitag, C Gasch, M Stoupiec, O Mauermann, S Peine, M Glatzel, MR Speicher, JB Geigl, M Westphal, K Pantel, and S Riethdorf. Hematogenous dissemination of glioblastoma multiforme. *Sci Transl Med*, 6:247ra101, 2014. doi: 10.1126/scitranslmed.3009095.

M Nakada, H Miyamori, D Kita, T Takahashi, J Yamashita, H Sato, R Miura, Y Yamaguchi, and Y Okada. Human glioblastomas overexpress ADAMTS-5 that degrades brevican. *Acta Neuropathol*, 110:239–246, 2005.

EA Nance, GF Woodworth, KA Sailor, TY Shih, Q Xu, G Swaminathan, D Xiang, C Eberhart, and J Hanes. A dense poly(ethylene glycol) coating improves penetration of large polymeric nanoparticles within brain tissue. *Sci Transl Med*, 4: 149ra119, 2012. doi: 10.1126/scitranslmed.3003594.

M Nasr, MK Ghorab, and A Abdelazem. In vitro and in vivo evaluation of cubosomes containing 5-fluorouracil for liver targeting. *Acta Pharm Sin B*, 5:79–88, 2015. doi: 10.1016/j.apsb.2014.12.001.

GN Naumov, IC MacDonald, PM Weinmeister, N Kerkvliet, KV Nadkarni, SM Wilson, VL Morris, AC Groom, and AF Chambers. Persistence of solitary mammary carcinoma cells in a secondary site: a possible contributor to dormancy. *Cancer Res*, 62:2162–2168, 2002.

GN Naumov, JL Townson, IC MacDonald, SM Wilson, VH Bramwell, AC Groom, and AF Chambers. Ineffectiveness of doxorubicin treatment on solitary dormant mammary carcinoma cells or late-developing metastases. *Breast Cancer Res Treat*, 82:199–206, 2003.

GN Naumov, E Bender, D Zurakowski, SY Kang, D Sampson, E Flynn, RS Watnick, O Straume, LA Akslen, J Folkman, and N Almog. A model of human tumor dormancy: an angiogenic switch from the nonangiogenic phenotype. *J Natl Cancer Inst*, 98:316–325, 2006.

ES Newlands, GR Blackledge, JA Slack, GJ Rustin, DB Smith, NS Stuart, CP Quarterman, R Hoffman, MF Stevens, and MH Brampton. Phase I trial of temozolomide (CCRG 81045:M&B 39831: NSC 362856. *Br J Cancer*, 65:287–291, 1992.

J Nichols, B Zevnik, K Anastassiadis, H Niwa, D Klewe-Nebenius, I Chambers, H Schoeler, and A Smith. Formation of pluripotent stem cells in the mammalian embryo depends on the POU transcription factor Oct4. *Cell*, 95:379–391, 1998.

E Nie, F Miao, X Jin, W Wu, X Zhou, A Zeng, T Yu, T Zhi, Z Shi, Y Wang, J Zhang, N Liu, and Y You. Fstl1/DIP2A/MGMT signaling pathway plays important roles in temozolomide resistance in glioblastoma. *Oncogene*, 38:2706–2721, 2019. doi: 10.1038/s41388-018-0596-2.

S Nobusawa, T Watanabe, P Kleihues, and Ohgaki H. IDH1 mutations as molecular signature and predictive factor of secondary glioblastomas. *Clin Cancer Res*, 15: 6002–6007, 2009. doi: 10.1158/1078-0432.CCR-09-0715.

K Nobutani, Y Shimono, K Mizutani, Y Ueda, T Suzuki, M Kitayama, A Minami, K Momose, K Miyawaki, K Akashi, T Azuma, and Y Takai. Downregulation of CXCR4 in Metastasized Breast Cancer Cells and Implication in Their Dormancy. *PLoS One*, 10, 2015. doi: 10.1371/journal.pone.0130032.

MM Nordling-David, R Yaffe, D Guez, H Meirow, D Last, E Grad, S Salomon, S Sharabi, Y Levi-Kalisman, G Golomb, and Y Mardor. Liposomal temozolomide drug delivery using convection enhanced delivery. *J Control Release*, 261:138–146, 2017. doi: 10.1016/j.jconrel.2017.06.028.

G Noël, R Schott, S Froelich, MP Gaub, P Boyer, D Fischer-Lokou, P Dufour, P Kehrli, and D Maitrot. Retrospective comparison of chemoradiotherapy followed by adjuvant chemotherapy, with or without prior gliadel implantation (carmustine) after initial surgery in patients with newly diagnosed high-grade gliomas. *Int J Radiat Oncol Biol Phys*, 82:749–755, 2012. doi: 10.1016/j.ijrobp.2010.11.073.

JW Oh, K Drabik, O Kutsch, C Choi, A Tousson, and EN Benveniste. CXC chemokine receptor 4 expression and function in human astroglioma cells. *J Immunol*, 166: 2695–2704, 2001a.

JW Oh, K Drabik, O Kutsch, C Choi, A Tousson, and EN Benveniste. CXC chemokine receptor 4 expression and function in human astroglioma cells. *J Immunol*, 166: 2695–2704, 2001b.

H Ohgaki, P Dessen, B Jourde, S Horstmann, T Nishikawa, PL Di Patre, C Burkhard, D Schueler, NM Probst-Hensch, PC Maiorka, N Baeza, P Pisani, Y Yonekawa, MG Yasargil, UM Luetolf, and P Kleihues. Genetic pathways to glioblastoma: a population-based study. *Cancer Res*, 64:6892–6899, 2004.

T Okuda, T Tasaki, S Nakata, K Yamashita, H Yoshioka, S Izumoto, A Kato, and M Fujita. Efficacy of Combination Therapy with MET and VEGF Inhibitors for MET-overexpressing Glioblastoma. *Anticancer Res*, 37:3871–3876, 2017. doi: 10.21873/anticanres.11767.

AI Oliveira, SI Anjo, J Vieira de Castro, SC Serra, AJ Salgado, B Manadas, and BM Costa. Crosstalk between glial and glioblastoma cells trigger the g̈o-or-growp̈henotype of tumor cells. *Cell Commun Signal*, 15:37, 2017. doi: 10.1186/s12964-017-0194-x.

R Oliveira, C Christov, JS Guillamo, S de Bouard, S Palfi, L Venance, M Tardy, and M Peschanski. Contribution of gap junctional communication between tumor cells and astroglia to the invasion of the brain parenchyma by human glioblastomas. *BMC Cell Biol*, 6:7, 2005.

S Ostermann, C Csajka, T Buclin, S Leyvraz, F Lejeune, LA Decosterd, and R Stupp. Plasma and cerebrospinal fluid population pharmacokinetics of temozolomide in malignant glioma patients. *Clin Cancer Res*, 10:3728–3736, 2004.

QT Ostrom, H Gittleman, G Truitt, A Boscia, C Kruchko, and JS Barnholtz-Sloan. CBTRUS Statistical Report: Primary Brain and Other Central Nervous System Tumors Diagnosed in the United States in 2011-2015. *Neuro Oncol*, 20:iv1–iv86, 2018. doi: 10.1093/neuonc/noy131.

S Ostrovsky, G Kazimirsky, A Gedanken, and C Brodie. Selective cytotoxic effect of ZnO nanoparticles on glioma cells. *Nano Res*, 2:882–890, 2009. doi: 10.1007/s12274-009-9089-5.

S Paglin, T Hollister, T Delohery, N Hackett, M McMahill, E Sphicas, D Domingo, and J Yahalom. A novel response of cancer cells to radiation involves autophagy and formulation of acidic vesicles. *Cancer Res*, 61:439–444, 2001.

H Papavlassopoulos, YK Mishra, S Kaps, I Paulowicz, R Abdelaziz, M Elbahri, E Maser, R Adelung, and C Röhl. Toxicity of functional nano-micro zinc oxide tetrapods: impact of cell culture conditions, cellular age and material properties. *PLoS One*, 9:e84983, 2014. doi: 10.1371/journal.pone.0084983.

J Park, JK Shim, JH Kang, J Choi, JH Chang, SY Kim, and SG Kang. Regulation of bioenergetics through dual inhibition of aldehyde dehydrogenase and mitochondrial complex I suppresses glioblastoma tumorspheres. *Neuro Oncol*, 20:954–965, 2018. doi: 10.1093/neuonc/nox243.

M Pasha, M Reddy, and M Krishnappa. Zinc dust: An extremely active and reusable catalyst in acylation of phenols, thiophenols, amines and alcohols in a solvent-free system. *Euro J Chem*, 1:385–387, 2010. doi: 10.5155/eurjchem.1.4.385-387.90.

AP Patel, I Tirosh, JJ Trombetta, AK Shalek, SM Gillespie, H Wakimoto, DP Cahill, BV Nahed, WT Curry, RL Martuza, DN Louis, O Rozenblatt-Rosen, ML Suvà, A Regev, and BE Bernstein. Single-cell RNA-seq highlights intratumoral heterogeneity in primary glioblastoma. *Science*, 344:1396–1401, 2014. doi: 10.1126/science.1254257.

R Patil, J Portilla-Arias, H Ding, S Inoue, B Konda, J Hu, KA Wawrowsky, PK Shin, KL Black, E Holler, and JY Ljubimova. Temozolomide delivery to tumor cells by a multifunctional nano vehicle based on poly(β-L-malic acid). *Pharm Res*, 27: 2317–2329, 2010. doi: 10.1007/s11095-010-0091-0.

RP Patil, DD Pawara, CS Gudewar, and AR Tekade. Nanostructured cubosomes in an in situ nasal gel system: an alternative approach for the controlled delivery of donepezil HCl to brain. *J Liposome Res*, 2:264–273, 2018. doi: 10.1080/08982104.2018.1552703.

G Pearson, F Robinson, T Beers Gibson, BE Xu, M Karandikar, K Berman, and MH Cobb. Mitogen-activated protein (MAP) kinase pathways: regulation and physiological functions. *Endocr Rev*, 22:153–183, 2001.

E Pedraza, AC Brady, CA Fraker, and CL Stabler. Synthesis of macroporous poly(dimethylsiloxane) scaffolds for tissue engineering applications. *J Biomater Sci Polymer Ed*, 24:1041–1056, 2013. doi: 10.1080/09205063.2012.735097.

L Peignan, W Garrido, R Segura, R Melo, D Rojas, JG Carcamo, R San Martin, and C Quezada. Combined use of anticancer drugs and an inhibitor of multiple drug resistance-associated protein-1 increases sensitivity and decreases survival of glioblastoma multiforme cells in vitro. *Neurochem Res*, 36:1397–1406, 2011. doi: 10.1007/s11064-011-0464-8.

G Perazzoli, J Prados, R Ortiz, O Caba, L Cabeza, M Berdasco, B Gonzalez, and C Melguizo. Temozolomide Resistance in Glioblastoma Cell Lines: Implication of MGMT, MMR, P-Glycoprotein and CD133 Expression. *PLoS One*, 10:e0140131, 2015. doi: 10.1371/journal.pone.0140131.

AV Peskin and CC Winterbourn. A microtiter plate assay for superoxide dismutase using a water-soluble tetrazolium salt (WST-1). *Clin Chim Acta*, 293:157–166, 2000.

HS Phillips, S Kharbanda, R Chen, WF Forrest, RH Soriano, TD Wu, A Misra, JM Nigro, H Colman, L Soroceanu, PM Williams, Z Modrusan, BG Feuerstein, and K Aldape. Molecular subclasses of high-grade glioma predict prognosis, delineate a pattern of disease progression, and resemble stages in neurogenesis. *Cancer Cell*, 9:157–173, 2006.

RO Pieper, JF Costello, RA Kroes, BW Futscher, U Marathi, and LC Erickson. Direct correlation between methylation status and expression of the human O-6-methylguanine DNA methyltransferase gene. *Cancer Commun*, 3:241–253, 1991.

DJ Pisapia. The Updated World Health Organization Glioma Classification: Cellular and Molecular Origins of Adult Infiltrating Gliomas. *Arch Pathol Lab Med*, 141: 1633–1645, 2017. doi: 10.5858/arpa.2016-0493-RA.

M Platten, A Kretz, U Naumann, S Aulwurm, K Egashira, S Isenmann, and M Weller. Monocyte chemoattractant protein-1 increases microglial infiltration and aggressiveness of gliomas. *Ann Neurol*, 54:388–392, 2003.

E Poteet, GR Choudhury, A Winters, W Li, MG Ryou, R Liu, L Tang, A Ghorpade, Y Wen, F Yuan, ST Keir, H Yan, DD Bigner, JW Simpkins, and SH Yang. Reversing the Warburg effect as a treatment for glioblastoma. *J Biol Chem*, 288:9153–9164, 2013. doi: 10.1074/jbc.M112.440354.

MD Prados, M McDermott, SM Chang, CB Wilson, J Fick, KW Culver, J Van Gilder, GE Keles, A Spence, and M Berger. Treatment of progressive or recurrent glioblastoma multiforme in adults with herpes simplex virus thymidine kinase gene vector-producer cells followed by intravenous ganciclovir administration: a phase I/II multi-institutional trial. *J Neurooncol*, 65:269–278, 2003.

LG Presta, H Chen, SJ O'Connor, V Chisholm, YG Meng, L Krummen, M Winkler, and N Ferrara. Humanization of an anti-vascular endothelial growth factor monoclonal antibody for the therapy of solid tumors and other disorders. *Cancer Res*, 57:4593–4599, 1997.

MC Preul. History of brain tumor surgery. *J Neurosurgery*, 18, 2005. doi: 10.3171/foc.2005.18.4.1.

DF Quail and JA Joyce. The Microenvironmental Landscape of Brain Tumors. *Cancer Cell*, 31:326–341, 2017. doi: 10.1016/j.ccell.2017.02.009.

JA Quinn, A Desjardins, J Weingart, H Brem, ME Dolan, SM Delaney, J Vredenburgh, J Rich, AH Friedman, DA Reardon, JH Sampson, AE Pegg, RC Moschel, R Birch, RE McLendon, JM Provenzale, S Gururangan, JE Dancey, J Maxwell,

S Tourt-Uhlig, JE 2nd Herndon, DD Bigner, and HS Friedman. Phase I trial of temozolomide plus O6-benzylguanine for patients with recurrent or progressive malignant glioma. *J Clin Oncol*, 23:7178–7187, 2005.

R Raghavan, ML Brady, MI Rodriguez-Ponce, A Hartlep, C Pedain, and JH Sampson. Convection-enhanced delivery of therapeutics for brain disease, and its optimization. *Neurosurg Focus*, 20:E12, 2006. doi: 10.3171/foc.2006.20.4.7.

R Ramachandran, VR Junnuthula, GS Gowd, A Ashokan, J Thomas, R Peethambaran, A Thomas, AK Unni, D Panikar, SV Nair, and M Koyakutty. Theranostic 3-Dimensional nano brain-implant for prolonged and localized treatment of recurrent glioma. *Sci Rep*, 7:43271, 2017. doi: 10.1038/srep43271.

MJ Ramalho, S Andrade, MÁN Coelho, JA Loureiro, and MC Pereira. Biophysical interaction of temozolomide and its active metabolite with biomembrane models: The relevance of drug-membrane interaction for Glioblastoma Multiforme therapy. *Eur J Pharm Biopharm*, 136:156–163, 2019. doi: 10.1016/j.ejpb.2019.01.015.

SH Ranganath and CH Wang. Biodegradable microfiber implants delivering paclitaxel for post-surgical chemotherapy against malignant glioma. *Biomaterials*, 29:2996–3003, 2008. doi: 10.1016/j.biomaterials.2008.04.002.

R Rangwala, R Leone, YC Chang, LA Fecher, LM Schuchter, A Kramer, KS Tan, DF Heitjan, G Rodgers, M Gallagher, S Piao, AB Troxel, TL Evans, AM DeMichele, KL Nathanson, PJ O'Dwyer, J Kaiser, L Pontiggia, LE Davis, and RK Amaravadi. Phase I trial of hydroxychloroquine with dose-intense temozolomide in patients with advanced solid tumors and melanoma. *Autophagy*, 10:1369–1379, 2014. doi: 10.4161/auto.29118.

M Rapp, J Baernreuther, B Turowski, HJ Steiger, M Sabel, and MA Kamp. Recurrence Pattern Analysis of Primary Glioblastoma. *World Neurosurg*, 103:733–740, 2017. doi: 10.1016/j.wneu.2017.04.053.

BH Rath, A Wahba, K Camphausen, and PJ Tofilon. Coculture with astrocytes reduces the radiosensitivity of glioblastoma stem-like cells and identifies additional targets for radiosensitization. *Cancer Med*, 4:1705–1716, 2015. doi: 10.1002/cam4.510.

D Razanajaona, S Joguet, AS Ay, I Treilleux, S Goddard-Leon, L Bartholin, and R Rimokh. Silencing of FLRG, an antagonist of activin, inhibits human breast tumor cell growth. *Cancer Res*, 67:7223–7229, 2007.

G Reifenberger, HG Wirsching, CB Knobbe-Thomsen, and M Weller. Advances in the molecular genetics of gliomas - implications for classification and therapy. *Nat Rev Clin Oncol*, 14:434–452, 2017. doi: 10.1038/nrclinonc.2016.204.

SA Rempel, S Dudas, S Ge, and JA Gutierrez. Identification and localization of the cytokine SDF1 and its receptor, CXC chemokine receptor 4, to regions of necrosis and angiogenesis in human glioblastoma. *Clin Cancer Res*, 6:102–111, 2000.

L Ricci-Vitiani, R Pallini, LM Larocca, DG Lombardi, M Signore, F Pierconti, G Petrucci, N Montano, G Maira, and R De Maria. Mesenchymal differentiation of glioblastoma stem cells. *Cell Death Differ*, 15:1491–1498, 2008. doi: 10.1038/cdd.2008.72.

W Roggendorf, S Strupp, and W Paulus. Distribution and characterization of microglia/macrophages in human brain tumors. *Acta Neuropathol*, 92:288–293, 1996.

ML Rosenblum, AF Jr Reynolds, KA Smith, BH Rumack, and MD Walker. Chloroethyl-cyclohexyl-nitrosourea (CCNU) in the treatment of malignant brain tumors. *J Neurosurg*, 39:306–314, 1973.

MR Rosenfeld, X Ye, JG Supko, S Desideri, SA Grossman, S Brem, T Mikkelson, D Wang, YC Chang, J Hu, Q McAfee, J Fisher, AB Troxel, S Piao, DF Heitjan, KS Tan, L Pontiggia, PJ O'Dwyer, LE Davis, and RK Amaravadi. A phase I/II trial of hydroxychloroquine in conjunction with radiation therapy and concurrent and adjuvant temozolomide in patients with newly diagnosed glioblastoma multiforme. *Autophagy*, 10:1359–1368, 2014. doi: 10.4161/auto.28984.

JL Ross, LAD Cooper, J Kong, D Gutman, M Williams, C Tucker-Burden, MR McCrary, A Bouras, M Kaluzova, WD Jr Dunn, D Duong, CG Hadjipanayis, and DJ Brat. 5-Aminolevulinic Acid Guided Sampling of Glioblastoma Microenvironments Identifies Pro-Survival Signaling at Infiltrative Margins. *Sci Rep*, 7:15593, 2017. doi: 10.1038/s41598-017-15849-w.

ML Rossi, JT Hughes, MM Esiri, HB Coakham, and DB Brownell. Immunohistological study of mononuclear cell infiltrate in malignant gliomas. *Acta Neuropathol*, 74: 269–277, 1967.

LO Roy, MB Poirier, and D Fortin. Chloroquine inhibits the malignant phenotype of glioblastoma partially by suppressing TGF-beta. *Invest New Drugs*, 33:1020–1031, 2015. doi: 10.1007/s10637-015-0275-x.

LJ Rubinstein, MM Herman, and VL Foley. In vitro characteristics of human glioblastomas maintained in organ culture systems. Light microscopy observations. *Am J Pathol*, 71:61–80, 1973.

S Sadetzki, A Chetrit, L Freedman, M Stovall, B Modan, and I Novikov. Long-term follow-up for brain tumor development after childhood exposure to ionizing radiation for tinea capitis. *Radiat Res*, 163:424–432, 2005.

R Saito, JR Bringas, TR McKnight, MF Wendland, C Mamot, DC Drummond, DB Kirpotin, JW Park, MS Berger, and KS Bankiewicz. Distribution of liposomes into brain and rat brain tumor models by convection-enhanced delivery monitored with magnetic resonance imaging. *Cancer Res*, 64:2572–2579, 2004.

S Sakakibara, T Imai, K Hamaguchi, M Okabe, J Aruga, K Nakajima, D Yasutomi, T Nagata, Y Kurihara, S Uesugi, T Miyata, M Ogawa, K Mikoshiba, and H Okano. Mouse-Musashi-1, a neural RNA-binding protein highly enriched in the mammalian CNS stem cell. *Dev Biol*, 176:230–242, 1996.

JH Sampson, ML Brady, NA Petry, D Croteau, AH Friedman, HS Friedman, T Wong, DD Bigner, I Pastan, RK Puri, and C Pedain. Intracerebral infusate distribution by convection-enhanced delivery in humans with malignant gliomas: descriptive effects of target anatomy and catheter positioning. *Neurosurgery*, 60:89–99, 2007.

JH Sampson, GE Archer, DA Mitchell, AB Heimberger, and DD Bigner. Tumor-specific immunotherapy targeting the EGFRvIII mutation in patients with malignant glioma. *Semin Immunol*, 20:267–275, 2008. doi: 10.1016/j.smim.2008.04.001.

B Sangro, C Gomez-Martin, M de la Mata, M Iñarrairaegui, E Garralda, P Barrera, JI Riezu-Boj, E Larrea, C Alfaro, P Sarobe, JJ Lasarte, JL Pérez-Gracia, I Melero, and J Prieto. A clinical trial of CTLA-4 blockade with tremelimumab in patients with hepatocellular carcinoma and chronic hepatitis C. *J Hepatol*, 59:81–88, 2013. doi: 10.1016/j.jhep.2013.02.022.

SR Satapathy, A Nayak, S Siddharth, S Das, D Nayak, and CN Kundu. Metallic gold and bioactive quinacrine hybrid nanoparticles inhibit oral cancer stem cell and angiogenesis by deregulating inflammatory cytokines in p53 dependent manner. *Nanomedicine*, 14:883–896, 2018. doi: 10.1016/j.nano.2018.01.007.

R Satchi-Fainaro, S Ferber, E Segal, L Ma, N Dixit, A Ijaz, L Hlatky, A Abdollahi, and N Almog. Prospective identification of glioblastoma cells generating dormant tumors. *PLoS One*, 7:e44395, 2012. doi: 10.1371/journal.pone.0044395.

CB Saw, N Suntharalingam, KM Ayyangar, and L Tupchong. Dosimetric considerations of stereotactic brain implants. *Int J Radiat Oncol Biol Phys*, 17:887–891, 1989.

WR Schelman, TA Mohammed, AM Traynor, JM Kolesar, RM Marnocha, J Eickhoff, M Keppen, DB Alberti, G Wilding, N Takebe, and G Liu. A phase I study of AT-101 with cisplatin and etoposide in patients with advanced solid tumors with an expanded cohort in extensive-stage small cell lung cancer. *Invest New Drugs*, 32: 295–302, 2014. doi: 10.1007/s10637-013-9999-7.

HJ Scherer. Structural development in gliomas. *Am J Cancer*, 34:333–351, 1938.

M Schneider, S Ströbele, L Nonnenmacher, MD Siegelin, M Tepper, S Stroh, S Hasslacher, S Enzenmüller, G Strauss, B Baumann, G Karpel-Massler, MA Westhoff, KM Debatin, and ME Halatsch. A paired comparison between glioblastoma ştem cellsänd differentiated cells. *Int J Cancer*, 138:1709–1718, 2016. doi: 10.1002/ijc.29908.

D Schols, S Struyf, J Van Damme, JA Este, G Henson, and E De Clercq. Inhibition of T-tropic HIV strains by selective antagonization of the chemokine receptor CXCR4. *J Exp Med*, 186:1383–1388, 1997.

F Schütt, S Signetti, H Krüger, S Röder, D Smazna, S Kaps, SN Gorb, YK Mishra, NM Pugno, and R Adelung. Hierarchical self-entangled carbon nanotube tube networks. *Nat Commun*, 8:1215, 2017. doi: 10.1038/s41467-017-01324-7.

G Sciumè, A Soriani, M Piccoli, L Frati, A Santoni, and G Bernardini. CX3CR1/CX3CL1 axis negatively controls glioma cell invasion and is modulated by transforming growth factor-β1. *Neuro Oncol*, 12:701–710, 2010. doi: 10.1093/neuonc/nop076.

R Scognamiglio, N Cabezas-Wallscheid, MC Thier, S Altamura, A Reyes, AM Prendergast, D Baumgaertner, LS Carnevalli, A Atzberger, S Haas, L can Paleske, T Boroviak, P Woersdoerfer, MA Essers, U Kloz, RN Eisenman, F Edenhofer, P Bertone, W Huber, F can der Hoeven, A Smith, and A Turmpp. Myc Depletion Incudes a Pluripotent Dormant State Mimicking Diapause. *Cell*, 164:668–680, 2016. doi: 10.1016/j.cell.2015.12.033.

JM Seitz, M Durisin, J Goldman, and JW Drelich. Recent advances in biodegradable metals for medical sutures: a critical review. *Adv Healthc Mater*, 4:1915–1936, 2015. doi: 10.1002/adhm.201500189.

KS Sellins and JJ Cohen. Gene induction by gamma-irradiation leads to DNA fragmentation in lymphocytes. *J Immunol*, 139:3199–3206, 1987.

D Senft and ZA Ronai. Immunogenic, cellular, and angiogenic drivers of tumor dormancy–a melanoma view. *Pigment Cell Melanoma Res*, 29:27–42, 2016. doi: 10.1111/pcmr.12432.

MY Seo and K Rhee. Caspase-mediated cleavage of the centrosomal proteins during apoptosis. *Cell Death Dis*, 9:571, 2018. doi: 10.1038/s41419-018-0632-8.

N Shao, J Mao, L Xue, R Wang, F Zhi, and Q Lan. Carnosic acid potentiates the anticancer effect of temozolomide by inducing apoptosis and autophagy in glioma. *J Neurooncol*, 141:277–288, 2019. doi: 10.1007/s11060-018-03043-5.

T Shapira-Furman, R Serra, N Gorelick, M Doglioli, V Tagliaferri, A Cecia, M Peters, A Kumar, Y Rottenberg, R Langer, H Brem, B Tyler, and AJ Domb. Biodegradable wafers releasing Temozolomide and Carmustine for the treatment of brain cancer. *J Control Release*, 295:93–101, 2019. doi: 10.1016/j.jconrel.2018.12.048.

AK Sharma, V Singh, R Gera, MP Purohit, and D Ghosh. Zinc Oxide Nanoparticle Induces Microglial Death by NAPDH-Oxidase-Independent Reactive Oxygen Species as well as Energy Depletion. *Mol Neurobiol*, 54:6273–6286, 2017. doi: 10.1007/s12035-016-0133-7.

ER Shearier, PK Bowen, W He, A Drelich, J Goldman, and F Zhao. In Vitro Cytotoxicity, Adhesion, and Proliferation of Human Vascular Cells Exposed to Zinc. *ACS Biomater Sci Eng*, 2:634–642, 2016. doi: 10.1021/acsbiomaterials.6b00035.

P Sheldon and AK Ommaya. Ventricular Dilatation Masking The Presence Of Cerebral Tumours. *Acta Radiol Diagn (Stockh)*, 1:628–637, 1963.

S Shen, Y Wu, K Li, Y Wang, J Wu, Y Zeng, and D Wu. Versatile hyaluronic acid modified AQ4N-Cu(II)-gossypol infinite coordination polymer nanoparticles: Multiple tumor targeting, highly efficient synergistic chemotherapy, and real-time self-monitoring. *Biomaterials*, 154:197–212, 2018. doi: 10.1016/j.biomaterials.2017.11.001.

X Shi, T Peng, Y Huang, L Mei, Y Gu, J Huang, K Han, G Li, C Hu, X Pan, and C Wu. Comparative studies on glycerol monooleate- and phytantriol-based cubosomes containing oridonin in vitro and in vivo. *Pharm Dev Technol*, 22:322–329, 2017. doi: 10.3109/10837450.2015.1121496.

KA Sillay, SG McClatchy, BA Shepherd, GT Venable, and TS Fuehrer. Image-guided convection-enhanced delivery into agarose gel models of the brain. *J Vis Exp*, 14, 2014. doi: 10.3791/51466.

T Simon, S Pinioti, P Schellenberger, V Rajeeve, F Wendler, PR Cutillas, A King, J Stebbing, and G Giamas. Shedding of bevacizumab in tumour cells-derived extracellular vesicles as a new therapeutic escape mechanism in glioblastoma. *Mol Cancer*, 17:132, 2018. doi: 10.1186/s12943-018-0878-x.

JR Simpson, J Horton, C Scott, WJ Curran, P Rubin, J Fischbach, S Isaacson, M Rotman, SO Asbell, and JS Nelson. Influence of location and extent of surgical resection on survival of patients with glioblastoma multiforme: results of three consecutive Radiation Therapy Oncology Group (RTOG) clinical trials. *Int J Radiat Oncol Biol Phys*, 26:239–244, 1993.

SK Singh, ID Clarke, M Terasaki, VE Bonn, C Hawkins, J Squire, and PB Dirks. Identification of a cancer stem cell in human brain tumors. *Cancer Res*, 63:5821–5828, 2003.

SK Singh, C Hawkins, ID Clarke, JA Squire, J Bayani, T Hide, RM Henkelman, MD Cusimano, and PB Dirks. Identification of human brain tumour initiating cells. *Nature*, 432:396–401, 2004.

DE Slagel, JC Dittmer, and CB Wilson. Lipid composition of human glial tumour and adjacent brain. *J Neurochem*, 14:789–798, 1967.

R Sleightholm, B Yang, F Yu, Y Xie, and D Oupicky. Chloroquine-Modified Hydroxyethyl Starch as a Polymeric Drug for Cancer Therapy. *Biomacromolecules*, 18: 2247–2257, 2017. doi: 10.1021/acs.biomac.7b00023.

G Solecki, M Osswald, D Weber, M Glock, M Ratliff, HJ Mueller, O Krieter, Y Kienast, W Wick, and F Winkler. Differential Effects of Ang-2/VEGF-A Inhibiting Antibodies in Combination with Radio- or Chemotherapy in Glioma. *Cancers (Basel)*, 11:E314, 2019. doi: 10.3390/cancers11030314.

VR Solomon and H Lee. Chloroquine and its analogs: a new promise of an old drug for effective and safe cancer therapies. *Eur J Pharmacol*, 625:220–233, 2009. doi: 10.1016/j.ejphar.2009.06.063.

J Sotelo, E Briceno, and MA Lopez-Gonzalez. Adding chloroquine to conventional treatment for glioblastoma multiforme: a randomized, double-blind, placebo-controlled trial. *Ann Intern Med*, 144:337–343, 2006.

A Sottoriva, I Spiteri, SG Piccirillo, A Touloumis, VP Collins, JC Marioni, C Curtis, C Watts, and S Tavaré. Intratumor heterogeneity in human glioblastoma reflects cancer evolutionary dynamics. *Proc Natl Acad Sci U S A*, 110:4009–4014, 2013. doi: 10.1073/pnas.1219747110.

S Sruthi and PV Mohanan. Investigation on cellular interactions of astrocytes with zinc oxide nanoparticles using rat C6 cell lines. *Colloids Surf B Biointerfaces*, 133: 1–11, 2015. doi: 10.1016/j.colsurfb.2015.05.041.

MN Stein, M Hussain, WM Stadler, G Liu, IV Tereshchenko, S Goodin, C Jeyamohan, HL Kaufman, J Mehnert, and RS DiPaola. A Phase II Study of AT-101 to Overcome Bcl-2–Mediated Resistance to Androgen Deprivation Therapy in Patients With Newly Diagnosed Castration-Sensitive Metastatic Prostate Cancer. *Clin Genitourin Cancer*, 14:22–27, 2016. doi: 10.1016/j.clgc.2015.09.010.

A Stevens, I Klöter, and W Roggendorf. Inflammatory infiltrates and natural killer cell presence in human brain tumors. *Cancer*, 61:738–743, 1988.

ZA Stewart, D Mays, and JA Pietenpol. Defective G1-S cell cycle checkpoint function sensitizes cells to microtubule inhibitor-induced apoptosis. *Cancer Res*, 59:3831–3837, 1999.

W Stummer, U Pichlmeier, T Meinel, OD Wiestler, F Zanella, HJ Reulen, and ALA-Glioma Study Group. Fluorescence-guided surgery with 5-aminolevulinic acid for resection of malignant glioma: a randomised controlled multicentre phase III trial. *Lancet Oncol*, 7:392–401, 2006.

W Stummer, HJ Reulen, T Meinel, U Pichlmeier, W Schumacher, JC Tonn, V Rohde, F Oppel, B Turowski, C Woiciechowsky, K Franz, T Pietsch, and ALA-Glioma Study Group. Extent of resection and survival in glioblastoma multiforme: identification of and adjustment for bias. *Neurosurgery*, 62:564–576, 2008. doi: 10.1227/01.neu.0000317304.31579.17.

R Stupp, WP Mason, MJ van den Bent, M Weller, B Fisher, MJB Taphoorn, K Belanger, AA Brandes, C Marosi, U Bogdahn, J Curschmann, RC Janzer, SK Ludwin, T Gorlia, A Allgeier, D Lacombe, JG Cairncross, E Eisenhauer, RO Mirimanoff, European Organisation for Research, Treatment of Cancer Brain Tumor, Radiotherapy Groups, and the National Cancer Institute of Canada Clinical Trials Group. Radiotherapy plus concomitant and adjuvant temozolomide for glioblastoma. *N Engl J Med*, 352:987–996, 2005.

R Stupp, ME Hegi, WP Mason, MJ van den Bent, MJ Taphoorn, RC Janzer, SK Ludwin, A Allgeier, B Fisher, K Belanger, P Hau, AA Brandes, J Gijtenbeek, C Marosi, CJ Vecht, K Mokhtari, P Wesseling, S Villa, E Eisenhauer, T Gorlia, M Weller, D Lacombe, JG Cairncross, RO Mirimanoff, European Organisation for Research, Treatment of Cancer Brain Tumour, Radiation Oncology Groups, and National Cancer Institute of Canada Clinical Trials Group. Effects of radiotherapy with concomitant and adjuvant temozolomide versus radiotherapy alone on survival in glioblastoma in a randomised phase III study: 5-year analysis of the EORTC-NCIC trial. *Lancet Oncol*, 10:459–466, 2009. doi: 10.1016/S1470-2045(09)70025-7.

S Sugiyama, Y Yamashita, T Kikuchi, R Saito, T Kumabe, and T Tominaga. Safety and efficacy of convection-enhanced delivery of ACNU, a hydrophilic nitrosourea, in intracranial brain tumor models. *J Neurooncol*, 82:41–47, 2007.

MG Sun, JF Shi, XY Li, Y Zhao, RJ Ju, LM Mu, Y Yan, XT Li, F Zeng, and WL Lu. Targeting Epirubicin Plus Quinacrine Liposomes Modified with DSPE-PEG2000-C(RGDfK) Conjugate for Eliminating Invasive Breast Cancer. *J Biomed Nanotechnol*, 11:1339–1353, 2015.

PL Swiecicki, E Bellile, AG Sacco, AT Pearson, JM Taylor, TL Jackson, DB Chepeha, ME Spector, A Shuman, K Malloy, J Moyer, E McKean, S McLean, A Sukari, GT Wolf, A Eisbruch, M Prince, C Bradford, TE Carey, S Wang, JE Nör, and FP Worden. A phase II trial of the BCL-2 homolog domain 3 mimetic AT-101 in combination with docetaxel for recurrent, locally advanced, or metastatic head and neck cancer. *Invest New Drugs*, 34:481–489, 2016. doi: 10.1007/s10637-016-0364-5.

G Szewczyk, J Rak, and JH Ruth. Inflammatory mediators of angiogenesis. *Mediators Inflamm*, page 610543, 2013. doi: 10.1155/2013/610543.

E Tabouret, A Tchoghandjian, E Denicolai, C Delfino, P Metellus, T Graillon, C Boucard, I Nanni, L Padovani, L Ouafik, D Figarella-Branger, and O Chinot. Recurrence of glioblastoma after radio-chemotherapy is associated with an angiogenic switch to the CXCL12-CXCR4 pathway. *Oncotarget*, 6:11664–11675, 2015. doi: 10.18632/oncotarget.3256.

B Taheri, M Soleimani, SF Aval, F Memari, and N Zarghami. C6 glioma-derived microvesicles stimulate the proliferative and metastatic gene expression of normal astrocytes. *Neurosci Lett*, 685:173–178, 2018. doi: 10.1016/j.neulet.2018.08.034.

Y Tanaka, S Nobusawa, H Ikota, H Yokoo, J Hirato, H Ito, T Saito, H Ogura, and Y Nakazato. Leukemia-like onset of bone marrow metastasis from anaplastic oligodendroglioma after 17 years of dormancy: an autopsy case report. *Brain Tumor Pathol*, 31:131–136, 2014. doi: 10.1007/s10014-013-0156-y.

S Tang, J Liao, and Y Long. Comparative assessment of the efficacy of gross total versus subtotal total resection in patients with glioma: A meta-analysis. *Int J Surg*, 63:90–97, 2019. doi: 10.1016/j.ijsu.2019.02.004.

CH Tator, A Day, R Ng, and L Liberman. Chemotherapy of an experimental glioma with nitrosoureas. *Cancer Res*, 37:476–481, 1977.

JM Taube, A Klein, JR Brahmer, H Xu, X Pan, JH Kim, L Chen, DM Pardoll, SL Topalian, and RA Anders. Association of PD-1, PD-1 ligands, and other features of the tumor immune microenvironment with response to anti-PD-1 therapy. *Clin Cancer Res*, 20:5064–5074, 2014. doi: 10.1158/1078-0432.CCR-13-3271.

R Tejero, Y Huang, I Katsyv, M Kluge, JY Lin, J Tome-Garcia, N Daviaud, Y Wang, B Zhang, NM Tsankova, CC Friedel, H Zou, and RH Friedel. Gene signatures of quiescent glioblastoma cells reveal mesenchymal shift and interactions with niche microenvironment. *EBioMedicine*, 19:252–269, 2019. doi: 10.1016/j.ebiom.2019.03.064.

G Tiram, S Ferber, P Ofek, A Eldar-Boock, D Ben-Shushan, E Yeini, A Krivitsky, R Blatt, N Almog, J Henkin, O Amsalem, E Yavin, G Cohen, P Lazarovici, JS Lee,

E Ruppin, M Milyavsky, R Grossman, Z Ram, M Calderón, R Haag, and R Satchi-Fainaro. Reverting the molecular fingerprint of tumor dormancy as a therapeutic strategy for glioblastoma. *FASEB J*, 2018. doi: 10.1096/fj.201701568R.

S Tivari, H Lu, T Dasgupta, MS De Lorenzo, and R Wieder. Reawakening of dormant estrogen-dependent human breast cancer cells by bone marrow stroma secretory senescence. *Cell Commun Signal*, 16:48, 2018. doi: 10.1186/s12964-018-0259-5.

A Tivnan, Z Zakaria, C O'Leary, D Kögel, JL Pokorny, JN Sarkaria, and JH Prehn. Inhibition of multidrug resistance protein 1 (MRP1) improves chemotherapy drug response in primary and recurrent glioblastoma multiforme. *Front Neurosci*, 9:218, 2015. doi: 10.3389/fnins.2015.00218.

A Tivnan, T Heilinger, EC Lavelle, and JH Prehn. Advances in immunotherapy for the treatment of glioblastoma. *J Neurooncol*, 131:1–9, 2017. doi: 10.1007/s11060-016-2299-2.

K Tomada, HC Chiang, KR Kozak, and GS Kwon. Injectable (-)-gossypol-loaded Pluronic P85 micelles for cancer chemoradiotherapy. *Int J Radiat Biol*, 93:402–406, 2017. doi: 10.1080/09553002.2016.1257833.

L Tong, L Yi, P Liu, IR Abeysekera, L Hai, T Li, Z Tao, H Ma, Y Xie, Y Huang, S Yu, J Li, F Yuan, and X Yang. Tumour cell dormancy as a contributor to the reduced survival of GBM patients who received standard therapy. *Oncol Rep*, 40: 463–471, 2018. doi: 10.3892/or.2018.6425.

LA Torres, MA Coca, JF Batista, A Casaco, G Lopez, I Garcia, A Perera, Y Pena, A Hernandez, Y Sanchez, S Romero, R Leyva, A Prats, and R Fernandez. Biodistribution and internal dosimetry of the 188Re-labelled humanized monoclonal antibody anti-epidemal growth factor receptor, nimotuzumab, in the locoregional treatment of malignant gliomas. *Nucl Med Commun*, 29:66–75, 2008.

S Torres, M Lorente, F Rodríguez-Fornés, S Hernandez-Tiedra, M Salazar, E Garcia-Taboada, J Barcia, M Guzman, and G Velasco. A combined preclinical therapy of cannabinoids and temozolomide against glioma. *Mol Cancer Ther*, 10:90–103, 2011. doi: 10.1158/1535-7163.MCT-10-0688.

MR Towler, S Kenny, D Boyd, T Pembroke, M Buggy, and RG Hill. Zinc ion release from novel hard tissue biomaterials. *Biomed Mater Eng*, 14:565–572, 2004.

VA Trinh, SP Patel, and WJ Hwu. The safety of temozolomide in the treatment of malignancies. *Expert Opin Drug Saf*, 8:493–499, 2009. doi: 10.1517/14740330902918281.

YY Tseng, TC Yang, YC Wang, WH Lee, TM Chang, YC Kau, and SJ Liu. Targeted concurrent and sequential delivery of chemotherapeutic and antiangiogenic agents to the brain by using drug-loaded nanofibrous membranes. *Int J Nanomedicine*, 12: 1265–1276, 2017. doi: 10.2147/IJN.S124593.

JM Unagolla and AC Jayasuriya. Enhanced cell functions on graphene oxide incorporated 3D printed polycaprolactone scaffolds. *Mater Sci Eng C Mater Biol Appl*, 102:1–11, 2019. doi: 10.1016/j.msec.2019.04.026.

A Uzdensky, B Kristiansen, J Moan, and A Juzeniene. Dynamics of signaling, cytoskeleton and cell cycle regulation proteins in glioblastoma cells after sub-lethal photodynamic treatment: antibody microarray study. *Biochim Biophys Acta*, 1820: 795–803, 2012. doi: 10.1016/j.bbagen.2012.03.008.

C Vaquette, C Frochot, R Rahouadj, S Muller, and X Wang. Mechanical and Biological characterization of A Porous Poly-L-Lactic Acid-Co-e-Caprolactone scaffold for Tissue Engineering. *Soft Materials*, 6:25–33, 2008. doi: 10.1080/15394450801887109.

V Varenika, P Dickinson, J Bringas, R LeCouteur, R Higgins, J Park, M Fiandaca, M Berger, J Sampson, and K Bankiewicz. Detection of infusate leakage in the brain using real-time imaging of convection-enhanced delivery. *J Neurosurg*, 109:874–880, 2008. doi: 10.3171/JNS/2008/109/11/0874.

U Varol, B Karaca, D Tunali, M Degirmenci, Y Cirak, DU Purcu, S Uzunoglu, C Sezgin, B Karabulut, UA Sanli, and R Uslu. The effect of racemic gossypol and at-101 on angiogenic profile of ovcar-3 cells: a preliminary molecular framework for gossypol enantiomers. *Exp Oncol*, 31:220–225, 2009.

N Varshney, AK Sahi, KY Vajanthri, S Poddar, CK Balavigneswaran, A Prabhakar, V Rao, and SK Mahto. Culturing melanocytes and fibroblasts within three-dimensional macroporous PDMS scaffolds: towards skin dressing material. *Cytotechnology*, 71:287–303, 2019. doi: 10.1007/s10616-018-0285-6.

AK Vellimana, VR Recinos, L Hwang, KD Fowers, KW Li, Y Zhang, S Okonma, CG Eberhart, H Brem, and BM Tyler. Combination of paclitaxel thermal gel depot with temozolomide and radiotherapy significantly prolongs survival in an experimental rodent glioma model. *J Neurooncol*, 111:229–236, 2013. doi: 10.1007/s11060-012-1014-1.

L Vera-Ramirez, SK Vodnala, R Nini, KW Hunter, and JE Green. Autophagy promotes the survival of dormant breast cancer cells and metastatic tumour recurrence. *Nat Commun*, 9:1944, 2018. doi: 10.1038/s414567-018-04070-6.

RG Verhaak, KA Hoadley, E Purdom, V Wang, Y Qi, MD Wilkerson, CR Miller, L Ding, T Golub, JP Mesirov, G Alexe, M Lawrence, M O'Kelly, P Tamayo, BA Weir, S Gabriel, W Winckler, S Gupta, L Jakkula, HS Feiler, JG Hodgson, CD James, JN Sarkaria, C Brennan, A Kahn, PT Spellman, RK Wilson, TP Speed, JW Gray, M Meyerson, G Getz, CM Perou, DN Hayes, and Cancer Genome Atlas Research Network. Integrated genomic analysis identifies clinically relevant subtypes of glioblastoma characterized by abnormalities in PDGFRA, IDH1, EGFR, and NF1. *Cancer Cell*, 17:98–110, 2010. doi: 10.1016/j.ccr.2009.12.020.

E Vidomanova, P Racay, I Pilchova, E Halasova, and J Hatok. Microfluidic profiling of apoptosis-related genes after treatment with BH3-mimetic agents in astrocyte and glioblasotma cell lines. *Oncol Rep*, 36:3188–3196, 2016. doi: 10.3892/or.2016.5191.

KL von Eckardstein, R Reszka, and JC Kiwit. Intracavitary chemotherapy (paclitaxel/carboplatin liquid crystalline cubic phases) for recurrent glioblastoma – clinical observations. *J Neurooncol*, 74:305–309, 2005.

V Voss, C Senft, V Lang, MW Ronellenfitsch, JP Steinbach, V Seifert, and D Kögel. The pan-Bcl-2 inhibitor (-)-gossypol triggers autophagic cell death in malignant glioma. *Mol Cancer Res*, 8:1002–1016, 2010. doi: 10.1158/1541-7786.MCR-09-0562.

R Wahab, N Kaushik, F Khan, NK Kaushik, EH Choi, J Musarrat, and AA Al-Khedhairy. Self-Styled ZnO Nanostructures Promotes the Cancer Cell Damage and Supresses the Epithelial Phenotype of Glioblastoma. *Sci Rep*, 6:19950, 2016. doi: 10.1038/srep19950.

HH Wang, TY Chang, WC Lin, KC Wei, and JW Shin. GADD45A plays a protective role against temozolomide treatment in glioblastoma cells. *Sci Rep*, 7:8814, 2017a. doi: 10.1038/s41598-017-06851-3.

J Wang, X Deng, F Zhang, D Chen, and W Ding. ZnO nanoparticle-induced oxidative stress triggers apoptosis by activating JNK signaling pathway in cultured primary astrocytes. *Nanoscale Res Lett*, 9:117, 2014. doi: 10.1186/1556-276X-9-117.

Q Wang, B Hu, X Hu, H Kim, M Squatrito, L Scarpace, AC deCarvalho, S Lyu, P Li, Y Li, F Barthel, HJ Cho, YH Lin, N Satani, E Martinez-Ledesma, S Zheng, E Chang, CG Sauvé, A Olar, ZD Lan, G Finocchiaro, JJ Phillips, MS Berger, KR Gabrusiewicz, G Wang, E Eskilsson, J Hu, T Mikkelsen, RA DePinho, F Muller, AB Heimberger, EP Sulman, DH Nam, and RGW Verhaak. Tumor Evolution of Glioma-Intrinsic Gene Expression Subtypes Associates with Immunological Changes in the Microenvironment. *Cancer Cell*, 32:42–56, 2017b. doi: 10.1016/j.ccell.2017.06.003.

SC Wang, JH Hong, C Hsueh, and CS Chiang. Tumor-secreted SDF-1 promotes glioma invasiveness and TAM tropism toward hypoxia in a murine astrocytoma model. *Lab Invest*, 92:151–162, 2012. doi: 10.1038/labinvest.2011.128.

X Wang, Y Qiu, Q Yu, H Li, X Chen, M Li, Y Long, Y Liu, L Lu, J Tang, Z Zhang, and Q He. Enhanced glioma therapy by synergistic inhibition of autophagy and tyrosine kinase activity. *Int J Pharm*, 536:1–10, 2018. doi: 10.1016/j.ipharm.2017.09.007.

Y Wang, X Ying, H Xu, H Yan, X Li, and H Tang. The functional curcumin liposomes induce apoptosis in C6 glioblastoma cells and C6 glioblastoma stem cells in vitro and in animals. *Int J Nanomedicine*, 12:1369–1384, 2017c. doi: 10.2147/IJN.S124276.

YI Wang, HE Abaci, and ML Shuler. Microfluidic blood-brain barrier model provides in vivo-like barrier properties for drug permeability screening. *Biotechnol Bioeng*, 114:184–194, 2017d. doi: 10.1002/bit.26045.

MV Wanjale and GSV Kumar. Peptides as a therapeutic avenue for nanocarrier-aided targeting of glioma. *Expert Opin Drug Deliv*, 14:811–824, 2017. doi: 10.1080/17425247.2017.1242574.

O Warburg. On the origin of cancer cells. *Science*, 23:309–314, 1956.

V Warnsmann, N Meyer, A Hamann, D Kögel, and HD Osiewacz. A novel role of the mitochondrial permeability transition pore in (-)-gossypol-induced mitochondrial dysfunction. *Mech Ageing Dev*, 170:45–58, 2018. doi: 10.1016/j.mad.2017.06.004.

M Watanabe, R Tanaka, and N Takeda. Magnetic resonance imaging and histopathology of cerebral gliomas. *Neuroradiology*, 34:463–469, 1992.

GS Watts, RO Pieper, JF Costello, YM Peng, WS Dalton, and BW Futscher. Methylation of discrete regions of the O6-methylguanine DNA methyltransferase (MGMT) CpG island is associated with heterochromatinization of the MGMT transcription start site and silencing of the gene. *Mol Cell Biol*, 17:5612–5619, 1997.

M Westphal, DC Hilt, E Bortey, P Delavault, R Olivares, PC Warnke, IR Whittle, J Jaeaeskelaeinen, and Z Ram. A phase 3 trial of local chemotherapy with biodegradable carmustine (BCNU) wafers (Gliadel wafers) in patients with primary malignant glioma. *Neuro Oncol*, 5:79–88, 2003.

M Westphal, Z Ram, V Riddle, D Hilt, E Bortey, and Executive Committee of the Gliadel Study Group. Gliadel wafer in initial surgery for malignant glioma: long-term follow-up of a multicenter controlled trial. *Acta Neurochir (Wien)*, 148:269–275, 2006.

GR Wickman, L Julian, K Mardilovich, S Schumacher, J Munro, N Rath, SA Zander, A Mleczak, D Sumpton, N Morrice, WV Bienvenut, and MF Olson. Blebs produced by actin-myosin contraction during apoptosis release damage-associated molecular pattern proteins before secondary necrosis occurs. *Cell Death Differ*, 20:1293–1305, 2013. doi: 10.1038/cdd.2013.69.

I Wilhelm, C Fazakas, and IA Krizbai. In vitro models of the blood-brain barrier. *Acta Neurobiol Exp (Wars)*, 71:113–128, 2011.

S Wilhelm, AJ Tavares, Q Dai, S Ohta, J Audet, HF Dvorak, and WCW Chan. Analysis of nanoparticle delivery to tumours. *Nat Rev Mater*, 1, 2016. doi: 10.1038/natrevmats.2016.14.

D Wion. Therapeutic dormancy to delay postsurgical glioma recurrence: the past, present and promise of focal hypothermia. *J Neurooncol*, 133:447–454, 2017. doi: 10.1007/s11060-017-2471-3.

SA Wissing, O Kayser, and RH Müller. Solid lipid nanoparticles for parenteral drug delivery. *Adv Drug Deliv Rev*, 56:1257–1272, 2004.

JP Woelber, P Ratka-Krueger, K Vach, and E Frisch. Decementation Rates and the Peri-Implant Tissue Status of Implant-Supported Fixed Restorations Retained via Zinc Oxide Cement: A Retrospective 10-23-Year Study. *Clin Implant Dent Relat Res*, 18:917–925, 2016. doi: 10.1111/cid.12372.

JB Wolinsky, YL Colson, and MW Grinstaff. Local drug delivery strategies for cancer treatment: gels, nanoparticles, polymeric films, rods, and wafers. *J Control Release*, 159:14–26, 2012. doi: 10.1016/j.jconrel.2011.11.031.

MD Wood, GF Reis, DE Reuss, and JJ Phillips. Protein Analysis of Glioblastoma Primary and Posttreatment Pairs Suggests a Mesenchymal Shift at Recurrence. *J Neuropathol Exp Neurol*, 75:925–935, 2016. doi: 10.1093/jnen/nlw068.

M Wrensch, M Lee, R Miike, B Newman, G Barger, R Davis, J Wiencke, and J Neuhaus. Familial and personal medical history of cancer and nervous system conditions among adults with glioma and controls. *Am J Epidemiol*, 145:581–593, 1997.

A Wrzeszcz, B Dittrich, D Haamann, P Aliuos, D Klee, I Nolte, T Lenarz, and G Reuter. Dexamethasone released from cochlear implant coatings combined with a protein repellent hydrogel layer inhibits fibroblast proliferation. *J Biomed Mater Res A*, 102:442–454, 2014. doi: 10.1002/jbm.a.34719.

A Wu, J Wei, LY Kong, Y Wang, W Priebe, W Qiao, R Sawaya, and AB Heimberger. Glioma cancer stem cells induce immunosuppressive macrophages/microglia. *Neuro Oncol*, 12:1113–1125, 2010. doi: 10.1093/neuonc/noq082.

DF Wu, YW Yu, ZM Tang, and MZ Wang. Pharmacokinetics of (+/-)-, (+)-, and (-)-gossypol in humans and dogs. *Clin Pharmacol Ther*, 39:613–618, 1986.

H Wu, J Lin, P Liu, Z Huang, P Zhao, H Jin, J Ma, L Wen, and N Gu. Reactive oxygen species acts as executor in radiation enhancement and autophagy inducing by AgNPs. *Biomaterials*, 101:1–9, 2016. doi: 10.1016/j.biomaterials.2016.05.031.

MP Wu, JA Tamada, H Brem, and R Langer. In vivo versus in vitro degradation of controlled release polymers for intracranial surgical therapy. *J Biomed Mater Res*, 28:387–395, 1994.

DM Wyatt and D Dorschel. A cubic-phase delivery system composed of glyceryl monooleate and water for sustained release of water-soluble drugs. *Pharm Technol*, 16:116, 1992.

S Würstle, F Schneider, F Ringel, J Gempt, F Lämmer, C Delbridge, W Wu, and J Schlegel. Temozolomide induces autophagy in primary and established glioblastoma cells in an EGFR independent manner. *Oncol Lett*, 14:322–328, 2017. doi: 10.3892/ol.2017.6107.

W Xiao, A Sohrabi, and SK Seidlits. Integrating the glioblastoma microenvironment into engineered experimental models. *Future Sci OA*, 3:FSO189, 2017. doi: 10.4155/fsoa-2016-0094.

H Xie, J Yin, MH Shah, ME Menefee, KC Bible, D Reidy-Lagunes, MA Kane, DI Quinn, DR Gandara, C Erlichmann, and AA Adjei. A phase II study of the orally administered negative enantiomer of gossypol (AT-101), a BH3 mimetic, in patients with advanced adrenal cortical carcinoma. *Invest New Drugs*, 37:755–762, 2019. doi: 10.1007/s10637-019-00797-1.

H Xin, X Sha, X Jiang, W Zhang, L Chen, and X Fang. Anti-glioblastoma efficacy and safety of paclitaxel-loading Angiopep-conjugated dual targeting PEG-PCL nanoparticles. *Biomaterials*, 33:8167–8176, 2012. doi: 10.1016/j.biomaterials.2012.07.046.

P Xue, Q Li, Y Li, L Sun, L Zhang, Z Xu, and Y Kang. Surface Modification of Poly(dimethylsiloxane) with Polydopamine and Hyaluronic Acid To Enhance Hemocompatibility for Potential Applications in Medical Implants or Devices. *ACS Appl Mater Interfaces*, 9:33632–33644, 2017. doi: 10.1021/acsami.7b10260.

H Yan, DW Parsons, G Jin, R McLendon, BA Rasheed, W Yuan, I Kos, I Batinic-Haberle, S Jones, GJ Riggins, H Friedman, D Reardon, J Herndon, KW Kinzler, VE Velculescu, B Vogelstein, and DD Bigner. IDH1 and IDH2 mutations in gliomas. *N Engl J Med*, 360:765–773, 2009. doi: 10.1056/NEJMoa0808710.

N Yang, T Yan, H Zhu, X Liang, L Leiss, PØ Sakariassen, KO Skaftnesmo, B Huang, DE Costea, PØ Enger, X Li, and J Wang. A co-culture model with brain tumor-specific bioluminescence demonstrates astrocyte-induced drug resistance in glioblastoma. *J Transl Med*, 12:278, 2014. doi: 10.1186/s12967-014-0278-y.

W Yang, RF Barth, DM Adams, MJ Ciesielski, RA Fenstermaker, S Shukla, W Tjarks, and MA Caligiuri. Convection-enhanced delivery of boronated epidermal growth factor for molecular targeting of EGF receptor-positive gliomas. *Cancer Res*, 62: 6552–6558, 2002.

AC Yeh and S Ramaswamy. Mechanisms of Cancer Cell Dormancy–Another Hallmark of Cancer? *Cancer Res*, 75:5014–5022, 2015. doi: 10.1158/0008-5472.CAN-15-1370.

WL Yeh, DY Lu, HC Liou, and WM Fu. A forward loop between glioma and microglia: glioma-derived extracellular matrix-activated microglia secrete IL-18 to enhance the migration of glioma cells. *J Cell Physiol*, 227:558–568, 2012. doi: 10.1002/jcp.22746.

GZ Yi, YW Liu, W Xiang, H Wang, ZY Chen, SD Xie, and ST Qi. Akt and β-catenin contribute to TMZ resistance and EMT of MGMT negative malignant glioma cell line. *J Neurol Sci*, 367:101–106, 2016. doi: 10.1016/j.jns.2016.05.054.

Z Yu, G Zhao, G Xie, L Zhao, Y Chen, H Yu, Z Zhang, C Li, and Y Li. Metformin and temozolomide act synergistically to inhibit growth of glioma cells and glioma stem cells in vitro and in vivo. *Oncotarget*, 6:32930–32943, 2015. doi: 10.18632/oncotarget.5405.

F Yuan, M Dellian, D Fukumura, M Leunig, DA Berk, VP Torchilin, and RK Jain. Vascular permeability in a human tumor xenograft: molecular size dependence and cutoff size. *Cancer Res*, 55:3752–3756, 1995.

WK Yung, MD Prados, R Yaya-Tur, SS Rosenfeld, M Brada, HS Friedman, R Albright, J Olson, SM Chang, AM O'Neill, AH Friedman, J Bruner, N Yue, M Dugan, S Zaknoen, and VA Levin. Multicenter phase II trial of temozolomide in patients with anaplastic astrocytoma or anaplastic oligoastrocytoma at first relapse. Temodal Brain Tumor Group. *J Clin Oncol*, 17:2762–2771, 1999.

D Zagzag, M Esencay, O Mendez, H Yee, I Smirnova, Y Huang, L Chiriboga, E Lukyanov, M Liu, and EW Newcomb. Hypoxia- and vascular endothelial growth factor-induced stromal cell-derived factor-1alpha/CXCR4 expression in glioblastomas: one plausible explanation of Scherer's structures. *Am J Pathol*, 173:545–560, 2008. doi: 10.2353/ajpath.2008.071197.

PS Zeiner, C Preusse, A Golebiewska, J Zinke, A Iriondo, A Muller, T Kaoma, K Filipski, M Müller-Eschner, S Bernatz, AE Blank, P Baumgarten, E Ilina, A Grote, ML Hansmann, MA Verhoff, K Franz, F Feuerhake, JP Steinbach, J Wischhusen, W Stenzel, SP Niclou, PN Harter, and M Mittelbronn. Distribution and prognostic

impact of microglia/macrophage subpopulations in gliomas. *Brain Pathol*, pages 513–529, 2018. doi: 10.1111/bpa.12690.

L Zeng, Y Zhao, T Ouyang, T Zhao, S Zhang, J Chen, J Yu, and T Lei. Label-retaining assay enriches tumor-initiating cells in glioblastoma spheres cultivated in serum-free medium. *Oncol Lett*, 12:815–824, 2016. doi: 10.3892/ol.2016.4690.

GM Zentner, R Rathi, C Shih, JC McRea, MH Seo, H Oh, BG Rhee, J Mestecky, Z Moldoveanu, M Morgan, and S Weitman. Biodegradable block copolymers for delivery of proteins and water-insoluble drugs. *J Control Release*, 72:203–215, 2001.

SF Zerp, TR Stoter, FJ Hoebers, MW van den Brekel, R Dubbelman, GK Kuipers, MC Lafleur, BJ Slotman, and M Verheij. Targeting anti-apoptotic Bcl-2 by AT-101 to increase radiation efficacy: data from in vitro and clinical pharmacokinetic studies in head and neck cancer. *Radiat Oncol*, 10:158, 2015. doi: 10.1186/s13014-015-0474-9.

G Zhai, J Wu, X Zhao, B Yu, H Li, Y Lu, W Ye, YC Lin, and RJ Lee. A liposomal delivery vehicle for the anticancer agent gossypol. *Anticancer Res*, 28:2801–2805, 2008.

B Zhang, M Montgomery, MD Chamberlain, S Ogawa, A Korolj, A Pahnke, LA Wells, S Masse, J Kim, L Reis, A Momen, SS Nunes, AR Wheeler, K Nanthakumar, G Keller, MV Sefton, and M Radisic. Biodegradable scaffold with built-in vasculature for organ-on-a-chip engineering and direct surgical anastomosis. *Nat Mater*, 15:669–678, 2016. doi: 10.1038/nmat4570.

C Zhang, EA Nance, P Mastorakos, J Chisholm, S Berry, C Eberhart, B Tyler, H Brem, JS Suk, and J Hanes. Convection enhanced delivery of cisplatin-loaded brain penetrating nanoparticles cures malignant glioma in rats. *J Control Release*, 263:112–119, 2017. doi: 10.1016/j.jconrel.2017.03.007.

J Zhang and XP Dong. Dysfunction of microtubule-associated proteins of MAP2/tau family in Prion disease. *Prion*, 6:334–338, 2012. doi: 10.4161/pri.20677.

J Zhang, S Sarkar, R Cua, Y Zhou, W Hader, and VW Yong. A dialog between glioma and microglia that promotes tumor invasiveness through the CCL2/CCR2/interleukin-6 axis. *Carcinogenesis*, 33:312–319, 2012. doi: 10.1093/carcin/bgr289.

X Zhang, K Ding, J Wang, X Li, and P Zhao. Chemoresistance caused by the microenvironment of glioblastoma and the corresponding solutions. *Biomed Pharmacother*, 109:39–46, 2019. doi: 10.1016/j.biopha.2018.10.063.

M Zhao, F Danhier, C Bastiancich, N Joudiou, LP Ganipineni, N Tsakiris, B Gallez, AD Rieux, A Jankovski, J Bianco, and V Préat. Post-resection treatment of glioblastoma with an injectable nanomedicine-loaded photopolymerizable hydrogel induces long-term survival. *Int J Pharm*, 548:522–529, 2018. doi: 10.1016/j.ijpharm.2018.07.033.

L Zhen, C Yufeng, S Zhenyu, and X Lei. Multiple extracranial metastases from secondary glioblastoma multiforme: a case report and review of the literature. *J Neurooncol*, 97:451–457, 2010. doi: 10.1007/s11060-009-0044-9.

M Zheng, S Wang, Z Liu, L Xie, and Y Deng. Development of temozolomide coated zinc oxide for reversing the resistance of malignant glioma stem cells. *Mater Sci Eng C Mater Biol Appl*, 83:44–50, 2018. doi: 10.1016/j.msec.2017.07.015.

J Zhu, J Zou, C Mu, W Yang, M Gu, J Lin, X Song, H Zheng, and F Li. Intranasal administration of pullulan-based nanoparticles for enhanced delivery of adriamycin into the brain: in vitro and in vivo evaluation. *Pharmazie*, 74:39–46, 2019. doi: 10.1691/ph.2019.8124.

H Zong, LF Parada, and SJ Baker. Cell of origin for malignant gliomas and its implication in therapeutic development. *Cold Spring Harb Perspect Biol*, 7:a020610, 2015. doi: 10.1101/cshperspect.a020610.

X Zou, S Wei, J Jasensky, M Xiao, Q Wang, CL Brooks Iii, and Z Chen. Molecular Interactions between Graphene and Biological Molecules. *J Am Chem Soc*, 139: 1928–1936, 2017. doi: 10.1021/jacs.6b11226.

M Zucchetti, CV Catapano, S Filippeschi, E Erba, and M D'Incalci. Temozolomide induced differentiation of K562 leukemia cells is not mediated by gene hypomethylation. *Biochem Pharmacol*, 38:2069–2075, 1989.

List of Figures

List of Tables

A Appendix

A.1 Supplementary data

		PDGFRA	EGFR	NF1	CDKN2A
cell line	A172	11.95	3.35	5.57	undet
	LN229	11.06	6.93	9.66	undet
	U251MG	4.90	5.61	9.37	undet
primary culture	27/07	5.46	7.45	7.90	12.29
	86/13	4.02	6.05	6.81	6.16
	116/14	6.91	12.72	8.84	12.43
	118/14	4.95	6.92	6.44	2.00
	124/15	7.62	9.47	9.88	3.85
	141/15	6.44	9.05	9.29	7.58

Figure A.1: Molecular profiles of GBM cell lines and primary cultures. GBM cell lines and primary cultures were analyzed by qRT-PCR regarding the expression of some subtype-associated genes, like *PDGFRA*, *EGFR*, *NF1* and *CDKN2A*. The results are depicted as ΔCT values in a color-coded heatmap, in which a the highest expression is shown with as the most red color and the lowest expression is colored in green for each analyzed gene. Values in between adapt to shades of red and green colors, while black highlights the median value (undet=undetectable).

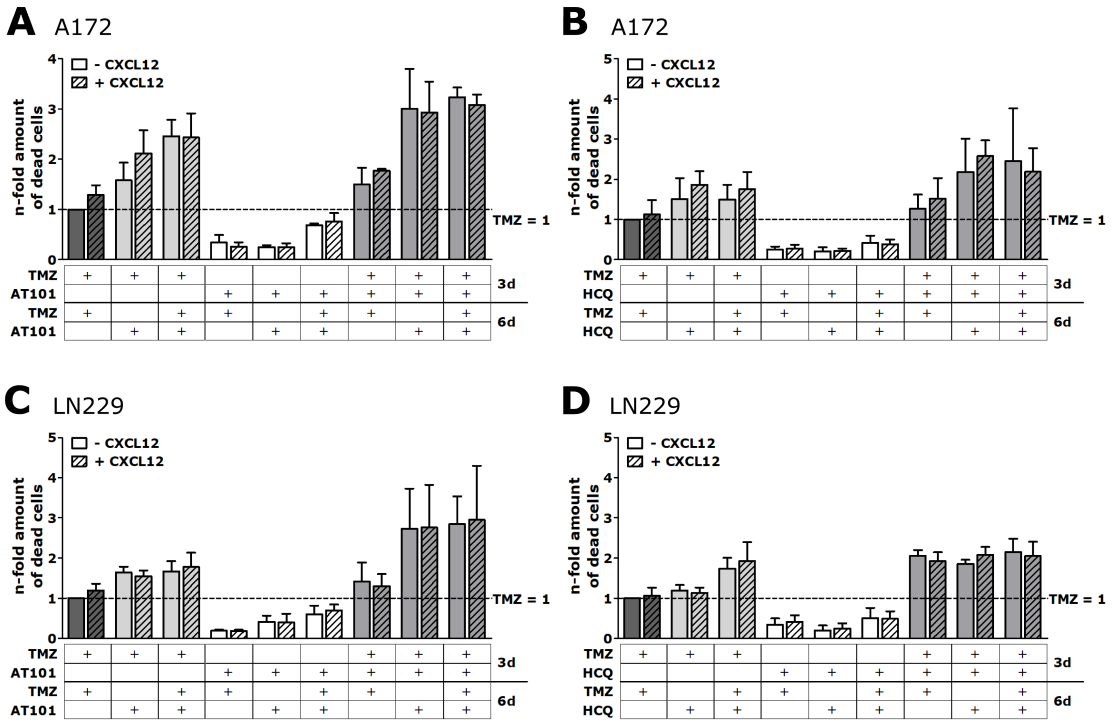

Figure A.2: Impact of CXCL12 co-administration on the cytotoxic effect of various treatment schemes on GBM cell lines. Two distinct GBM cell lines, A172 (**A**, **B**) and LN229 (**C**, **D**), were stimulated with various treatment schemes (illustrated in fig. 4.7) including combinations of classical, TMZ (50 μM), and either AT101 (2.5 μM, **A**, **C**) or HCQ (6 μM, **B**, **D**) as alternative therapeutics for three and six days. Additional to each treatment scheme, GBM cells were stimulated with 1 nM CXCL12, likewise. The cytotoxicity of each stimulation regimen was calculated after three and six days by the percentage of dead cells compared to whole cell counts. The data are depicted as n-fold percentage of dead cells in comparison with the classical therapy with TMZ (n=3-4).

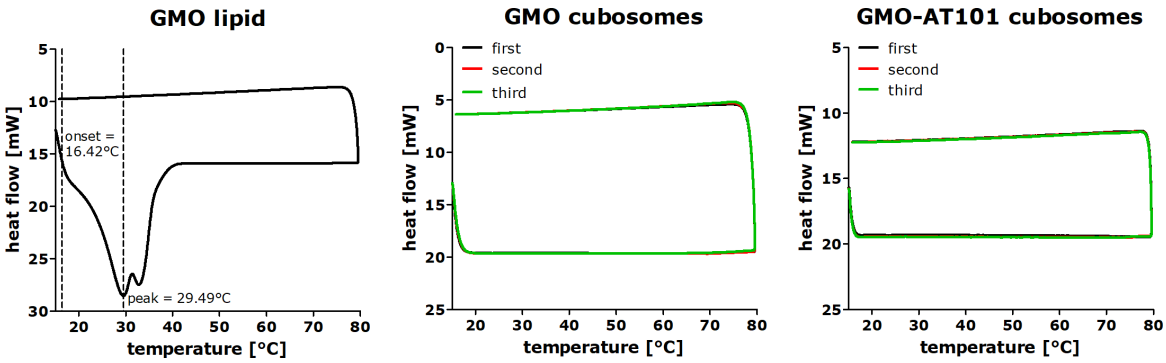

Figure A.3: Overall thermal stability of the GMO lipid and blank GMO, GMO-AT101 cubosomes. The physical behavior of the GMO lipid itself, blank GMO cubosomes as well as AT101-loaded cubosomes was analyzed by DSC measurements between 15°C and 80°C.

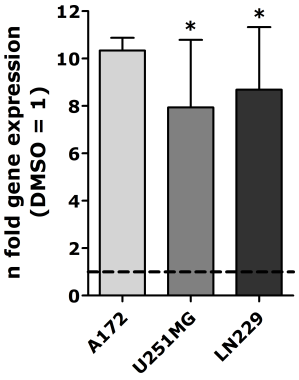

Figure A.4: Gene expression regulation of *CDKN1A* upon TMZ treatment. A172, U251MG and LN229 were treated with 500 μM TMZ or DMSO, respectively, for ten days. Afterwards, stimulated cells were analyzed by qRT-PCR regarding their expression of *CDKN1A*, a cell cycle marker. The data are depicted as n-fold regulation compared to DMSO and statistically analyzed by paired student's t test (n=3).

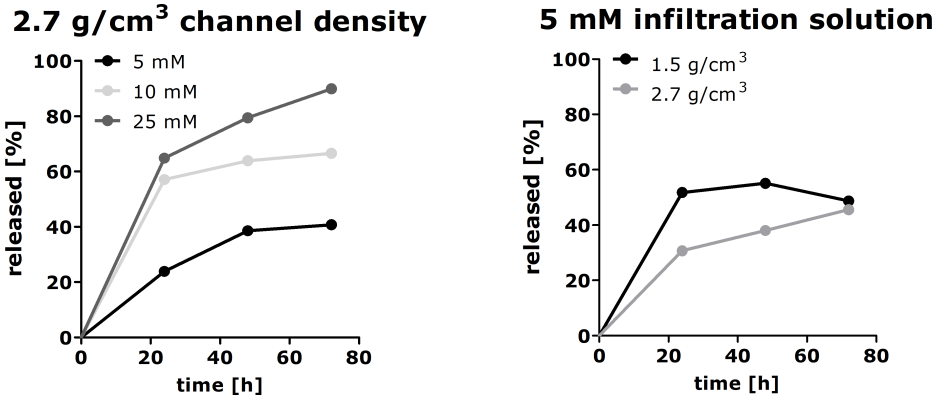

Figure A.5: Percental release measurements of AT101 upon different parameter settings. PDMS scaffolds with different parameter settings were produced on the basis of tetrapodal ZnO networks in collaboration with Florian Rasch (Institute for Materials Science). Those were filled with different concentrations of AT101 solution. To analyze release kinetics under cell-culture conditions, different parameters such as increasing concentrations of AT101 in the infiltration solution (left) and the channel density (right) were adjusted. The data are depicted as percentage of the amount of the released drug compared to the amount that was filled.

A.2 Publications related to this thesis

Rasch F*, Meyer RJ*, Schmitt C*, **Adamski V**, Saure LM, Schütt F, Lucius R, Hattermann K, Synowitz M, Held-Feindt J#, Adelung R#. Development of a 3D porous PDMS-network for glioblastoma therapy. 2019, *in preparation*

own contribution: assistance in template preparation, drug-release studies and data analysis

Adamski V, Hattermann K, Flüh C, Kubelt C, Lucius R, Synowitz M, Held-Feindt J. Chemotherapeutically induced dormancy entry and exit of glioma cells is differentially regulated by chemokines CXCL12, CXCL16 and CX3CL1. 2019, *in preparation*

own contribution: performed experiments regarding immunohistochemistry of tumor tissue, stimulations with single chemokines, knock-out studies and data analysis

Mehner M, Kubelt C, **Adamski V**, Schmitt C, Synowitz M, Held-Feindt J. Combined treatment of AT101 and demethoxycurcumin yield an enhanced anti-proliferative effect in human primary glioblastoma cells. 2019, *in preparation*

own contribution: assistance in preparation of experiments and data analysis

Flak DK*, **Adamski V***, Nowaczyk G, Szutkowski K, Przysiecka L, Synowitz M, Jurga S, Held-Feindt J. AT101-loaded cubosomes as an alternative for improved glioblastoma therapy. 2019, *in preparation*

own contribution: assistance in cubosome preparation and characterization, performed experiments regarding *in-vitro* studies of cubosomes

Schmitt C*, **Adamski V***, Rasch F, Adelung R, Lucius R, Synowitz M, Hattermann K, Held-Feindt J. Establishment of an in vivo adapted in vitro glioblastoma (in)complete resection co-culture model suitable for drug testing. *Ann Anat*, 2019, *submitted*

own contribution: performed experiments regarding the incomplete-resection model and data analysis

Flüh C, Mafael V, **Adamski V**, Synowitz M, Held-Feindt J. Dormancy and NKG2D system in brain metastases: Analysis of immunogenicity. *Oncol Rep*, 2019, *submitted*

own contribution: assistance in data analysis

Flüh C, Chitadze G, **Adamski V**, Hattermann K, Synowitz M, Kabelitz D,

Held-Feindt J. NKG2D ligands in glioma stem-like cells: expression in situ and in vitro. *Histochem Cell Biol*, 149:219 – 233, 2018. doi: 10.1007/s00418-018-1633-5

own contribution: assistance in preparation of experiments and data analysis

Adamski V*, Schmitt C*, Ceynowa F, Adelung R, Lucius R, Synowitz M, Hattermann K, Held-Feindt J. Effects of sequentially applied single and combined temozolomide, hydroxychloroquine and AT101 treatment in a long-term stimulation glioblastoma in vitro model. *J Cancer Res Clin Oncol*, 144:1475 – 1485, 2018. doi: 10.1007/s00432-018-2680-y

own contribution: performed experiments with tumor cells and data analysis

Adamski V, Hempelmann A, Flüh C, Lucius R, Synowitz M, Hattermann K#, Held-Feindt J#. Dormant glioblastoma cells acquire stem cell characteristics and are differentially affected by Temozolomide and AT101 treatment. *Oncotarget*, 8:108064 – 108078, 2017. doi: 10.18632/oncotarget.22514

own contribution: performed all experiments except for those presented in fig. 1 and data analysis

*/# these authors contributed equally

A.3 Further publications

Niemeyer J, Mentrup T, Heidasch R, Müller SA, Biswas U, Meyer RJ, Papadopoulou AA, Dederer V, Haug-Kröper M, **Adamski V**, Lüllmann-Rauch R, Bergmann M, Mayerhofer A, Saftig P, Wennemuth G, Jessberger R, Fluhrer R, Lichtenthaler SF, Lemberg MK, Schröder B. The intramembrane protease SPPL2c promotes male germ cell development by cleaving phospholamban. *EMBO Rep*, 20:e46449, 2019. doi: 10.15252/embr.201846449

Adamski V, Mentlein R, Lucius R, Synowitz M, Held-Feindt J, Hatterman K. The chemokine receptor CXCR6 evokes reverse signaling via the transmembrane chemokine CXCL16. *Int J Mol Sci*, 18:E1468, 2017. doi: 10.3390/ijms18071468

Adamski V, Schmitt AD, Flüh C, Synowitz M, Hattermann K, Held-Feindt J. Isolation and characterization of fast migrating human glioma cells in progression of malignant gliomas. *Oncol Res*, 25:341 – 353, 2017. doi: 10.3727/096504016X14737243054982

A.4 Danksagung

In den vergangenen dreieinhalb Jahren hat mich nicht nur die Arbeit an meiner Dissertation geprägt, sondern auch unzählige, unvergessliche Momente mit Freunden und Kollegen, die mir in dieser Zeit beigestanden und die Zeit mit mir zusammen erlebt haben. Keinen Augenblick aus dieser Zeit möchte ich missen, da sie mich bis hierhin und auf meinen weiteren Lebensweg geführt haben.

Ich möchte zunächst Professor Dr. Axel Scheidig danken, der bereits während meines Studiums immer ein offenes Ohr für Fragen und Probleme hatte und sich bereit erklärt hat, das Erstgutachten meiner Arbeit zu übernehmen.

Meinen ganz besonderen Dank möchte ich Professor Dr. Dr. Janka Held-Feindt aussprechen. Sie hat mich vor mittlerweile viereinhalb Jahren im Rahmen meiner Masterarbeit warmherzig in ihr Labor aufgenommen. Mit ihr habe ich wissenschaftliche und private Höhen und Tiefen durchlebt. Gemeinsame, fruchtbare Diskussionen, wunderbare, persönliche Gespräche und bedeutsame Momente auf Tagungen und Konferenzen haben mich in den viereinhalb Jahren enorm geprägt. Sie hat mich immerwährend ermutigt und mir die Möglichkeit gegeben, mich selbst zu verwirklichen.

Darüber hinaus wurde ich stets tatkräftig im Labor von Brigitte Rehmke und Fereshteh Ebrahim unterstützt. Durch ihre beständige Fröhlichkeit und Hilfsbereitschaft haben sie meinen Laboralltag bereichert. Dazu gehören auch Moiken Mehner und Rieke Johanna Meyer, die ich während ihrer medizinischen Doktorarbeit bzw. Masterarbeit begleiten durfte und die maßgeblich an unseren gemeinsamen Projekten gearbeitet haben.

Während dieser Zeit habe ich nicht nur wunderbare Kollegen, sondern auch Freunde wie Christina Schmitt, Anna-Sophia Buschhoff und Florian Rasch gewonnen. Neben wissenschaftlichen Diskussionen beim gemeinsamen Döneressen werden mir auch Twerking und "den Buschhoff machen" auf ewig in Erinnerung bleiben.

Ganz besonders wichtig war für mich der Rückhalt und das Verständnis meiner Eltern sowie die zahllosen, schönen Augenblicke mit all meinen Freunden, die mein Leben neben dem Labor verschönert haben. Eine unerschöpfliche Quelle an Kraft war mir meine beste Freundin Elena Reuber, ohne die mein Leben lange nicht so erfrischend, glücklich und lustig wäre.

Vielen Dank euch allen.

A.5 Eidesstattliche Erklärung

Hiermit erkläre ich an Eides Statt, dass ich die vorliegende Dissertation nach Inhalt und Form selbstständig unter der Beratung durch meinen Betreuer und ohne fremde Hilfe oder nicht aufgeführte Quellen angefertigt habe. Wörtlich oder inhaltlich zitierte Stellen sind als solche kenntlich gemacht.
Außerdem versichere ich, dass weder ich noch ein anderer diese Arbeit an einer anderen Stelle im Rahmen eines Promotionsprüfungsverfahrens vorgelegt haben.
Teile dieser Arbeit wurden bereits in wissenschaflichen Fachmagazinen publiziert oder sind zur Veröffentlichung eingereicht.
Weiterhin wurde die Arbeit unter Einhaltung der Regeln über gute wissenschaftliche Praxis der Deutschen Forschungsgemeinschaft erstellt.
Zusätzlich bekräftige ich, dass mir noch kein akademischer Grad entzogen wurde.

Kiel, den

Vivian Adamski